$LiNbO_3$ and $Li_6Y(BO_3)_3$ as optical materials for telecommunication

zur Erlangung des akademischen Grades eines DOKTORS
DER NATURWISSENSCHAFTEN (Dr. rer. nat.) dem Department
Physik der Fakultät für Naturwissenschaften
der Universität Paderborn

genehmigte
DISSERTATION

von

M.Sc. Sara Arceiz Casas

aus Zaragoza, Spanien

Referent:	Prof. Dr. Siegmund Greulich-Weber
Korreferent:	Prof. Dr. Wolf Gero Schmidt

(Dissertation Universität Paderborn)

Vorwort

Die vorliegende Arbeit entstand während meiner Tätigkeit als wissenschaftliche Mitarbeiterin am Lehrstuhl für Nanostrukturierung, Nanoanalytik und Photonische Materialien der Universität Paderborn unter der Leitung von Herrn Prof. Dr. Jörg Lindner. Allen, die mich bei dieser Arbeit unterstützt haben, möchte ich an dieser Stelle herzlich danken.

An erster Stelle gilt der Dank meinem Doktorvater Herrn Prof. Dr. Siegmund Greulich-Weber, der mich in den vergangenen Jahren in fachlicher sowie persönlicher Hinsicht gefördert und motiviert hat. Seine wertvollen Hinweise und Anregungen trugen wesentlich zum Gelingen dieser Arbeit bei. Herrn Prof. Dr. Wolf Gero Schmidt danke ich sehr herzlich für die freundliche Übernahme des Koreferats.

Mein Dank gilt allen meinen Kollegen am Lehrstuhl die mich im Laufe der Zeit immer wieder unterstützten und motivierten. Die Zusammenarbeit mit Euch hat mir immer große Freude gemacht und euer starkes Engagement und der persönliche Beistand haben mir eine schöne und mit Sicherheit unvergessliche Zeit beschert. Dafür möchte ich Euch danken!

Viele der in dieser Arbeit umgesetzten Ideen entstanden durch eine Zusammenarbeit mit Prof. Dr. Simone Sanna und Dr. Gábor Corradi und wurden durch interessante Gespräche mit den Projektpartnern angeregt. Ich möchte Ihnen für die fruchtbare Zusammenarbeit danken.

Ganz besonders möchte ich mich bei meinen Eltern und Familie bedanken. Ohne Eure Unterstützung hätte ich diese Arbeit nicht fertigstellen können. Dieser Dank geht ebenfalls an meinem lieben "querido" Eduardo. Deine Interesse am Gelingen der Arbeit hat mich stets motiviert.

Paderborn, März 2018

Sara Arceiz Casas

Contents

Abstract

This thesis is devoted to the investigation of two optical materials that are currently employed in a wide range of applications.

Lithium niobate is the most relevant material for optoelectronic devices, because of its good optical quality and high electrooptic coefficients. Waveguides and integrated optic devices have useful applications, and are made of titanium indiffused in lithium niobate. However, titanium indiffused lithium niobate waveguides are heavily affected by small percentages of iron impurities. Indeed, the photorefractive sensitivity is increased by the presence of a few ppm of iron impurities in the waveguides. In addition, it was suggested that titanium stabilizes iron against oxidation, enhancing the photorefractive sensitivity. Unfortunately, neither the complexes formed by iron and titanium nor the mechanisms leading to this optical damage are known.

The first purpose of this thesis is to report the microscopic and electronic structures of iron and titanium dopants in lithium niobate. By means of electron paramagnetic resonance spectroscopy, iron and titanium ions were investigated in nearly stoichiometric and congruent lithium niobate samples. Evidence of a weak (but not negligible) interaction between iron and titanium was presented and, therefore, the stabilisation of iron by titanium seems to be unlikely.

On the other hand, the lithium yttrium borate crystal is a good host material for lasers due to the easy incorporation of rare earths. Indeed, erbium is interesting in telecommunications due to its near infrared emission, whereas ytterbium is favourable for tuneable and ultra-fast lasers owing to its broad emission band. Although the doping with both ions has been previously investigated, EPR experiments in erbium and ytterbium doped lithium yttrium borate crystals were still missing. Therefore, a detailed EPR analysis of the ground state is performed. Furthermore, the novel iron dopant lithium yttrium borate crystal was studied for the first time.

Zusammenfassung

Diese Arbeit ist der Untersuchung zweier optischer Materialien gewidmet, die derzeit in einer breiten Palette von Anwendungen benutzt werden.

Lithiumniobat ist aufgrund seiner guten optischen Qualität und hohen elektrooptischen Koeffizienten das wichtigste Material für optoelektronische Bauelemente. Wellenleiter und integriert-optische Bauelemente finden Anwendung in der Telekommunikation, und bestehen aus Titan eindiffundiert in Lithiumniobat. Jedoch werden Titan eindiffundierte Lithiumniobat-Wellenleiter stark durch geringe Konzentration an Eisenverunreinigungen beeinflusst. Tatsächlich wird die photorefraktive Empfindlichkeit durch die Anwesenheit von einigen ppm Eisen in den Wellenleitern erhöht. Darüber hinaus wurde vorgeschlagen, dass Titan Eisen gegen Oxidation stabilisiert, was die photorefraktive Empfindlichkeit verbessert. Leider sind weder die aus Eisen und Titan gebildete Komplexe noch die Mechanismen, die zu dieser optischen Beeinträchtigung führen, bekannt.

Das erste Ziel dieser Arbeit ist, die mikroskopischen und elektronischen Strukturen von Eisen und Titan-Dotierstoffen in Lithiumniobat zu beschreiben. Mittels paramagnetischer Elektronenspinresonanz Spektroskopie wurden Eisen- und Titan-Ionen in Proben aus nahezu stöchiometrischem und kongruentem Lithiumniobat untersucht. Der Nachweis einer schwachen (aber nicht vernachlässigbaren) Wechselwirkung zwischen Eisen und Titan wird vorgestellt und daher scheint die Stabilisierung von Eisen durch Titan unwahrscheinlich.

Lithium-Yttrium-Borat ist ein vielversprechendes Wirtsmaterial für Laseranwendungen wegen der einfachen Aufnahme von Seltenen Erden in das Gitter. Bekanntermaßen ist Erbium aufgrund seiner Nah-Infrarot-Emission interessant in der Telekommunikation, während Ytterbium aufgrund seiner breiten Emissionsbande für abstimmbare und ultraschnelle Laseranwendungen günstig ist. Obwohl die Dotierung mit beiden Ionen bereits zuvor untersucht wurde, ist die genaue mikroskopische und elektronische Struktur dieser Dotierung nicht bekannt. Mit EPR-Experimenten an Erbium- und Ytterbium-dotiertem Lithium-Yttrium-Borat sollen helfen, die Struktur aufzuklären. Daher wurde eine detaillierte EPR Analyse des Grundzustands durchgeführt. Weiterhin wurde erstmals Eisen-dotiertes Lithium-Yttrium-Borat untersucht.

1 Introduction

Diamonds are a girl's best friend. ∼(Marilyn Monroe).

Although pure diamonds are perfectly transparent and colourless, diamonds exist also in a variety of colours (grey, white, blue, yellow, orange, red, green, pink, brown and black). The colour of the diamonds is due to interstitial impurities or structural defects, currently addressed to as colour centres. Small impurity concentrations (of the order of 0.1 mol %) result in different coloured diamonds, indeed. Following this visual example, point defects in solid state can change not only the colour of the material but also many of its physical properties, including the optical properties. As an example, titanium is indiffused in lithium niobate, with the aim of increasing the refractive index to create single mode waveguides. Therefore, the knowledge of the microscopic and electronic structure of the impurities is the key to understand the properties of intentionally or unintentionally doped crystals and also to enhance (if it is necessary) their physical properties.

Suitable methods to investigate the microscopic and electronic structure of point defects are magnetic resonance methods and, in particular, electron paramagnetic resonance (EPR). The electron paramagnetic resonance is the standard method to enlighten the structure of a paramagnetic impurity. Owing to EPR spectroscopy, essential contributions to the characterization of defects are provided. In addition, combined with photoluminescence (PL) the energy levels of the defects are studied in the band gap [1]

Amongst the most important applications of ferroelectric lithium niobate, frequency converters and holographic devices are commercially relevant. Titanium indiffusion is used to introduce the refraction index profiles needed, for instance, for the realization of waveguides; while iron doping enhances electrooptic coefficients and the photorefractive properties, for instance, for holographic data storage. On the one hand, titanium indiffusion in lithium niobate provides single mode waveguides for visible and infrared beams and, in addition, titanium increases both the ordinary and extraordinary refractive indexes without directly increasing the photorefractivity. On the other hand, the photorefractive effect or light-induced change in the refractive index causes degradation of the waveguide and therefore impairs its performance, particularly in the UV and

visible spectral regions. This effect heavily depends on the presence of different valence states of iron (Fe^{2+} and Fe^{3+}), the prototypical photorefractive dopant [2, 3].

Unfortunately, iron impurities are frequently found even in undoped (nominally pure) lithium niobate crystals. Consequently, the optical properties of titanium indiffused lithium niobate waveguides are worsened by the presence of a small percentage of iron impurities as low as a few ppm. Indeed, Gericke et al. pointed out that Ti^{4+} ions stabilize Fe^{2+} ions in the waveguide, although the stabilization process was not really understood [4]. Unluckily, neither the complexes formed by iron and titanium ions nor the mechanism leading to this optical damage are known. Therefore, the key question is to verify the assumption that Fe^{2+} in lithium niobate is stabilized by the presence of titanium against Fe^{3+} and to understand the processes which lead to the stabilization. The first part of this work is dedicated to this question.

With the aim of answering “how titanium stabilizes iron”, iron single doped, titanium single doped and iron-titanium co-doped nearly stoichiometric and congruent lithium niobate samples were expressly grown. These samples were investigated by experimental techniques such as EPR spectroscopy and PL and within a theoretical approach involving density functional theory (DFT) calculations. After the comprehension of the microscopic and electronic structure of iron and titanium single doped lithium niobate crystals; iron-titanium co-doped lithium niobate crystals were considered in order to understand the kind of complex that they form and/or the interaction that they experience amongst each other in the lithium niobate host material.

In the second part of this thesis lithium yttrium borate crystals (LYB) were considered. Lithium yttrium borate single crystals are good candidates for laser materials due to their flexibility and the easy incorporation of rare earth dopants (e.g. Er^{3+}, Yb^{3+}) [5, 6]. Indeed, LYB single crystals may serve as excellent host matrices with long enough dipole relaxation times of the rare earth ions suitable for quantum optical experiments where atomic coherence plays a crucial role.

Erbium doped materials have been widely investigated due to its emission around 1550nm, which is eye-safe and located in the optical communication window [7]. Therefore, it has attracted more and more attention for many practical applications such as eye-safe LIDAR, range finder and telecommunication [8]. In addition, erbium doped LYB crystal, with relatively large stimulated emission cross section and broad emission band, has been reported to be a promising medium for tunable and ultra-short lasers as well as laser amplifiers used in optical communication [8]. Although different spectroscopic analysis of Er^{3+} in LYB have also been reported, a detailed microscopic and electronic structure of erbium in LYB was still missing. Therefore, a detailed EPR

analysis of the ground state is given in this thesis.

On the other hand, ytterbium doped materials have shown a very simple energy level diagram consisting of two manifolds (the ground state $^2F_{7/2}$ and the $^2F_{5/2}$ excited state). The broad emission band characteristic of Yb^{3+} is very favourable for tunable or ultra-fast lasers. Ytterbium doped lithium yttrium borate crystal is especially interesting because of its long fluorescence lifetime of 1.1 ms and the broad fluorescence spectrum [9], which are promising for high energy laser systems and short pulse generation. Although the Yb:LYB system has been well documented [6, 10], EPR experiments on ytterbium doped LYB single crystal were still missing. Consequently, detailed EPR investigation of the ground state has been performed and described here.

Finally, a novel dopant material for lithium yttrium borate was investigated: Fe. Iron doped samples were specifically grown and studied by EPR spectroscopy. Iron centres seem to behave similarly as iron centres in LN, although the host material is different.

This thesis is organized as follows. It begins with the introduction of the considered host materials, which is covered in Chapter 2 Materials. Therein, not only the host materials are presented but also their relevant dopants are shown. In the next chapter (Chapter 3 Methods), the focus changes to the utilized experimental and theoretical methods, which lead to the characterization of the extrinsic defects in the crystal. A detailed overview of the EPR and PL measurements that are considered in the present work is given in Chapter 4 Measurements. In Chapter 5 Results, a review over the experimentally obtained results is presented. In Chapter 6 Discussion, the experimental results were interpreted and discussed. Finally, a summary of the thesis is given in Chapter 7 Summary.

2 Materials

Lithium niobate plays a prominent role amongst ferroelectric materials, as it is employed in manifold applications. Lithium yttrium borate seems to have a good potential as a laser host material, instead. In this chapter, the host materials and different dopant ions investigated in this thesis are presented. In the first part, lithium niobate and a choice of its most prominent dopants (iron, titanium single doping and co-doping) are introduced. In the second part, lithium yttrium borate and its more relevant dopants (erbium, ytterbium and iron) are presented. The purpose of this chapter is to describe and understand the systems investigated in this work and how doping affects their properties.

2.1 Lithium niobate

Lithium niobate ($LiNbO_3$) is an artificial material composed by lithium (Li), niobium (Nb) and oxygen (O). It is colourless, insoluble in water and organic solvents, chemically stable and possesses high melting point ($T \approx 1200\ ^\circ C$) [11]. Lithium niobate (LN) is ferroelectric at room temperature, and is characterized by large pyroelectric, piezoelectric, electro-optic and photo-elastic coefficients. In addition, it is naturally birefringent and exhibits a very strong photovoltaic effect. The mutual combination of thermal, mechanic, electric and optic properties makes lithium niobate one of the most widely employed materials in a broad field of applications. Thereby lithium niobate is an ideal candidate in many applications such as acoustic wave transducers, acoustic filters, optical amplitude modulators, optical phase modulators, second-harmonic generators, beam deflectors, dielectric waveguides, memory elements, holographic data processing devices and much more.

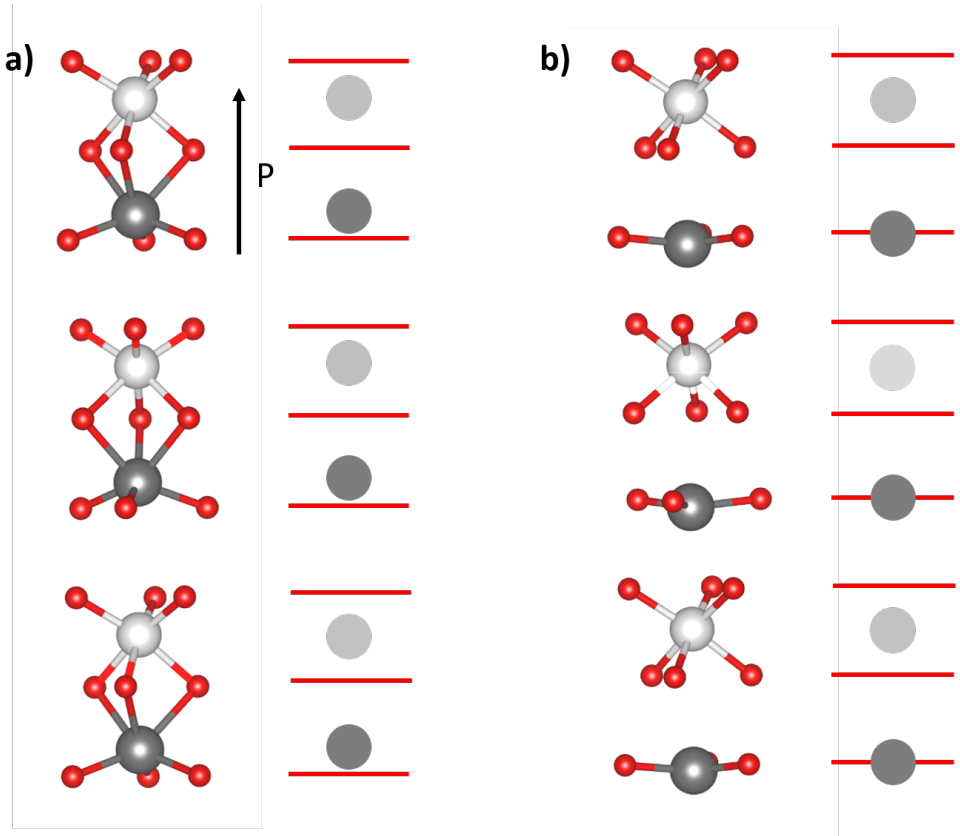

Figure 1: Crystal structure of $LiNbO_3$ at temperature (a) below (ferroelectric phase) and (b) above (paraelectric phase) the Curie temperature ($\theta_c = 1206$ °C) [11]. The crystal structure is shown with oxygen atoms in red, lithium atoms in light grey and niobium in dark grey circles. On the right side, a schematic representation of the crystal structure viewed perpendicular to the principal axis c. The horizontal red lines represent the oxygen layers. Picture was redrawn from [12].

At room temperature, the lithium niobate crystal belongs to the rhombohedral (trigonal) space group R3c, with a point group 3m (C_{3v} in Schönflies notation). In this configuration, the crystal structure is invariant under rotation of 120° and exhibits a mirror plane containing the rotation axis. At temperatures above the Curie temperature ($\theta_c = 1206$ °C for stoichiometric lithium niobate) [11] it belongs to the space group $R\bar{3}c$, with a point group $\bar{3}m$ (D_{3d} in Schönflies notation). In this case, the structure includes the symmetry operation of the C_{3v} group and, in addition, is invariant under inversion, rotation of 180° and improper rotation of 60° [14]. Figure 1 shows a schematic representation of crystal structure for the ferroelectric (C_{3v}) and paraelectric phase (D_{3d}).

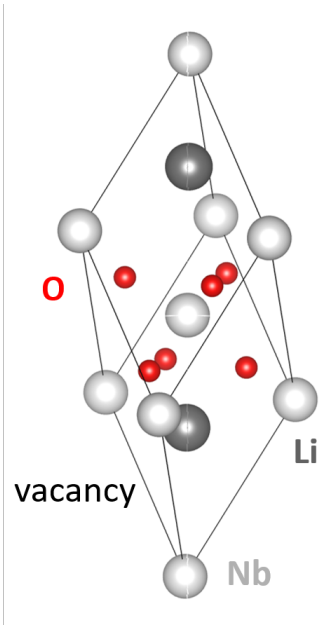

Figure 2: Rhombohedral cell of lithium niobate. Light grey circles denote niobium ions, dark grey lithium and red oxygen.

In the paramagnetic phase, niobium atoms are embedded in the centre of oxygen octahedra. Although in Figure 1 (**b**) the lithium atoms are shown in an average position, i.e. in the oxygen layer, they swing around the oxygen plane at high temperatures. Within this configuration, the crystal is non-polar. Lowering the temperature, lithium ions moved upwards (or downwards) from their average position, lying above (or below) the oxygen layer, as seen in Figure 1 (**a**). Nb ions are no longer at the center of the oxygen cages. Due to the coulomb repulsion, both cations are displaced in the same direction (see Figure 1 (**b**)). This atomic rearrangement has two important consequences. On the one hand, the crystal loses the inversion symmetry and becomes non-centrosymmetric (space group R3c), which has a crucial influence on the optical properties. On the other hand, the barycenter of the positive and negative charges is displaced, giving rise to a pronounced spontaneous polarization along the c axis, which is as large as 0.7 C/m^2 [11]. The polarization is parallel to the cation displacement. Crystal cuts perpendicular to the polarization give rise to polar surfaces. The spontaneous polarization points out of the positive surface. Experimentally, the positive surface is the one that becomes negative upon compression. Alternatively, the positive surface is the one which becomes negative upon heating. As the reader can imagine, both cationic displacements in the positive and in the negative direction can occur, providing antiparallel domains observed in ferroelectric crystals.

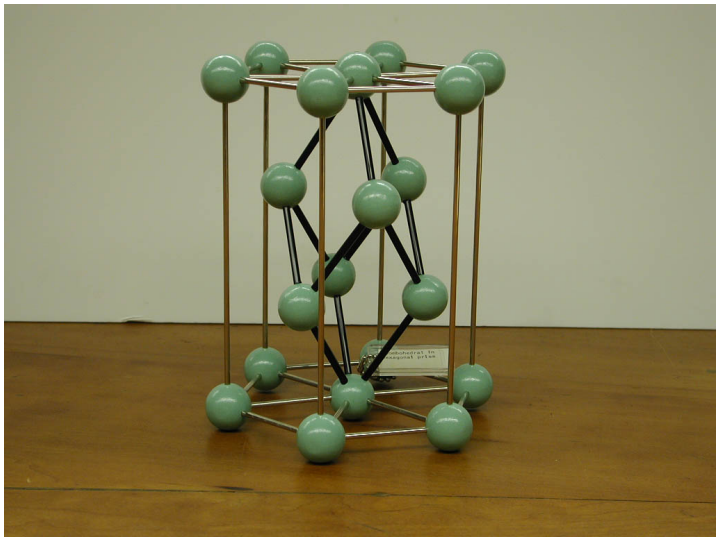

Figure 3: Rhombohedral cell (black lines) embedded in a hexagonal cell (gold lines). The graphic is taken from [13].

With the aim of establishing a reference system for lithium niobate, in the following not only the rhombohedral choice of axes but also hexagonal and orthogonal choice of axes are discussed. The rhombohedral cell of lithium niobate is represented in Figure 2. In a rhombohedral cell, the axes possess equal length and equal interaxial angles (about 56°). The principal axis (c, parallel to the polarization vector) is in the body diagonal of the rhombohedron. Rhombohedral and hexagonal cells are related, with the first one is embedded in the last one, as Figure 3 shows. The hexagonal axes can be selected perpendicular to the mirror planes (x_H, y_H both defining the lattice parameter a_H) and the third axis is conveniently chosen as the piezoelectrically positive axis (z_H or c principal axis, whose lattice parameter is denoted by c_H). Rhombohedral and hexagonal cells are advantageous as they contain a small number of atoms (10 and 30, respectively) [14]. In Table 1, the unit cell parameters are summarized for the described cells.

Rhombohedral	$a_\mathrm{R} = 5.496$Å	$\alpha_\mathrm{R} = 55.87°$
Hexagonal	$a_\mathrm{H} = 5.150$Å	$c_\mathrm{H} = 13.867$Å

Table 1: Unit cell parameters for rhombohedral (R) and hexagonal (H) choice of axes [14]. a_R is the lattice parameter and α_R the angle that the axes form in the rhombohedral cell. a_H and c_H are the lattice parameter perpendicular and parallel to the z axis respectively in the hexagonal unit cell.

However, for most typical applications, an orthorhombic (cartesian) coordinate system is considered. Most tensor components of physical properties are given respect to these axes (elastic moduli, piezoelectric coefficients, dielectric constants, etc.). In the cartesian system, the z axis is chosen parallel to the c axis (or z_H, the principal axis) and x is chosen to coincide with any of the a_R axes. Finally, y is perpendicular to z and x, forming a right-handed system and lying in a plane of mirror symmetry [14].

At the beginning of the chapter, it was mentioned that LN is an artificial material, which means that lithium niobate is grown from a melt of LiO_2 and Nb_2O [11]. The concentration of each compound determines the growth of a stoichiometric or congruent crystal. The last one is Li deficient. It is assumed that Nb ions are partially incorporated in Li vacancies, leading to intrinsic defects (V_{Li} and Nb_{Li}). Correspondingly, further lattice defects must occur to warrant charge neutrality. The most energetically favourable mechanism is the compensation of Nb antisites by Li vacancies. Oxygen vacancies in as grown material are less probable to occur because they are not very favourable energetically [11, 15]. In contrast, a stoichiometric crystal is almost defect free. It is well known that the concentration rate ([Li]/[Nb]) affects several physical properties strongly (like phase transition temperatures, birefringence or UV band edge).

Due to the Li deficiency and to the presence of 1/3 vacant octahedra, dopant ions are easily incorporated in the lithium niobate lattice. Indeed, LN is known to be able to host a fairly highly number of extrinsic defects (several mol % of transition metal ions or about 1 mol % of rare earths) [14]. The largest part of dopants is incorporated at the Li lattice site. This fact may qualitatively be explained owing to the size difference between the octahedra containing Li and the octahedral containing Nb atoms. The octahedron containing Li atoms is larger than the one containing Nb, and therefore impurities are predominantly incorporated at Li place [16]. Oxygen vacancies are energetically unfavourable; however they might provide a model for hole polarons, identified by Schirmer and von der Linde [17]. Self-trapped hole centres are accompanied by a strong, wide optical absorption band.

Point defects in $LiNbO_3$ as induced e.g. by reduction treatments and photoexcitation might provide structural models for electronic polarons, which are employed to interpret the optical spectra of LN. A polaron is a charger carrier self-trapped at essentially one site in the host material. They are formed due to Coulomb interaction and phonon coupling of the photoexcited charge carriers with the host ions [11]. The free polaron (Nb_{Nb}^{4+}) is characterized by a broad optical absorption band centred at about 1.0 eV ($\approx$ 1280 nm). The bound small polaron (Nb_{Li}^{4+}) is accompanied by

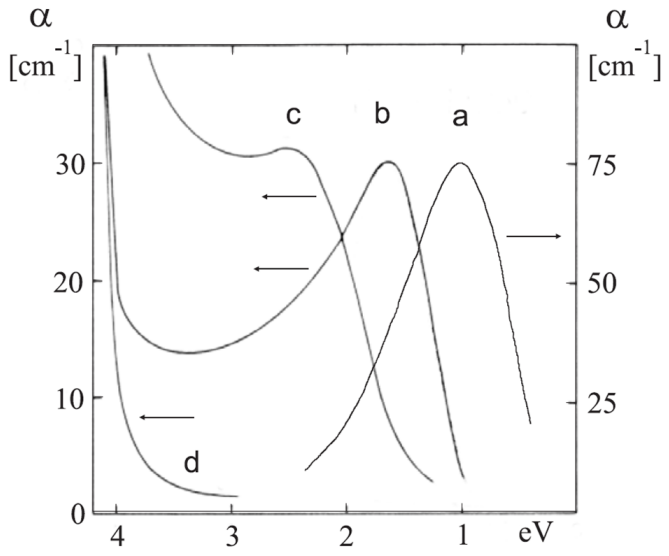

Figure 4: Optical absorption bands of reduced congruent $LiNbO_3$ (a) free polaron Nb^{4+}_{Nb} (b) bound polaron Nb^{4+}_{Li} (c) bound bipolaron Nb^{4+}_{Nb}-Nb^{4+}_{Li} (d) untreated crystal. Band a (1 eV) results after a reduction of a 6%Mg doped crystal, during 9h at 500°C. Band b (1.6 eV) results after 1h at 900°C in the dark and by illumination (xenon arc at 80 K) and band c (2.5 eV) before illumination. The graphic was taken from [18].

an absorption band centred at 1.6 eV ($\approx$ 760 nm). Bipolarons (Nb^{4+}_{Nb}-Nb^{4+}_{Li}) feature a broad absorption band at 2.5 eV ($\approx$ 500 nm) (see Figure 4) [18].

Lithium niobate is known to be a photorefractive material. Under illumination, refractive index changes are produced, commonly referred as photorefractive effect. Indeed, it is a two steps process: first charge migration (by diffusion, drift, bulk photovoltaic effect or a combination of them) followed by an electro-optic effect (linear and/or quadratic). In lithium niobate the dominant charge migration mechanism is bulk photovoltaic and the dominant electro-optic effect is linear (Pockels effect) [12]. The photorefractive sensitivity is modified by dopant ions as, for example, iron.

2.1.1 Iron doped lithium niobate

Iron is a transition metal (with atomic electronic configuration [Ar] $3d^6 4s^2$) and occurs with a charge state Fe^{+2} or Fe^{+3} in lithium niobate. It is still a theme of discussion, where iron ions are

embedded in the lithium niobate crystal structure. There exist three different sites (Li, Nb or V place) where iron ions could be accommodated. Iron has been suggested to replace both lithium or niobium, and the precise lattice determination of the lattice site is a challenging task. The lithium and niobium sites possess the same axial symmetry C_3 and similar octahedra surroundings. In addition, the ionic radii of Fe^{+3} (0.064 nm) is similar both to that of Li^{+} (0.068 nm) and of Nb^{5+} (0.069 nm). Another feature that should be taken into account is the different amount of excess electric charge that should be compensated if iron is accommodated at the in Li, Nb or vacancy place. Finally, depending on the crystal composition (stoichiometric or congruent crystal) and the concentration of impurities, the position of iron in the crystal structure is influenced [19].

Iron doped lithium niobate has been matter of study since more than five decades. Electron paramagnetic resonance investigations have demonstrated that iron centres have C_3 symmetry (lower symmetry than the host lattice, with a zero-field splitting of the order 1700 MHz [19–28]. However, this excludes charge compensations in the neighbourhood: lithium vacancies (V_{Li}) for iron substituting lithium (Fe_{Li}^{3+}) or oxygen vacancies (V_O) for iron substituting niobium (Fe_{Nb}^{3+}) would lower the symmetry of the defect centres. Fe^{3+} ions were found at the lithium site [19–21, 29] as well as at the Nb site [23, 30, 31]. Although several authors affirm that Fe^{3+} occupies both Nb and Li places [25–28, 32–34] in lithium niobate.

In the frame of this thesis, it seems plausible that iron ions substitute lithium in stoichiometric lithium niobate and this is shown at the end of the dissertation. This assumption is suggested by the Li deficiency in congruent crystals and is generally accepted [19, 35]. Moreover, niobium forms a strong covalent bond with the surrounding oxygen octahedron. Therefore, the octahedron is smaller than the lithium octahedron, hardly providing enough place for Fe^{3+} defects. In highly doped iron lithium niobate, iron ions are expected to first occupy the lithium site and later, after a threshold concentration, the niobium site. This holds both for stoichiometric and congruent LN. It should be taken into account that in congruent lithium niobate, the defect quantity is higher than in a stoichiometric crystal [11]. This feature is reflected in the EPR spectra by broadening the linewidth.

Absorption spectra of iron doped lithium niobate are shown in Figure 5. They show the most intense feature for a photon energy of about 2.5 eV. This optical excitation is a broad band ranging from 400 nm to 550 nm due to the excitation of electrons from Fe^{2+} into the conduction band [36].

In lithium niobate, iron plays a special role in the photorefractive process. Iron doping produces a large enhancement of the photorefractive sensitivity, that is changing the refractive index by light

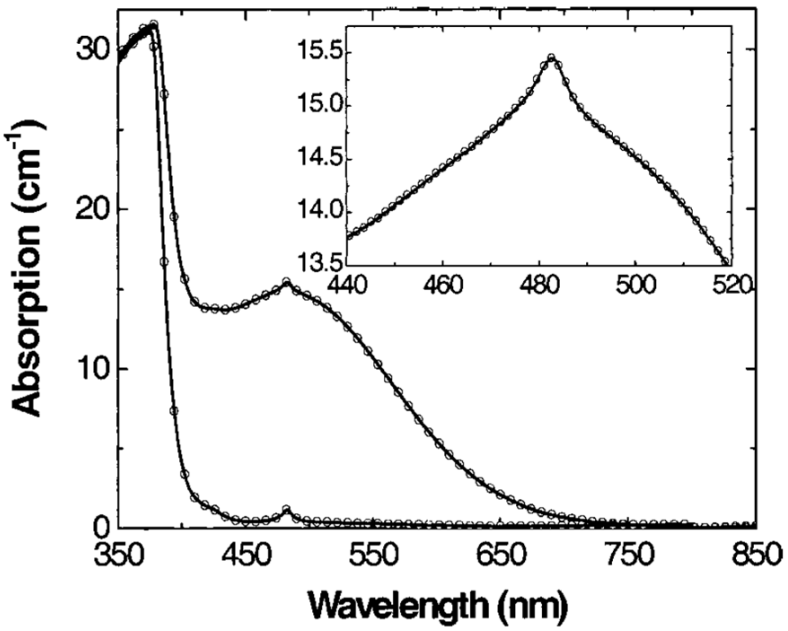

Figure 5: Absorption spectra of a reduced and oxidized iron doped lithium niobate crystal. Circles are experimental data. Graphic is taken from [36].

irradiation. This property may be used for storage of information in holographic applications. Nevertheless, it is undesirable for optical devices such as waveguides exploiting the nonlinear optical and electro optic properties and it is therefore addressed to as “optical damage” [37, 38].

As a reminder, iron is incorporated in lithium niobate in the valence states Fe^{+2} and Fe^{+3}. Photorefractivity occurs as a result of electro optic effect and photoconductivity. On the one hand, electric fields in electro-optic materials produce changes in the refractive index (Pockels effect). On the other hand, light of a determined wavelength on a photoconductive material generates electric charge carriers that move freely under the action of inner electric fields. In the case of iron doped lithium niobate, both effects involve Fe centres: upon illumination, one electron from Fe^{+2} is excited to the conduction band; owing to drift, diffusion and bulk photovoltaic effect they migrate until they are trapped by a Fe^{3+} in dark areas [37]. For light intensities higher than 100 W/cm^2, shallow centres play a role (Nb_{Li}) in the charge transport process (as shows Figure 6) [39, 40]. Under inhomogeneous illumination, the charge carriers accumulate in the dark areas and with opposite charge in the bright areas, producing an electric field and, therefore, the refractive index is changed [38].

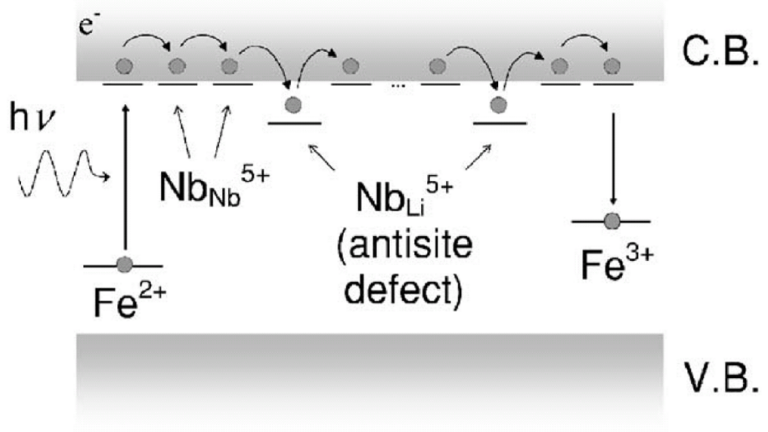

Figure 6: Schematic representation of the photorefractive process in iron doped lithium niobate. Under illumination, an electron from Fe^{2+} is promoted to the conduction band (C.B.) and later recombined through Nb_{Li}^{5+} to a Fe^{3+}. The graphic was taken from [41].

The recording of a holographic grating is due to an interference light pattern. In $LiNbO_3$, holograms can be stored several months and read-out is performed owing to the diffraction of a weak probe beam at the Bragg condition ($2d \sin\theta = n\lambda$). The photorefractive sensitivity of iron doped lithium niobate samples within an external electric field has been studied recently. Figure 7 shows the result of the experiments carried by Luennemann [42]. The photorefractive sensitivity is proportional to the application of high external electric fields and proportional to the concentration of Fe^{2+} [42].

However, lithium niobate is also often used as an optical device (for example waveguides), which exploits its nonlinear optical and electro-optic properties. For these applications, the photorefractive effect is undesired and considered as optical damage. Unfortunately, several ppm of iron are always found in nominally undoped lithium niobate [37], which already enhance the photorefractive properties of the material. To control and reduce the photorefractive sensitivity, the concentration of iron centres might be reduced by introducing some optical damage resistant ions (for example Mg, Zn, In) or increasing the operating temperature or by oxidation treatment [43].

As it is shown in Figure 8, increasing the Zn concentration (4% and 5.3%) in lithium niobate, the photorefraction is reduced, independently of the light intensity.

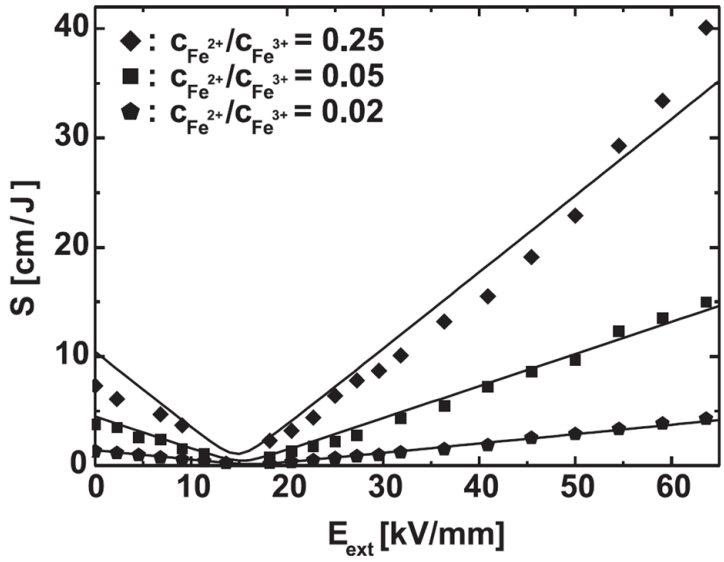

Figure 7: Sensitivity (S) versus external applied electric field (E_{ext}) for the three samples with the same concentration of iron but different concentration of Fe^{3+} and Fe^{2+}. The symbols represent the experimental data and the lines are fit using the one-centre model. Graphic was taken from [42].

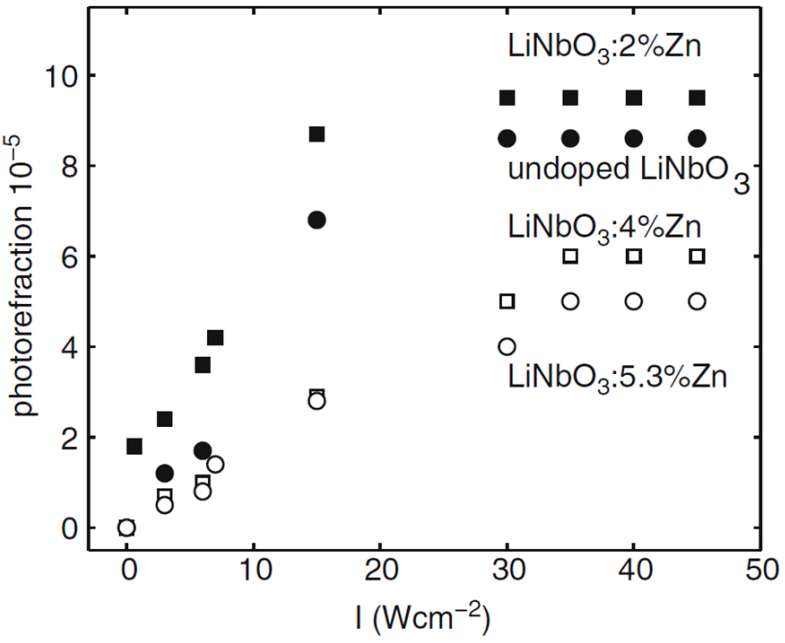

Figure 8: Photorefraction as a function of the light intensity for Zn doped $LiNbO_3$ by different Zn concentrations. Graphic was taken from [11].

2.1.2 Titanium doped lithium niobate

Titanium is a transition metal (atomic electronic configuration [Ar] $3d^2$ $4s^2$) and is introduced in lithium niobate within the fourfold valence state (Ti^{4+}). Similar to iron, it could occupy three equivalent sites (Li, Nb or V). However, Ti^{4+} is a non-paramagnetic ion precluding EPR investigation to identify its position. A reduction treatment must be performed to obtain paramagnetic Ti^{3+}. After a thermal treating, titanium was found at the lithium place [3, 44, 45] but also at the niobium site in magnesium co-doped lithium niobate [46]. Moreover, Juppe and Schirmer suggested that Ti moves under reduction from niobium to lithium site. Electron paramagnetic resonance investigations describe titanium ion in lithium niobate as an axial centre with an axial g-tensor [44].

At the end of the thesis, it will be supported that titanium, in a similar way as iron, occupies a regular lithium site in LN sample. It is supposed, that the large Li octahedron offers more space than the smaller niobium octahedron, thus facilitating the Ti incorporation at the Li site. Moreover, owing to the stable Coulomb interaction between oxygen and niobium, the niobium substitution requires higher energy than lithium substitution.

Titanium is usually indiffused in lithium niobate to fabricate waveguides. The advantage to fabricate waveguide in lithium niobate with titanium is the formation of single modes waveguides for visible and near infrared beams produced for all sample cuts (x, y and z) [47]. In addition, Ti is the only known dopant which increases both the ordinary and extraordinary refractive index of the material without directly increasing the photorefractivity. Nevertheless, its utility is limited due to other photorefractive sources. Small percentages of iron impurities are frequently found even in undoped (nominally pure) crystals [2]. To reduce the optical damage (also known as photorefractive effect), several techniques were used: thermal fixing (heating at 150°C) and adding optical damage resistant ions (for example Mg, Zn or In).

Under illumination of reduced titanium doped lithium niobate crystals, two absorption bands are observed. For Ti at the lithium site, the peaks are at about 1.8 and 3.0 eV and for Ti at the niobium site the same peaks are found at 1.62 and 2.65 eV [48]. The optical absorption spectra is illustrated in Figure 9.

Until now, the effect of a single dopant (either Fe or Ti) in lithium niobate crystals was described. However, intentionally or unintentionally co-doped samples may enhance physical properties as for example the already mentioned photorefractivity.

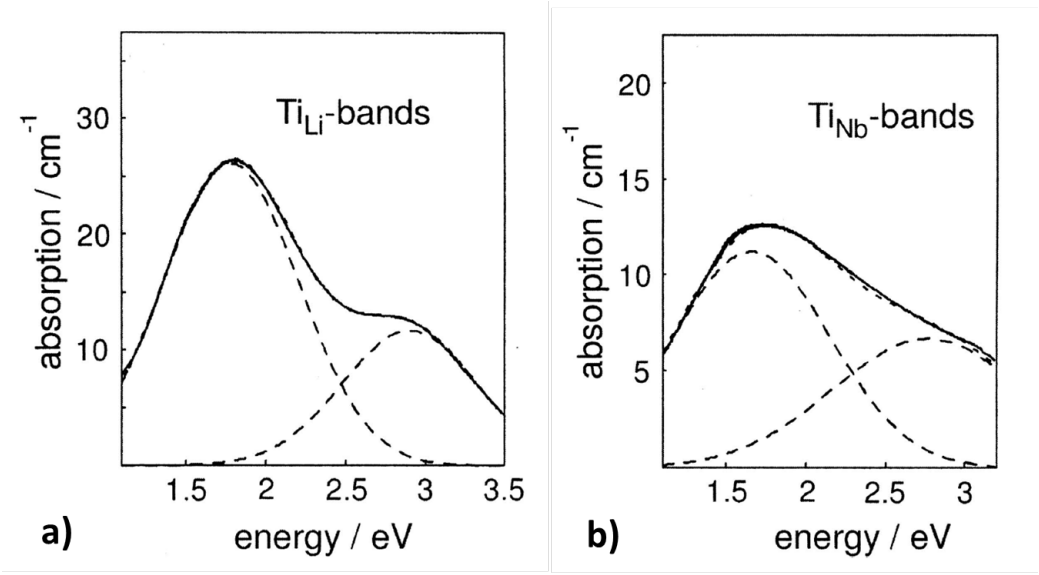

Figure 9: Optical absorption spectra of reduced Ti-doped lithium niobate at room temperature of z-cut crystals. Graphic was taken from [48].

2.1.3 Iron-titanium co-doped lithium niobate

Unfortunately, some ppm of iron are always present in lithium niobate, causing optical damage in titanium indiffused lithium niobate waveguides. In 1985, Nisius et al. [2] assumed the stabilization of Fe^{2+} centres in the region of large titanium concentrations. Two years later, this assumption was demonstrated [4]. In contrast, further two years later Sanz-García et al. [3] affirmed that titanium does not influence the reduction behaviour of iron, because iron is reduced before titanium.

In the frame of this thesis, iron and titanium single doping as well as iron titanium co-doping were investigated to understand the complex interaction that exists between iron and titanium in co-doped lithium niobate.

2.2 Lythium yttrium borate

Lithium yttrium borate ($Li_6Y(BO_3)_3$) is an artificial material containing lithium (Li), yttrium (Y), boron (B) and oxygen (O). It is colourless and has a high melting point (T≈800 °C). Borate crystals present a complex lattice structure providing nonlinear optic, acousto-optic and piezo electric

properties [49]. Consequently, borate compounds are currently very attractive, for example, as scintillators, phosphors and laser materials [6].

Lithium yttrium borate single crystal belongs to the space group $P2_1/c$ (C_{2h} in Schönflies notation). In this symmetry group, the crystal is invariant under rotation of 180° about the principal axis (z), inversion and it possesses a mirror plane perpendicular to the principal axis. A schematic representation of the crystal structure is shown in Figure 10.

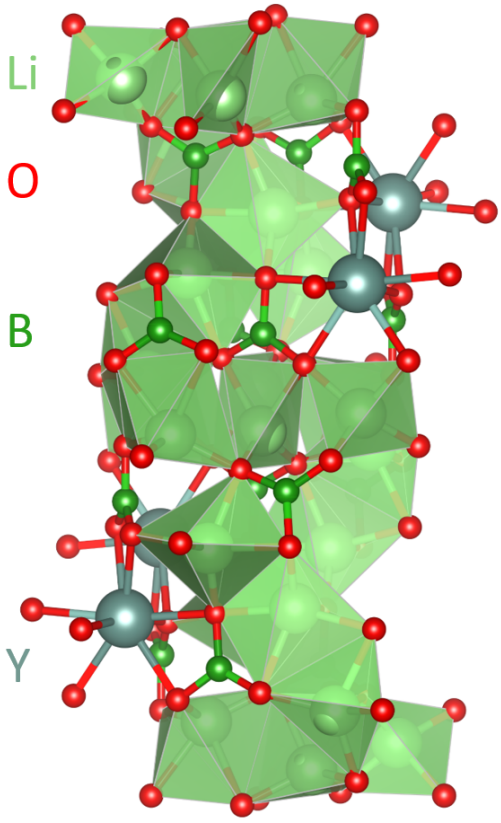

Figure 10: Crystal structure of lithium yttrium borate. Lithium ions are represented by light green balls, boron ions by dark green balls, yttrium by grey balls and oxygen by red oxygen. To distinguish light and dark green (i.e. lithium from boron respectively), polyhedrons around lithium ions are visible.

Lithium yttrium borate has a monoclinic crystal structure whose cell constants are a =7.157 Å, b =16.378 Å, c =6.623 Å, β =105.32° (angle between $\vec{a}$ and $\vec{c}$ vectors) and the density of the crystal is 2.747 g/cm^3 [5]. The structure unit of $Li_6Y(BO_3)_3$ consist of triangles of a boron ion and three oxygen ions (see Figure 10 where boron is represented by dark green balls in the middle

of the triangle and oxygen in the vertex), distorted hexahedron of yttrium (in the middle) and oxygen (eight ions in the vertex), distorted lithium-oxygen trigonal pyramids and lithium-oxygen double tetrahedra. Through the polyhedrons that involve lithium ions in Figure 10, tetrahedra and distorted trigonal pyramids can be straightforward visualized. In the first case, lithium ion is surrounded by five oxygen ions enclosing the ion. Whereas in the second case, lithium forms a double tetrahedron with four oxygen ions and the polyhedron does not encompass completely the lithium ions. In addition, yttrium-oxygen cage are distributed in pairs. The smallest distance is 3.849 Å and between pairs in the same layer is 8.749 Å [5].

The above described monoclinic crystal cell is very convenient in crystallography. However, in this thesis a cartesian coordinate system is used. In the cartesian system, the z axis is chosen parallel to the b axis (the principal axis) in Figure 10 and y is along the normal of the planes with Miller indices (-102). Finally, x is perpendicular to z and y, forming a right-handed system i.e. x axis makes angles 26.94° and 78.38° with the a and c crystallographic axes, respectively [50].

At the beginning it was mentioned that lithium yttrium borate is an artificial material, which means that it grows from a melt of Li_2CO_3, H_3BO_3 and Y_2O_3. The concentration of each compound stablishes the growth of a stoichiometric or congruent crystal. Single crystal grown by Czochraski method has been considered in this thesis.

Lithium yttrium borate is an advantageous host material for laser applications due to its flexibility and easy incorporation of the rare earth dopants (for example ytterbium Yb^{3+} or erbium Er^{3+}). In the following subsections, the most relevant properties of this dopants are summarized.

2.2.1 Erbium doped lithium yttrium borate

Erbium is a rare earth ion (with electronic configuration [Xe] $4f^{12}$ $6s^2$) and penetrates as Er^{3+} in lithium yttrium borate (LYB). The yttrium (Y) replacement is reasonable because of the charge compensation and ionic radii. In the host, Li^+, Y^{3+}, and B^{3+} ions possess an ionic radio of 0.090 nm, 0.093 nm and 0.022 nm respectively. Whereas the Er^{3+} ionic radio is 0.096 nm similar to Y^{3+} and, moreover, with the same electronic charge [51].

Erbium ions are specially interesting due to their near infrared emission suitable for optical telecommunication systems. In addition, diode-pumped 1594 nm laser performance has already been realized in Er and Yb co-doped LYB [5].

2.2.2 Ytterbium doped lithium yttrium borate

Ytterbium is a rare earth with electronic configuration [Xe] $4f^{14}$ $6s^2$. It is introduced in LYB as a trivalent Yb^{3+} and it is assumed that it replaces Y site (see erbium doped lithium niobate subsection).

Ytterbium ion (Yb^{3+}) has many excellent properties such as no excited-state absorption, long lifetime and low concentration quenching. The energy level diagram of Yb^{3+} consists of two manifolds, the $^2F_{7/2}$ ground state and the $^2F_{5/2}$ excited state. Therefore, a high level of ytterbium can be introduced before the critical concentration threshold for luminescence quenching is reached[10]. The absorption band in most ytterbium materials lies between 900-980 nm (region covered by the high-power InGaAs laser diodes commercially available), therefore, diode pumped ytterbium doped materials are emerging as efficient and compact solid-state lasers. On the other hand, the broad emission band characteristic of Yb^{3+} is very favourable for tuneable or ultra-fast lasers [6].

2.2.3 Iron doped lithium yttrium borate

In an analogous way as in lithium niobate, iron ion enters with two different charges (Fe^{2+} and Fe^{3+}) to lithium yttrium borate. It is plausible that iron replaces yttrium to compensate its charge.

In contrast to erbium and ytterbium doped lithium yttrium borate, where quite a few investigations were already published, iron doped lithium niobate seems to be a new and promising material. In addition, it seems that no measurements of electron paramagnetic resonance have been reported so far. Consequently, one of the purposes of this thesis is to show and study iron in lithium yttrium borate. Therefore, lithium yttrium borate was doped with iron to investigate if EPR measurement could work.

3 Methods

In this chapter, the experimental and theoretical techniques used in this thesis for the characterization of the samples are outlined. The samples were prepared in two different institutions (University of Padova, Italy, and Wigner Research Centre of Budapest, Hungary). Electron para-magnetic resonance and photoluminescence experiments were carried in Prof. Dr. Lindner's group at the Paderborn University, whereas the density functional theory calculations were performed by Prof. Dr. Sanna at the Justus-Liebig-University in Giessen. In the first part of this chapter, the preparation of lithium niobate and lithium yttrium borate samples is introduced. In the second part, the electron paramagnetic resonance is explained in some detail, with a particular focus on magnetic resonance and spin Hamiltonian. Subsequently, the custom-built X-Band spectrometer and the simulation tool (EasySpin) are described. Thereafter, photoluminescence measurements are explained, and finally the density functional theory is shortly outlined.

3.1 Sample preparation

In this section, the sample preparation and annealing treatment is described. To understand the interaction between iron and titanium ions in co-doped lithium niobate, sample doped either with iron or with titanium were firstly required. Lithium niobate with the congruent composition was grown at the university of Padova (Italy), while crystals with the nearly stoichiometric composition were grown at the Wigner Research Centre for Physics in Budapest (Hungary). Lithium yttrium borate single crystals were also grown at the Wigner Research Centre for Physics.

3.1.1 Lithium niobate crystal

Iron doped lithium niobate was grown using the Czochralski technique at the University of Padova (Italy). In the melt, the dopant concentration was 0.1 mol % Fe (corresponding to 18.8 x 10^{18} atoms/cm^{-3}) (samples numbers **155312**, **155313vs** and **155313ss**). The boule was grown along

the z axis of the material and was pulled with a rate of 1 mm/h. After the growth, the boule was x-ray oriented and cut in different samples.

Additionally, sample **155313vs** was co-doped with titanium by diffusion with a semi-gaussian concentration profile. The concentration at the surface was 1.1 x 10^{21} atoms/cm^3, and the average depth was 1.1 µm.

Sample **155313ss** was co-coped with iron and titanium by diffusion method with a semi-gaussian concentration profile. At the surface, the concentration of Fe was 1.9 x 10^{19} atoms/cm^3 with an average diffusion depth of 10 µm and the concentration of Ti was 1.1 x 10^{21} atoms/cm^3 with an average depth of 1.1 µm.

Nearly stoichiometric lithium niobate was grown using the high temperature top seeded solution growth (HTTSSG) technique [52] at the Wigner Research Centre for Physics in Budapest (Hungary). The procedure of the HTTSSG method corresponds to a combination of the well-known Czochralski technique and solution growth processes to grow crystals from high temperature flux solutions [53]. Using high temperature top seeded solution growth (HTTSSG) from K_2O containing flux, crystals close to the stoichiometric composition can be grown (see Figure 11). In the doped iron sample (**21616**), the concentration of iron in the melt was 0.06 mol %. In the doped titanium sample (**179803**), the concentration of titanium in the melt was 0.05 mol %. The co-doped iron-titanium sample (**21615**) was grown from a melt with 0.06 mol % of iron and 0.06 mol % of titanium. Crystal boules were pulled along the z direction with a pull rate of 1.44 mm/h and a rotation speed of 12 rpm [52].

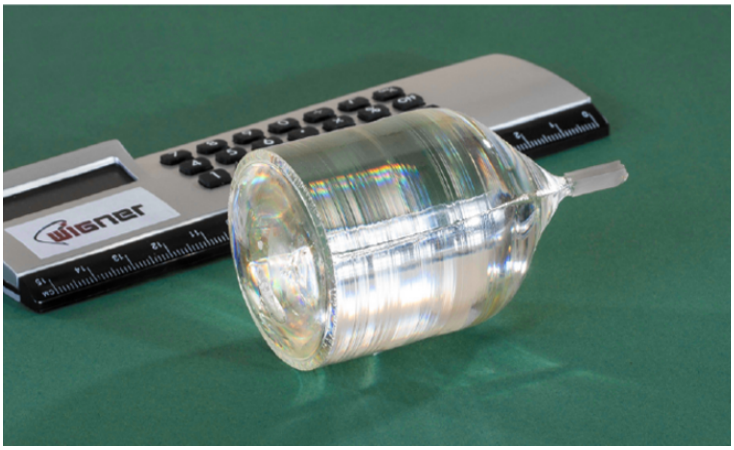

Figure 11: High quality $LiNbO_3$ single crystal grown by HTTSSG method. Photo was taken from [49].

Sample	Stoichiom./ congruent	Dopant	Conc. (mol %)	Conc. (10^{19} at/cm^3)	Bulk/surf. doping	Colour
155312	congruent	Fe	0.1	1.9	bulk	dark orange
155313vs	congruent	Fe	0.1	1.9	bulk	dark orange
		Ti	-	110	surface	
155313ss	congruent	Fe	-	1.9	surface	transparent
		Ti	-	110	surface	
21616	stoichiom.	Fe	0.06	1.1	bulk	light orange
179803	stoichiom.	Ti	0.05	0.95	bulk	white
21615	stoichiom.	Fe	0.06	1.1	bulk	dark orange
		Ti	0.06	1.1	bulk	

Table 2: Doped lithium niobate samples studied in this thesis. The number of the sample is shown in the first column. The stoichiometric (stoichiom.) or congruent composition of the melt is listed in the second column. The dopant ion is given in the third column. The dopant concentration (conc.) in mol % and atoms/cm^3 is provided in the fourth and fifth columns respectively. The doping process is indicated in the sixth column. The colour of the samples is described in the seventh column.

Several units of the different doped and co-doped nearly stoichiometric samples where provided, to be studied not only as grown, but also after a reduction treatment [48]. The annealing process was carried out in vacuum (less than 1 mbar) at temperatures between 500 °C and 900 °C for 3 hours (at lower temperatures) or for 0.5 hours (at elevated temperatures) at the Paderborn University. To avoid the lithium out-diffusions, samples were covered with Li_2CO_3 powder. In Table 2 the main information of the investigated samples is listed. An overview of the as grown and annealed lithium niobate samples is given in Appendix A.

3.1.2 Lithium yttrium borate crystal

Lithium yttrium borate single crystals were grown using the Czochralski method (see Figure 12) [49]. The samples were pulled from a platinum crucible in air. The crystal pulling rate was 0.2 - 0.3 mm/h and the rotation speed of 8 rpm. The single crystal was pulled along the b $=<$ 010 $>$ axis

or normal to the (-102) plane. Doped single crystals were grown by the Czochralski method with specific concentrations of erbium (0.05 or 1 mol % [Er]), ytterbium (1 mol % [Yb]) and iron (0.02 mol % [Fe]) in the melt. In Table 3 the main information of the investigated samples is provided. In contrast to lithium niobate samples, lithium yttrium borate samples were not submitted under thermal treatment (see Appendix A).

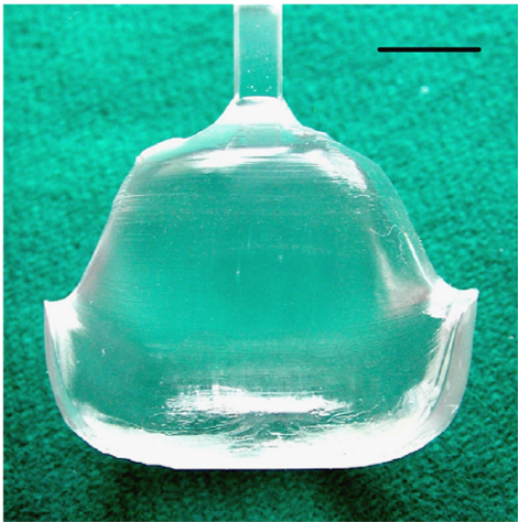

Figure 12: $Li_6Y(BO_3)_3$ single crystal grown by the Czochralski method. The crystal was pulled along <010>. The mark denotes a length of 1 cm. The photo was taken from [49].

Sample	Stoichiom./ congruent	Dopant	Conc. (mol %)	Bulk/surface doping	Colour
91103	stoichiometric	Er	0.05	bulk	transparent
91105	stoichiometric	Er	1	bulk	transparent with light pink tones
91202	stoichiometric	Yb	1	bulk	light milky
91501	stoichiometric	Fe	0.02	bulk	light yellow

Table 3: Doped lithium yttrium borate samples studied in this thesis. The number of the sample is listed in the first column. The stoichiometric or congruent melt composition is indicated in the second column. The dopant ion is indicated in the third column. The dopant concentration in mol % is shown in the fourth column. The doping process is provided in the fifth column. The colour of the samples is described in the sixth column.

3.2 Electron paramagnetic resonance

Whereas samples preparations were described in the last section, the technique to investigate their point defects is shown in this section.

Crystalline solids possess a periodic crystalline structure. Atoms are located at determined positions, forming patterns that are repeated for a fixed distance, the unit cell parameter. However, the arrangement of atoms is usually not perfect, that is, the periodicity is interrupted by crystallographic defects. Depending on the dimensions of the crystallographic defects, they are classified into three categories: three-, two- and one-dimensional defects. Bulk defects such as clusters, voids (clusters of vacancies), cracks or inclusions, also called three dimensional or macroscopic defects, are larger aggregates of atoms or vacancies. Interfaces are two dimensional defects, for instance interfaces between crystals. Dislocations or grain boundaries are stacking faults through the crystal where atoms lose their crystallographic registry, for example in edge or screw dislocations. Finally, point defects are zero dimensional defects and occur at an isolated site. They can be classified as intrinsic defects, which appear in a pure material and extrinsic defects caused by wanted or unwanted impurity atoms. Vacancies, interstitials, Frenkel and Schottky defects, anti-sites or substitutional defects are examples of common point defects [54].

In the frame of this work, the focus is put into point defects, as they can be employed to tailor the materials properties via so called defect engineering. Very often even small concentrations of point defects as low as 10^{16} atoms/cm^{-3}, strongly influence the macroscopic properties of solids, that is its optical, mechanical or electrical properties. As an example, titanium indiffused in lithium niobate increases the refractive index of the material, which can be then used as an optical waveguide. Another example is ytterbium doped LYB, which is commonly used as a laser host. Despite their importance, the actual knowledge of point defects in LN and LYB is limited. Indeed, the determination of the structure of the defects is not a straightforward task. Point defects are not effectively investigated using a high-resolution electron microscopy. Moreover, very sensitive methods are required, if low defect concentrations have to be investigated.

Electron paramagnetic resonance (EPR) is one of the most powerful techniques for the investigation of defects in solid state, as it yields information about the geometrical and electronic structure of the defects. One major restriction for the applicability of this technique is that the defects must be paramagnetic to be investigated. This means, that in presence of an extern magnetic field the defect acquires a magnetic moment, whose size is determined by the field [55]. Fortunately,

this occurs very often: for example, transition metal ions (Fe, Ti) or rare earth ions (Er, Yb) are paramagnetic or might be made paramagnetic modifying their valence state, e.g. by oxidation or reduction treatments.

In this section, the basic concepts required for the description of the point defects in a bulk phase within EPR are presented.

3.2.1 Magnetic resonance

In solid state, amorphous, polycrystalline and crystalline structures might be studied. However, only crystals or crystalline solids with high ordered arrangements of atoms are much more advantageously investigated in EPR studies than in other techniques. In crystalline solids indeed, even small percentages of impurities can be detected and studied by EPR. Single crystals with well-defined crystal orientations are employed in this work to perform all the investigations.

In a diamagnetic crystal with a paramagnetic centre, the magnetic dipole transition is induced between the energy levels of electron spins in a static magnetic field, which are characterized by the magnetic quantum number m_s. To induce a magnetic dipole transition, a microwave frequency ν must be applied with the oscillatory magnetic component (B_1) perpendicular to the external magnetic field (B_0). In fact, the magnetic dipole transition occurs for a given frequency ν and a determined magnetic field B_0, which characterizes the EPR transition (see Figure 13):

$$h\nu = \mu_B g_e B_0 \tag{1}$$

where h is the Planck constant, μ_B the Bohr magneton, g_e the electron g-factor and B_0 the external magnetic field [55].

In a basic experiment, the sample in the spectrometer is inside of a resonant cavity and a constant microwave frequency is applied. By increasing the magnetic field, the resonant condition is fulfilled and the sample absorbs electromagnetic energy to induce a magnetic dipole transition between the electronic energy levels. The absorption, which carries the information of the sample, is processed by a lock-in amplifier and the derivative of the absorption, known as EPR spectrum, is obtained (see Figure 13).

Statistical mechanics is the basis that provides the link between the microscopic states of matter and macroscopic properties. Molecular modeling and simulation, based on statistical

thermodynamics, uses the intermolecular interactions to predict the macroscopic thermophysical properties. The intermolecular interactions are fully described by the molecular model. By simply defining the interactions between molecules, properties of pure fluids as well as mixtures can be calculated [56]. In the following, the most important thermodynamic properties discussed in the present work are introduced.

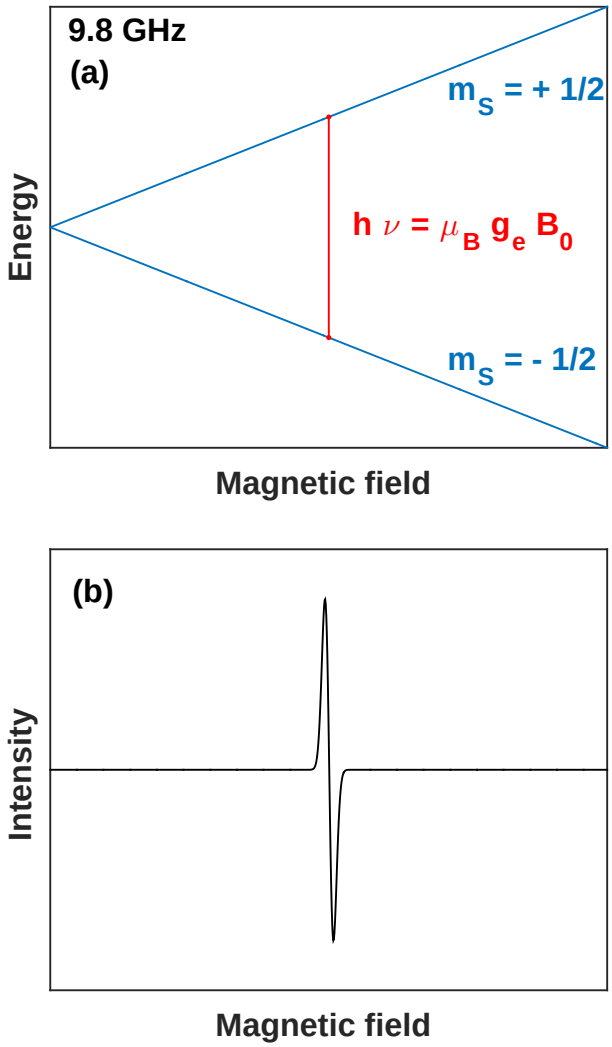

Figure 13: (**a**) Energy levels splitting of electronic spins $m_s = -1/2$ and $m_s = +1/2$ for an increasing magnetic field. For a given microwave frequency ν, the EPR resonance condition is fulfilled and the sample absorbs $h\nu$ energy to induce a magnetic dipole transition. (**b**) The EPR absorption is represented as a derivative function. The picture was redrawn from [56].

3.2.2 Spin Hamiltonian

In general, an EPR spectrum is rather complex due to the different electronic transitions. The magnetic field at the positions of the peaks depends on the applied frequency and, if the crystal is anisotropic, the EPR spectra have a dependence on the orientation of the crystal with the static magnetic field. A reliable description of these circumstances can be achieved using a spin Hamiltonian, which is derived by a microscopic theory of magnetism and adjusted to take in account the crystal and the defect symmetry [55].

The spin Hamiltonian describes thus the energy of the system (for example Fe sitting at a regular lithium place in lithium niobate). The introduction of the concept of the spin Hamiltonian permits to analyse EPR spectra without a deep understanding of the complex wave function of the system. Indeed, it is a summation of terms that describes the interaction between the electron, nucleus and crystal field. The total spin Hamiltonian operator ($\widehat{H}_{SHO}$) is:

$$\widehat{H}_{SHO} = \widehat{H}_{EZI} + \widehat{H}_{FI} + \widehat{H}_{HFI} + \widehat{H}_{NZI} + \widehat{H}_{QI} + \widehat{H}_{EEI} \tag{2}$$

$\widehat{H}_{EZI} = \mu_B \mathbf{B_0}^T \cdot \tilde{g} \cdot \widehat{\mathbf{S}}$	electron Zeeman interaction
$\widehat{H}_{FI} = \widehat{\mathbf{S}}^T \cdot \tilde{D} \cdot \widehat{\mathbf{S}}$	fine structure interaction
$\widehat{H}_{HFI} = \widehat{\mathbf{S}}^T \cdot \tilde{A} \cdot \widehat{\mathbf{I}}$	hyperfine interaction
$\widehat{H}_{NZI} = -g_n \mu_n \mathbf{B_0}^T \cdot \widehat{\mathbf{I}}$	nuclear Zeeman interaction
$\widehat{H}_{QI} = \widehat{\mathbf{I}}^T \cdot \tilde{Q} \cdot \widehat{\mathbf{I}}$	nuclear quadrupole interaction
$\widehat{H}_{EEI} = \widehat{\mathbf{S}}^T \cdot \tilde{J} \cdot \widehat{\mathbf{S}}$	electron-electron interaction

Where μ_B is the Bohr magneton, $\mathbf{B_0}^T$ is the static magnetic field vector (T means transpose), $\tilde{g}$ the electron g-tensor, $\widehat{\mathbf{S}}$ the electron spin operator, $\tilde{D}$ the fine structure tensor, $\tilde{A}$ the hyperfine structure tensor, g_n the nuclear g factor, μ_n the nuclear magneton, $\widehat{\mathbf{I}}$ the nuclear spin operator, $\tilde{Q}$ the nuclear quadrupole tensor and $\tilde{J}$ the electron-electron tensor.

The first term $\widehat{H}_{EZI}$ in the equation [2] represents the Electron Zeeman Interaction and describes the interaction between the electron and the static magnetic field. The second term $\widehat{H}_{FI}$ (fine structure term or zero field term) gives the energy component of a system with S > 1/2 when the static magnetic field is zero. The third term $\widehat{H}_{HFI}$ describes the interaction between the electron and its nucleus. This occurs only in the case S = 1/2. The nuclear Zeeman interaction ($\widehat{H}_{NZI}$),

analogous to electron Zeeman term, expresses the energy of the interaction between the nucleus and the static magnetic field. The nuclear quadrupole interaction ($\widehat{H}_{QI}$) represents the interaction between two nuclei in the crystal and, similarly, the electron-electron interaction ($\widehat{H}_{EEI}$) describes the interaction between two unpaired electrons [54]. The most relevant terms are reported with more detail in the next section.

The spin Hamiltonian gives a complete description of the terms that contribute to the total energy of the system. Usually, not all terms play a similar role in the equation. Depending on the considered system, some terms contribute with a larger energy amount and some terms may be considered negligible. Before presenting the spin Hamiltonian for the considered system in this thesis, an overview about the most important terms is given.

Electron Zeeman interaction

The electron Zeeman term describes the energy levels splitting of a paramagnetic defect in a magnetic field. A system with spin S splits in 2S+1 states with $m_s = -S, -S+1, \ldots, S-1, S$. The interaction between the electron and the static magnetic field is characterized by the g-tensor.

$$\widehat{H}_{EZI} = \mu_B \mathbf{B_0}^T \cdot \tilde{g} \cdot \widehat{\mathbf{S}} \tag{3}$$

Depending on the system, the g-tensor can be isotropic ($g_{xx} = g_{yy} = g_{zz}$), axial ($g_{xx} = g_{yy} \neq g_{zz}$) or rhombohedral ($g_{xx} \neq g_{yy} \neq g_{zz}$). Moreover, the tensor axis can be tilted respect to the reference frame. Through the Euler angles (see Appendix B), the g tensor can be described in its principal axis or in the reference frame (for example the laboratory reference frame, see Appendix D) [54].

Usually, the Zeeman contribution

$$\widehat{H}_{EZI} = \mu_B \mathbf{B_0}^T \cdot \tilde{g} \cdot \widehat{\mathbf{S}}$$

is not enough to describe the interaction between the electron and magnetic field, because the spin-orbital coupling should be considered. When spin and orbital momentum are present, the value of g depends on the nature of the coupling between them. In this case, the resultant quantum number is J = L+S and the energy levels split into a multiplet with $m_J = -J, -J+1, \ldots, J-1, J$ [55].

Fine structure interaction

In the case that a defect has more than one unpaired electron (S $>$ 1/2), an additional interaction can occur: fine structure interaction. Its origin is the influence of the electrical crystal field, which is felt by the spins due to the spin-orbit interaction and the magnetic dipole-dipole interaction. This fine structure interaction leads to a splitting of the energy states in zero magnetic field. A proper interpretation of the fine structure is rather complicated because of the symmetry of the defect, the spin and the size of the interaction [54]. This term is described commonly by the fine structure tensor $\tilde{D}$:

$$\widehat{H}_{FI} = \widehat{\mathbf{S}}^T \cdot \tilde{D} \cdot \widehat{\mathbf{S}} \tag{4}$$

Nevertheless, for S $>$ 2 a complete set of high order operators in S_x, S_y and S_z are needed to describe the fine structure term:

$$\widehat{H}_{FI} = \sum_{k,q} B_k^q O_k^q(S_x, S_y, S_z) \tag{5}$$

Where O_k^q are the Stevens operators and B_k^q their corresponding scalar coefficients of degree k and order q (see Appendix C). Allowed values are $0 \leq k \leq 2S$ and $-k \leq q \leq +k$. The k term represents the k^{th}-degree of interaction that the spins felt and reflects the symmetry of the crystal field [57].

Hyperfine interaction

The interaction between the electron of the paramagnetic centre and its nucleus is described by the hyperfine term. The hyperfine interaction results in a further energy levels splitting. This term is described by the hyperfine tensor $\tilde{A}$:

$$\widehat{H}_{HFI} = \widehat{\mathbf{S}}^T \cdot \tilde{A} \cdot \widehat{\mathbf{I}} \tag{6}$$

The hyperfine tensor can be decomposed in an isotropic and an anisotropic component:

$$\tilde{A} = (a\tilde{1} + \tilde{B}) \tag{7}$$

The scalar term a is the Fermi contact term. The anisotropic component $\tilde{B}$ tensor is written in its principal axes as following:

$$\tilde{B} = \begin{pmatrix} -b+b' & 0 & 0 \\ 0 & -b-b' & 0 \\ 0 & 0 & 2b' \end{pmatrix}$$

Here b and b' describe the axial and non-axial part of the hyperfine interaction respectively [58].

The hyperfine tensor $\tilde{A}$ is diagonal in its principal frame, however, it can be tilted with respect to the laboratory frame. Euler angles will be used to describe the position of the hyperfine tensor in the laboratory frame (see Appendix B).

After this overview of all the relevant spin Hamiltonian terms, the appropriate spin Hamiltonians used in this thesis for the investigated systems are presented in the next subsections. For the construction of the Hamiltonian, system specific features must be considered. Thus, the most relevant features of the host crystal are introduced at first, and then the specific defect centres are taken into account and analysed.

3.2.3 Spin Hamiltonian in lithium niobate samples

In Chapter 2 Materials, it was already mentioned that lithium niobate displays an orthogonal symmetry with a trigonal distortion (point group C_{3v}, see Figure 1 in Chapter 2 Materials). Due to the peculiar crystal structure, consisting of oxygen octahedra that are either occupied by Nb, Li or vacant, several non-equivalent places are available for the incorporation of foreign ions [19]. The introduced (electrically charged) ions in a lithium niobate could substitute lithium (Li), niobium (Nb), or could be placed at the structural vacancy (V). In any case, the additional charge should be compensated by the creation of other defects such as Li vacancies (see Chapter 2 for a detailed discussion).

Let's now suppose that a trivalent ion (called for example M) is incorporated in lithium niobate. The electronic charge with respect to the crystal lattice is M_{Li}^{2+}, if the defect is incorporated at the Li site, or M_{Nb}^{2-}, if the ion is incorporated at the Nb lattice site, or M_{V}^{3+}, in the case that the foreign atoms occupies the structural vacancy. From the three possible options, the trivalent ion in the structural vacancy is for the largest part of the known defects energetically not favourable, leading to two feasible substitutional sites: Li and Nb (see Chapter 2 Materials for a detailed discussion). It is generally accepted that most foreign ions in lithium niobate are incorporated at the Li lattice site, as it offers more place than the Nb lattice site. Also in this thesis, it is assumed that the

considered trivalent ions (iron and titanium) substitute the Li atom when incorporated in lithium niobate. In this assumption, one of the electrons of the foreign atom (iron or titanium) is involved in the bound with the neighbour atoms, whereas the remaining electrons are available as free charge carriers. As Li has a rather large ionic radius, the incorporation of foreign atoms at the Li lattice site usually leads to the shrinking of the oxygen octahedron hosting the foreign atom [35]. This remains true also for the Fe and Ti dopants investigated in this work.

Hereafter, the spin Hamiltonian equation for iron Fe^{3+} and Ti^{3+} in lithium niobate will be reported.

Iron doped lithium niobate

Iron can enter with two different charge states in lithium niobate: Fe^{2+} and Fe^{3+}. Both charge states are stable and paramagnetic, however only Fe^{3+} can be observed in an X-band spectrometer. Fe^{2+} exhibits a very large fine structure splitting that can be only studied using high-frequency spectrometer (100-200 GHz), though. Therefore, Fe^{2+} is not observed in standard X-band spectrometers and is considered in several works as "EPR-silent" [59].

To obtain the spin Hamiltonian of iron in lithium niobate, the relevant terms (Zeeman interaction, hyperfine interaction...) from Equation 2 are analysed. As a reminder, the atomic iron electronic configuration is [Ar] $3d^6$ $4s^2$. Fe^{3+} exhibits three electrons less, that is [Ar] $3d^5$ and the corresponding electronic spin configuration is $S = 5/2$ (i.e. Zeeman and zero field splitting must be considered). Fe does not possess nuclear spin (I=0), which means that hyperfine, nuclear Zeeman and quadrupole interactions are negligible. Moreover, the electron-electron interaction is negligible too if compared with the Zeeman and fine structure terms [1]. Consequently, from the entire spin Hamiltonian equation 2, the spin Hamiltonian for Fe^{3+} in lithium niobate can be approximated by the two main terms:

$$\widehat{H}_{Fe^{3+}} = \widehat{H}_{EZI} + \widehat{H}_{FI} = \mu_B \mathbf{B_0}^T \cdot \tilde{g} \cdot \widehat{\mathbf{S}} + \sum_{k,q} B_k^q O_k^q(S_x, S_y, S_z) \tag{8}$$

Only electron Zeeman and zero field splitting contribute to the spin Hamiltonian. Fe^{3+} has spin $S = 5/2$, knowing that $0 \leq k \leq 2S$, the different values for the subindex k are $k = 1, 2, 3, 4, 5$. In addition, only $k = 2, 4$ can be determined because the odd rank (k odd) terms are not allowed by the time reversal symmetry constraint [60–62]. In the previous section, it was seen that q values are given by the value k, following $-k \leq q \leq +k$:

$$\text{For } k=2: \qquad q=-2,-1,0,+1,+2$$

$$\text{For } k=4: \qquad q=-4,-3,-2,-1,0,+1,+2,+3,+4$$

Due to the C_{3v} symmetry just a few of these terms are relevant in the calculation of the fine structure term and the spin Hamiltonian for iron doped lithium niobate can be written as:

$$\widehat{H}_{Fe^{3+}} = \mu_B \mathbf{B_0}^T \cdot \tilde{g} \cdot \widehat{\mathbf{S}} + B_2^0 O_2^0 + B_4^3 O_4^3 + B_4^0 O_4^0 + B_4^{-3} O_4^{-3} \tag{9}$$

The magnetic contribution to the total energy of a Fe^{3+} ion sitting at the lithium place in a lithium niobate crystal is thus described by the spin Hamiltonian above (Equation 9). Moreover, due to the glide mirror plane in lithium niobate, there are two electrically equivalent centres with C_3 symmetry (R and L). Both have the same absolute value of g-tensor and zero field splitting parameters (B_k^q). However, they are magnetically non-equivalent. Replacing B_4^3 for $-B_4^3$, transforms R in L.

Until now, the spin Hamiltonian of Fe^{3+} in lithium niobate was discussed. It describes the unique environment of the centre in the host crystal, and the eigenvalues of the spin Hamiltonian are the energy levels that split the ground state of the system. If a Fe^{3+} ion is considered in vacuum, the five energy levels of the d orbitals are degenerated (see Figure 14 (**a**)). Introducing Fe^{3+} in an octahedral host crystal, the energy levels split into a twofold degenerated energy level (doublet) and a threefold degenerated energy level (triplet). Depending on the host material, the triplet is lower or higher in energy (see Figure 14 (**b**)). With an additional trigonal distortion as occurring in lithium niobate, the triplet splits into a non-degenerate state (lower energy) and a doublet (higher energy). This is exactly the case of Fe^{3+} ion in lithium niobate (see Figure 14 (**c**)). In absence of a magnetic field, the ground state is split in two double degenerated states and one non-degenerated state and it is described by the zero-field splitting term in the Hamiltonian. Applying a magnetic field, the three degenerated and non-degenerated states are splitting into six different states ($m_s = -5/2, -3/2, -1/2, +1/2, +3/2, +5/2$) due to Zeeman splitting. Selection rules indicate allowed transitions between energy levels ($\Delta m_S = 1$) that are observable by EPR measurements.

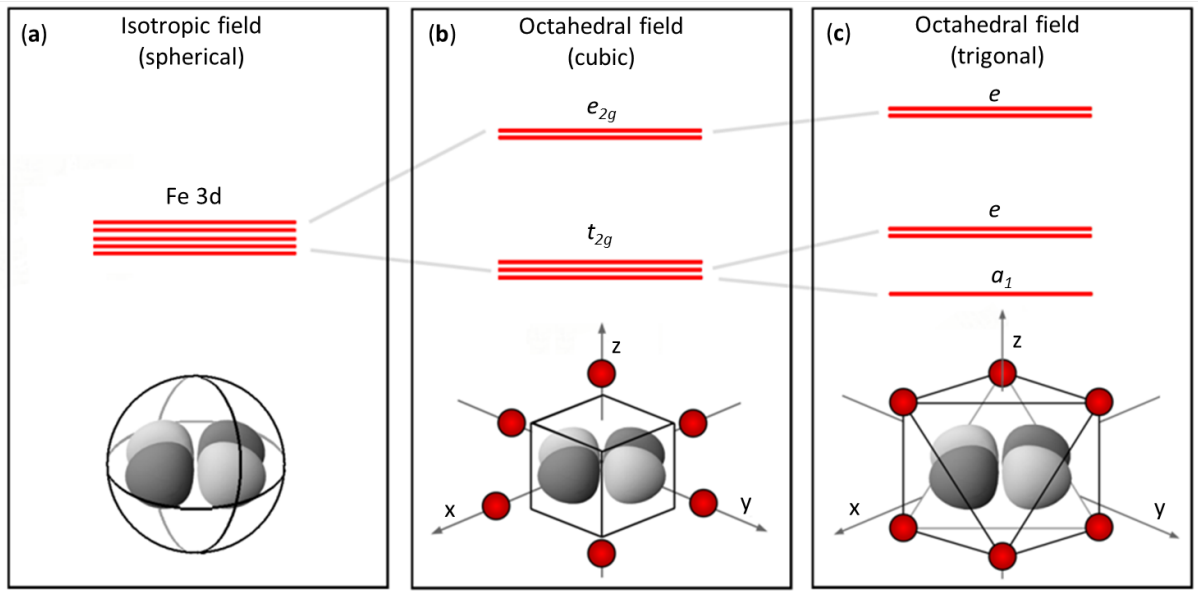

Figure 14: (**a**) d orbital energy levels of an iron ion in vacuum (five degenerated energy levels). (**b**) Introducing Fe in an octahedral symmetry system, energy levels split into two degenerated energy levels (a doublet e_{2g} and a triplet t_{2g}). (**c**) Energy levels of iron in an octahedral field with a trigonal distortion split in a singlet (a_1) and two doblets (e). The figures below the energy levels represent one exemplar d orbital of iron ion in the different case of symmetry. The red balls are oxygen atoms. Redrawn from [35].

Titanium doped lithium niobate

Titanium enters in lithium niobate as Ti^{4+} and it is supposed to substitute lithium. The electronic configuration of atomic titanium (Ti) is [Ar] $3d^2$ $4s^2$. If four electrons are promoted to the host, Ti^{4+} has the same electronic configuration as the noble gas argon [Ar] and cannot be detected using EPR spectroscopy, being non-paramagnetic. However, owing to annealing procedure (reduction) an electron can be captured by Ti^{4+} to give rise to Ti^{3+}, a paramagnetic ion with $S = 1/2$.

Similarly to iron, titanium has a nuclear spin of zero, even though the electronic spin for Ti^{3+} is $S=1/2$ and the system lacks fine structure splitting. In this case, the spin Hamiltonian of the system is dominated by the Zeeman splitting term:

$$\widehat{H}_{Ti^{3+}} = \mu_B \mathbf{B_0}^T \cdot \tilde{g} \cdot \widehat{\mathbf{S}} \tag{10}$$

Due to the trigonal symmetry (C_{3v}) of lithium niobate, Ti^{3+} sitting in lithium place behaves as an axial centre. This characteristic is reflected in the g-tensor, which possesses two components: one perpendicular to the principal axes ($g_{xx} = g_{yy} = g_{\perp}$) and one parallel to the principal axes ($g_{zz} = g_{\parallel}$).

In absence of a magnetic field, the energy level of the ground state is doubly degenerated, however applying a magnetic field it splits into two energy levels ($m_S = +1/2$ and $-1/2$) due to the Zeeman interaction (see Figure 13).

3.2.4 Spin Hamiltonian in lithium yttrium borate samples

Lithium yttrium borate is a monoclinic crystal with point group symmetry C_{2h}. Trivalent positive dopants (for instance erbium (Er) or ytterbium (Yb)) are considered in this thesis to substitute yttrium ions in the host crystal (detailed description in Chapter 2). Two centres are observed in this system. Both have the same parameters; however, one is 180° rotated about the principal axes ($z = C_2$). In the next subsections, the spin Hamiltonian for Er^{3+}, Yb^{3+} and Fe^{3+} is presented and described.

Erbium doped lithium yttrium borate

Erbium is a rare earth with atomic electronic configuration [Xe] $4f^{12}$ $6s^2$. Losing three electrons, Er^{3+} ([Xe] $4f^{11}$) is supposed to substitute yttrium in the host crystal. The last incomplete shell is $4f^{11}$ with eleven electrons in seven possible energy levels giving $S = 3/2$. Because the electrons in the f-orbitals are screened from the electrons of the neighbour atoms by outer shells, the spin-orbit splitting is larger than the crystal field. It leads to define the total angular momentum J ($J = L + S$), as a better quantum number than L or S for rare earth ions. The Er^{3+} ground state is thus defined as $^4I_{15/2}$, that means, $S = 3/2$, $L = 6$ and the total angular momentum is $J = 15/2$. Moreover, Er^{3+} has several isotopes (^{162}Er, ^{164}Er, ^{166}Er, ^{168}Er and ^{170}Er) with vanishing nuclear spin and ^{167}Er with nuclear spin $I = 5/2$. The spin Hamiltonian includes thus two dominant terms: electron Zeeman splitting with an effective spin S=1/2 (see Appendix E) and hyperfine structure interaction:

$$\widehat{H}_{Er^{3+}} = \mu_B \mathbf{B_0}^T \cdot \tilde{g} \cdot \widehat{\mathbf{S}} + \widehat{\mathbf{S}}^T \cdot \tilde{A} \cdot \widehat{\mathbf{I}} \tag{11}$$

In the ideal case of atomic Er^{3+} in vacuum, the seven energy levels are degenerated. If Er^{3+} is confined in $Li_6Y(BO_3)_3$ with C_{2h} point group of symmetry, the energy levels split in seven singlets. In absence of a magnetic field, the energy levels are split in seven, however, applying a magnetic field they split in sixteen (2J+1) states due to the spin-orbit splitting.

Ytterbium doped lithium yttrium borate

As erbium, ytterbium is also a rare earth, with an atomic electronic configuration [Xe] $4f^{14}$ $6s^2$. Trivalent ytterbium is assumed to substitute yttrium in $Li_6Y(BO_3)_3$ with an almost completed shell [Xe] $4f^{13}$ and an electronic spin $S = 1/2$. Similar to erbium, spin-orbit splitting is larger than the crystal field due to the electronic screening. The ytterbium ground state is $^2F_{7/2}$, leading to a $S = 1/2$, $L = 3$ and the total angular momentum $J = 7/2$. In addition, ytterbium has several isotopes with zero nuclear spin (^{168}Yb, ^{170}Yb, ^{172}Yb, ^{174}Yb and ^{176}Yb), one isotope ^{171}Yb with nuclear spin $I = 1/2$ and one further isotope ^{173}Yb with $I = 5/2$. In this case, the dominant terms in the spin Hamiltonian are electron Zeeman and hyperfine structure splitting:

$$\widehat{H}_{Yb^{3+}} = \mu_B \mathbf{B_0}^T \cdot \tilde{g} \cdot \widehat{\mathbf{S}} + \widehat{\mathbf{S}}^T \cdot \tilde{A} \cdot \widehat{\mathbf{I}} \tag{12}$$

Yb^{3+} in vacuum possesses seven degenerate energy levels. Introducing Yb^{3+} in $Li_6Y(BO_3)_3$ the energy levels split in seven singlets due to C_{2h} crystal symmetry. In presence of a non-zero magnetic field, owing to the Zeeman, spin-orbit and hyperfine interaction, these levels are split in eight states (2J+1).

Iron doped lithium yttrium borate

In analogy to erbium and ytterbium, trivalent iron is considered to replace the yttrium atom in lithium yttrium borate. Iron is incorporated in the threefold positive valence state, leading to an electronic spin of $S = 5/2$ (high spin configuration). Similarly to iron in lithium niobate, Zeeman and zero field splitting terms dominate in the spin Hamiltonian:

$$\widehat{H}_{Fe^{3+}} = \widehat{H}_{EZI} + \widehat{H}_{FI} = \mu_B \mathbf{B_0}^T \cdot \tilde{g} \cdot \widehat{\mathbf{S}} + \sum_{k,q} B_k^q O_k^q(S_x, S_y, S_z)$$

Nevertheless, in this case the C_{2h} symmetry reflects the relevant Stevens Operators terms in the calculation of the fine structure term (see Appendix C), and the spin Hamiltonian for iron doped

lithium yttrium borate reads:

$$\begin{aligned}\widehat{H}_{Fe^{3+}} =& \mu_B \mathbf{B_0}^T \cdot \tilde{g} \cdot \widehat{\mathbf{S}} + B_2^2 O_2^2 + B_2^0 O_2^0 + B_2^{-2} O_2^{-2} + \\ & B_4^4 O_4^4 + B_4^2 O_4^2 + B_4^0 O_4^0 + B_4^{-2} O_4^{-2} + B_4^{-4} O_4^{-4}\end{aligned} \tag{13}$$

The magnetic contribution to the total energy of Fe^{3+} centres sitting at the yttrium place in a lithium yttrium crystal is thus described by the spin Hamiltonian above.

3.3 Electron paramagnetic resonance spectrometer

EPR Measurements were carried out with a custom-built X-band spectrometer. It was built by Martin Pohl in 1998, providing several advantages with respect to other commercial spectrometers. First, it is an X-band spectrometer offering the best compromise between resolution and intensity. Second, the temperature can be adjusted from 4.5 K up to 300 K. Third, the spectrometer was designed to facilitate the measurements and eventually reparation work [56]. Figure 15 shows an overview of the EPR setup.

The spectrometer can be divided in three parts: microwave bridge, magnetic field components and cryostat. In the following these components are described.

3.3.1 Microwave bridge

In this subsection, the microwaves path from the source until the detection is described. In the EPR spectrometer of the University Paderborn, microwaves are produced by a YIG oscillator, then they are confined in a rectangular waveguide and guided to a directional coupler. Owing to the directional coupler, microwaves are divided in to three paths:

- One part is leaded to the frequency counter, where the frequency is measured
- The second part is conduced to a phase shifter and will be used as a reference to automatically adjust the frequency (AFC-automatic frequency control)
- The third microwave part goes through a circulator into the resonance cavity where the sample is placed.

The reflexion cavity is a cylindrical TE_{011} mode resonator, providing a larger Q factor than a

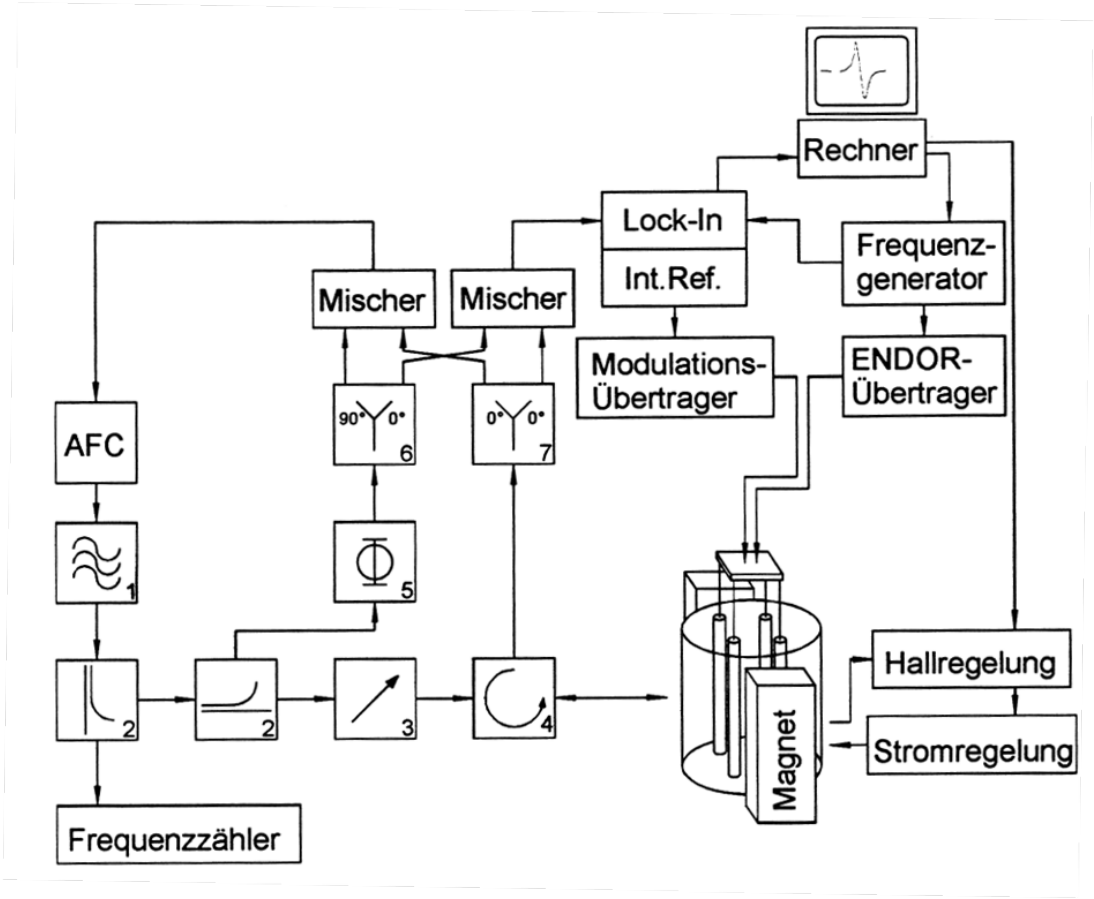

Figure 15: Schema of the EPR spectrometer setup. The picture is taken from [56].

rectangular cavity and enabling the detection of small absorption effects. Standing electromagnetic waves are generated in the resonator when microwaves arrive. The sample is placed in the middle of the resonator, where the standing magnetic field is maximal and the electric field minimal. The incoming microwave power is attenuated and coupled with the cylindrical cavity by an iris. The iris size determines the amount of microwave power entering in the resonator. Next to the iris there is a small plate (attached to the iris screw) that can be moved up and down until the resonance condition is satisfied and, in the best case, the reflexion is zero. When the sample absorbs the microwave power, Q is lowered because of the increased losses and the coupling changes, so microwaves will be reflected, resulting in an EPR signal [56].

The obtained signal is reflected and directed through the circulator to an amplifier and a phase splitter dividing the wave into two parts without phase shift. In a similar way, the reference

microwave is split (by a phase splitter) also in two parts, however one of them is rotated by 90°. On the one hand, the reflected and reference microwaves without a phase shift are multiplied using a mixer, resulting in an absorption signal. On the other hand, using a second mixer, the phase shift of the reflected and reference microwaves are multiplied and result in the dispersion signal. The absorption and dispersion signals correspond to the imaginary and real part of the magnetic susceptibility of the sample respectively [58].

On one side, the dispersion signal is carried to the AFC (automatic frequency control) to maintain the resonance frequency constant. On the other side, the absorption signal is conduced to a lock-in amplifier before being detected. The analogue EPR output signal is transformed to a digital signal owing to an analogue digital converter (ADC) before being stored in a computer [56].

3.3.2 Magnetic field components

The cylindrical resonant cavity is placed between two electromagnets, whose coils are water cooled. The magnetic field produced near the sample ranges from 0 until 1100 mT, and is measured by means of a Hall effect sensor placed between the cavity and the electro magnet. During the measurement, the external magnetic field is modulated to increase the sensitivity of the spectrometer, diminishing the noise from the detector diode (lock-in technique). The absorption signal is modulated with a sinusoidal magnetic field ($B = 100KHz \cdot \sin(\theta)$) resulting in an absorption derivative output signal (see Figure 16). This derivative representation permits to obtain better resolution of the data, because the resonant line is in a null position and not in an extreme position, and the signal-noise ratio has been increased. In contrast, a disadvantage is that the area below the line does not correspond to the concentration of the observed species.

The spectrometer is controlled by a computer that allows the user to adjust several parameters, for instance angle of the sample rotation or microwave modulation. In addition, the experimental data and relevant set up parameters are saved in the computer.

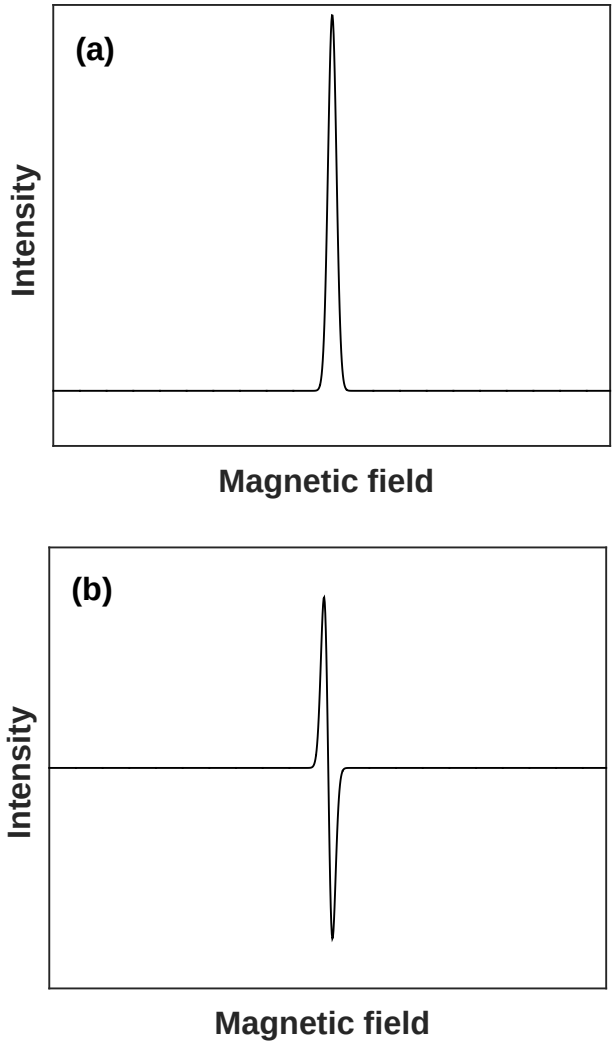

Figure 16: (**a**) Absorption EPR spectra, for which the area below the curve corresponds to the defect concentration. (**b**) Derivative absorption EPR spectra after the lock in amplifier.

3.3.3 Cryostat

The resonant cavity is placed in a continuous-flow cryostat. Liquid helium flows from the helium dewar trough a transfer line to the resonator walls using a pump. Helium is distributed by four small tubes made of sinter material, cooling the resonant cavity between 4.5 K and room temperature. Near the four sinter material tubes are four small return lines that facilitate the gas return. To

maintain a constant temperature, the helium flow can be regulated manually and a heating resistance is located below the resonance cavity with an automatic and a manual control. Finally, the temperature is measured by a thermistor [56].

The cold resonator is protected from the hot environment by a high vacuum owing to a combination of a rotary vane pump and a diffusion pump.

In this custom-built X-band spectrometer, the following components were used: a pulse/cw microwave frequency counter (model 588C) made by EIP, an RF amplifier (model 155LCR) and electro magnets both produced by BRUKER, an intelligent temperature controller (OXFORD ITC4), a signal generator (2022D) made by MARCONI INSTRUMENTS, a dual analogue-IEEE converter and a lock-in amplifier (399) both produced by ITHACO.

3.4 EasySpin

In the previous section, it was mentioned that EPR spectra contain information about the structure of the defects in a host material. Experienced spectroscopists are usually able to identify the dominant contributions in Equation 2 for a determined ion in a known host, and are thus able to qualitatively interpret the spectra. However, for an accurate and quantitative analysis of the experimental data, computerized data processing, numerical spectra simulations and iterative parameter fitting are essential. Dedicated computer algorithms allow to model different spin configurations and take in account different crystal field distortions. In the framework of this thesis, EasySpin was utilized to perform the simulations, because of its powerful, highly flexible and integrated analysis and simulation environment in EPR spectroscopy [57].

EasySpin is a computational package based on Matlab (a commercial technical computation software, whose programming language is based on matrices and very efficient matrix algorithms). The reasons why EasySpin was chosen in this thesis are several: it is a freely available toolbox of Matlab, Matlab has a simple syntax (using short instructions a precise command is generated), it is extensive and flexible (modification in graphics do not require a post processing) and is also highly portable (Matlab is available for different platforms). For all these reasons, EasySpin is a powerful, flexible and integrated analysis and simulation environment for EPR spectroscopy [57].

Moreover, EasySpin is highly versatile, because not only the simulation but also the fitting of the spectra can be performed. EasySpin is able to reproduce EPR and ENDOR for liquid- or solid-state systems. In general, EasySpin supports more than two electrons and several nuclei in a system [57].

Basically, EasySpin is able to model any spin system in a host material and predict corresponding EPR spectra (exactly what is desirable to study in EPR spectroscopy). Several parameters are required to describe the spin system, for example the considered ion, the spin configuration (S $= 1/2$ or S $= 5/2$), g-factor and A-tensor. Also, experimental parameters have to be provided to obtain the desired EPR spectra, for instance the excitation frequency and the magnetic field range. At this point, a specific function is called to generate the simulated EPR spectrum. Summarizing, knowing the spin Hamiltonian and the experimental parameters, an EPR simulation of the considered system is developed using EasySpin [57].

Nevertheless, the spin Hamiltonian is usually unknown and only experimental data is available. In this case, a fitting program is required to obtain the needed spin Hamiltonian parameters. To reach this goal, the usual method of analysis employs perturbation theory, which is applicable if the off-diagonal terms of the spin Hamiltonian matrix are sufficiently small. More sophisticated methods using exact computer diagonalization of the spin Hamiltonian matrix are not suitable for peculiar cases with large off-diagonal terms. However, least-squares fitting works equally good both in case of small and large off-diagonal terms in the spin Hamiltonian matrix. In addition, the computation time is considerably reduced in comparison with the former methods [63].

The idea behind the least-squares fitting is to find a vector a_{min} (whose components are a set of the spin Hamiltonian parameters) that corresponds to the absolute minimum value of chi-squared (χ^2) and can be obtained from the vector a_I (whose components are the starting parameters).

$$a = a_I - \left(\frac{\partial^2 \chi^2}{\partial a_j \partial a_k}\right)^{-1}_{a_I} \cdot \left(\frac{\partial \chi^2}{\partial a_j}\right)_{a_I} \tag{14}$$

The second term on the right side of this equation represents the second and first derivative of χ^2 with respect to the spin Hamiltonian parameters, evaluated at a_I, and

$$\chi^2 \equiv \sum_i \frac{(|\Delta E_i - h\nu_i)^2}{\sigma_i^2}. \tag{15}$$

The summation over the index of summation i represents all the resonant line positions used in the fitting, ΔE_i is the calculated energy difference between two energy levels participating in a resonance, h is the Planck's constant, ν_i are the applied frequencies and σ_i is the effective weight factor for the i-th line position. A new vector a is obtained from equation 14 and used to provide the new starting parameters in the next iteration step. The cycle is repeated until a sufficiently small χ^2, consistent with the experimental results, is obtained (if convergence is achieved, $\chi^2 = \chi^2_{min}$). Then, the resulting parameters (a_{min}) are the best fit for the EPR spectra. The computer time is considerably reduced if the starting parameters are close to the best fit parameters [64].

There is an important question, after obtaining the best fit parameters for the spin Hamiltonian: the determination of the "goodness of the fit" of the least-squares solution. To answer this question, error margins must be assigned to the spin Hamiltonian parameters. In this case, errors were calculated by a brute-force method, which is illustrated in the following. The starting point is given by the best fit parameters a_{min} with χ^2_{min}. Then, a determined parameter a_p is considered and a fixed offset δa_p is given. Now, the remaining parameters are optimised by least-squared fitting and a corresponding χ^2_0 is obtained. The process is repeated varying the fixed offset δa_p until χ^2_0 is sufficiently small for calculated EPR lines to give a close fit respect to the best fit. Finally, the offset δa_p is considered as the error margin in the parameter a_p. This method is unfortunately numerically elaborate and time consuming [65].

3.5 Photoluminescence

Photoluminescence is a further commonly employed method to investigate intrinsic defects and dopants in solid states. Point defects, for example donors or acceptors, are characterized by strongly localized energy levels in the band gap, which host electrons or holes. Luminescence can be induced, for instance, irradiating the samples with high energy photons. Thereby, electrons localized at the defect levels are transferred to the conduction band, moreover but also holes are produced in the valence band by the excitation of valence electrons into the conduction band or into a defect level. Excited electrons and holes move within the sample, due to the thermal energy or driven by electric fields in the crystal, and finally relax to the ground state. The relaxation occurs with different mechanisms, for example by radiative recombination, in which the excess energy is emitted in form of a photon (photoluminescence). Electron-hole-pair recombination can

thus be detected by its photoluminescence. Furthermore, radiative recombination may lead to the identification of defect states, as they may play a role in the recombination path of the excited charge carriers. Each luminescence recombination path has a determined energy, for example the exciton binding energy (electron-hole-pair), which characterizes the defect in case that an exciton is bound to the defect.

The first study of the optical absorption in bulk doped Fe:$LiNbO_3$ was carried out by Clark et al. [66]. It was assumed that iron occupies the Li lattice site in lithium niobate and due to the C_{3v} crystal symmetry, the iron energy levels split into three levels, two e twofold degenerated levels and one a non-degenerated level. These iron-induced energy levels lie in the middle of the lithium niobate band gap. In this way, one photon can induce electron transitions between the valence band, the transition metal levels and conduction band. In the absorption spectra, several bands are present [66, 67]. The A band is centred at 1.1 eV and is mainly obtained by perpendicular (ordinary) polarization and induced by crystal field transitions a $\rightarrow$ e of the Fe^{2+} ions. The D band appearing at 2.6 eV for perpendicular and parallel (ordinary and extraordinary respectively) polarization is due to the electronic transfer between Fe^{2+} and Nb^{5+}, that promotes an electron from the iron energy levels to the conduction band. The F bands are weak bands, mainly excited

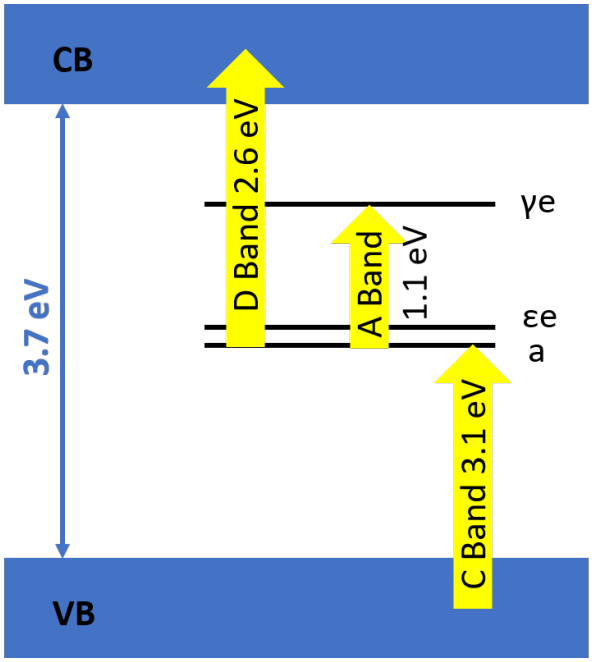

Figure 17: Energy level diagram of iron doped lithium niobate. Optical bands A, C and D involved in photoexcitation processes are indicated. Redrawn from reference [41].

by ordinary (or perpendicular) polarization, and attributed to spin forbidden interband d-d transitions within Fe^{3+} centres. The C band is a broad spectral feature, which starts at 3.1 eV and extends to higher photon energies. This band is excited mainly by ordinary polarization and is related to electronic transitions from the host to Fe^{2+} and Fe^{3+} ions, that is, by the excitation of electrons from the valence band to the transition metal ion levels [36, 41, 79]. A schematic picture of the different transition bands is shown in Figure 17

The ordinary polarization (perpendicular to the principal axis) is the most convenient polarization to investigate the transition involving Fe orbitals in lithium niobate (see Table 4). Moreover, F bands are weak and difficult to be observed. Similarly, C band is not easily visible, as it overlaps with the fundamental absorption of the substrate. In contrast, A and D bands are directly observable and related to Fe^{2+} centres. Yükselici et al. observed that the Fe^{2+} related main absorption band broadens and shifts to higher energies increasing the annealing temperature [68]. Kovács et al. developed a method to determine the composition of $LiNbO_3$ by measuring the UV absorption edge [69].

transition	**E$\|\|$z**	**E$\perp$z**
a $\rightarrow \varepsilon$e	forbidden	allowed
a $\rightarrow \gamma$e	forbidden	allowed
εe $\rightarrow$a	forbidden	allowed
εe $\rightarrow \gamma$e	allowed	allowed

Table 4: Selection rules involved in iron doped lithium niobate under photoexcitation. Rewritten from reference [41].

Titanium doped lithium niobate was investigated by Corradi et al. [48] They assumed that Ti occupies either the Li or the Nb lattice site (in co-doped samples with Mg and Ti). After subtracting a weighted absorption spectrum of the nominally undoped sample, they determined two absorption peaks at 1.78 eV and 2.9 eV [48].

The study of optical absorption spectra is represented by the absorption coefficient (k) versus the energy or wavelength of the transmitted beam. Absorption coefficient is defined as the ratio between the absorbance A and the thickness d of the sample:

$$k = A/d \tag{16}$$

Absorbance is the logarithm of incident intensity (I_0) divided by the intensity of the beam passed through the sample (I):

$$A = \log\left(I_0/I\right) \tag{17}$$

Using Equation 16 and 17, PL measurements are displayed in Chapter 4 Measurements.

3.6 Density functional theory

In the EPR subsection it was pointed out that structural defects strongly influence the materials properties and, owing to EPR analysis, paramagnetic point defects in a host crystal are described. However, a quantum theory is needed to provide a correct and fundamental understanding of the wide variety of phenomena that take place in the considered system. As Payne et al. indicate in [70], nearly all physical properties are associated to total energies or to differences between total energies. One example is given by the equilibrium lattice parameters of a crystal, while another example are the structural properties of point and extended defects in solids. In both cases the total energy is minimized, in the first case for a given lattice constant and in the second case for a defect structure. Predicting the total energy of a system of electrons and nuclei, quantum mechanical calculations are able to anticipate material properties.

Quantum mechanical modelling can be used in every system, especially when an experiment is impossible or when the experiment is hard to carry out (for example an isolated defect that is clouded by other impurities). Nonetheless, calculations require significant computer time, even for systems containing few atoms. Even though quantum mechanical modelling has been continuously refined and the calculations have become much more efficient in the last decade, it needs powerful computers to reduce the calculation time and increase the number of atoms in the considered system [70].

The aim of the quantum mechanical modelling employed in this work (density functional theory) is to obtain the approximate solution of the time-independent and non-relativistic Schrödinger

equation:

$$\widehat{H}\Psi_i\left(\vec{r}_1,\vec{r}_2,...,\vec{r}_N,\vec{R}_1,\vec{R}_2,...,\vec{R}_M\right) = E_i\Psi_i\left(\vec{r}_1,\vec{r}_2,...,\vec{r}_N,\vec{R}_1,\vec{R}_2,...,\vec{R}_M\right) \tag{18}$$

Where $\widehat{H}$ is the Hamiltonian operator of the system with N electrons and M nuclei in absence of electric and magnetic fields.

In the Born-Oppenheimer approximation, the slow motion of the nuclei is separated from the fast motion of the electrons, and the Hamiltonian operator is divided in an electronic and a nuclear part.

Considering the nuclei as classical particles (coupled with electrons by Coulomb interactions), electrons move in the potential generated by nuclei. In this way, the original problem is reduced to solving the electronic Hamiltonian:

$$\widehat{H}\Psi_i\left(\vec{r}_1,\vec{r}_2,...,\vec{r}_N\right) = E_i\Psi_i\left(\vec{r}_1,\vec{r}_2,...,\vec{r}_N\right) \tag{19}$$

Even with this simplification, the many body problem remains formidable. Nevertheless, further simplifications can be considered, allowing the calculation of the total energy of an atomic system in an accurate and efficient form.

The pillars of the density functional theory (DFT) are the Hohenberg-Kohn theorems, which reduce considerably the complexity of the equations [71]. In the first theorem, the charge density is chosen as the central quantity of the theory. The ground state density univocally determines the external potential V_{ext} that specifies the Hamiltonian operator $\widehat{H}$. The second theorem states that only the ground state density delivers the ground state energy of the system. In other words, it states that the density functional $E\left[n\right]$ has a minimum for the ground state charge density n_0.

Owing to the Hohenberg-Kohn theorems, the electronic Hamiltonian is written in terms of electronic density $n(\vec{r})$, reducing the number of variables from 3N to 3, and making the many body problem accessible. The Hamiltonian can be written as a sum of the kinetic energy (T) and the potential energy (V) of all the electrons moving in an external potential due to the nuclei:

$$H\left[n\left(\vec{r}\right)\right] = T\left[n\left(\vec{r}\right)\right] + V\left[n\left(\vec{r}\right)\right] \tag{20}$$

In general, kinetic and potential energy are complex terms due to the fermion character of electrons and their Coulomb interaction. The wave function of many-electron system must be

antisymmetric under exchange of two electrons because electrons are fermions. This wave function anisotropy produces a special separation between electrons with the same spin, reducing the Coulomb energy of the system. This energy reduction is called exchange energy. In this way, the total energy of the system can be expressed as a functional of the charge density, given as the sum of the kinetic (T_0) and potential (V_0) energy of electrons that do not interact with each other (but leading to the charge density $n(\vec{r})$) plus the exchange and correlation potential V_{xc} which takes into account the interactions.

$$E[n(\vec{r})] = T[n(\vec{r})] + V[n(\vec{r})] = T_0[n(\vec{r})] + V_0[n(\vec{r})] + V_{xc}[n(\vec{r})] \tag{21}$$

In a quantum mechanical formulation, the energy functional can be expressed as:

$$\begin{aligned} E[n] = \sum_{i=1}^{N} -\frac{h^2}{2m} \int \varphi_i^*(\mathbf{r}) \nabla^2 \varphi_i(\mathbf{r}) d^3r + \int V_{ext}(r) n(r) d^3r + \\ \frac{e^2}{2} \int \int \frac{n(r) n(r')}{4\pi\varepsilon_0 |r - r'|} d^3r' d^3r + E_{xc}[n] + E_{lat} \end{aligned} \tag{22}$$

The first term is the kinetic energy, the second the external potential due to the nuclei, the third one the potential energy of the electrons, E_{xc} is the exchange-correlation energy, which collects everything that is unknown (non-classical effects of self-interaction correction, exchange and correlation and part from the kinetic energy) and E_{lat} is the lattice energy. The ground state is the minimum $E[n]$ value. That means, the derivative of $E[n]$ with respect to $\varphi_i^*(r)$ setting that $\varphi_i(r)$ is normalized:

$$\frac{\delta}{\delta \varphi_i^2} \left\{ E[n] - \sum_{i=1}^{N} \varepsilon_i \left(\int |\varphi_i^*(\mathbf{r})|^2 d^3r \right) \right\} = 0 \tag{23}$$

This gives the Kohn-Sham equation:

$$\left\{ -\frac{h^2}{2m} \nabla^2 + V_{ext}(r) + V_{Hartree}(r) + \frac{\delta E_{xc}[n]}{\delta n(r)} \right\} \varphi_i(r) = \varepsilon_i \varphi_i(r) \tag{24}$$

Here, the first term is the kinetic potential, the second term the external potential, the third one is the Hartree potential due to the interaction between electrons and the last term is the exchange-correlation potential. The effective potential in the Kohn-Sham equation depends on the charge density of the ground state, which has to be calculated. If the correct exchange-correlation energy is known, the Schrödinger equation is in principle exact. Nonetheless, the exchange-correlation energy is unknown for most systems and has to be approximated. Moreover, the Kohn-Sham

equation, whose potential depends on the change density itself, must be solved self-consistently. That is: the starting charge density is guessed and the equation is solved; with this solution, a new potential is generated and utilized to solve the Kohn-Sham equation again. The cycle is repeated until the solution of the Kohn-Sham equation does not change considerably from iteration to iteration. The quality of the density functional approach hinges on the accuracy of the chosen approximation to the exchange-correlation potential.

Introducing a basic approximation (local density approximation, LDA), the exchange-correlation energy as a local function of the electronic density can be calculated. LDA assumes that the exchange-correlation energy per electron at a determined point in the electronic system is the exchange-correlation energy per electron in a homogeneous electron gas with the same electronic density. Thus:

$$E_{xc}^{LDA} = \int_V e_{xc}^{hom}\left[n\left(\mathbf{r}\right)\right] n\left(\mathbf{r}\right) d^3 r \tag{25}$$

Here, the exchange correlation energy (e_{xc}^{hom}) per particle of a uniform electron gas will be parametrised. In this approximation, the charge density changes slowly in the space, so it is assumed that it is nearly homogeneous. LDA contributes with rather satisfactory results, however it delivers a moderate accuracy in peculiar compounds such as those with strongly correlated electrons.

Another method to approximate the exchange and correlation energy is the generalized gradient approximation (GGA), which considers not only a local density at a determined point (as LDA) but also the density gradient. With this improvement, the non-homogeneity of the true electron density is taken into account. Now the exchange and correlation energy is expressed as:

$$E_{xc}^{GGA} = \int_V f\left[n\left(\mathbf{r}, \nabla n\left(\mathbf{r}\right)\right)\right] d^3 r \tag{26}$$

The functional $f\left[n\left(\mathbf{r}, \nabla n\left(\mathbf{r}\right)\right)\right]$ improves in many cases the accuracy of the calculations. For example, PW86 and PW91 functionals, introduced by Perdew and Wang, describe the neighbourhood with a gradient correction and neglect large distance effects. So, if it is necessary, GGA can improve LDA results.

Until now, the many body system has been reduced to an effective single-particle problem. Knowing the total energy of the system, the material properties can be investigated, for example, for a single defect embedded in a host. Supposing that the system to study is a single defect embedded in a host crystal with ordered arrays of atoms periodically repeated in the space (ideal

crystal), the number of atoms in a real crystal is too high to be simulated. Only a limited region around the defect can be described, and two strategies can be applied. The first method consists in modelling a part of the lattice with an embedded defect. The surface of this cluster is passivated by pseudo-hydrogen atoms, needed to avoid dangling bonds in the surface. The second method, known as supercell method, assumes periodic boundary conditions, so that atoms at the surface in the supercell are neighbours with the atoms at the opposite side and can interact with them [71].

In this thesis, ab initio total energy calculation using spin-polarized density functional theory as implemented in the VIENA AB INITIO SIMULATION PACKAGE (VASP) were performed [72]. The number of valence electrons employed was three for lithium, thirteen for niobium and six for oxygen. Remaining electrons as well as nuclei were dealt within the pseudopotential approach. The generalized gradient approximation (GGA) in its PW91 formulation was utilized in the frame of this work [35, 73]. Moreover, electronic wave functions were described in a plane wave basis with a maximal kinetic energy of 400 eV. Rhombohedral cells of 80 atoms (848.16 $Å^3$) with a single defect or a defect pair were employed, mirroring a rather high doping concentration of 6.25 mol % [35, 74]. The atomic positions were relaxed until the Hellmann-Feymann forces acting on each atom were lower than 0.01 eV/Å.

Furthermore, transition metals (as for instance Ti, Fe and Nb) contain strongly correlated d electrons, which are distinguished by a strong on-site Coulomb repulsion. Rollmann et al. [75] and Nahm and Park [76] mentioned the importance of a description beyond the mean field theory for the 4d and 5d electrons of Fe and Nb atoms in hematite and lithium niobate, respectively.

With the aim of overcoming the issues of the DFT with semilocal potentials, the simplified approach to the DFT+U [77] method introduced by Dudarev et al. [78] was used in this work. Within this approach, localized occupied d orbitals are shifted to lower energies, while empty d orbitals are raised to higher energies proportionally to an effective U [77] parameter. This parameter is defined as the difference between the spherical averaged Hubbard parameter representing the Coulomb interaction and the screened exchange energy. In addition, the effective U parameter can be in principle determined self consistently. Nevertheless, a value of 4 eV for Nb, Fe and Ti was employed for consistency reasons in the frame of this work [35, 76].

4 Measurements

On the one hand, the host materials (lithium niobate and lithium yttrium borate) and their relevant dopants were described in Chapter 2 Materials. On the other hand, the used experimental and theoretical techniques were outlined in Chapter 3 Methods. In this chapter, the experimental measurements are displayed. The following chapters will be based in these data; thus, experimental results can be found in Chapter Results and, finally, the interpretation of the data is given in Chapter Discussion.

This chapter is organized as follows: it starts with lithium niobate samples. Lithium niobate was measured by means of EPR and PL. Therefore, firstly the EPR measurements are shown and secondly the PL measurements. In both subsections, iron doped lithium niobate is presented in the first place, followed by titanium doped lithium niobate and, finally iron-titanium co-doped lithium niobate. In the second part of the chapter, lithium yttrium borate samples were investigated through EPR spectroscopy. First erbium doping is introduced, then yttrium doping and lastly iron doped lithium yttrium borate.

4.1 Lithium niobate samples

Nearly stoichiometric and congruent lithium niobate samples were specifically grown for the development of this thesis (for more details see the Chapter 3 Methods, about sample preparation). Moreover, lithium niobate samples were single doped and co-doped with iron and titanium. Hence, three kinds of lithium niobate doped samples were considered: iron single doped, titanium single doped and iron-titanium co-doped lithium niobate crystals. A compact description of the studied samples is shown in Appendix A. In the following, the obtained electron paramagnetic and photoluminescence data in stoichiometric and congruent lithium niobate are presented.

4.1.1 Electron paramagnetic resonance

Electron paramagnetic resonance was performed at the University Paderborn using a custom-built X-band EPR spectrometer (see Chapter 3 Methods). Measurements were performed at low temperature (∼5 K) to obtain narrow resonance peaks; using frequencies of the order of 9 - 10 GHz and a magnetic field range from 50 mT to 1100 mT. In addition, samples were rotated about x, y and/or z axis with a step of 5° to 15° to obtain angle dependent EPR spectra. Not only as grown but also annealed lithium niobate doped and co-doped samples were measured (see Appendix A). Calibration was performed with DPPH powder (di(phenyl)-(2,4,6-trinitrophenyl)iminoazanium), whose chemical formula is $C_{18}H_{12}N_5O_6$.

The EPR spectra of doped lithium niobate are introduced below. The first part is dedicated to iron single doped in nearly stoichiometric and congruent lithium niobate. In the second part, titanium single doped in nearly stoichiometric lithium niobate is introduced. In the third part, iron-titanium co-doped nearly stoichiometric and congruent lithium niobate crystals are investigated. Finally, a comparison of the measured spectra is shown.

Iron doped nearly stoichiometric lithium niobate

Nearly stoichiometric lithium niobate was grown with 0.06 mol % of iron in the melt, leading to a homogeneous iron doped $LiNbO_3$ single crystal with a characteristic light orange colour.

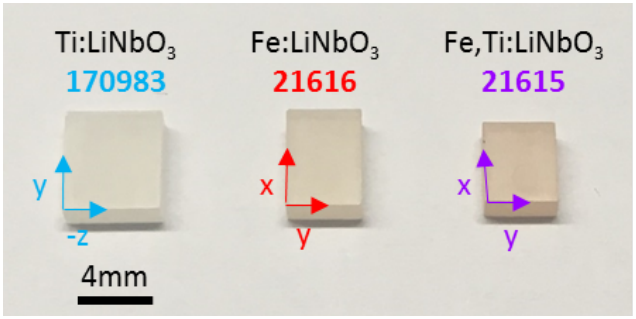

Figure 18: Nearly stoichiometric lithium niobate samples doped with titanium (left), iron (centre) and iron-titanium co-doping (right). The sample are identified by the numbers **170983**, **21616** and **21615**, respectively. Pristine lithium niobate samples are rather transparent, however, they become milky by titanium doping, light orange by iron doping and dark orange by iron-titanium co-doping.

The dimensions of the studied samples were $6 \times 5 \times 1.2$ (mm^3). The iron doped nearly stoichiometric lithium niobate samples are shown in Figure 18.

The iron doped nearly stoichiometric lithium niobate sample (**21616**) was introduced in the resonator cavity and a constant microwave frequency was applied. Increasing the magnetic field, the EPR resonance condition is fulfilled and the EPR spectra are obtained (for a detailed explanation see Chapter 3 Methods). In this case, resonance peaks were distributed in a magnetic field range of almost 1 T (see Figure 19).

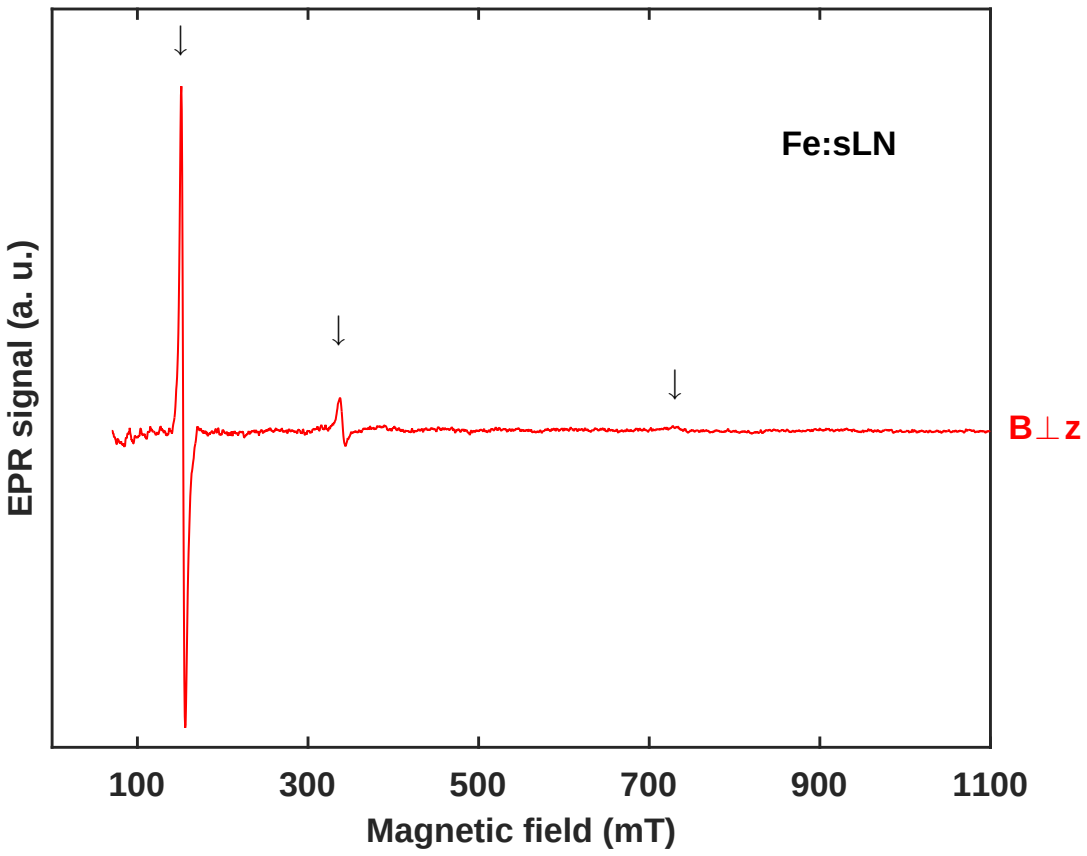

Figure 19: EPR spectrum of iron doped nearly stoichiometric lithium niobate (**21616**). The magnetic field is approximately perpendicular to the z axis. The measurement was carried at low temperatures ($T \approx 5$ K) and the excitation frequency was around 9.88 GHz. The background was subtracted to visualize the resonance peaks clearly.

The three peaks shown in Figure 19 represent three EPR transitions due to Fe^{3+} in lithium niobate. Each peak is due to a different transition (for example $1\rightarrow$ or $3\rightarrow 4$). However, six EPR transitions were expected. In Chapter 3 Methods it was mentioned that Fe^{3+} has an electronic spin of $S=5/2$, therefore $(2S+1) = 6$ EPR allowed transition lines are expected. The assignment of each resonance peak to the corresponding transition is, therefore, a difficult task. Although a broad magnetic field range from 50 mT to 1100 mT was measured, only three resonance peaks are observed. Others do not appear in the recorded spectrum, because the EPR resonance

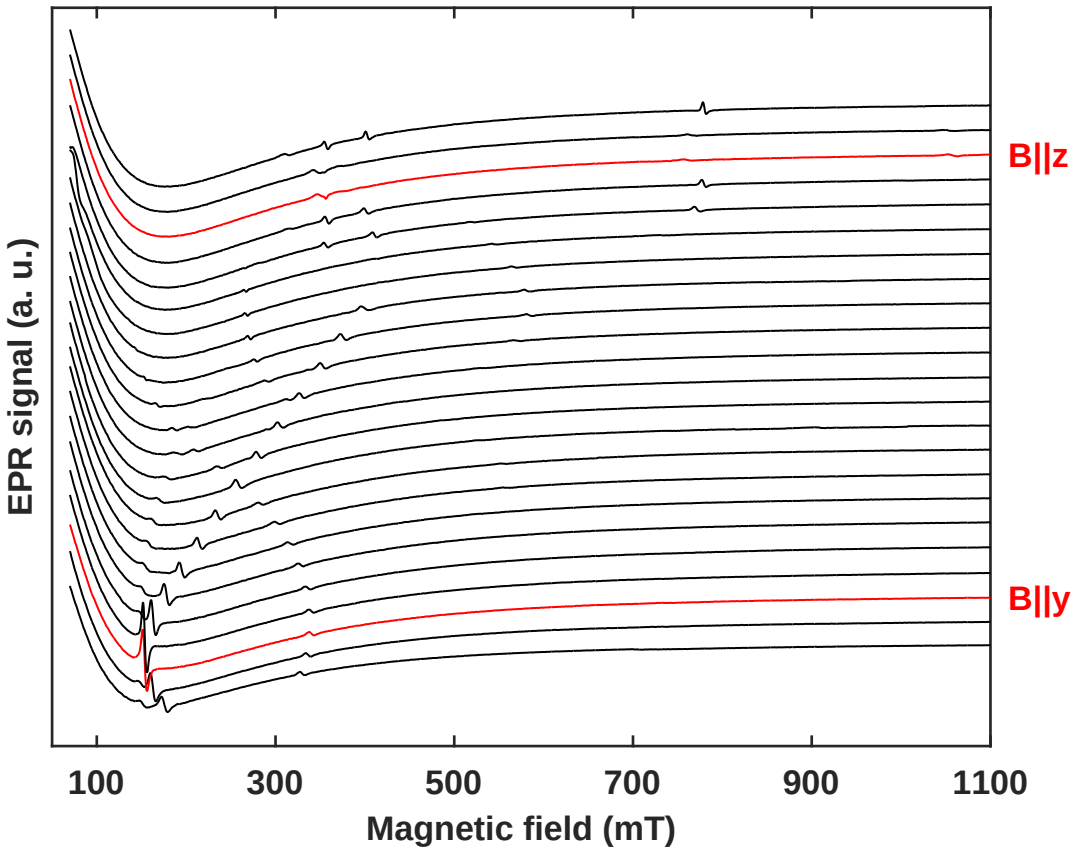

Figure 20: Angle dependence of the EPR spectra of iron doped nearly stoichiometric lithium niobate (**21616**) for rotations about the x axis. Spectra were measured at 5K, with an excitation frequency of 9.877 GHz and with an angle step of 5°. Red spectra denote that the magnetic field was approx. perpendicular (bottom) or parallel (top) to the principal axis (z).

condition is not fulfilled (see Chapter 5 Results). Focusing in the detected peaks, intense EPR peaks correspond to allowed transitions; whereas weak EPR peaks can be allowed ($\Delta m_S = 1$) or even not allowed transitions ($\Delta m_S \neq 1$), depending on their transition probability. In theory, forbidden transitions are not likely to occur, however, in real samples they can occur due to magnetic field perturbations.

In addition, a change in the measurement frequency influences the magnetic field position of the EPR peak in the spectrum (see Figure 13). The linewidth is about 4-5 mT in the nearly stoichio-

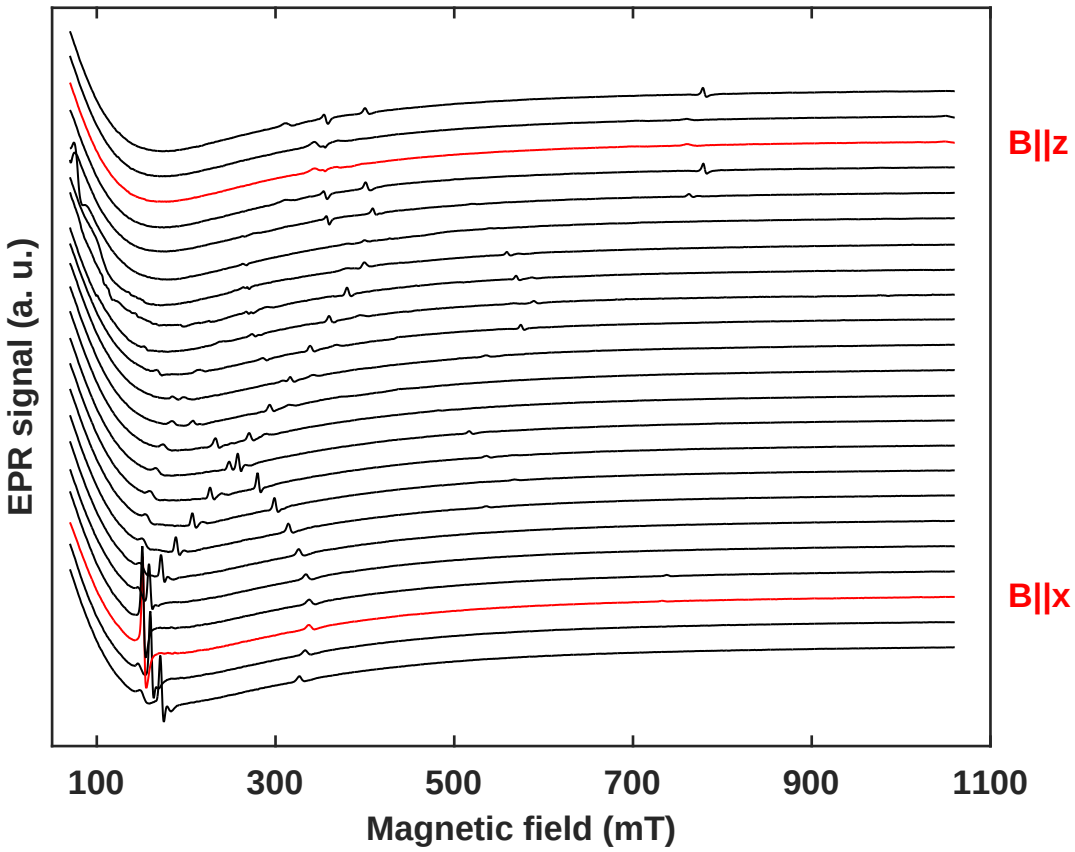

Figure 21: Angle dependence of the EPR spectra of iron doped nearly stoichiometric lithium niobate (**21616**) for rotations about the y axis. The measurements were carried out at 5K, with an excitation frequency of 9.879 GHz and with an angle step of 5°. Red spectra denote that the magnetic field was perpendicular (bottom) or parallel (top) to the principal axis (z).

metric lithium niobate samples. Surprisingly, when the sample is rotated with respect to the applied magnetic field, resonance peaks change their position within the magnetic field or even disappear. Consequently, angle dependent measurements were performed from 50 mT to 1100 mT, including a rotation of at least 120° in steps of 5°. Thus, two different planes (the yz plane shown in Figure 20 and the xz plane shown in Figure 21) of an iron doped nearly stoichiometric lithium niobate crystal were evaluated while the sample was rotated.

Resonance peaks in the rotation about the principal axis (z axis) remain at the same position in spite of the rotation of the sample, since lithium niobate has an axial symmetry. Consequently, only two planes in Fe:$LiNbO_3$ were investigated, because in the third plane no additional information is acquired.

The angle dependent EPR spectra for rotations about the x axis (Figure 20) and about the y axis (Figure 21) are quite similar, however, the EPR spectra for rotations about the y axis present some additional resonance peaks (for a detailed discussion see Chapter 6 Discussion).

The spectra measured for iron doped nearly stoichiometric lithium niobate upon annealing treatment at 600 °C for three hours in vacuum (residual pressure less than 1 mbar and with sample number **21616+600**), are very similar to the spectra displayed in Figures 20 and 21 and are not shown in this work. Furthermore, EPR measurements were carried out at different temperatures to distinguish Fe^{2+} from Fe^{3+}. Nonetheless, no Fe^{2+} features were detected.

Iron doped congruent lithium niobate

Congruent lithium niobate was grown with 0.1 mol % of iron in the melt, leading to a homogeneous iron doped $LiNbO_3$ crystal. The dimensions of the studied sample were $15 \times 4 \times 2.5$ (mm^3), the sample shows a characteristic dark orange colour (see Figure 22).

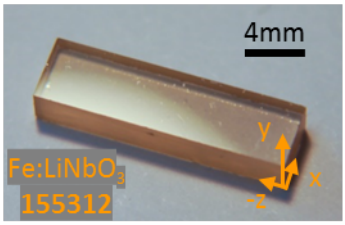

Figure 22: Iron doped congruent lithium niobate (**155312**) with polished y-cut faces.

Angle dependent electron paramagnetic resonance measurements were carried out in an as grown samples for rotations about the three cartesian axes (x, y and z). Iron doped lithium niobate was measured at around 5 K, and about 9.8 GHz in a magnetic field range from 50 mT to 1100 mT. Similarly to iron doped nearly stoichiometric lithium niobate, resonance peaks from a determined transition are found at different magnetic fields, or even disappear by rotating the sample. The angle dependence of the EPR spectra at different planes are shown in Figures 23, 24 and 25 (rotations about x, y and z, respectively).

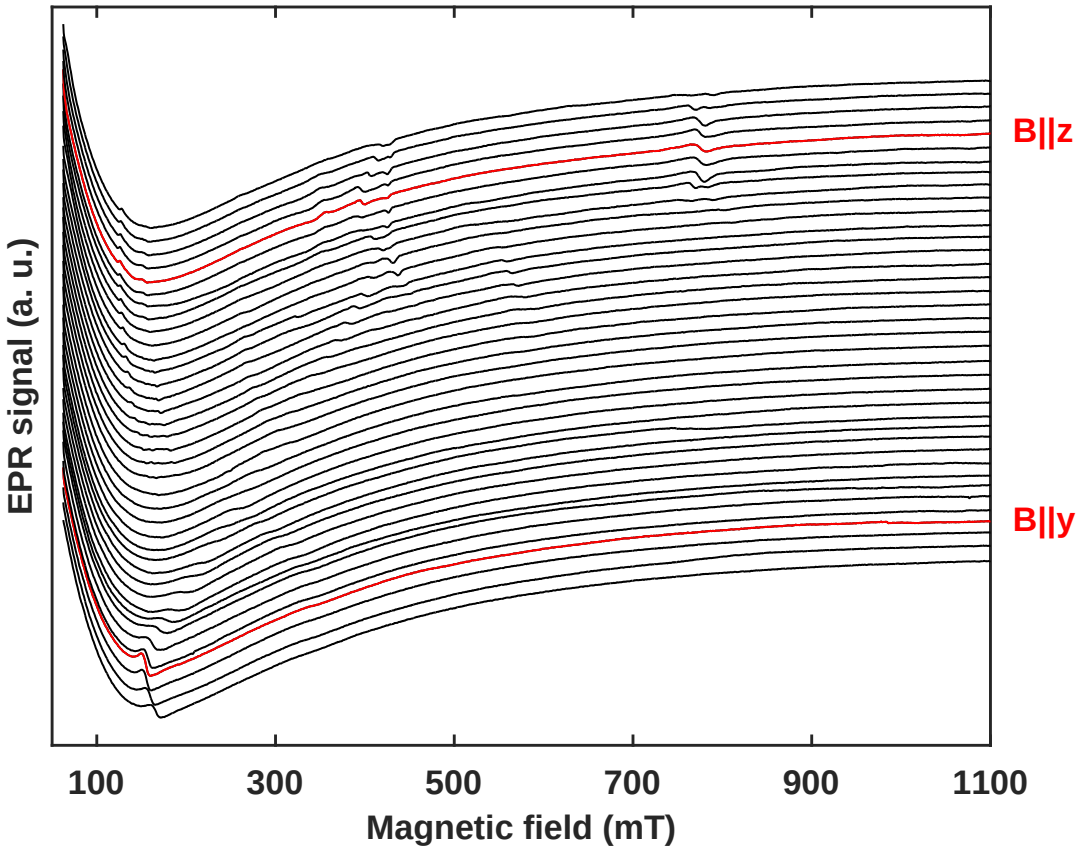

Figure 23: Angle dependent EPR spectra of iron doped congruent lithium niobate (155312) for rotations about the x axis. Spectra were measured at 5K, 9.873 GHz and with an angle step of 3°. The red spectra denote that the magnetic field was approximately perpendicular (bottom) or parallel (top) to the principal axis (z).

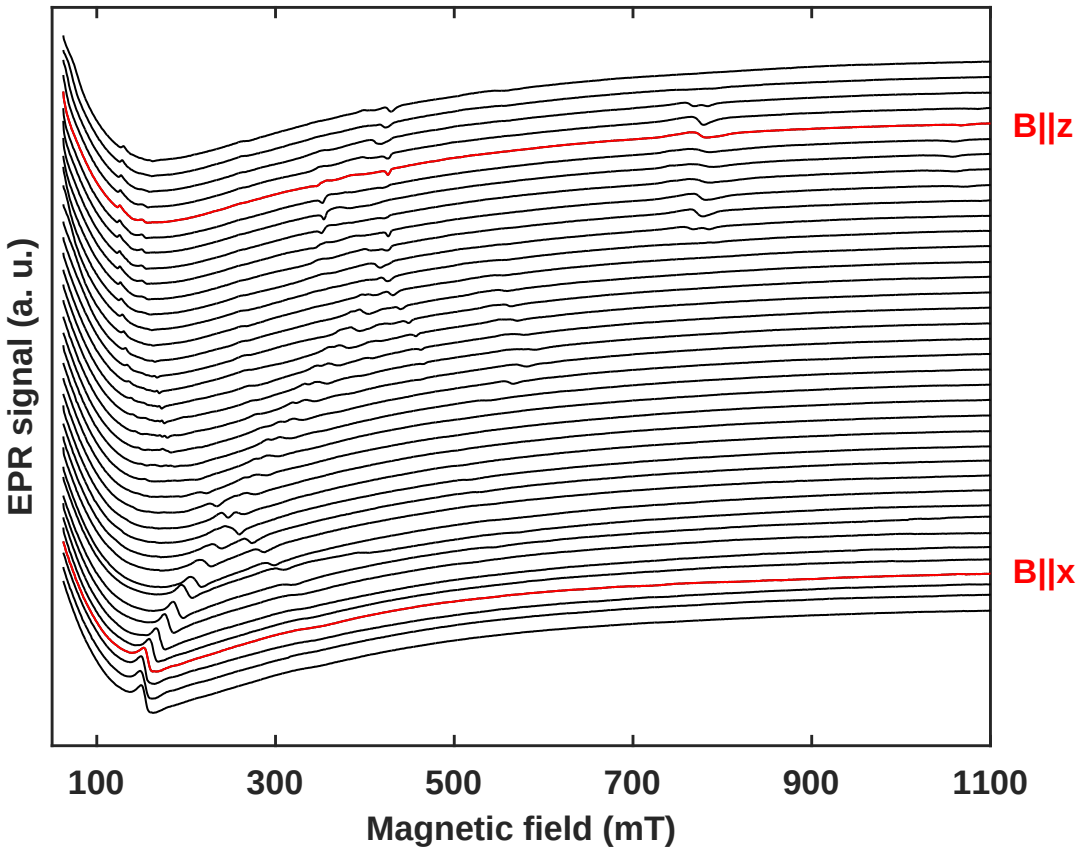

Figure 24: Angle dependence of the EPR spectra of iron doped congruent lithium niobate (**155312**) for rotations about the y axis. Spectra were measured at 5 K, 9.833 GHz and with an angle step of 3°. The red spectra denote that the magnetic field was approximately perpendicular (bottom) or parallel (top) to the principal axis (z).

Comparing iron doped congruent (**155312** Figures 23, 24 and 25) and nearly stoichiometric (**21616** Figures 20 and 21) samples, it appears that the EPR spectra are slightly different. First, the resonance peak intensities are larger in nearly stoichiometric than in congruent samples. However, it would be expected that resonance peaks in congruent samples are more intense because of the larger number of defects (doping concentration is larger in **155312** congruent sample than **21616** nearly stoichiometric sample). Under an applied magnetic field, spins interact with the surroundings in such a way that they tend to restore the equilibrium energy of the system. Consequently, these energy transferences between the spin states with the lattice, influence the

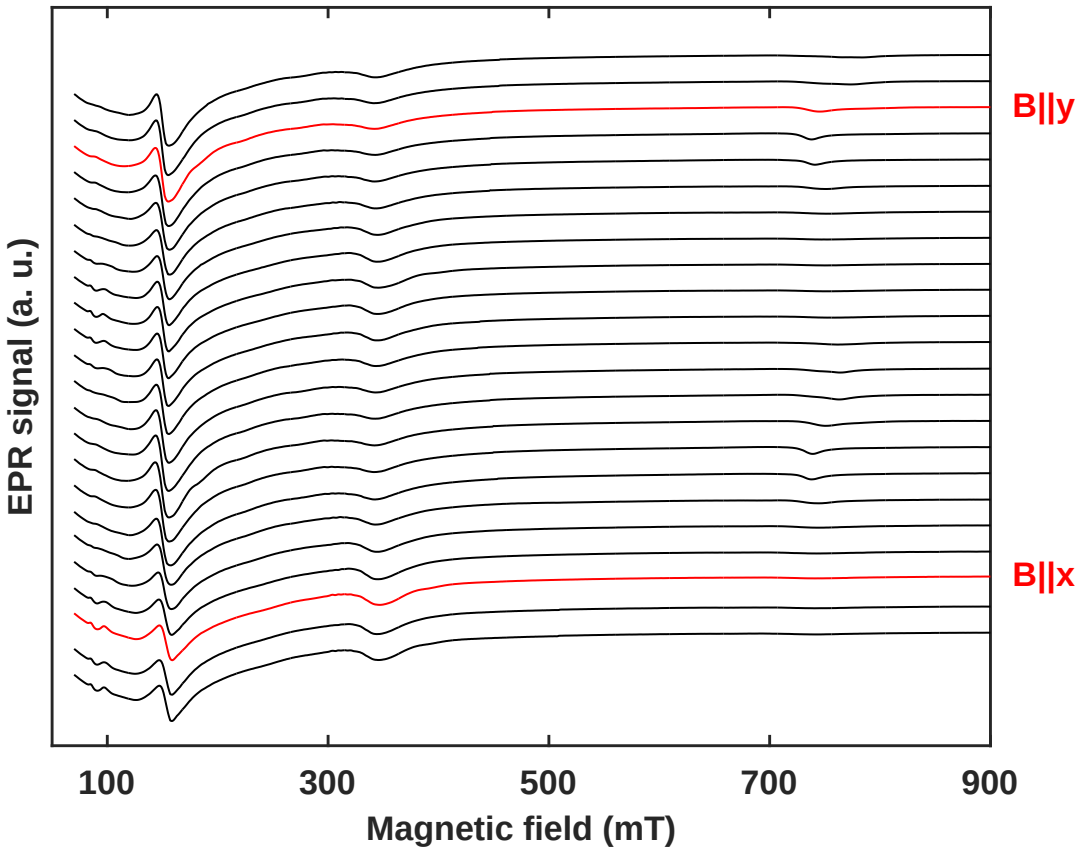

Figure 25: Angle dependence of the EPR spectra of iron doped congruent lithium niobate (155312) for rotations about z axis. Spectra were measured at 5 K, 9.832 GHz and with an angle step of 5°. The red spectra denote that the magnetic field was approximately parallel to the x axis (bottom) and parallel to y axis (top).

EPR absorption. This mechanism is known as spin-lattice relaxation process. Therefore, stoichiometry (or congruency) of the lithium niobate crystals including defects influence the spin-lattice relaxation process, i.e. the efficiency of the EPR absorption. Second, the linewidth is broader in the congruent sample (12-15 mT compared with 4-5 mT in nearly stoichiometric iron doped lithium niobate) due to the number of defects in the crystal (as for example V_{Li} or Nb_{Li}). However, both samples are characterized by a similar angle dependence of the spectra, suggesting a similar iron ion surrounding for both congruent and nearly stoichiometric lithium niobate hosts. The differences between spectra in congruent and nearly stoichiometric samples can be caused

by tilt and offset angles of the sample with respect to the magnetic field in the resonant cavity during the measurement.

Titanium doped nearly stoichiometric lithium niobate

In the subsection above, the results concerning iron doped lithium niobate samples were presented. Before studying iron-titanium co-doped lithium niobate crystals, titanium single doped was investigated. In the nearly stoichiometric lithium niobate melt, 0.05 mol % titanium were introduced.

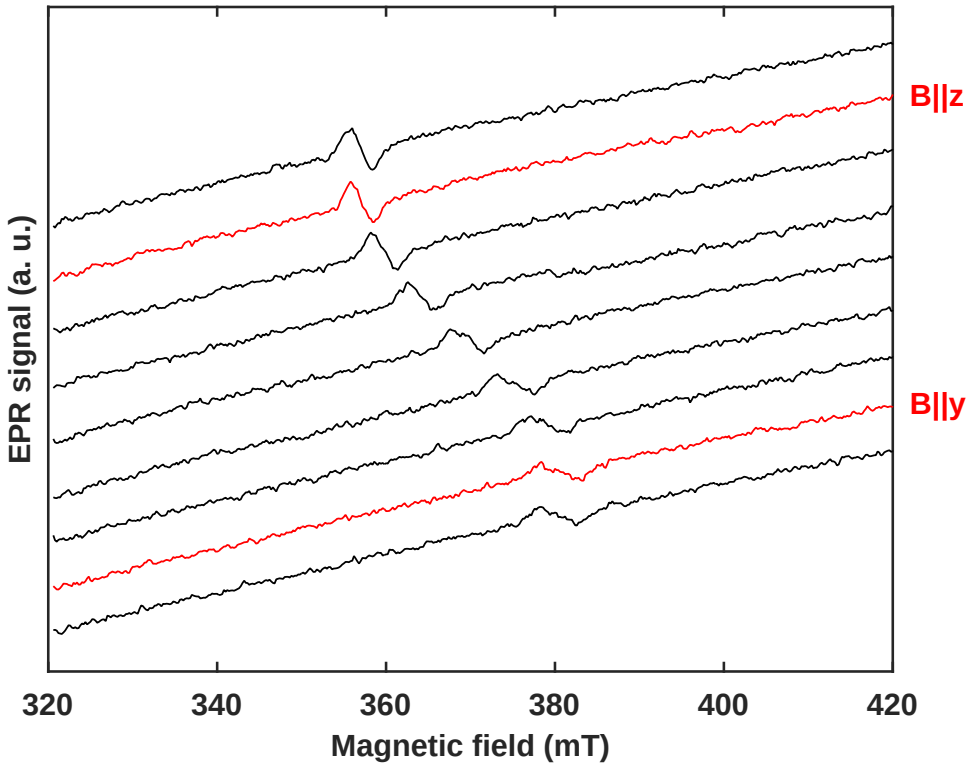

Figure 26: Angle dependent EPR spectra of reduced titanium doped nearly stoichiometric lithium niobate (**170983+900**) for rotations about the x axis. Spectra were measured at 5 K, at 9.873 GHz and with an angle step of 15°. The red spectra denote that the magnetic field was perpendicular (bottom) or parallel (top) to the principal axis (z).

The dimensions of the homogeneous titanium doped $LiNbO_3$ single crystal samples were $6\times5\times1.5$ (mm^3). The titanium doped crystal (**170983**) presents a characteristic milky colour, as it can be seen in Figure 18.

As a reminder, titanium is incorporated in lithium niobate as Ti^{4+} ion which is, unfortunately, a non-paramagnetic configuration (see Chapter 2 Materilas). Nevertheless, applying an annealing treatment (i.e. a reduction process), a paramagnetic ion Ti^{3+} is obtained, which can be measured by EPR. In addition, titanium doped nearly stoichiometric lithium niobate was annealed at 600 °C for 3 hours (**170983+600**) and at 900 °C for 0.5 hours (**170983+900**) in vacuum (residual pressure less than 1 mbar). To reduce lithium out-diffusion, the sample was covered by Li_2CO_3 during the reduction treatment. Only in the sample annealed at high temperature the formation of Ti^{3+} was observed. The axial EPR spectra of the sample annealed at 900 °C (**170983+900**) are illustrated in Figure 26.

Iron-titanium co-doped nearly stoichiometric lithium niobate

In the previous sections, single doping lithium niobate crystals were considered and investigated. In the following, iron-titanium co-doped lithium niobate nearly stoichiometric and congruent crystals are investigated. First, co-doped nearly stoichiometric crystals are presented and second, co-doped congruent crystals are introduced. At the end, a comparison of the two cases is given.

In nearly stoichiometric lithium niobate crystals, 0.06 mol % iron and 0.06 mol % titanium were introduced in the melt, leading to a homogeneous iron-titanium co-doped $LiNbO_3$ single crystal. The colour of the sample is dark orange and the dimensions of the studied samples were $5\times4\times1.5$ (mm^3) (**21615** see Figure 18).

The as grown iron-titanium co-doped nearly stoichiometric lithium niobate crystal (**21615**) was measured at 5 K, at 9.8 GHz and rotating the sample about the x (Figure 27), the y (Figure 28) and the z (Figure 29) axis.

Iron doped nearly stoichiometric (sample **21616**, Figures 20 and 21) and iron-titanium co-doped nearly stoichiometric (**21615** Figures 27, 28 and 29) lithium niobate samples have very similar EPR spectra. This means that in an as grown iron-titanium co-doped sample only Fe^{3+} is observable. In addition, further EPR lines can be seen by rotating the sample about the y axis (just as in the case of rotation about the y axis in iron doped nearly stoichiometric lithium niobate).

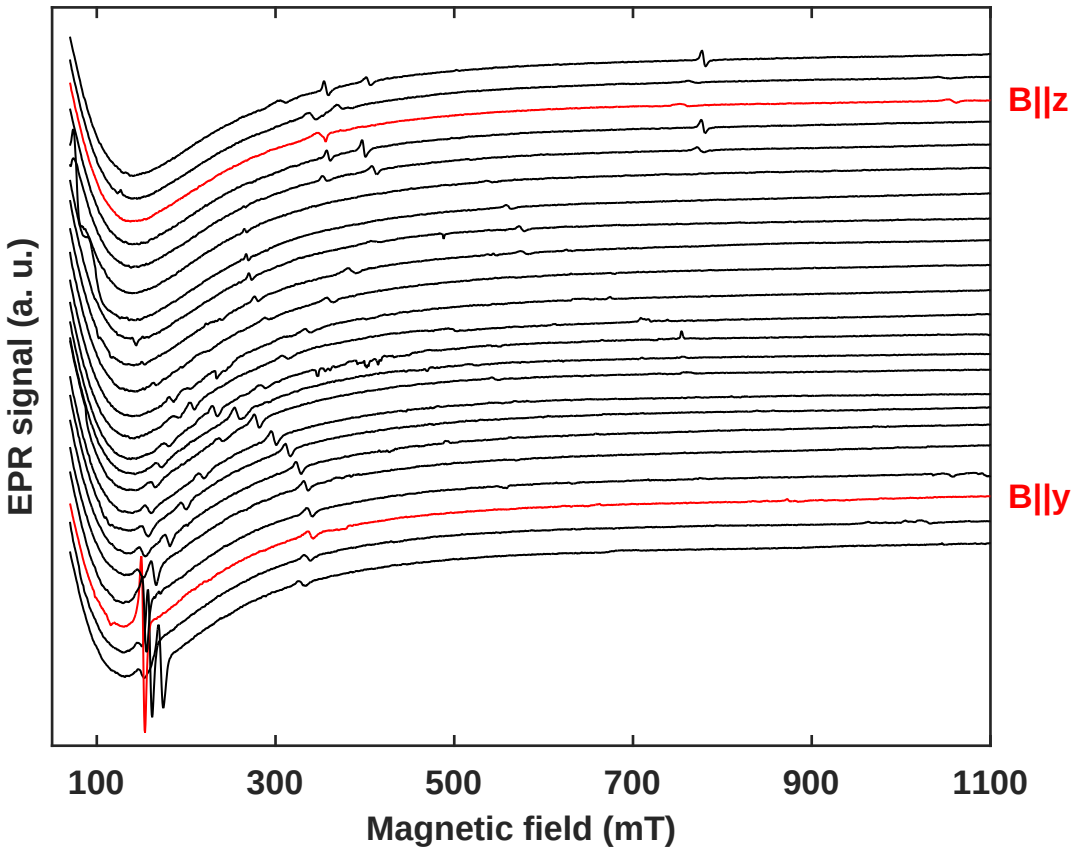

Figure 27: Angle dependence of the EPR spectra of as grown iron-titanium co-doped lithium niobate (**21615**) for rotations about the x axis. The spectra were measured at 5 K, at 9.875 GHz and with an angle step of 5°. The red spectra denote that the magnetic field was perpendicular (bottom) or parallel (top) to the principal axis (z).

With the aim of obtaining titanium related features in the EPR spectra of co-doped lithium niobate, EPR measurements were performed illuminating the sample in the microwave resonator with different frequencies (i.e. colours). Therefore, different frequency high-power LEDs were used as shown in Figure 30.

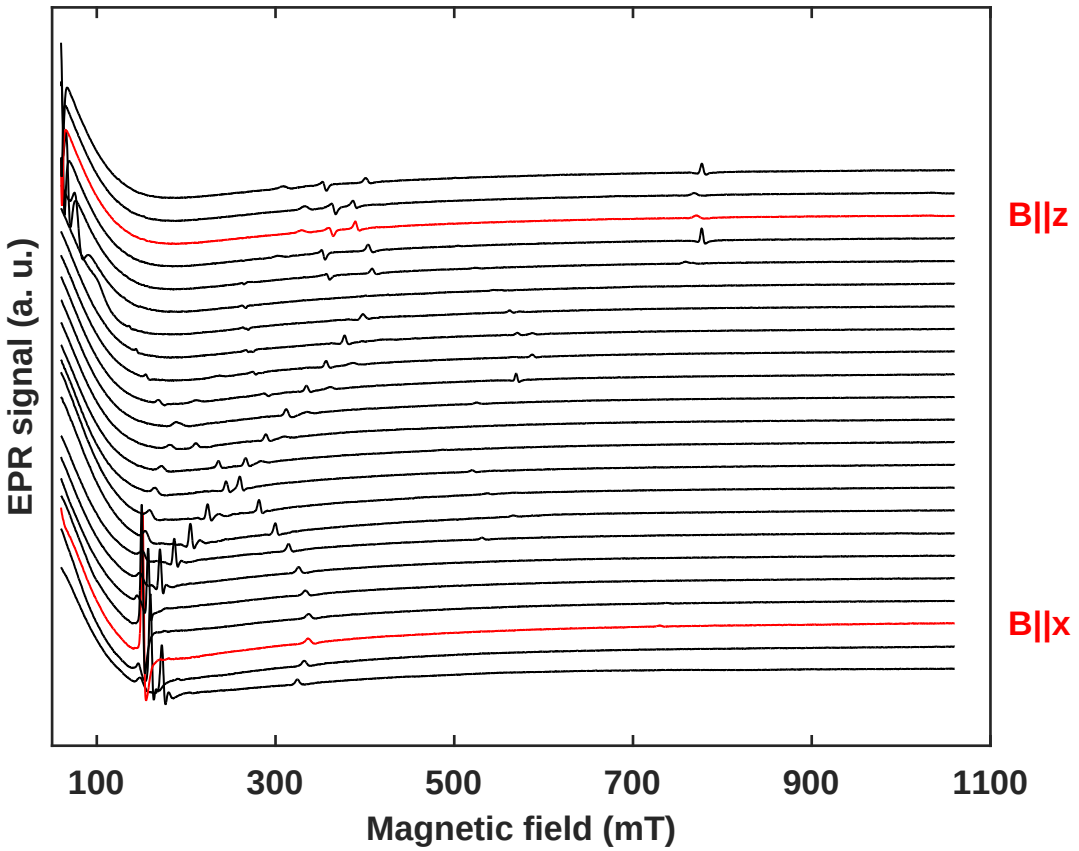

Figure 28: Angle dependence of the EPR spectra of as grown iron-titanium co-doped lithium niobate (**21615**) for rotations about the y axis. The spectra were measured at 5 K, at 9.878 GHz and with an angle step of 5°. The red spectra denote that the magnetic field was perpendicular (bottom) or parallel (top) to the principal axis (z).

However, no new EPR lines with titanium related features were found while illuminating the sample with LEDs during the EPR measurement. The EPR spectra in Figure 30 show three resonance peaks due to iron (Figure 19). The light energy is energetically not enough to excite the titanium energy level from the Fermi level, indeed. Annealing treatment was consequently performed (similar to titanium single doped lithium niobate) to permanently create the EPR visible Ti^{3+} defect centres.

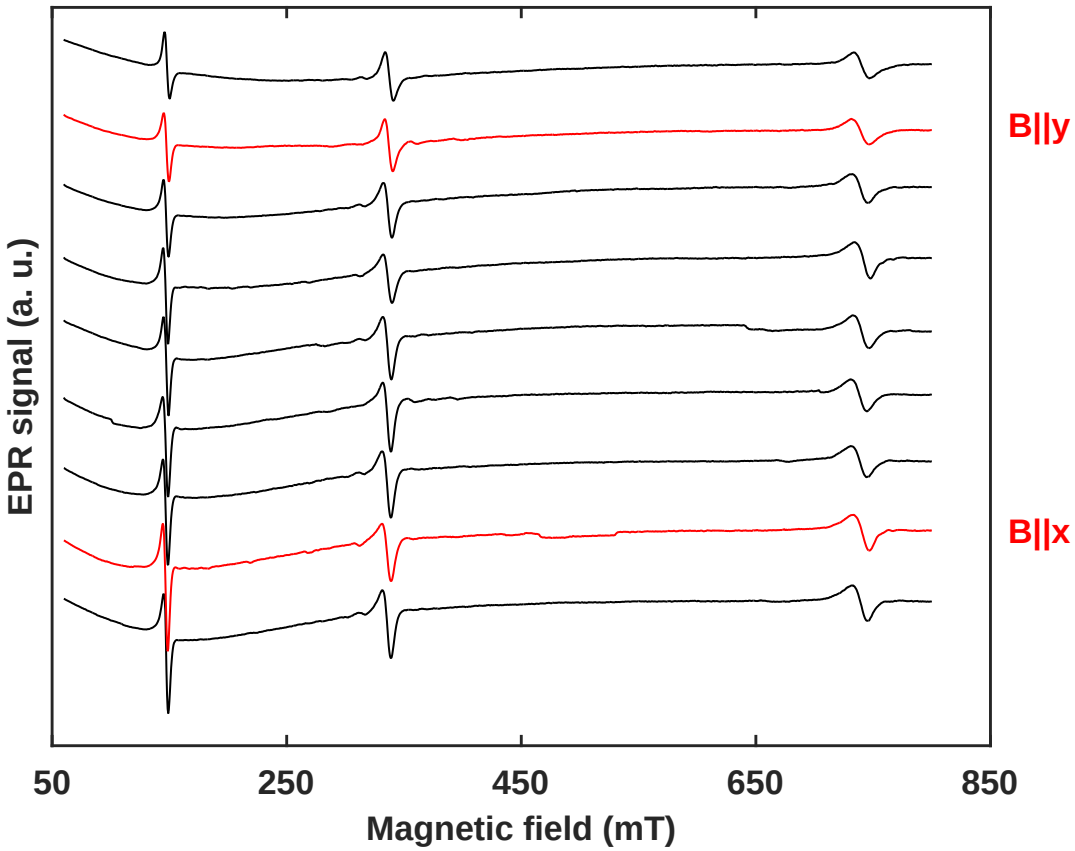

Figure 29: Angle dependent EPR spectra of as grown iron-titanium co-doped lithium niobate (**21615**) for rotations about the z axis. The spectra were measured at 5 K, at 9.853 GHz and with an angle step of 15°. The red spectra denote that the magnetic field was parallel (bottom) to the x axis and parallel (top) to the y axis.

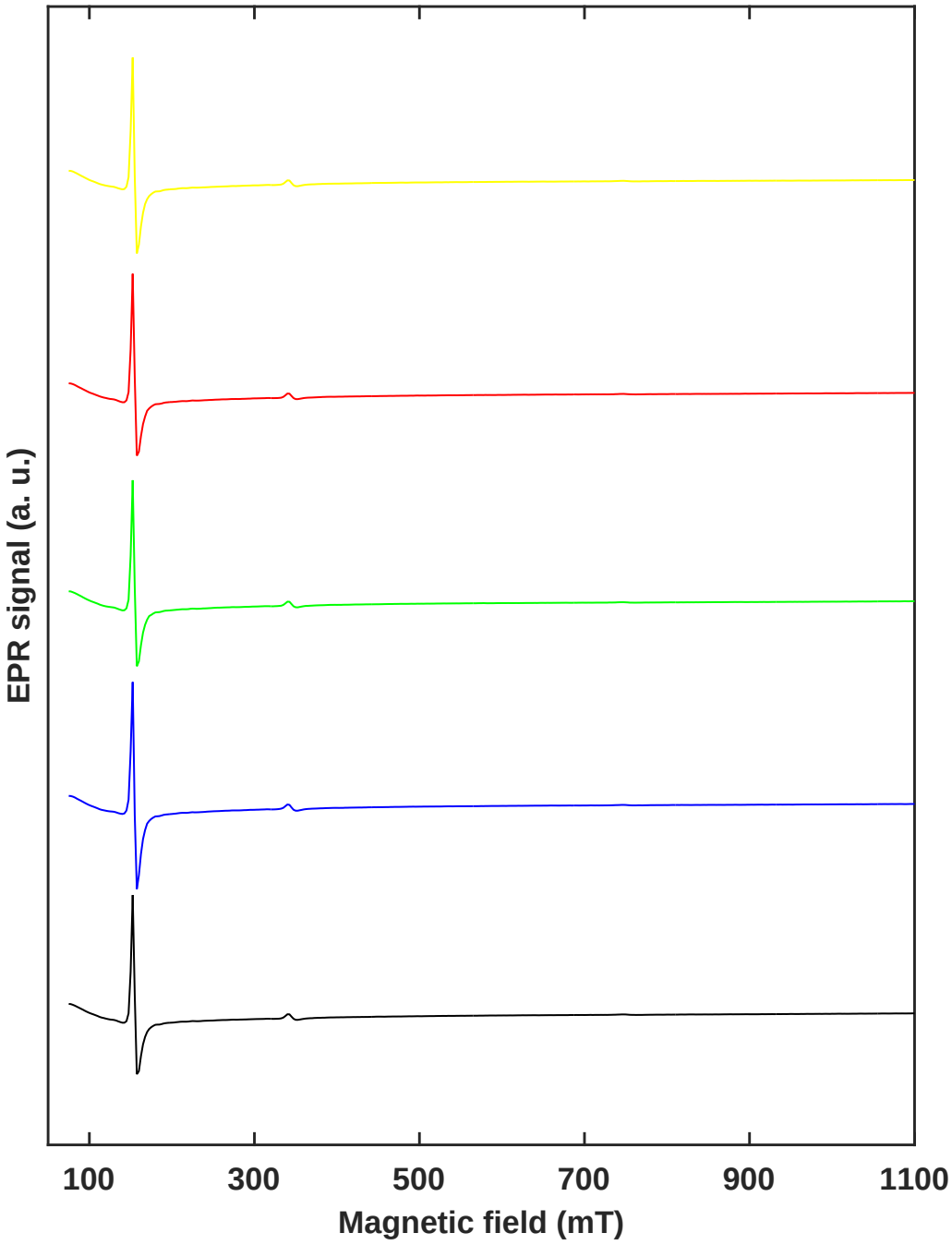

Figure 30: EPR spectra of as grown iron-titanium co-doped lithium niobate illuminated with white colour light (in yellow), red light (in red 623 nm), green light (in green 525 nm), blue light (in blue 470 nm) and without illumination (in black). The measurement was performed at 5 K, at 9.864 GHz and the magnetic field perpendicular to the principal axis (z).

Iron-titanium co-doped lithium niobate was annealed at 500 °C (**21615+500**), 600 °C (**21615+600**) and 900 °C (**21615+900**) for three hours or thirty minutes in vacuum (residual pressure less than 1 mbar). In addition, samples were covered with Li_2CO_3 during the reduction to avoid lithium evaporation. As can be seen in Figure 31, the aspect of the crystal heavily changes after annealing.

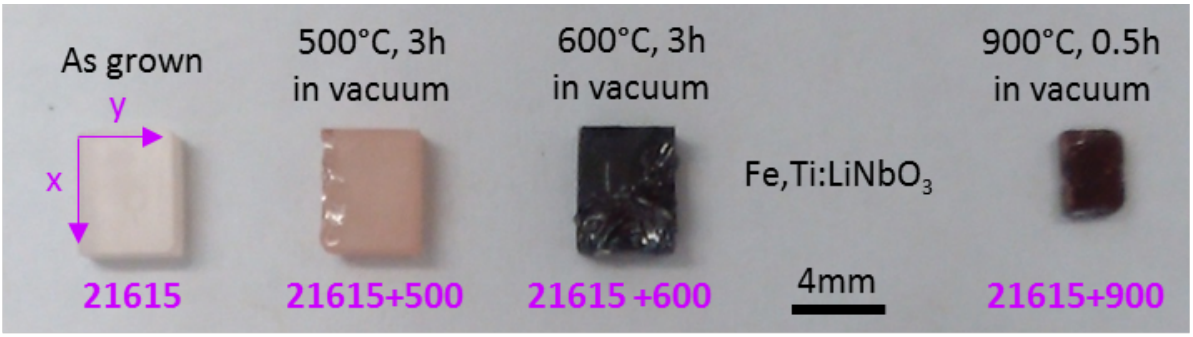

Figure 31: Iron-titanium co-doped nearly stoichiometric lithium niobate crystals (from left to right): as grown (**21615**), annealed at 500 °C for three hours (**21615+500**), annealed at 600 °C for three hours (**21615+600**) and annealed at 900 °C (**21615+900**) for thirty minutes. The temperature treatment was performed in vacuum (residual pressure less than 1 mbar).

At the beginning of the chapter, it has been shown that iron-titanium co-coping has a darker orange colour compared to iron single doped lithium niobate (see Figure 18). In addition, after reduction at 500 °C the colour turns to orange-red, at 600 °C it turns dark grey and at 900 °C deep brown with red tones. Initially, all samples had the same dimensions, however after the annealing treatment at 900 °C the sample became much smaller (see Figure 31). This fact can be explained due to the mechanical cleaning after the reduction. Lithium carbonate (Li_2CO_3), whose melting point is 723 °C, was covering the sample and at considerably elevated temperatures it melted, sticking to the sample. Therefore, mechanical procedure (blade) was applied to eliminate the Li_2CO_3 layer on the surface, carrying away some pieces of the sample (leading to the curved edges). On the other hand, crystals annealed at 500 °C and 600 °C also present irregularities. This is justified by the mechanical and chemical cleaning after the EPR measurement. Crystals are fixed with glue to the sample holder before being introduced in the resonant cavity.

Until now, as grown iron-titanium co-doped nearly stoichiometric lithium niobate (Figures 27, 28 and 29) was studied and only Fe^{3+} ion was observed. In the following, EPR measurements are performed with reduced iron-titanium doped nearly stoichiometric lithium niobate samples. Iron-titanium co-doped lithium niobate samples annealed at 500 °C show the same spectra of the iron doped samples, thus revealing the presence only of the Fe^{3+} centres. However, after the annealing treatment at 600 °C, new lines appear in the angle dependent spectra (see Figure 32).

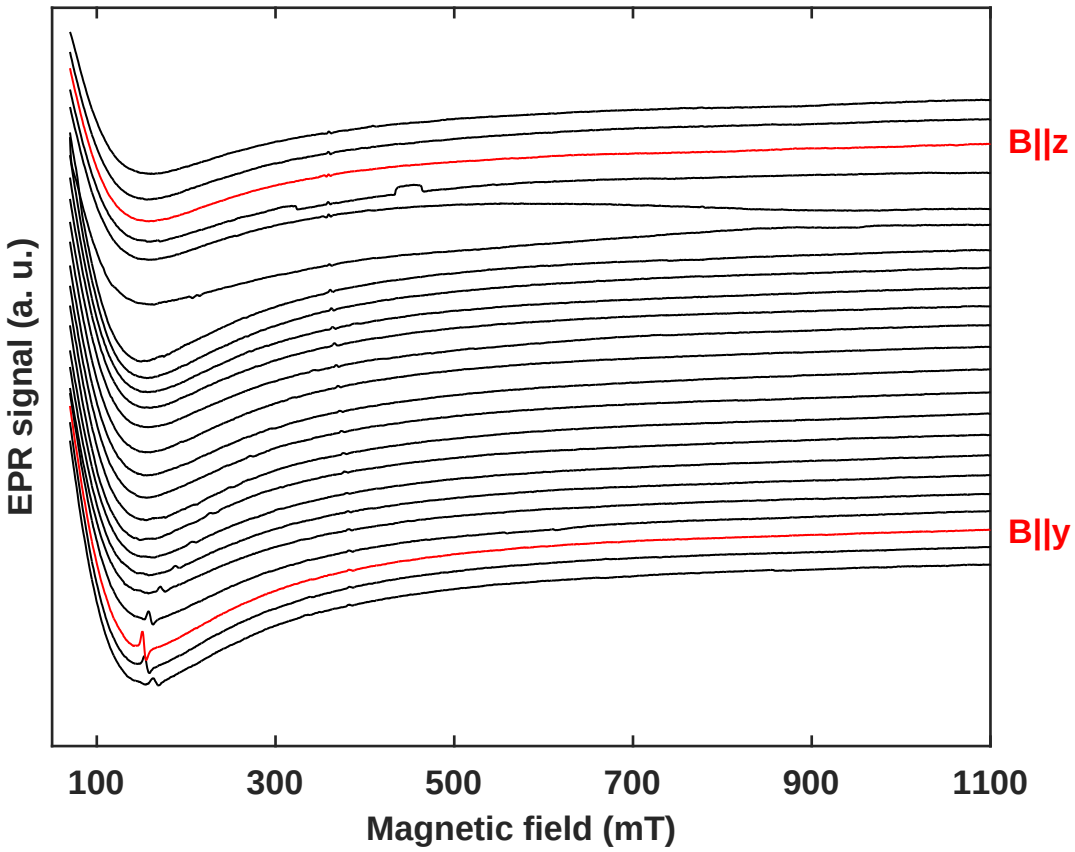

Figure 32: Angle dependent EPR spectra of reduced iron-titanium co-doped nearly stoichiometric lithium niobate for rotations about the x axis. The spectra were measured at 5 K, at 9.878 GHz and with an angle step of 5°. The reduction treatment was performed at 600 °C for three hours in vacuum (**21615+600**). The red spectra denote that the magnetic field was perpendicular (bottom) or parallel (top) to the principal axis (z).

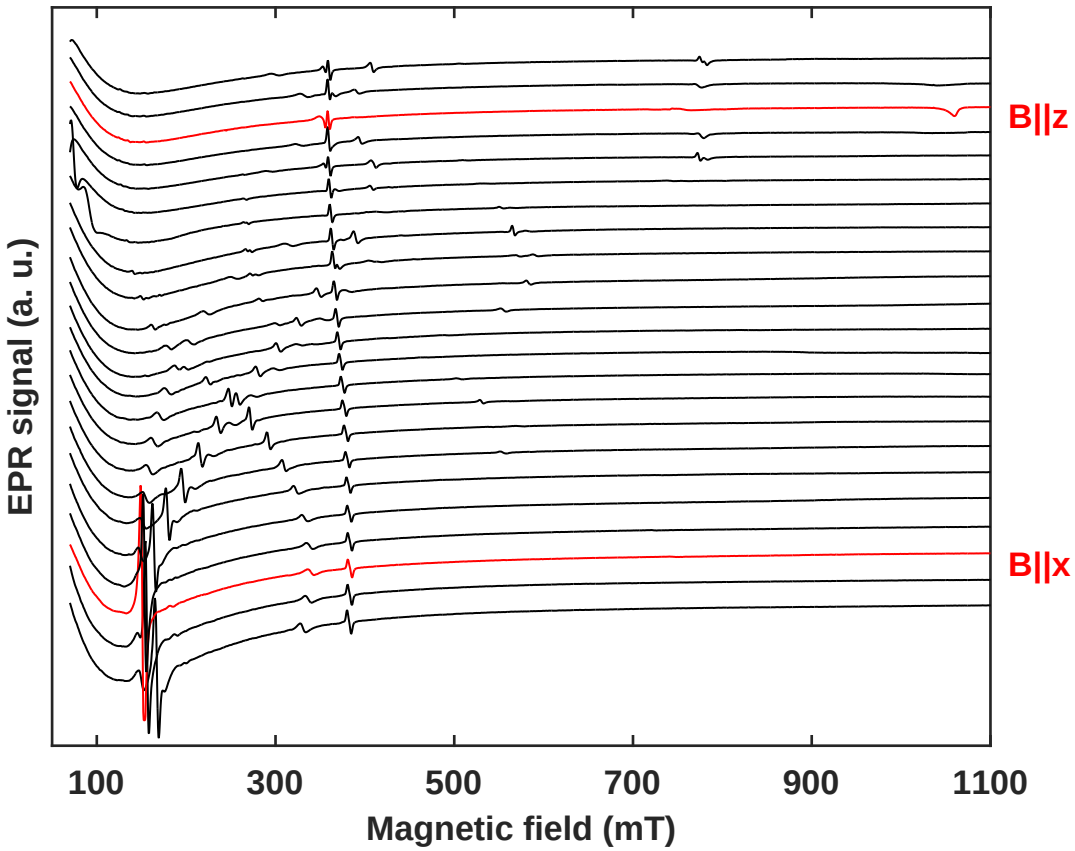

Figure 33: Angle dependence of the EPR spectra of reduced iron-titanium co-doped nearly stoichiometric lithium niobate for rotations about the y axis. The spectra were measured at 5 K, at 9.866G Hz and with an angle step of 5°. The reduction treatment was performed at 600 °C for three hours in vacuum (**21615+600**). Red spectra denote that the magnetic field was perpendicular (bottom) or parallel (top) to the principal axis (z).

After the reduction treatment, Ti^{3+} centres are created, which are EPR-visible and induce signatures next to the iron peaks, as it can be well seen in Figures 32 and 33. Similarly to titanium single doped lithium niobate, the EPR lines are observed between 320 mT and 420 mT (see Figure 34).

Iron-titanium co-doped lithium niobate was also annealed at 900 °C for 30 minutes in vacuum (**21615+900**). In this case, only Ti^{3+} was detected and the Fe^{3+} signatures have disappeared.

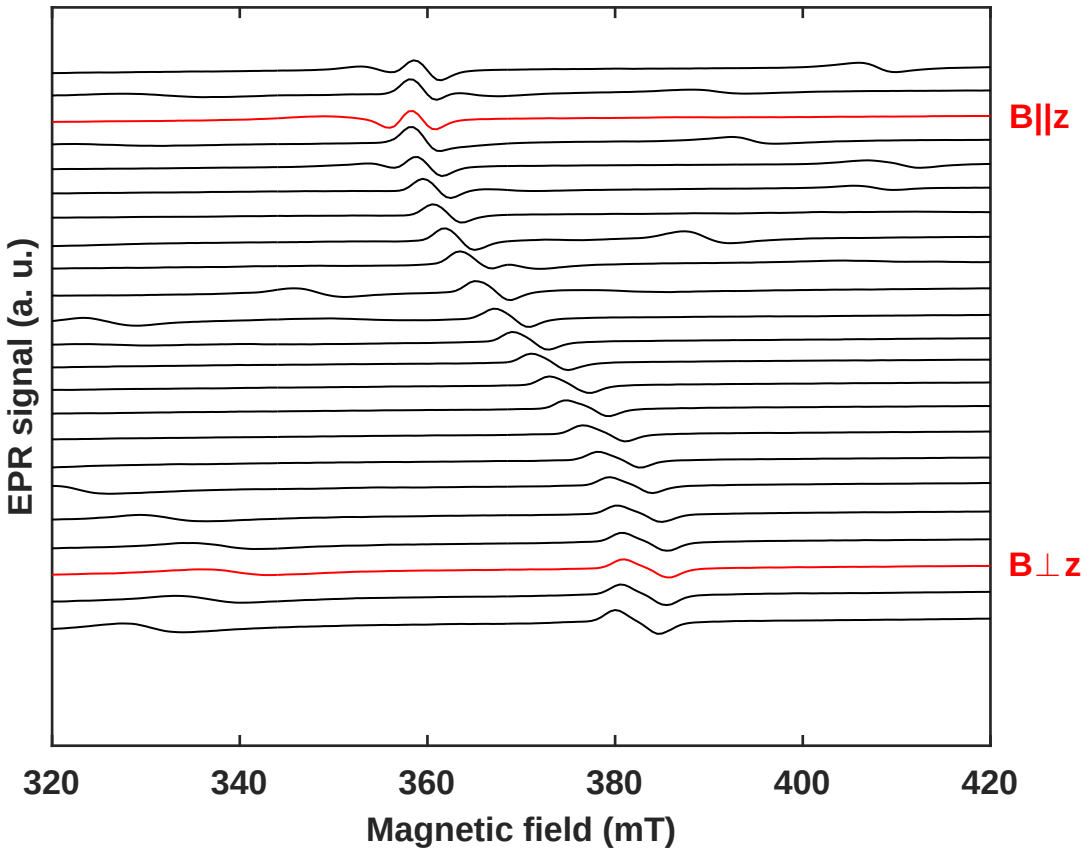

Figure 34: Zoom of the EPR angular dependence shown in Figure 33, in the magnetic field range 320 mT - 420 mT.

Iron-titanium co-doped congruent lithium niobate

In contrast to nearly stoichiometric samples, where linewidth of EPR spectra are narrow (7 - 8 mT for reduced iron-titanium co-coped lithium niobate) in congruent samples the linewidth is broader (12 - 15 mT). In the following, EPR spectra of co-doped lithium niobate samples are presented. The first sample (**155313vs**) was grown with 0.1 mol % of iron in the melt and later titanium was indiffused. Whereas in the second sample, both dopants were indifussed in the second sample (**155313ss**), instead. The corresponding doping concentrations are 1.9×10^{19} at/cm^3 of iron and 110×10^{19} at/cm^3 of titanium.

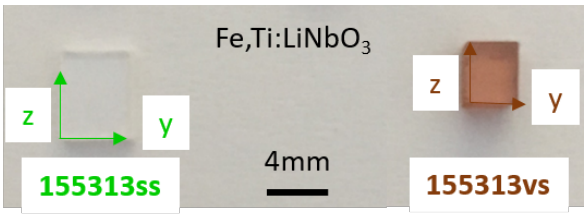

Figure 35: Iron-titanium co-coped lithium niobate crystals. The dark orange sample (**155313vs**) was doped with iron (in the melt) and with titanium (by indiffusion). The transparent sample (**155313ss**) was doped by both iron and titanium indiffusion.

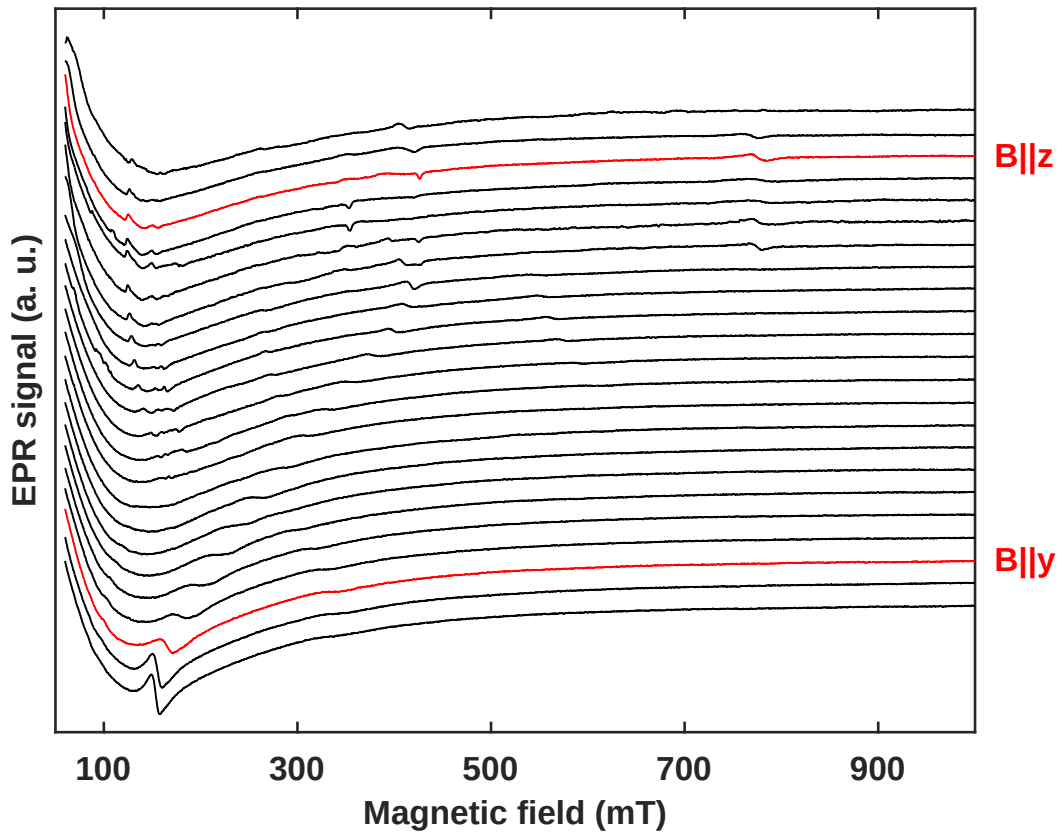

Figure 36: Angle dependence of the EPR spectra of as grown iron-titanium co-doped congruent lithium niobate for rotations about the x axis. The spectra were measured at 5 K, at 9.871 GHz and with an angle step of 5°. The doping process was performed during the crystal growth (bulk doping) for iron and by indiffusion for titanium (**155313vs**). Red spectra denote that the magnetic field was perpendicular (bottom) or parallel (top) to z.

EPR measurements were performed in both crystals, however in the iron and titanium indiffused sample (**155313ss**) no EPR resonance peaks were detected due to the low concentration of paramagnetic dopants (see green spectra in Figures 38 and 39). Concerning the as grown iron doped and titanium indiffused sample (**155313vs**), only Fe^{3+} ion was observed (see Figures 36 and 37).

Similarly to iron single dope lithium niobate, with the aim of promoting the partial reduction of Fe^{3+} to Fe^{2+}, a reduction treatment at 800 °C during 3 hours in argon atmosphere was performed

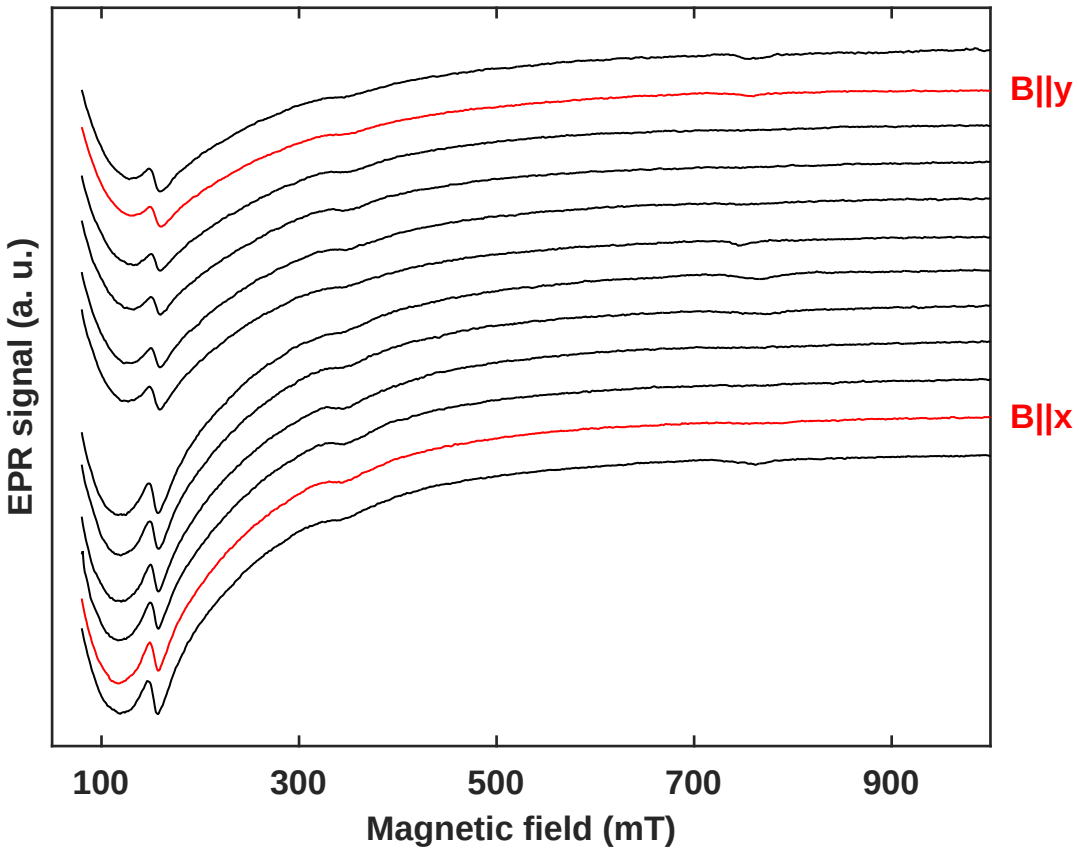

Figure 37: Angle dependent EPR spectra of as grown iron-titanium co-doped lithium niobate for rotations about the z axis. Spectra were measured at 5 K, at 9.863 GHz and with an angle step of 10°. The doping process was performed during the crystal growth (volume doping) for iron and by indiffusion for titanium (**155313vs**). Red spectra denote that the magnetic field was parallel to the axis x and y.

(**155313vs+800**). Unfortunately, no EPR signatures of Fe^{2+} were detectable and neither EPR features of Ti^{3+}.

The EPR spectra measured for the as grown iron-titanium co-doped in congruent lithium niobate (**155313vs**, see Figures 36 and 37) and of the as grown iron-titanium co-doped in nearly stoichiometric lithium niobate (**21615** see Figures 32 and 33) are slightly different. First, peak intensities are larger in nearly stoichiometric than in congruent samples. Although the number of iron ion impurities is larger in congruent than in nearly stoichiometric samples, the spin-lattice relaxation process is different due to the changes in the crystal lattice. Second, the linewidth is broader in the congruent sample (12 - 15 mT compared with 4 - 5 mT in nearly stoichiometric iron doped lithium niobate) due to the high number of other defects in the crystal (as for example V_{Li} or Nb_{Li}) increasing the disorder in the crystal lattice. However, both samples are characterized by a similar angle dependence of the EPR spectra, suggesting a similar iron ion surrounding in both congruent and in nearly stoichiometric lithium niobate hosts.

Differences between spectra in congruent and nearly stoichiometric samples can be furthermore due to tilt and offset angles of the sample respect to the magnetic field in the resonant cavity during the measurement. In addition, under annealing treatment up to 600 °C in vacuum, Ti^{3+} was found in nearly stoichiometric samples. In contrast, in congruent sample annealed at 800 °CC in argon no Fe^{2+} nor Ti^{3+} EPR signatures were found.

Comparison of lithium niobate samples

In the last sections, EPR spectra of single doped and co-doped nearly stoichiometric as well as congruent lithium niobate were detailed. Both iron and titanium were introduced in lithium niobate (by bulk and surface doping techniques) as single dopants and in co-doped samples. In addition, both as grown as well as reduced samples were measured. In this section, the investigated samples are compared to visualize the similarities and differences. For a consistent comparison, analogous experimental conditions must be considered, as for instance the measurement temperature or the angle between rotation axes and the magnetic field.

In the first part, the spectra of iron doped samples is discussed and, in the second part, the spectra of iron and titanium doped samples is discussed. In both parts, EPR resonant peaks induced by iron (and later by titanium) ions are compared regardless of the host material and the doping technique.

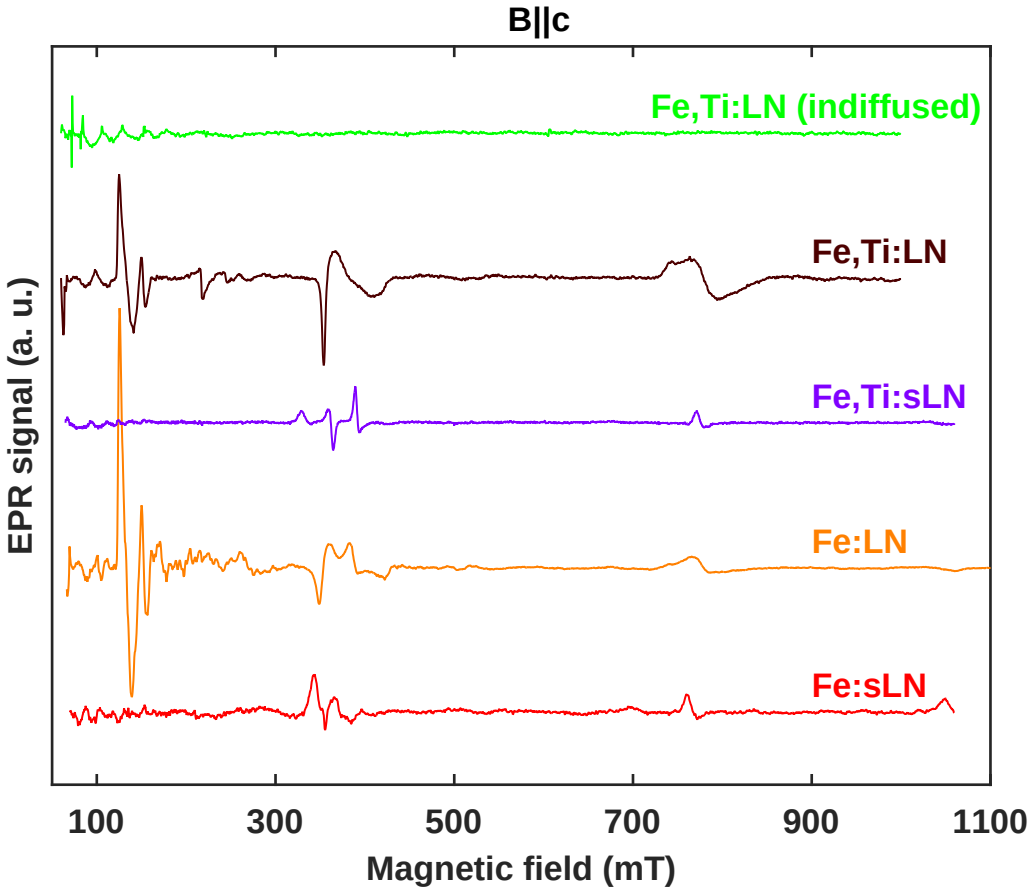

Figure 38: EPR spectra of iron single doped nearly stoichiometric (Fe:sLN **21616**), iron single doped congruent lithium niobate (Fe:LN **155312**), iron-titanium co-doped nearly stoichiometric $LiNbO_3$ (Fe,Ti:sLN **21615**), iron in volume doped and titanium in surface co-doped lithium niobate (Fe,Ti:LN **155313vs**) and iron-titanium indiffused in lithium niobate (Fe,Ti:LN **155313ss**). EPR spectra were recorded at 5 K with the magnetic field parallel to the principal axis.

First iron centre in lithium niobate is analised. Therefore, not only as grown single doped but also co-doped lithium niobate samples are considered (see Figures 38 and 39). As it can be seen in both Figures, resonance peaks are approximately obtained at the same magnetic field position in the different considered samples. This fact evidences that similar iron centres are found in single doped and co-doped samples.

Comparing Figures 38 and 39, the EPR spectra in Figure 38 have less fluctuations than in Figure 38. In other words, resonance peaks are more intense when the magnetic field is perpendicular to the principal axis (Figure 39). This could be due to a different magnetization in lithium niobate for a magnetic field parallel or perpendicular to the principal axis.

On the one hand, comparing congruent samples (**155312**, **155313vs** and **155313ss**) versus nearly stoichiometric samples (**21616** and **21615**), the linewidth becomes broader because more

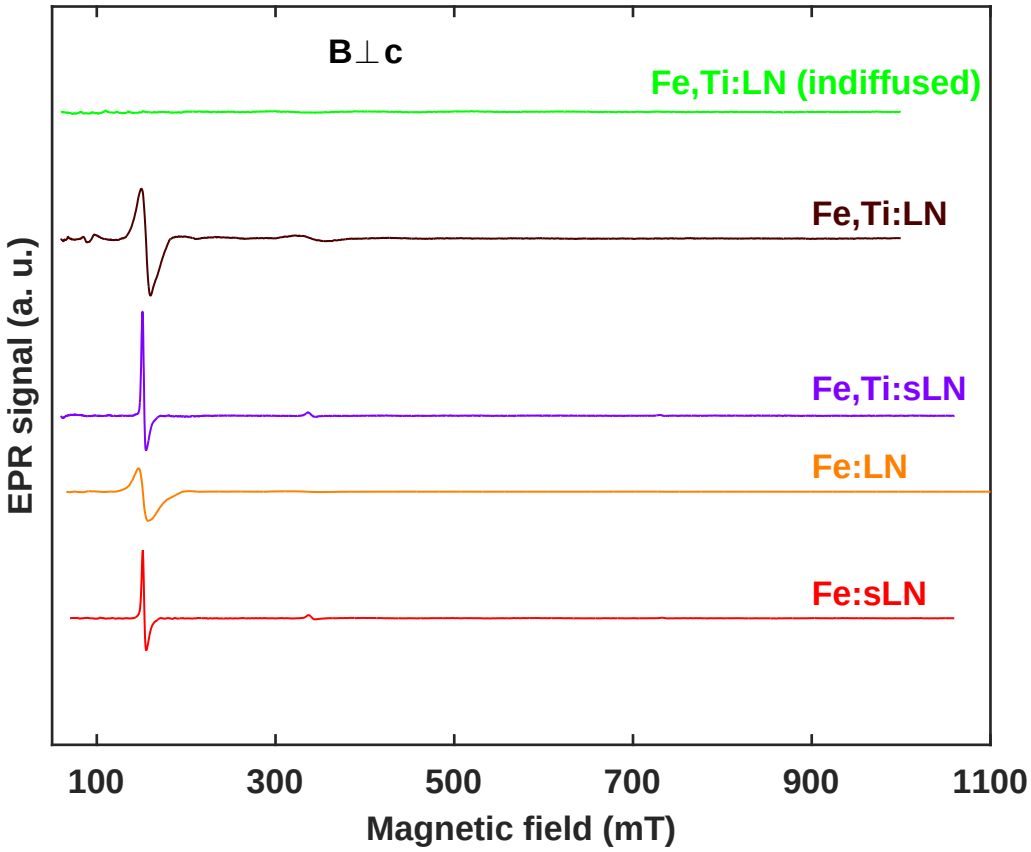

Figure 39: EPR spectra of iron single doped nearly stoichiometric (Fe:sLN **21616**), iron single doped congruent lithium niobate (Fe:LN **155312**), iron-titanium co-doped nearly stoichiometric $LiNbO_3$ (Fe,Ti:sLN **21615**), iron in volume doped and titanium in surface co-doped lithium niobate (Fe,Ti:LN **155313vs**) and iron-titanium indiffused in lithium niobate (Fe,Ti:LN **155313ss**). EPR spectra were recorded at 5 K with a magnetic field perpendicular to the principal axis.

lithium deficiencies are found in congruent samples. On the other hand, the peak intensity in co-doped lithium niobate samples is larger than in single doped samples. The reason could be the interaction between titanium and iron, which influences the spin-lattice relaxation process increasing EPR absorption in co-doped samples. A detailed discussion is given in Chapter 6 Disscusion.

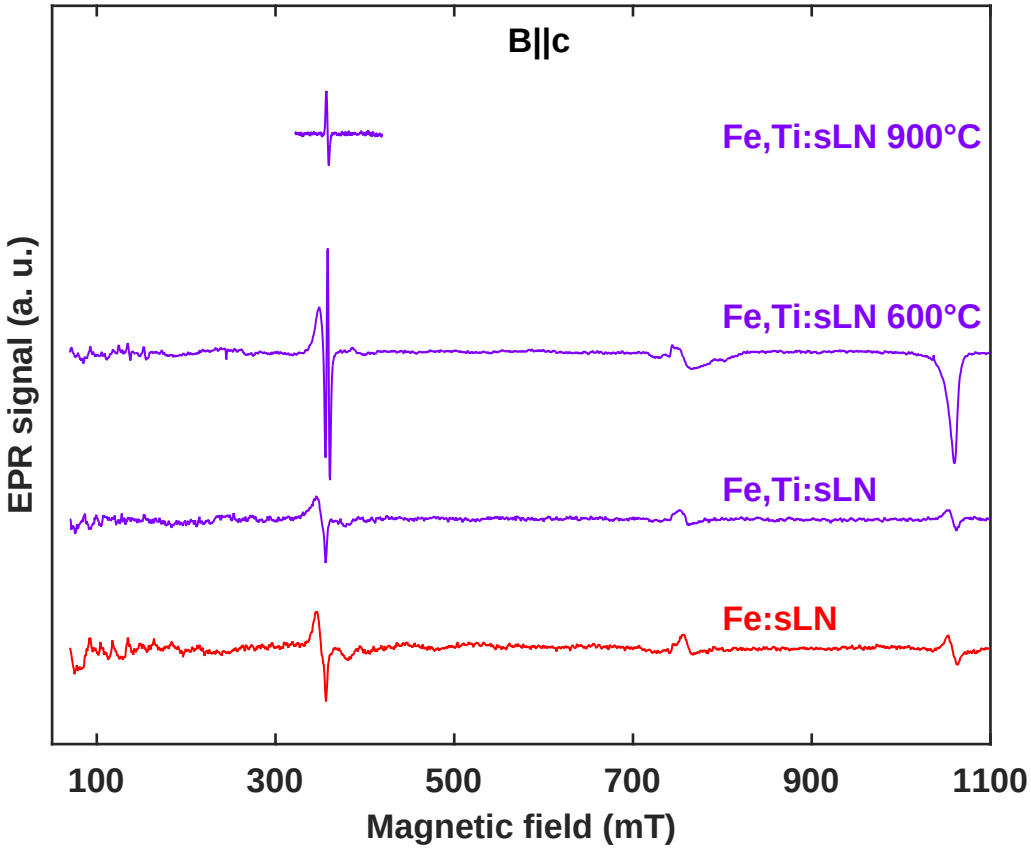

Figure 40: EPR spectra of as grown iron single doped nearly stoichiometric (Fe:sLN **21616**), as grown iron-titanium co-doped nearly stoichiometric $LiNbO_3$ (Fe,Ti:sLN **21615**), at 600 ° C for 3 hours in vacuum annealed iron-titanium co-doped nearly stoichiometric $LiNbO_3$ (Fe,Ti:sLN **21615+600**), at 900 ° C for 0.5 hours in vacuum annealed iron-titanium co-doped nearly stoichiometric $LiNbO_3$ (Fe,Ti:sLN **21615+900**). EPR spectra were recorded at 5 K with the magnetic field parallel to the principal axis.

Changing the focus to the possible interaction between titanium and iron centres in lithium niobate, not only as grown but also annealed co-doped nearly stoichiometric samples are displayed in Figures 40 and 41. Again, the resonance peaks for a magnetic field perpendicular to the principal axis (Figure 41) are more intense than for a magnetic field parallel to z (Figure 40). In as grown co-doped nearly stoichiometric sample (**21615**), iron centre is observed and,

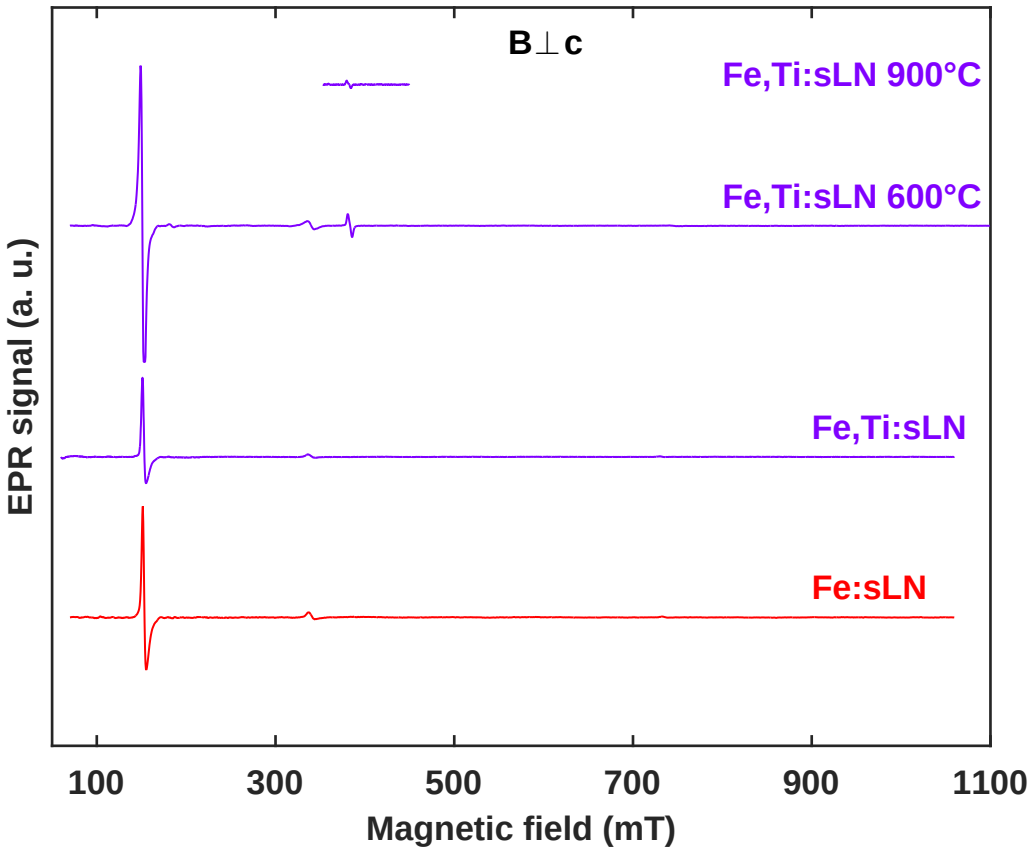

Figure 41: EPR spectra of as grown iron single doped nearly stoichiometric (Fe:sLN **21616**), as grown iron-titanium co-doped nearly stoichiometric $LiNbO_3$ (Fe,Ti:sLN **21615**), at 600 °C for 3h ours in vacuum annealed iron-titanium co-doped nearly stoichiometric $LiNbO_3$ (Fe,Ti:sLN **21615+600**), at 900 °C for 0.5 hours in vacuum annealed iron-titanium co-doped nearly stoichiometric $LiNbO_3$ (Fe,Ti:sLN **21615+900**). EPR spectra were recorded at 5 K with a magnetic field perpendicular to the principal axis.

the resonance peaks coincide with the ones of iron single doped lithium niobate (Fe:sLN **21616**). After a moderate annealing treatment (600 °C), iron centres are still recorded in the EPR spectra next to titanium centres. However, under a reduction at higher temperature (900 °C) only Ti^{3+} is observed. It seems that no classical complex between iron and titanium centres is built because no new resonance peaks is recorded.

4.1.2 Photoluminescence

In the above section, electron paramagnetic resonance measurements were shown, whereas in this section photoluminescence is presented. Typically, stoichiometric lithium niobate is transparent in the visible range. Nevertheless, small amounts of impurities produce absorption bands in the visible spectra, leading to coloured samples (see for example Figure 18 in this chapter).

With the aim of understanding the colour difference of the different annealed samples, photoluminescence measurements were carried out. Therefore, all the samples were fixed to a sample holder. The broadband laser-driven light source (EQ-99X made by Energetiq) was focused on the sample. Part of the light beam is absorbed by the sample and another part goes through the sample. The light beam is detected after passing through a splitter. Then the light intensity is detected for each wave length. Room temperature measurements were performed in the visible range (from 350 nm to 800 nm). To calculate the absorption coefficient Equations 16 and 17 in Chapter 3 Methods were considered and, a measurement without sample was carried out.

In this section, the absorption spectra of doped lithium niobate are presented. First, iron single doped lithium niobate is shown. Second, titanium single doped is illustrated and, at the end, iron-titanium co-doped lithium niobate is described.

Iron doped lithium niobate

Iron doped lithium niobate was illuminated by the light beam and the transmitted light beam was measured. The absorption coefficient versus light beam energy is illustrated in Figure 42. A broad absorption band at 2.6 eV is obtained in iron doped congruent (**155312**) and nearly stoichiometric lithium niobate samples **21616**, as it was expected (Figure 5 in Chapter 2 Materials). In the reduced sample, the absorption coefficient increases considerably 1.9 eV and 3.0 eV. A detailed discussion is given in Chapter 6 Discussion.

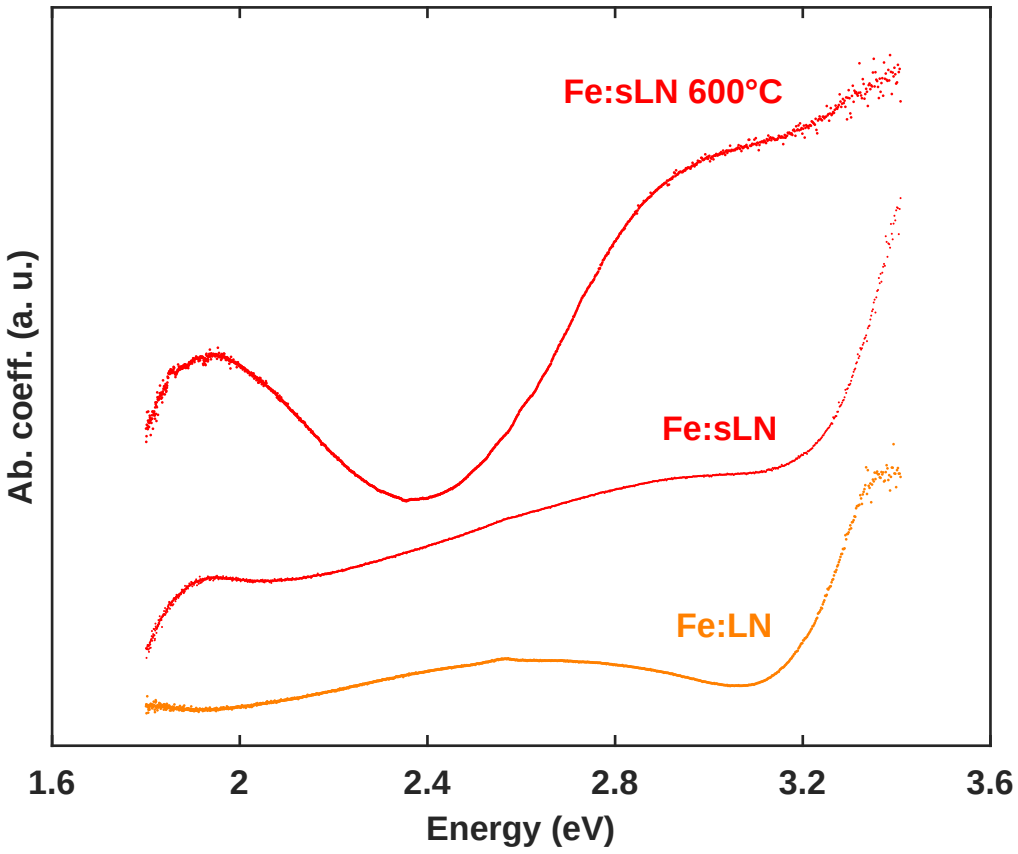

Figure 42: Absorption spectra of iron doped lithium niobate. An absorption band at 2.6 eV is observed in as grown samples. The light beam is perpendicular to the principal axis in iron doped congruent lithium niobate (**155312**), in contrast to as grown (**21616**) and at 600 °C for 3hours in vacuum annealed iron doped nearly stochiometric lithium niobate (**21616+600**), where the beam is parallel to the principal axis.

Titanium doped lithium niobate

Similarly to iron single doped, titanium doped nearly stoichiometric lithium niobate was investigated by photoexcitation. From the three different considered samples (as grown, annealed at 600 °C and at 900 °C), only two of them were examined: as grown and reduced at 600 °C. Due to the strongly reduced dimensions of the **179803+900** sample, the holding procedure was unsuccessful.

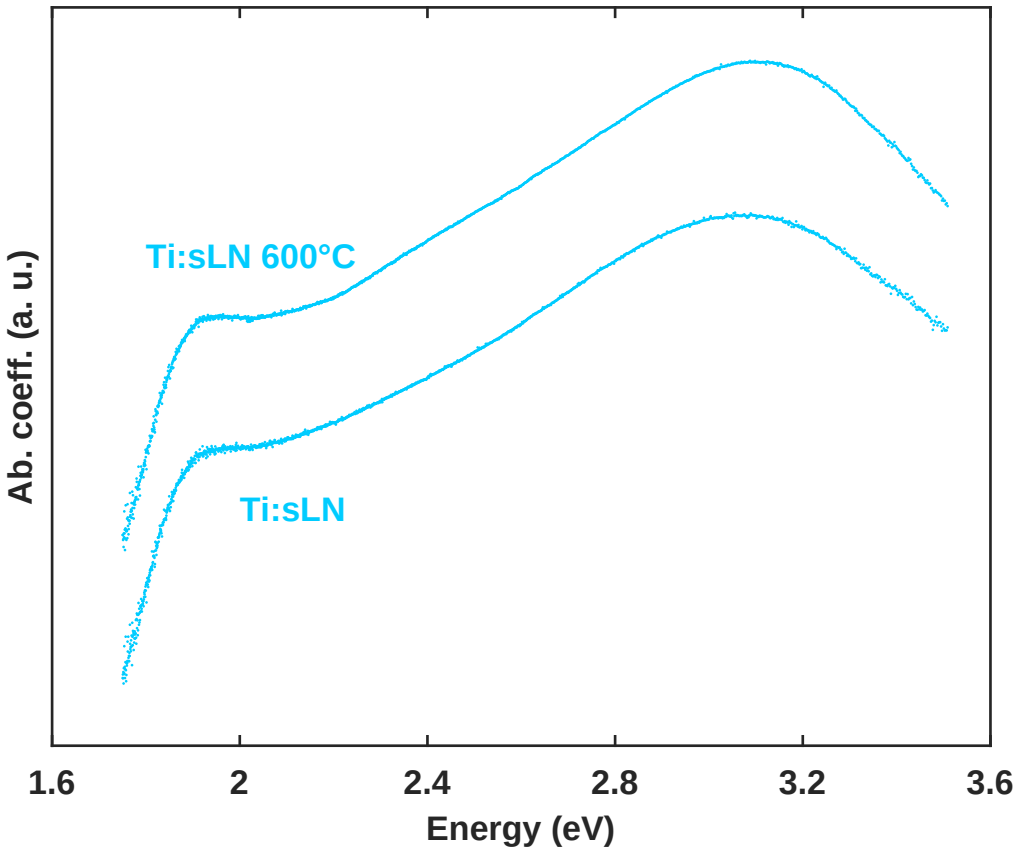

Figure 43: Absorption spectra of titanium doped nearly stoichiometric lithium niobate as a function of the light energy. Two absorption bands at 1.9 eV and 3.2 eV are observed. The light beam was perpendicular to the principal axis.

Not only in the reduced but also in the as grown sample two absorption bands appear at 1.9 eV and 3.2 eV, as it can be seen in the absorption spectra (Figure 43). In Chapter 6 Discussion a detailed discussion is given.

Iron-titanium co-doped lithium niobate

After the measurement of iron single doped and titanium single doped lithium niobate, iron-titanium co-doped is measured and it is illustrated in Figure 44.

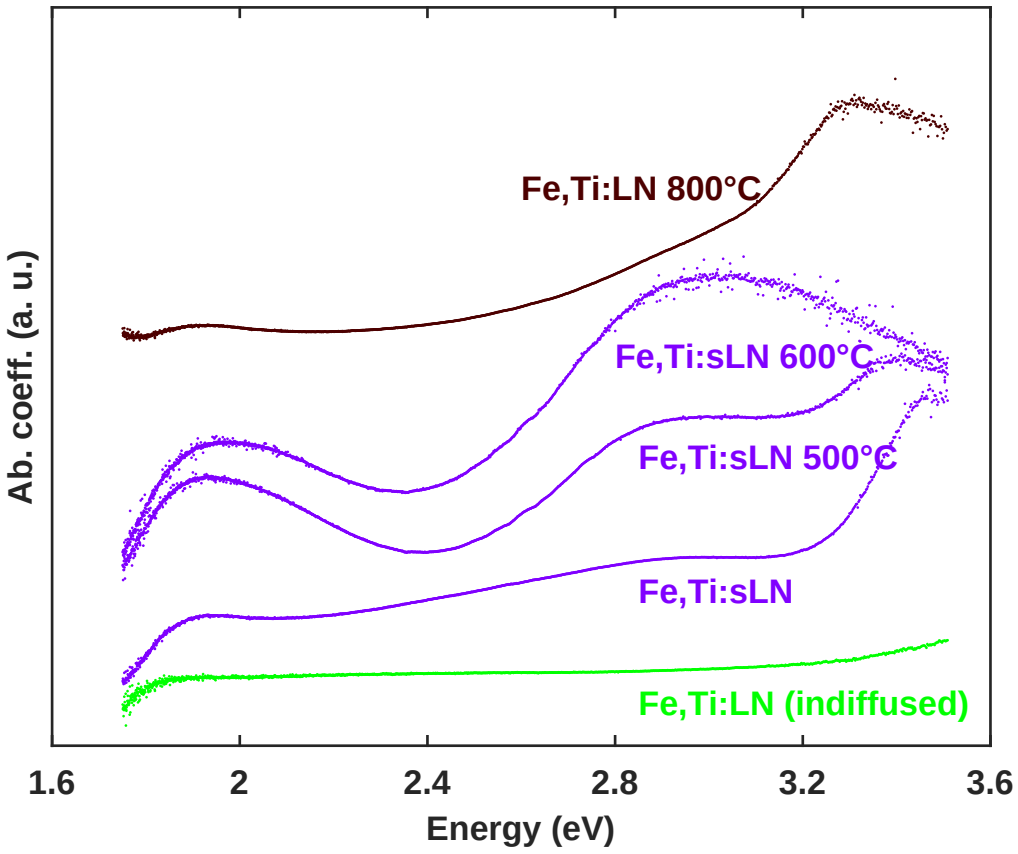

Figure 44: Absorption spectra of iron-titanium co-doped lithium niobate. The light beam was perpendicular to the principal axis in iron-titanium indifussed lithium niobate (**155313ss**) and in the at 800 °C for 3 hours in argon annealed iron in volume doped and titanium in surface co-doped lithium niobate (**155313vs+800**). On contrary, in the iron-titanium co-doped nearly stoichiometric lithium niobate (as grown **21615**, at 500 °C for 3 hours in vacuum annealed **21615+500** and at 600 °C for 3 hours in vacuum annealed **21615+600**), the beam is parallel to the principal axis.

As grown iron-titanium co-doped nearly stoichiometric lithium niobate (**21615**) sample, possesses similar absorption bands as titanium single doped lithium niobate. However, after annealing treatment the absorption bands increase and the shoulders are more pronounced. Surprisingly, iron-titanium indifussed in lithium niobate (**155313ss**) does not absorb light. On the other way, at 800 °C for 3 hours in argon annealed iron in volume doped and titanium in surface co-doped

lithium niobate (**155313vs+800**) absorbs in an equivalent way as titanium single doped lithium niobate, but with less intensity. A detailed discussion is given in Chapter 6 Discussion.

4.2 Lithium yttrium borate samples

Nearly stoichiometric doped lithium yttrium borate crystals were investigated in this thesis (for detailed growth procedure, see Section 3.1 about sample preparation). Relevant dopants, as erbium (Er), ytterbium (Yb) and iron (Fe), were studied in the LYB crystal. In the following, the obtained electron paramagnetic measurements in nearly stoichiometric lithium yttrium borate doped with Er, Yb and Fe are introduced and discussed.

Electron paramagnetic resonance was performed using a custom X-band EPR spectrometer (see Section 3.3). Measurements were performed at low temperature (about 5 to 10 K) to obtain narrow resonance peaks; using frequencies of the order of 9 - 10 GHz and in a magnetic field range from 50 mT to 600 mT. In addition, samples were rotated about the x, y and z axis with 5°, 10° or 15° steps to obtain the angle dependence of the EPR spectra. With the aim of checking the spin Hamiltonian parameters, a fourth plane was investigated as for example a rotation about the $<101>$ axis. Calibration was performed with DPPH powder.

In the following, EPR spectra of doped lithium yttrium borate are introduced. First, erbium doped nearly stoichiometric lithium yttrium borate is investigated. Second, ytterbium doped nearly stoichiometric lithium yttrium borate was studied. Third, iron doped nearly stoichiometric lithium yttrium borate crystals is presented. A compact description of the samples is shown in Appendix A.

4.2.1 Erbium doped lithium yttrium borate

Nearly stoichiometric lithium yttrium borate crystal was doped with 0.05 mol % (sample number **91103**) and 1 mol % (sample number **91105**) of erbium in the melt, leading to a transparent with light pink tones homogeneous erbium doped LYB single crystal. The dimensions of the studied

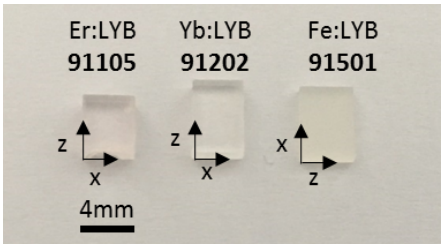

Figure 45: Nearly stoichiometric lithium yttrium borate doped with erbium (left), ytterbium (middle) and iron (right). Erbium doped LYB crystal is almost transparent with light pink tones (1 mol % of Er). The ytterbium doped LYB crystal is light milky and iron doped crystal is light yellow.

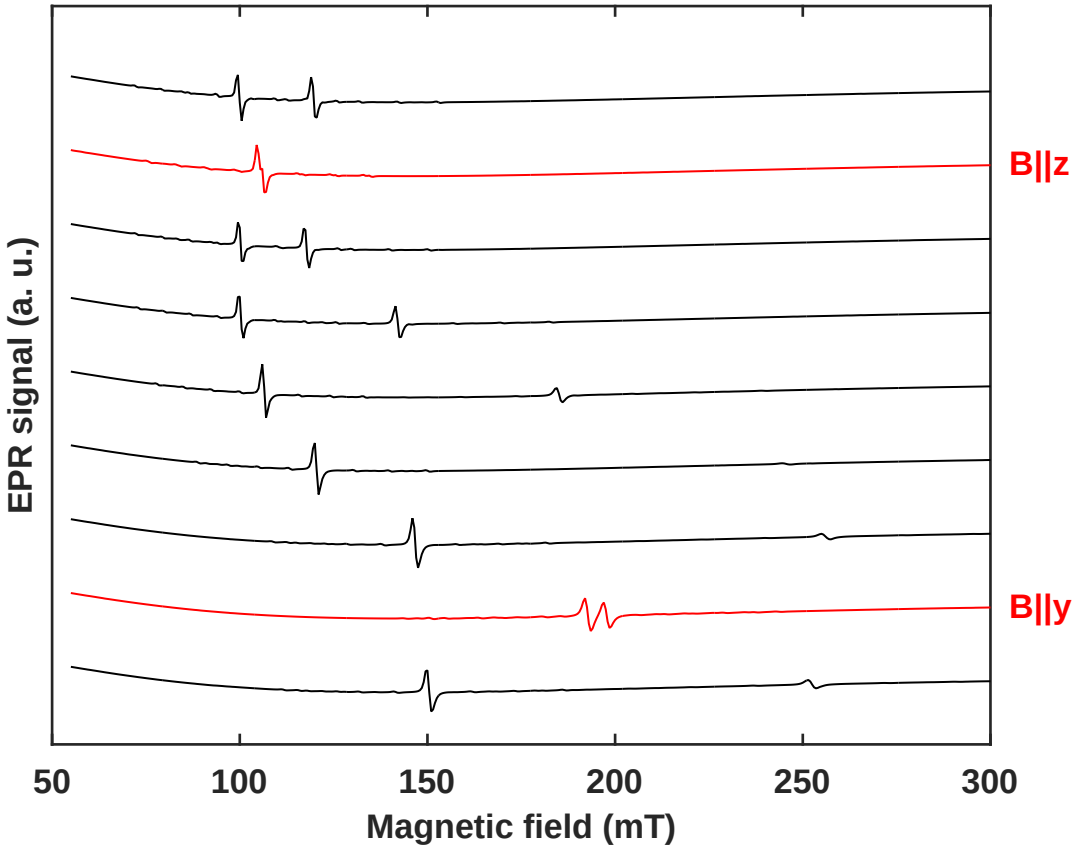

Figure 46: Angle dependence of the EPR spectra of as grown erbium doped nearly stoichiometric lithium yttrium borate (**91103**) for rotations about the x axis. Spectra were measured at 5 K, at 9.880 GHz and with an angle step of 15°. Red spectra denote that the magnetic field was approximately parallel to y axis (bottom) and parallel to z axis (top).

samples were 5×4×2 (mm^3) and 4.4×4×2 (mm^3) for the 0.05 mol % and 1 mol % Er in the melt, respectively. Figure 45 shows a picture of nearly stoichiometric lithium yttrium borate doped with erbium, ytterbium and iron.

Electron paramagnetic resonance was carried out in an as grown sample, where the paramagnetic resonance peaks were distributed in the magnetic field range from 50 mT to 300 mT. In addition, the sample was rotated about the x, y, z, $<101>$ and $<110>$ axes in steps of 15° (see Figures 46 to 50). Measurements were performed at low temperature (T ≈ 5 K, to achieve narrow peaks) and the excitation frequency was 9 - 10 GHz.

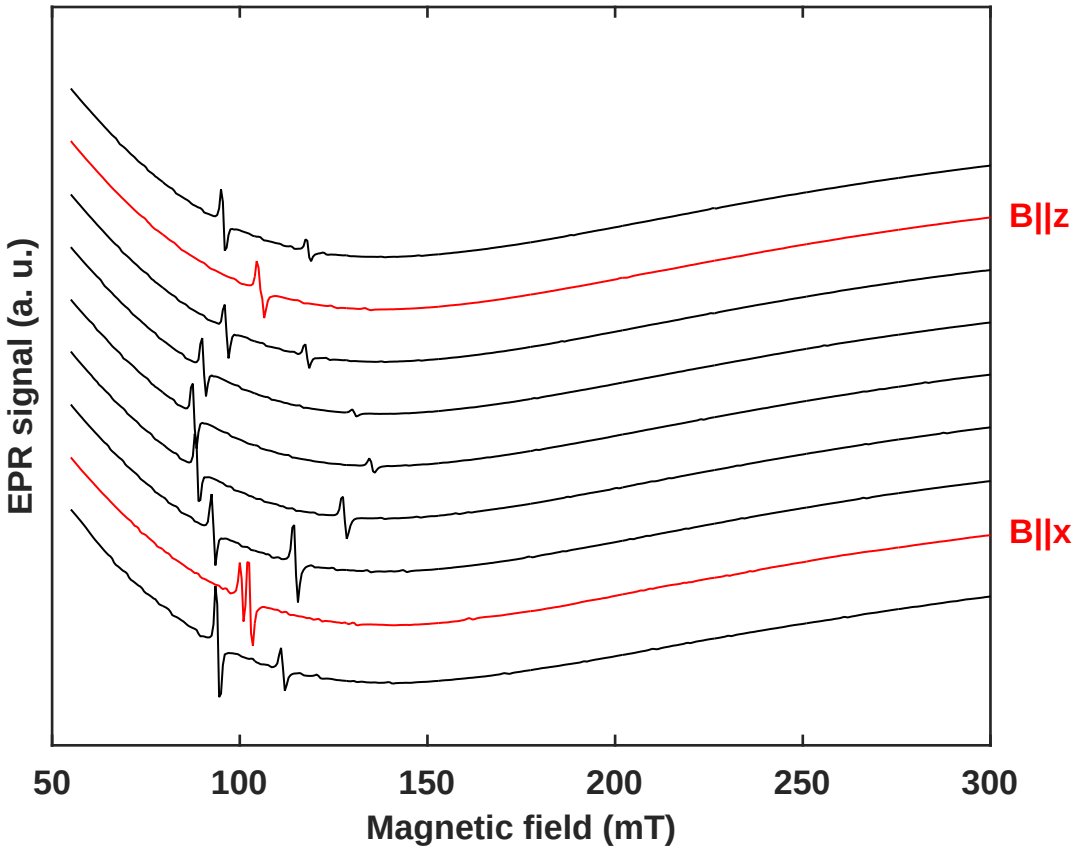

Figure 47: Angle dependence of the EPR spectra of as grown erbium doped nearly stoichiometric lithium yttrium borate (**91103**) for rotations about the y axis. Spectra were measured at 5 K, at 9.883 GHz and with an angle step of 15°. Red spectra denote that the magnetic field was approximately parallel to x axis (bottom) and parallel to z axis (top).

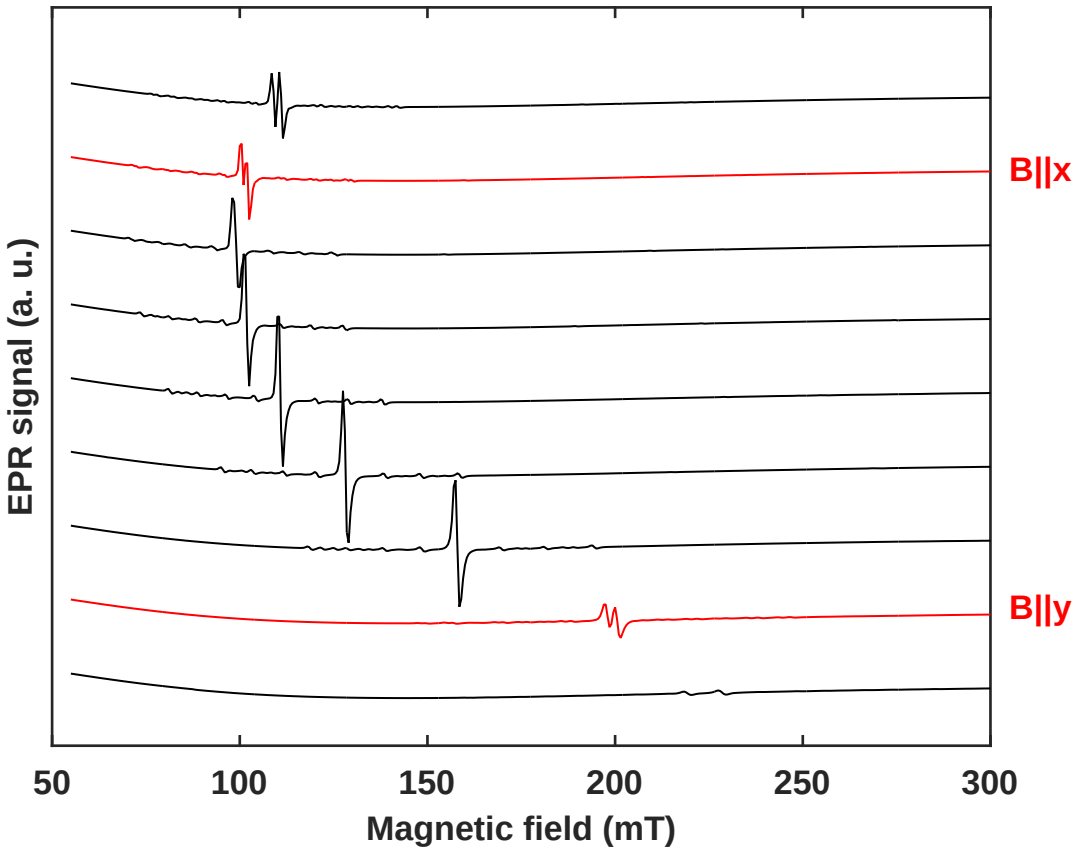

Figure 48: Angle dependent EPR spectra of as grown erbium doped nearly stoichiometric lithium yttrium borate (**91103**) for rotations about the z axis. Spectra were measured at 5 K, at 9.883 GHz and with an angle step of 15°. Red spectra denote that the magnetic field was approximately parallel to y axis (bottom) and parallel to x axis (top).

Similarly to iron and titanium in lithium niobate, erbium builds anisotropic centres, leading to a displacement of the resonant peak with the rotation of the sample with respect to the magnetic field. As shown in Figures 46 and 47, the position of the two main (more intense) peaks can be straightforwardly visualized. In addition, sharpening the view several much less intense peaks can be noticed next to each of the main peaks (a maximum of sixteen). For a detailed discussion see Chapter 5 Results.

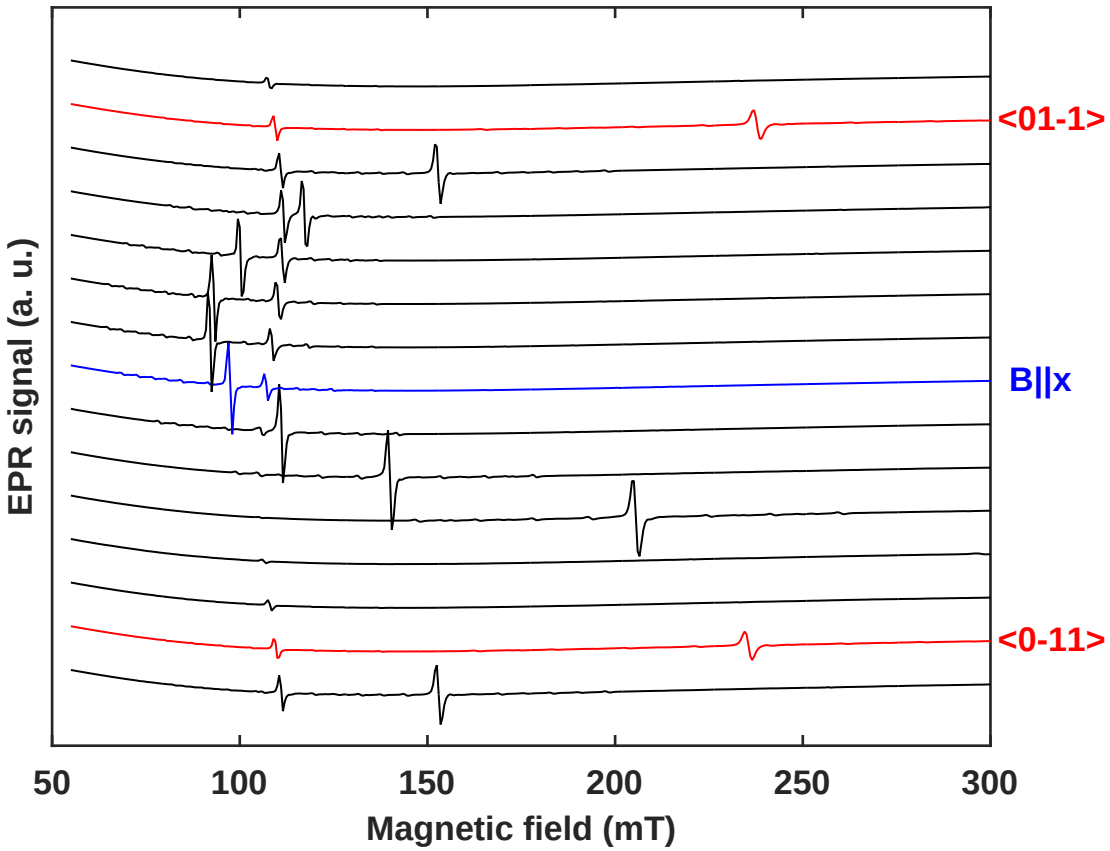

Figure 49: Angle dependence of the EPR spectra of as grown erbium doped nearly stoichiometric lithium yttrium borate (**91103**) for rotations about the $<011>$ axis. The spectra were measured at 5 K, at 9.881 GHz and with an angle step of 15°. Red spectra denote that the magnetic field was approx. parallel to $<0-11>$ axis (bottom) and $<01-1>$ axis (top). Blue spectrum indicates that the magnetic field was approx. parallel to x.

In contrast to Figures 46 and 47, where two intense peaks are observed, in Figure 48 only a single intense peak with its satellite less intense peaks is observable.

Similarly to the rotations about the x and y axes (Figures 46 and 47, respectively), rotating the sample about the $<011>$ and $<101>$ (Figures 49 and 50, respectively) two intense peaks again appear at different magnetic field positions. A detailed description of the system is presented in Chapter 5 Results.

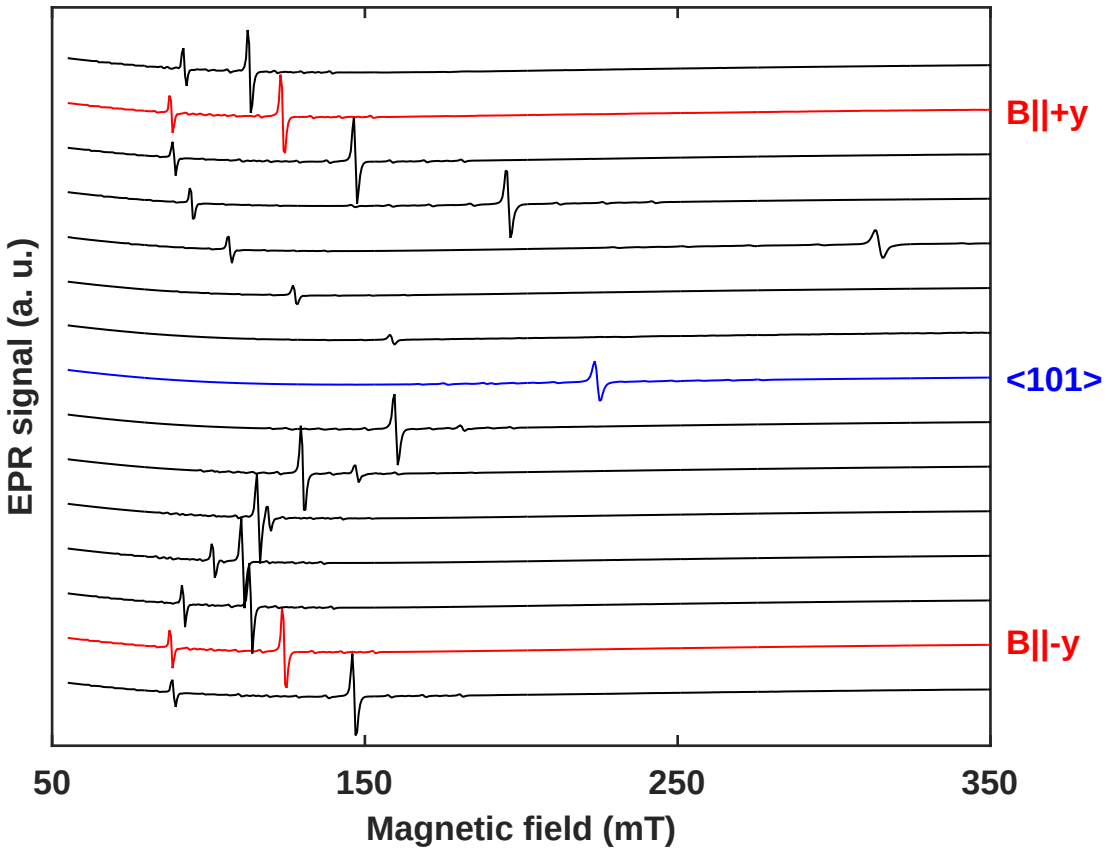

Figure 50: Angle dependence of the EPR spectra of as grown erbium doped nearly stoichiometric lithium yttrium borate (**91103**) for rotations about the $<101>$ axis. The spectra were recorded at 5 K, at 9.880 GHz and with an angle step of 15°. Red spectra denote that the magnetic field was approx. parallel to the $-y$ axis (bottom) and $+y$ axis (top). The blue spectrum indicates that the magnetic field was approximately parallel to the $<-101>$ axis.

Lithium yttrium borate doped with 1 mol % of erbium had similar spectra as the sample with the lower concentration of 0.05 mol % (see Figure 51). It is expected for a higher Er concentration in LYB to increase the intensity of the EPR resonance peaks. Moreover, additional weak EPR peaks would be expected if Er atoms pairs had built. This interpretation was suggested by a private communication with Dr. Corradi.

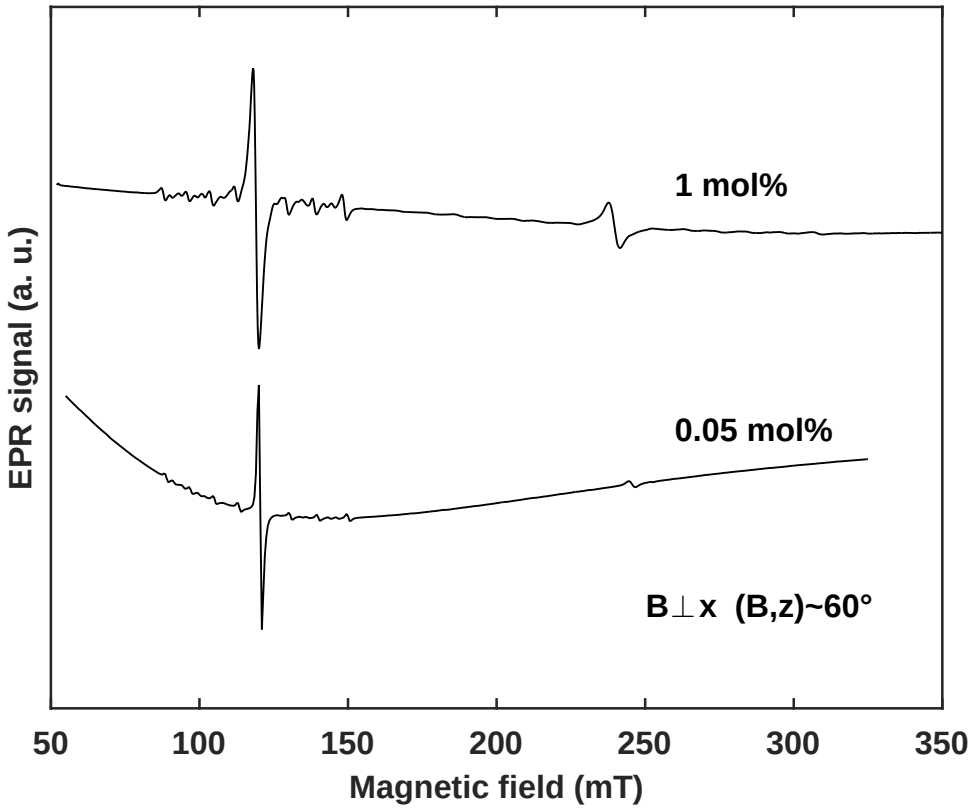

Figure 51: EPR spectrum of 1 mol % (up) and 0.05 mol % (down) erbium doped nearly stoichiometric lithium yttrium borate. The magnetic field was perpendicular to the x axis and forming approx. 60° with the principal axis z. Higher dopant concentration is related directly with the peak intensity.

Accidentally, EPR spectra measured at 5 K and 15 K have different linewidth in the resonance peak. Therefore, erbium doped nearly stoichiometric lithium yttrium borate was investigated by temperature dependent measurements in order to quantify the activation energy from the ground state to the upper state (see Appendix F). Therefore, a specific orientation was searched, and the EPR spectra were measured at different temperatures, starting from 5 K until 25 K with a step of two degrees. Increasing the temperature, peak intensities decrease and linewidths broaden. Figure 52 shows the temperature dependent measurements.

Clearly, at low temperatures, the EPR peaks are narrower and more intense than at higher temperatures (see Figure 52). In addition, the ERP spectra could not be observed above 25 K.

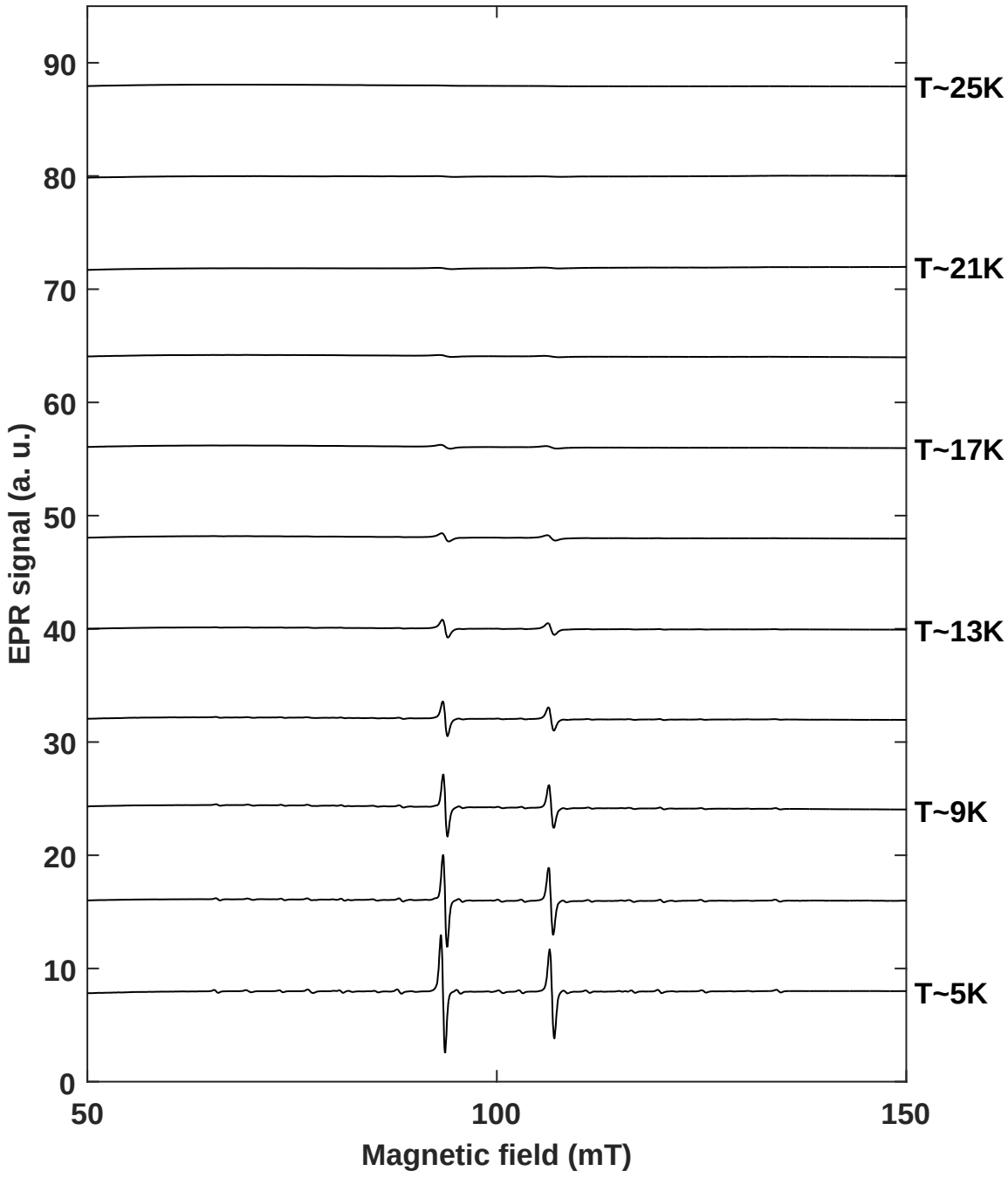

Figure 52: Temperature dependence of the EPR spectra of erbium doped lithium yttrium borate (**91103**). The temperature increases from the bottom (5 K) to the top (25 K) of the figure in steps of 2 K. The magnetic field is perpendicular to the y axis and forms an angle of $\sim -10°$ with the x axis. At temperatures above 25 K, no resonance peak is detected.

4.2.2 Ytterbium doped lithium yttrium borate

In the above section, erbium doped lithium yttrium borate was explained. Showing up next, ytterbium doped lithium yttrium borate (**91202**) is investigated. In the nearly stoichiometric lithium yttrium borate melt, 1 mol % ytterbium was introduced. Homogeneous ytterbium doped LYB single crystal was grown. The studied sample dimensions were $5\times3\times1.5$ (mm^3) and it presents a characteristic milky colour (Figure 45).

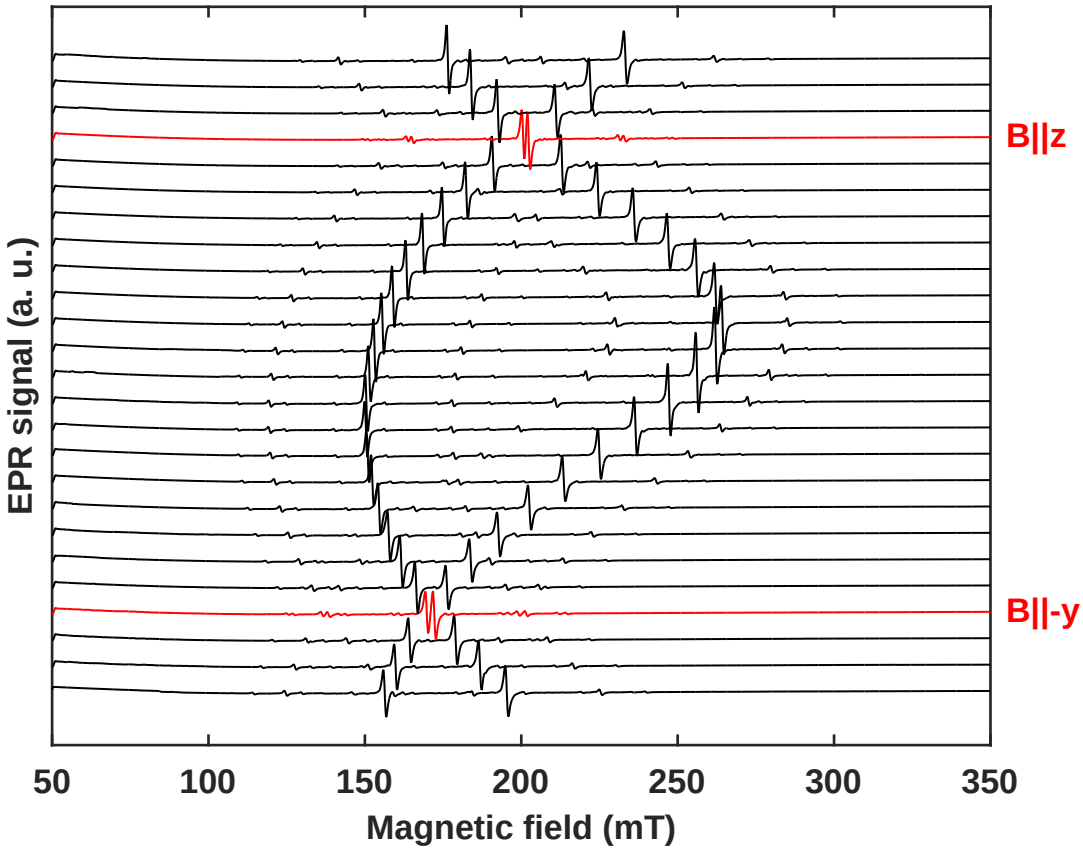

Figure 53: Angle dependence of the EPR spectra of as grown ytterbium doped lithium yttrium borate (**91202**) for rotations about the x axis. The spectra were measured at 5 K, at 9.879 GHz and with an angle step of 5°. Red spectra denote that the magnetic field was parallel to the $-y$ axis (bottom) and to the $+z$ axis (top).

As grown ytterbium doped lithium yttrium borate crystal was measured at 5K, at 9 - 10 GHz and rotating the sample about the x, y, z, $<011>$, $<101>$ and $<110>$ axes. Figures 53 to 58 illustrate the angle dependence of the EPR spectra.

Similarly to Er:LYB, two intense EPR lines predominate in the angle dependence. Next to these two intense lines, four middle intense peaks and twelve weak peaks are found (see Figure 87 in Chapter 5 Results). By rotating the sample respect to the magnetic field, the resonant peaks (with high, middle and low intensity) change their magnetic field positions with almost constant distance between the peaks (like a hair comb).

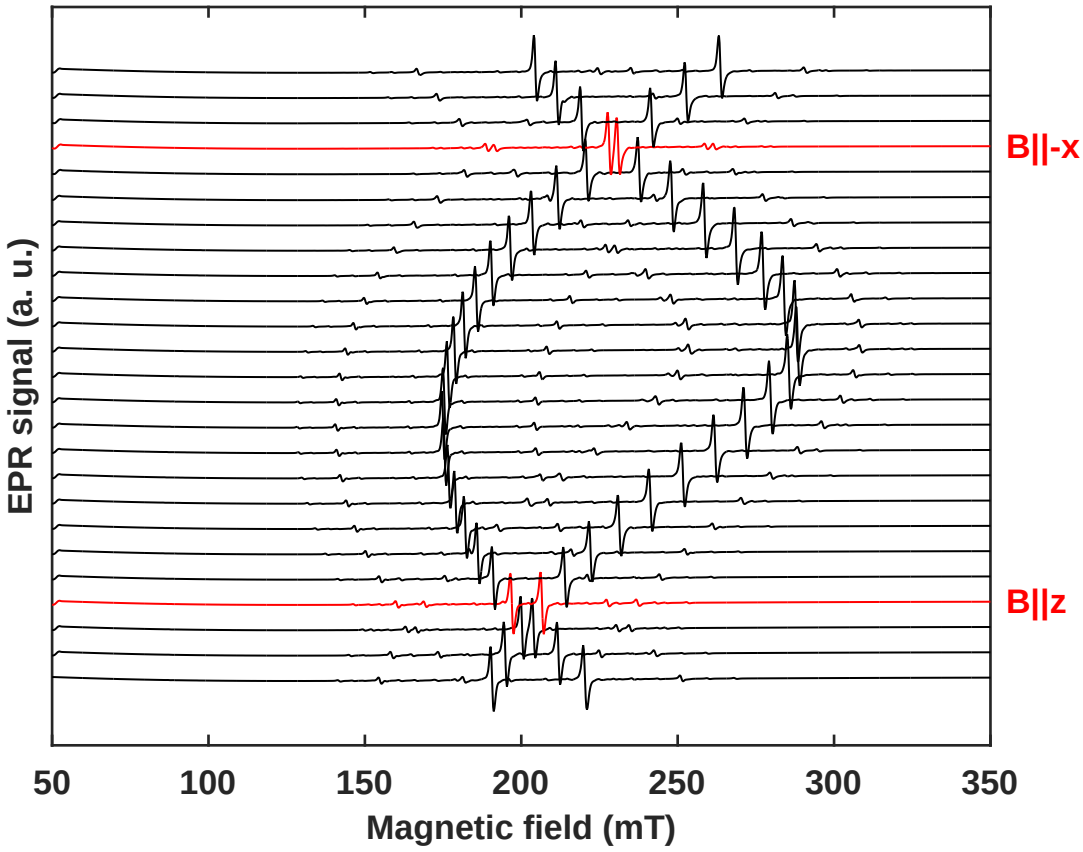

Figure 54: Angle dependence of the EPR spectra of as grown ytterbium doped lithium yttrium borate (**91202**) for rotations about the y axis. The spectra were measured at 5 K, at 9.880 GHz and with an angle step of 5°. Red spectra denote that the magnetic field was parallel to the z axis (bottom) and to the $-x$ axis (top).

Under rotation about z axis, the two intense peaks share the same magnetic field position. Therefore, only one intense, two middle and six weak peaks are observed, for example, at a magnetic field parallel to $-y$ axis. However, two intense resonance peaks are observed also in Figure 55 due to the tilt and offset angles. If the tilt and offset angles would be zero, only one intense peak and two middle and six weak peaks would have been observed. To check the experimental results, further rotations about intermediate directions were performed (see Figures 56 to 58).

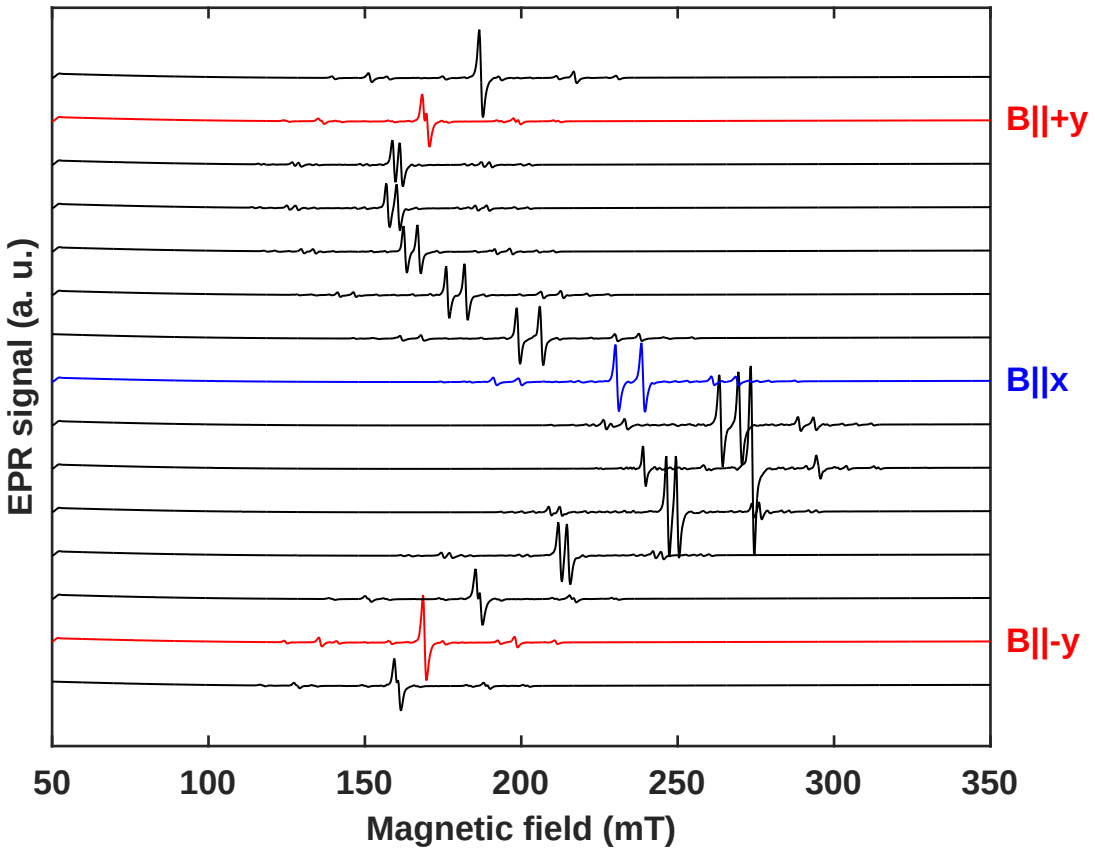

Figure 55: Angle dependence of the EPR spectra of as grown ytterbium doped lithium yttrium borate (**91202**) for rotations about the z axis. The spectra were measured at 5 K, at 9.877 GHz and with an angle step of 5°. Red spectra denote that the magnetic field was parallel to the $-y$ axis (bottom) and to the $+y$ axis (top). Blue spectrum indicates that the magnetic field was approximately parallel to the x axis.

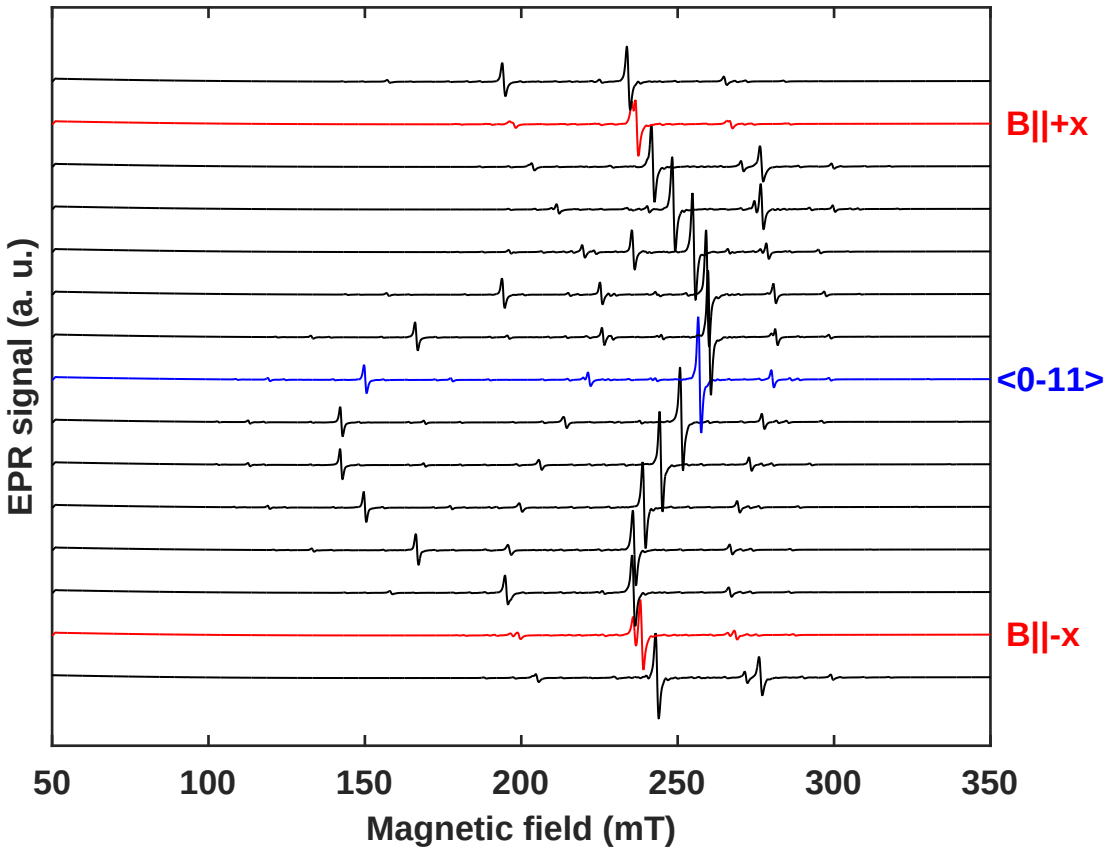

Figure 56: Angle dependence of the EPR spectra of as grown ytterbium doped lithium yttrium borate (**91202**) for rotations about the $<0-1-1>$ axis. Spectra were measured at 5 K, at 9.878 GHz and with an angle step of 15°. Red spectra denote that the magnetic field was parallel to the $-x$ axis (bottom) and $+x$ axis (top). Blue spectrum indicates that the magnetic field was approximately parallel to the $<0-11>$ axis.

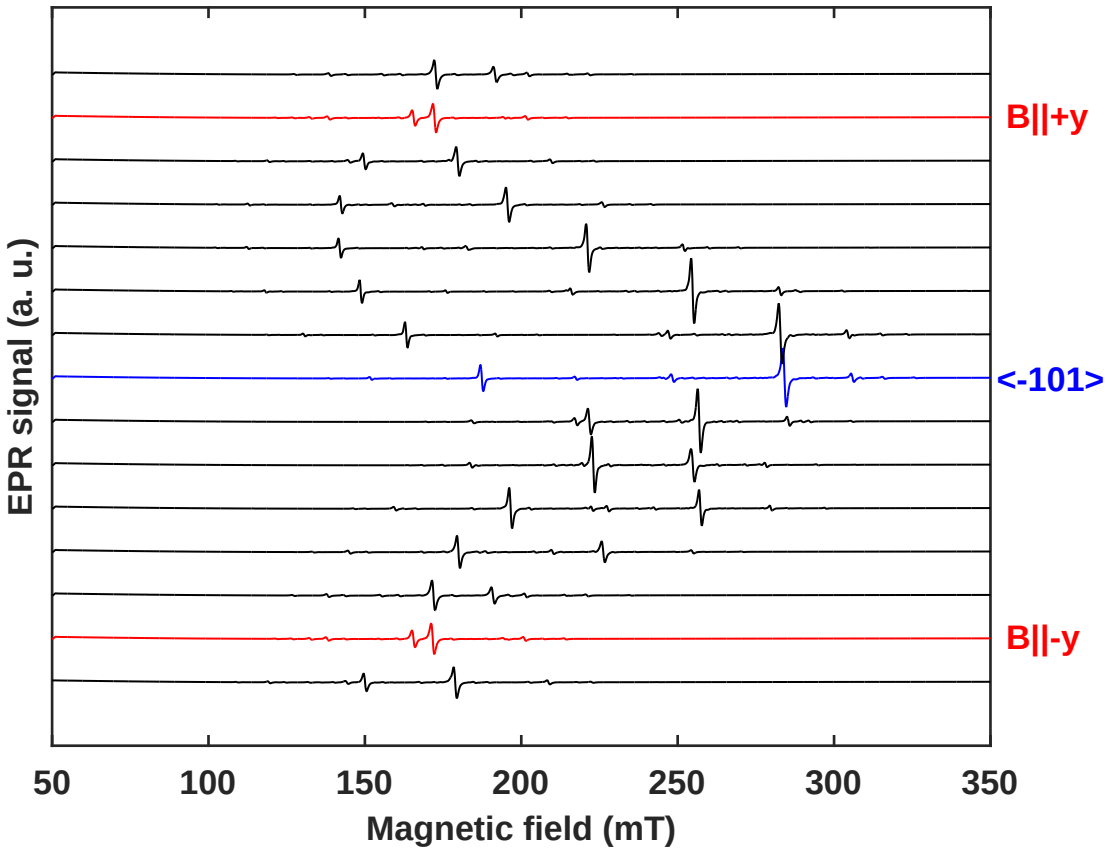

Figure 57: Angle dependent EPR spectra of as grown ytterbium doped lithium yttrium borate (**91202**) for rotations about the $<10-1>$ axis. The spectra were measured at 5 K, at 9.877 GHz and with an angle step of 15°. Red spectra denote that the magnetic field was parallel to the $-y$ axis (bottom) and to the $+y$ axis (top). Blue spectrum indicates that the magnetic field was approximately parallel to the $<101>$ axis.

One more time, two main peaks (accompanied by middle and weak satellite peaks) are obtained under rotation about the $<0-1-1>$, $<10-1>$ and $<1-10>$ axis.

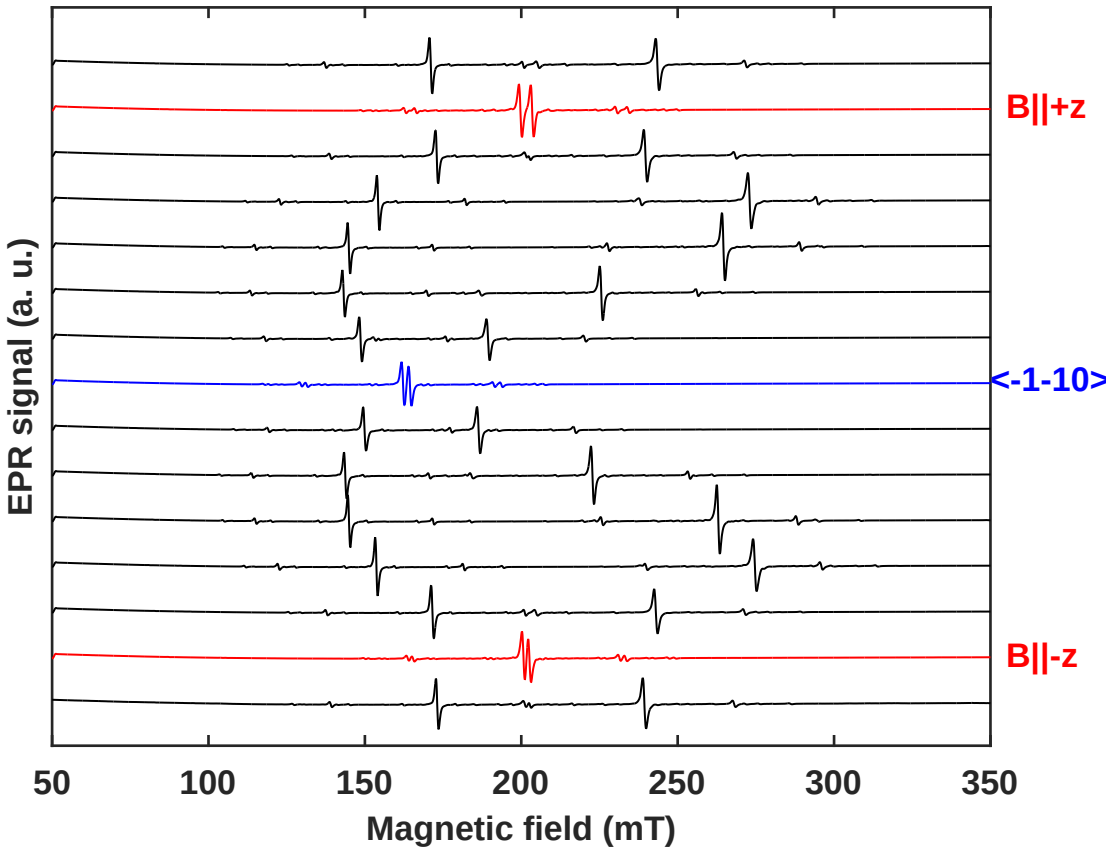

Figure 58: Angle dependence of the EPR spectra of as grown ytterbium doped lithium yttrium borate (**91202**) for rotations about the $<1-10>$ axis. The spectra were measured at 5 K, at 9.881 GHz and with an angle step of 15°. Red spectra denote that the magnetic field was parallel to the $-z$ axis (bottom) and to the $+z$ axis (top). Blue spectrum indicates that the magnetic field was approximately parallel to the $<-1-10>$ axis.

In addition, yttrium doped lithium yttrium borate was measured at different temperature to quantify the activation energy (see Appendix F). Therefore, a specific orientation was chosen and temperature dependence EPR measurements were performed, starting from 5 K until 50 K with a step of five degrees. Increasing the temperature, peak intensities decrease and the linewidths broaden. Figure 59 shows the temperature dependent measurements.

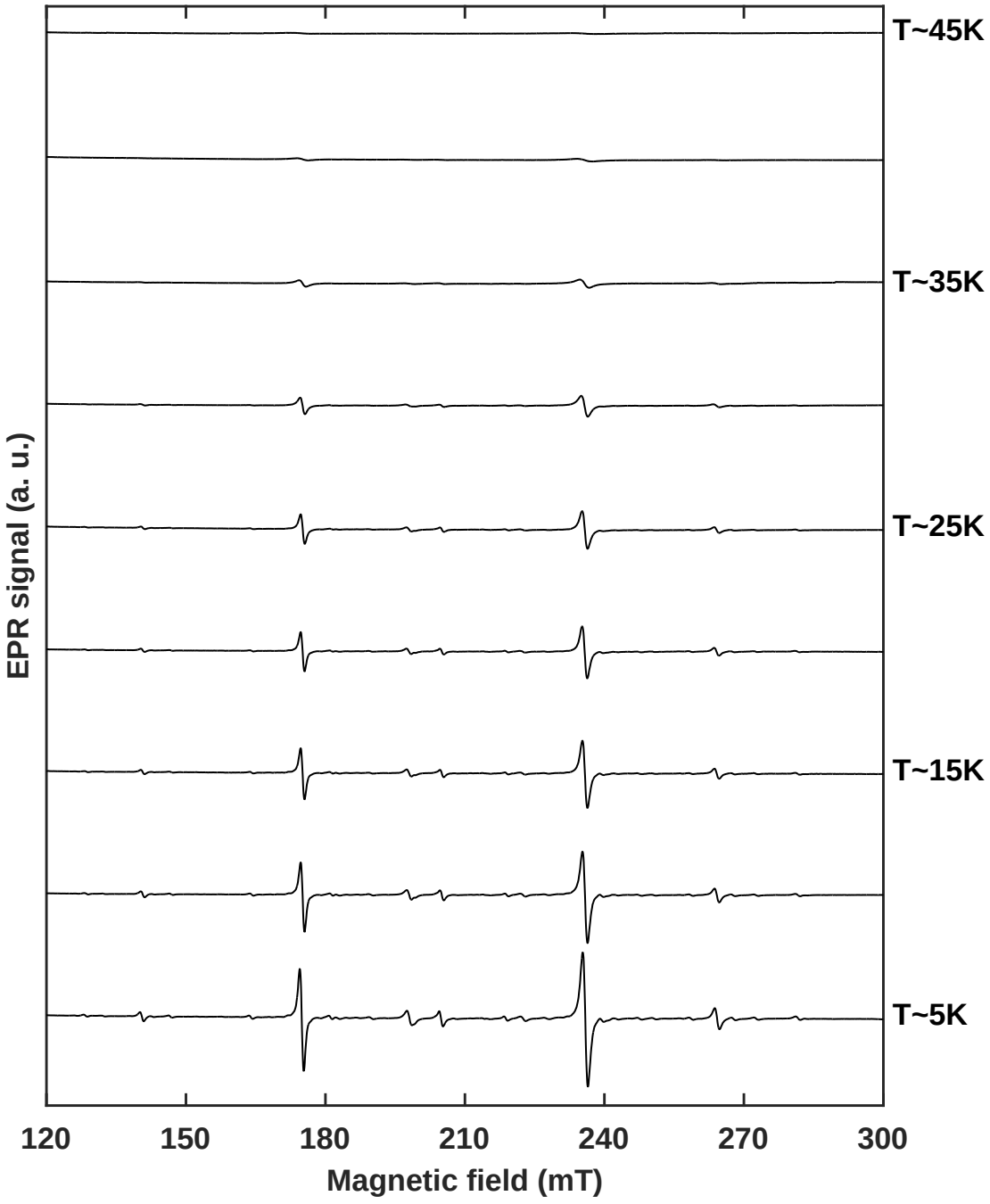

Figure 59: Temperature dependence of the EPR spectra of ytterbium doped lithium yttrium borate (**91202**). Temperature is increasing from the bottom (5 K) to the top (50 K) of the figure in steps of 5 K. The magnetic field is perpendicular to the x axis and forms an angle of $\sim$80° with the $-y$ axis. At temperatures above 40 K, no resonance peak is detected.

4.2.3 Iron doped lithium yttrium borate

Lithium yttrium borate was not only doped with rare earths (as in the sections above with Er and Yb) but also with a transition metal. In this section, iron doped lithium yttrium borate is presented and investigated.

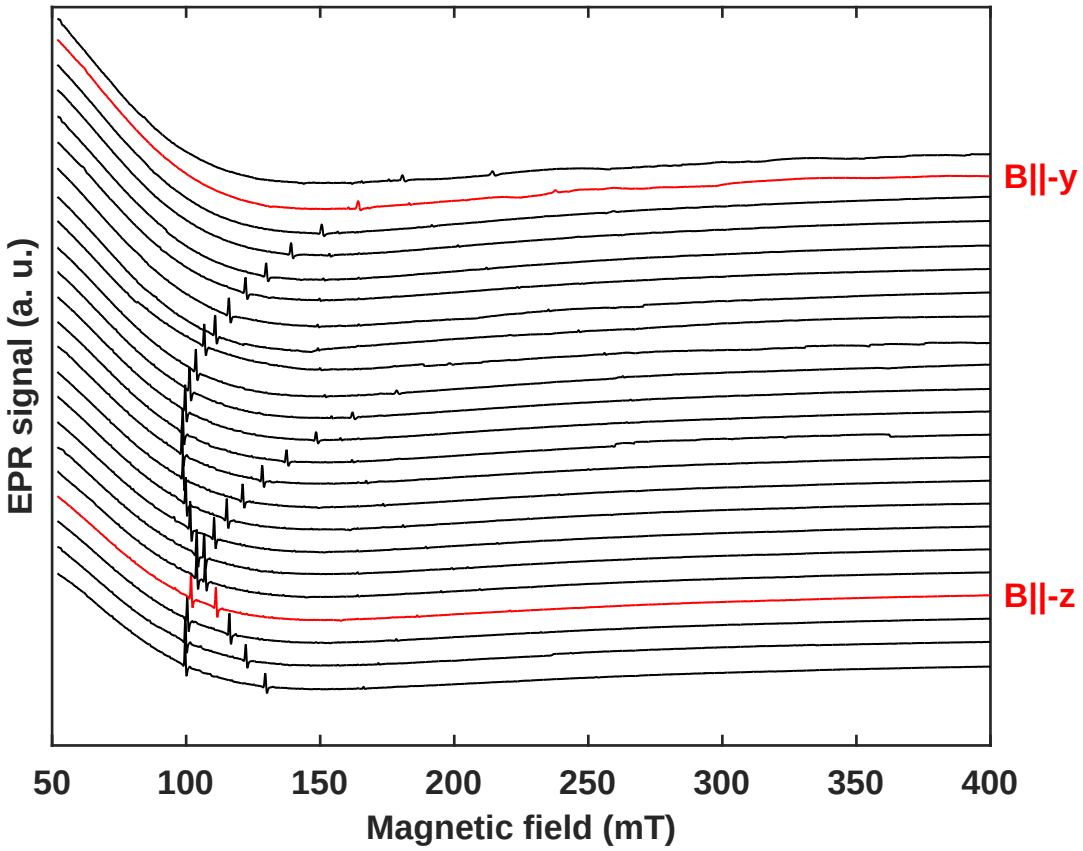

Figure 60: Angle dependence of the EPR spectra of as grown iron doped lithium yttrium borate (**91501**) for rotations about the x axis. Spectra were measured at 5 K, at 9.886 GHz and with an angle step of 5°. Red spectra denote that the magnetic field was parallel to the $-z$ axis (bottom) and to the $-y$ axis (top).

Nearly stoichiometric lithium yttrium borate was doped during the crystal growth, with 0.02 mol % iron introduced in the melt. As it can be seen in Figure 45, a homogeneous iron doped LYB single crystal was grown. The dimensions of the studied sample were $5 \times 4 \times 1$ (mm^3) and it presents a characteristic light-yellow colour (sample number **91501** see Figure 45).

As grown iron doped lithium yttrium borate crystal was measured at 5 K, at 9 - 10 GHz and rotating the sample about x, y, z, $<011>$, $<101>$ and $<110>$ axes. Figures 60 to 64 illustrate the angle dependence of the EPR spectra.

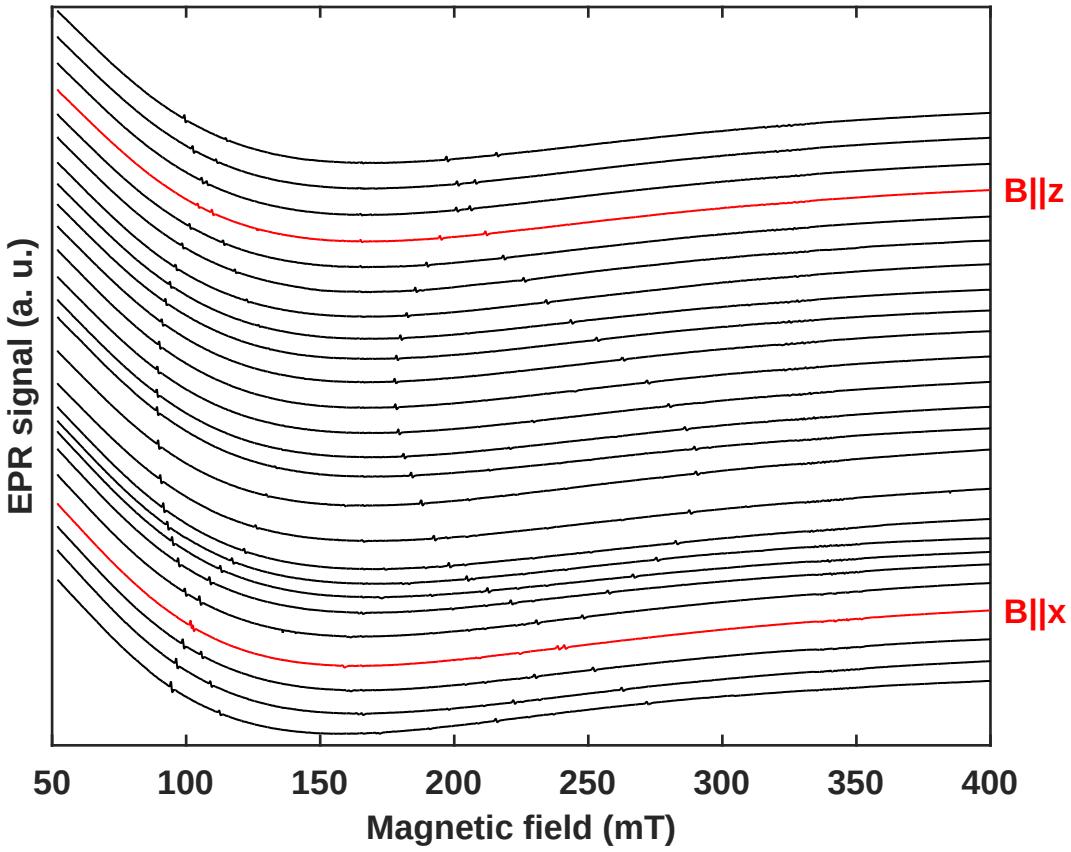

Figure 61: Angle dependence of the EPR spectra of as grown iron doped lithium yttrium borate (**91501**) for rotations about the y axis. The spectra were measured at 5 K, at 9.886 GHz and with an angle step of 5°. Red spectra denote that the magnetic field was parallel to the $+x$ axis (bottom) and to the $+z$ axis (top).

In iron doped lithium yttrium borate, two intense lines are observed on the left side of Figure 60 and two weak lines are at the right side.

Under the rotation about z, similarly as in erbium and ytterbium doped LYB, EPR lines tend to share the same magnetic field position. Therefore, the resonant peaks tend to remain together. However, still four resonance peaks distinguish themselves due to the tilt angle.

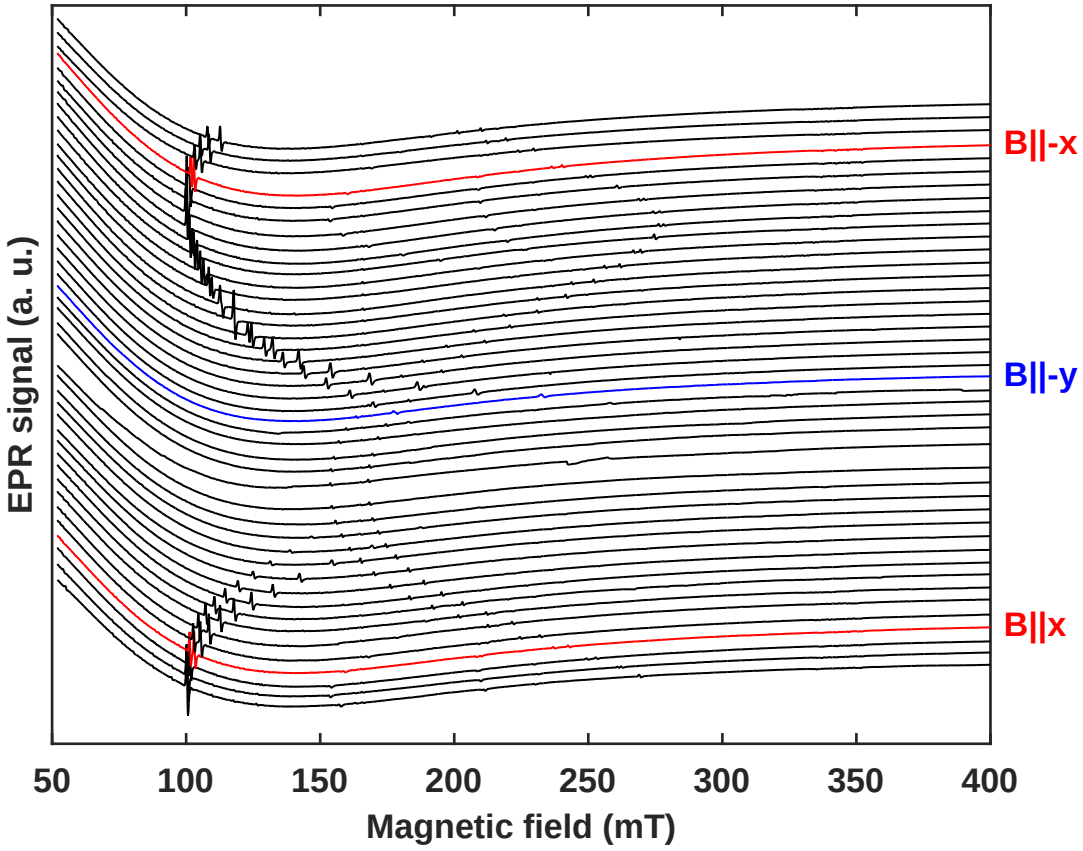

Figure 62: Angle dependence of the EPR spectra of as grown iron doped lithium yttrium borate (**91501**) for rotations about the z axis. The spectra were measured at 5 K, at 9.885 GHz and with an angle step of 5°. Red spectra denote that the magnetic field was approximately parallel to the x axis (bottom) and to the $-x$ axis (top). The blue spectrum indicates that the magnetic field was approximately parallel to the $-y$ axis.

Under rotation about $<101>$ and $<110>$, again four different EPR lines are observed. The experimental results are presented in Chapter 5 Results.

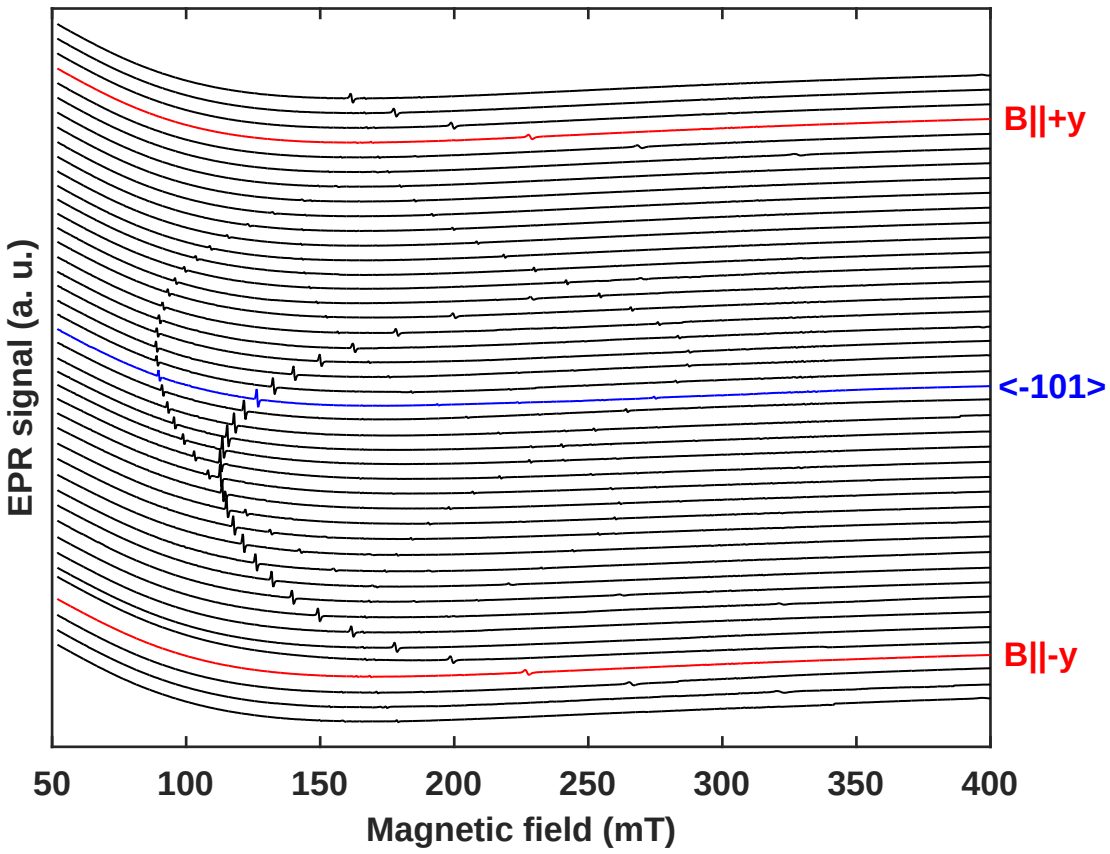

Figure 63: Angle dependence of the EPR spectra of as grown iron doped lithium yttrium borate (**91501**) for rotations about the $<101>$ axis. The spectra were measured at 5 K, at 9.890 GHz and with an angle step of 5°. Red spectra denote that the magnetic field was approximately parallel to the $-y$ axis (bottom) and to the $+y$ axis (top). The blue spectrum indicates that the magnetic field was approximately parallel to the $<-101>$ axis.

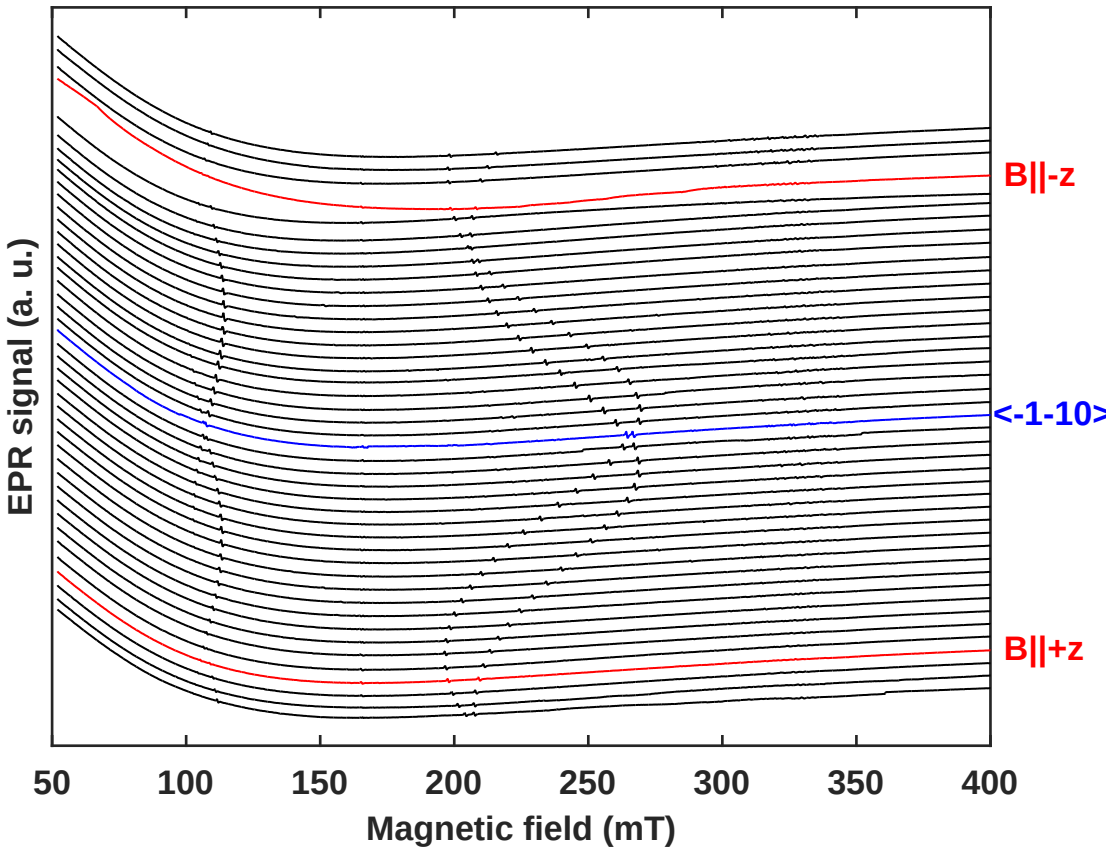

Figure 64: Angle dependence of the EPR spectra of as grown iron doped lithium yttrium borate (**91501**) for rotations about the $<110>$ axis. The spectra were measured at 5 K, at 9.886 GHz and with an angle step of 5°. The red spectra denote that the magnetic field was approximately parallel to the $+z$ axis (bottom) and to the $-z$ axis (top). The blue spectrum denotes that the magnetic field was approximately parallel to the $<-1-10>$ axis.

Until now the experimental measurements have been shown with the aim of understanding the microscopic and electronic structure of the different relevant dopants in LN and LYB. The experimental results are collected in Chapter 5 Results, whereas the interpretation of the different centres is given in Chapter 6 Discussion.

5 Results

In the last chapter, the obtained EPR and PL measurements have been seen, whereas in the following one the experimental results are presented. That is, the spin Hamiltonian parameters (studied in Chapter 3 Methods) obtained from the experimental data (shown in Chapter 4 Measurements) are presented and discussed. The EPR results are analysed in this chapter and build up the core of this thesis. By analogy, the structure of this chapter is identical to the Measurements chapter. First, lithium niobate is presented, followed by lithium yttrium borate. The discussion of each ferroelectric material is organised according to the different dopant ions. Starting with iron single doped, followed by titanium single doped and finally iron-titanium co-doped in lithium niobate. In lithium yttrium borate, erbium doped samples are presented first, then ytterbium doped samples and at the end iron doped lithium yttrium borate.

5.1 Lithium niobate samples

EPR spectra contain information about the structure of the defects in a host material (see Chapter 3). For an accurate and quantitative analysis of the EPR parameters, EasySpin (a toolbox of Matlab) was employed. Thereby, a fitting program was developed in order to obtain the spin Hamiltonian parameters of the considered systems. The idea behind this goal is to compare the experimental data with the simulated EasySpin data (with guessed/known spin Hamiltonian parameters). After several iterations, the least-square fitting program converges giving the best spin Hamiltonian parameters for the considered system. The same procedure was applied to each considered sample in this thesis.

In the following section, the spin Hamiltonian parameters for the different samples are presented, followed by a visual representation of the experimental and simulated data. The process employed to obtain the spin Hamiltonian parameters is described in detail in the first subsection. Therefore, iron single doped in nearly stoichiometric lithium niobate is used as an example. Using the same procedure, the spin Hamiltonian parameters of the other samples are obtained. At the end of

each section dedicated to a particular material, a summary table with the experimental results is listed.

5.1.1 Iron single doped nearly stoichiometric lithium niobate

Spin Hamiltonian parameters are calculated by comparison of experimental data with simulated (by EasySpin) data. On the one hand, the resonance peak position and the associated rotation angle of the sample with respect to the magnetic field are essential to describe the iron ion in lithium niobate. On the other hand, the dominant interaction terms of the spin Hamiltonian equation are necessary to obtain the correct tensor values. Consequently, a good compromise of both (measured data and considered spin Hamiltonian parameters) leads to a successful result. First, resonance peaks in the EPR spectra are searched for. In this case, an iron singe doped nearly stoichiometric lithium niobate (**21616**) sample was measured at 5 K, with a frequency 9.8 GHz rotating the sample about the x axis. For example, for a magnetic field perpendicular to the z axis, three resonance peaks with different intensities are found in the EPR spectrum of iron doped lithium niobate (see Figure 19).

As it can be seen from Figure 13, the resonance peak positions change by rotating the sample with respect to the magnetic field. Consequently, the resonance peak position and the rotation angle of the sample with respect to the magnetic field is listed and saved in a file. The peak position is defined as the magnetic field at which the first derivative of the absorption peak is zero. Following the resonance peaks with the same intensity through the EPR spectra at different rotation angles, the transitions lines are established. Since iron is a transition metal with a large fine structure term (it will be explained later in this subsection), some resonance peaks disappear for a given rotation angle, leading to an incomplete transition line. In addition, the transition probability changes with the sample rotation, causing peaks with different intensities (as observed in Figure 19). An additional difficulty is to associate the obtained resonance peaks to a determined electronic transition. Therefore, all possible combinations must be considered (allowed and forbidden transitions).

Until now, the selection and the order of the resonance peaks were described. The aim of the least square fitting program is to obtain the spin Hamiltonian parameters comparing the experimental with the simulated resonance peaks. These simulated resonance peaks require a guessed spin Hamiltonian and, in addition, some experimental parameters as frequency of

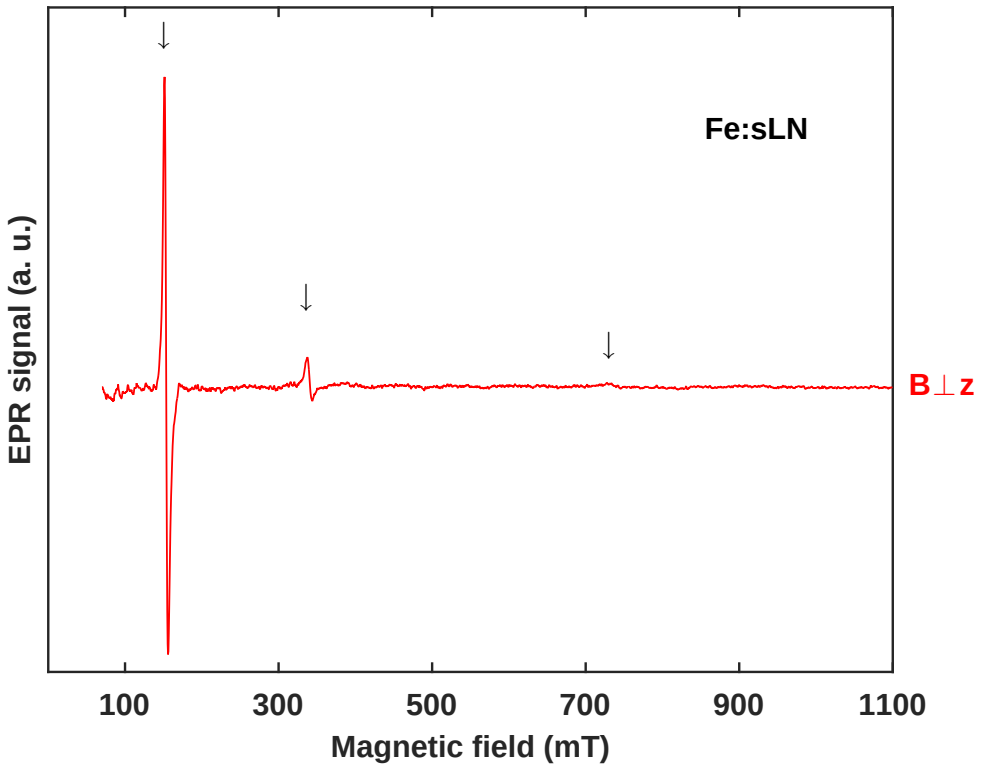

Figure 19: EPR spectrum of iron single doped nearly stoichiometric lithium niobate (**21616**) when the magnetic field was approximately perpendicular to the principal axis z. The background was suppressed to facilitate the visualization. The resonance peaks are marked with an arrow.

excitation, temperature and symmetry of the host material. The spin Hamiltonian for iron in lithium niobate is given in Equation 9.

$$\widehat{H}_{Fe^{3+}} = \mu_B \mathbf{B_0}^T \cdot \tilde{g} \cdot \widehat{\mathbf{S}} + B_2^0 O_2^0 + B_4^3 O_4^3 + B_4^0 O_4^0 + B_4^{-3} O_4^{-3}$$

Trivalent iron (Fe^{3+}) is a transition metal characterized by an isotropic g tensor, i.e. ($g_{xx} = g_{yy} = g_{zz}$). This is because the first excited state is energetically far enough from the ground state. Therefore, electrons influence only slightly the iron atom providing an isotropic g factor. As a reminder, the ground state of iron is defined as ^6S (see Chapter 3 Methods for more details). To understand the complexity of iron doped lithium niobate, the influence of the fine structure term is explained for three different cases. First, if the fine splitting term is insignificant compared with the applied frequency, the energy levels would be degenerated at a zero magnetic field and only one

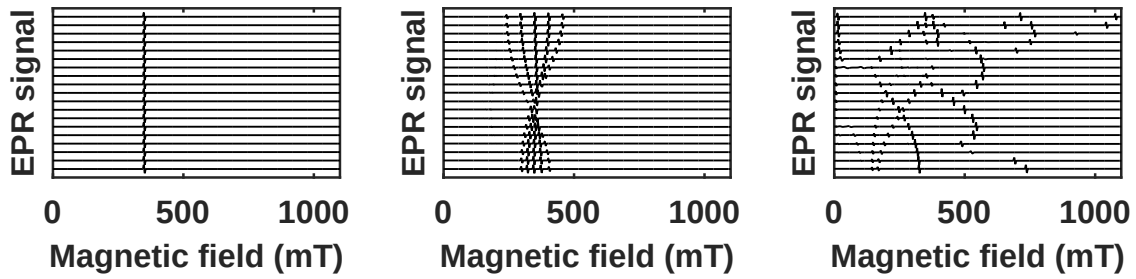

Figure 66: Simulated angle dependence of the EPR spectra of iron doped lithium niobate for rotations about the x axis. The rotation was about x axis, from a magnetic field parallel to y axis (bottom spectrum) up to a magnetic field parallel to z axis (upper spectrum). The g-factor was considered isotropic (g=2). When the fine structure interaction is zero, the resonance peak remains constant rotating the sample (left hand side). For a small fine structure interaction ($B_2^0 = 250$ MHz), five EPR lines appear and change the resonance peak positions by rotation (central panel). In contrast, for a large fine structure interaction ($B_2^0 = 1700$ MHz), more than five EPR lines are observed (right hand side) and, in addition, the intensity of the resonance peaks changes by rotation, and they even disappear.

resonance peak (or EPR resonance line rotating the sample, Figure 66, left hand panel) would be observed under a non-zero magnetic field. Second, if the fine splitting term is small compared with the applied frequency, the fine interaction can be considered as a perturbation and five different resonance lines are observed (see Figure 66, central panel).

However, it was already mentioned that iron in lithium niobate is characterized by a large fine structure term, that cannot be contemplated as a perturbation anymore. A fine structure term of the order of 1700 MHz influences the applied frequency of 9.8 GHz. Therefore, more than five resonance lines are observed changing the peak intensity by rotating the sample with respect to the magnetic field. Moreover, resonance peaks even disappear for a determined rotation angle and magnetic field (see Figure 66, right hand panel). The difficulty resides in associating the resonance peaks with their corresponding transitions (see Figure 67). Consequently, because the exact matching is not known, every combination must be tested. For example, the resonance peak at B $\sim$ 150 mT when the magnetic field is perpendicular to the principal axis (z), is quite intense (see Figure 19). So it is probably an allowed transition 1 to 2, 2 to 3, 3 to 4, 4 to 5 or 5 to 6, if the energy levels are numerated from lower to higher energy. In the hypothetical case that the resonance peak at B $\sim$ 150 mT does not correspond to an allowed transition, the forbidden

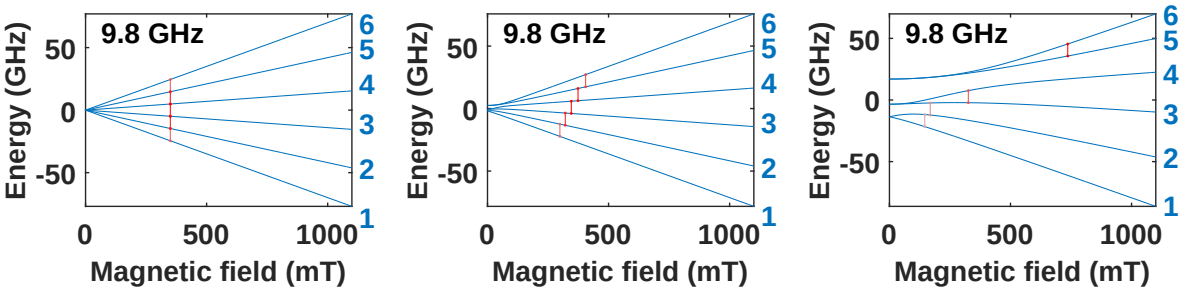

Figure 67: Simulated energy level splitting of the ground state by applying a magnetic field in iron single doped lithium niobate. The magnetic field is parallel to the y axis (as the bottom spectrum in Figure 66) and the applied frequency is 9.8GHz. The g-factor was considered isotropic (g=2) and three different fine structure term values are displayed. When the fine structure is zero, the energy levels are degenerated in a zero magnetic field and they split into six energy levels for a non-zero magnetic field. The allowed resonance peaks (1 to 2, 2 to 3, 3 to 4, 4 to 5 and 5 to 6) are represented in red and are observed at the same magnetic field (left hand side). For a small fine structure interaction ($B_2^0 = 250$ MHz), allowed resonance peaks do not occur at the same position. Therefore, five resonance peaks are observed. Rotating the sample respect to the magnetic field the energy levels change and, consequently, the resonance peak positions for each transition (central panel). For a large fine structure term ($B_2^0 = 1700$ MHz), not only allowed transitions (red lines) but also forbidden transitions (light red lines) can occur. Rotating the sample respect to the magnetic field, the energy levels vary and wherefore the resonance peak positions (right hand side), too.

transitions should be taken into account, for instance 1 to 3 or 1 to 4. As the reader can imagine, it can be a time-consuming task to associate the resonance peaks with their transitions.

The transition was associated to the resonance peaks in Figure 68 using the fitting program. Therefore, one resonance peak was associated to the transition, for example 1 to 2. If the guessed spin Hamiltonian parameters and the transition order (i.e. 1 to 2) are correct, the result tends to converge. However, if one of them is false, the result does not converge. To verify the transition order, the obtained spin Hamiltonian parameters are checked next to the measured data. If they match, the next peak is considered; otherwise another transition (for example 2 to 3) is checked.

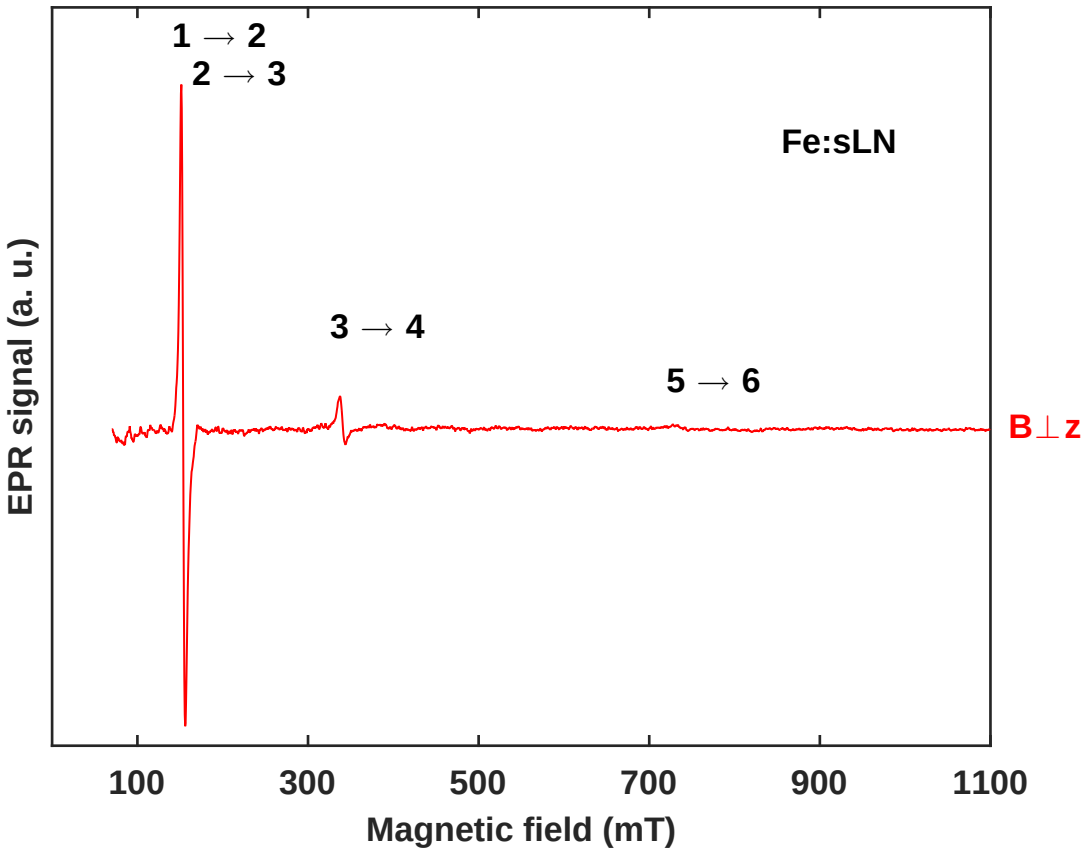

Figure 68: EPR spectrum of iron single doped nearly stoichiometric lithium niobate (**21616**) when the magnetic field is approximately perpendicular to the principal axis z. The background was suppressed to visualize the resonance peaks more clearly. The numbers next to the resonance peaks represent the transition between the energy levels (1 is the lowest level in energy and 6 the highest level in energy). The resonance peaks were associated to each transition by means of a trial and error method.

The resonance peak intensity depends on the transition probability. Clearly, the resonance peak at B $\sim$ 150 mT is a superposition of two transitions (1 to 2 and 2 to 3), therefore it is the most intense peak in Figure 68. In contrast, the resonance peak at B $\sim$ 320 mT is due to the transition between 3 and 4 and is less intense because it is due to a single transition. Unfortunately, the resonance peak at B $\sim$ 750 mT is even less intense due to the transition probability. Furthermore, the sample was not measured at a magnetic field exactly parallel to the y axis. The crystal lattice

of the sample is tilted with respect to the magnetic field because the sample can be only oriented based on its outer appearance. The sample may also be oriented using x-ray, but it would require a considerable experimental effort which is not justified. By means of EasySpin, the tilt and offset angles can be corrected.

After the correct selection of transitions that correspond to the measured resonance peaks (see Figure 68), the fitting program is applied to calculate the spin Hamiltonian parameters, in this special case, of iron single doped nearly stoichiometric lithium niobate. Not only Zeeman and fine structure terms but also the tilt and offset angles of the sample are calculated. Consequently, a unique spin Hamiltonian equation is obtained, which describes iron single doping in nearly stoichiometric lithium niobate. The results were calculated with 51 experimental resonance peaks and they are listed in Table 5. In addition, several **21616** samples were investigated with comparable results considering the experimental error.

g	B_0^2 (MHz)	B_3^4 (MHz)	B_0^4 (MHz)	B_{-3}^4 (MHz)
1.99 $\pm$ 0.01	1706 $\pm$ 17	106 $\pm$ 30	-2.7 $\pm$ 0.5	6 $\pm$ 3

Table 5: Calculated spin Hamiltonian parameters of iron single doped nearly stoichiometric lithium niobate (**21616**). The g-factor is listed in the first column. The second order Stevens operator coefficient is given in the second column. The fourth order Stevens operator coefficients are indicated from the third to the fifth columns. The errors were calculated by a brute-force method.

Iron single doping in nearly stoichiometric lithium niobate has an isotropic g-factor of about 2, as expected. On one hand, the second order of Steven operator coefficient B_2^0 is not a mere small perturbation, but it is comparable with the applied frequency (9.8 GHz) and, therefore, the EPR spectra in the X-band appear as distorted. On the other hand, the fourth order Stevens operator coefficients B_4^3, B_4^0 and B_4^{-3} modify slightly the resonance peaks in the spectra. With the aim of visualizing the goodness of the experimental results from the Table 5, the measured data with the simulated spin Hamiltonian parameters are plotted together in Figures 69 and 70.

It was already mentioned that resonance peaks of a determined transition vary their positions when the sample is rotated with respect to the magnetic field, as it can be seen from Figure 69. Some resonance transitions occur under all circumstances, independently of the angle between

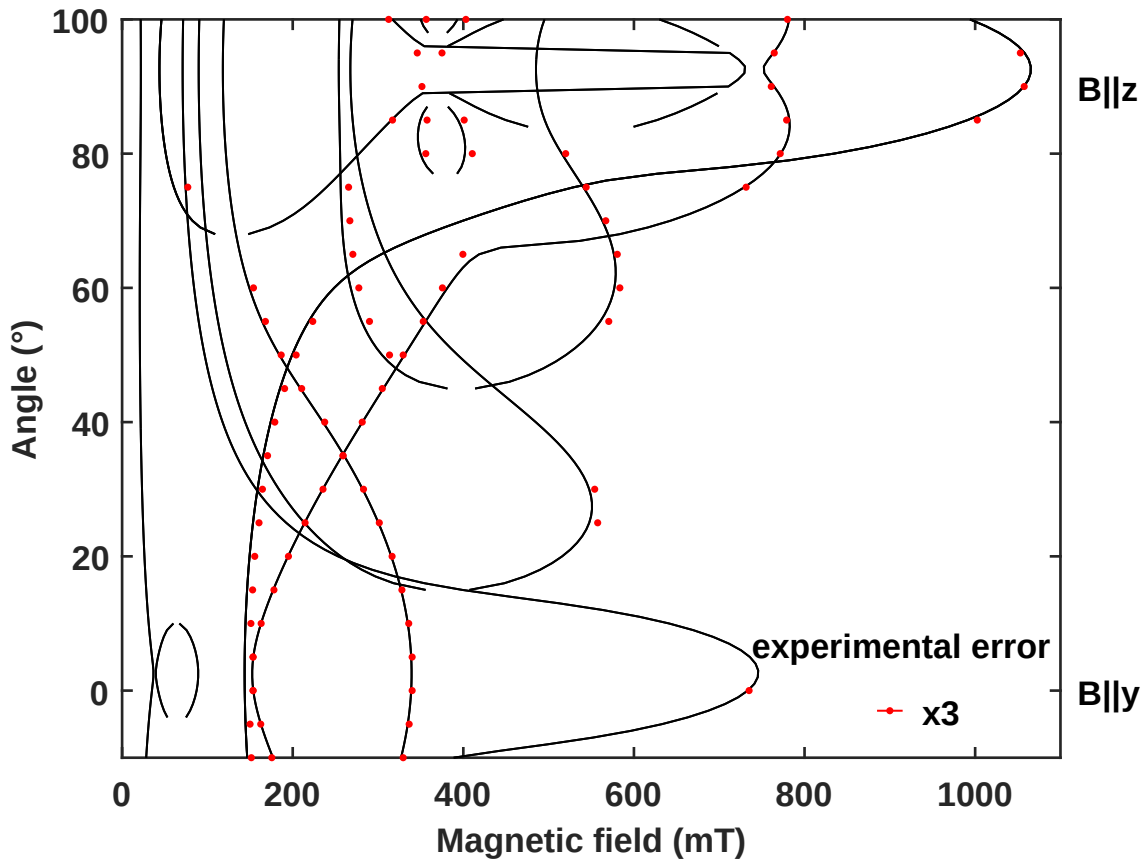

Figure 69: Measured (red dots) and simulated (black lines) angle dependence EPR spectra of iron single doped nearly stoichiometric lithium niobate (**21616**) for rotations of the crystal about the x axis with respect to the magnetic field. The simulated spectra were calculated using the spin Hamiltonian parameters of Table 5. The magnetic field was approximately perpendicular and parallel to the principal axis (z), when the sample was forming an angle of zero or ninety degrees respect to the magnetic field, respectively. The experimental error of the red dots is about 4-5 mT and it is drawn in the bottom right corner.

the sample and the magnetic field. However, other resonance peaks appear only at a determined angular range. For example, when the sample forms an angle of 10° with respect to the y axis (considering a rotation about x axis), only three resonance peaks are observed in the measurements. In contrast, for an angle of 60° or 85°, four and five resonance peaks are

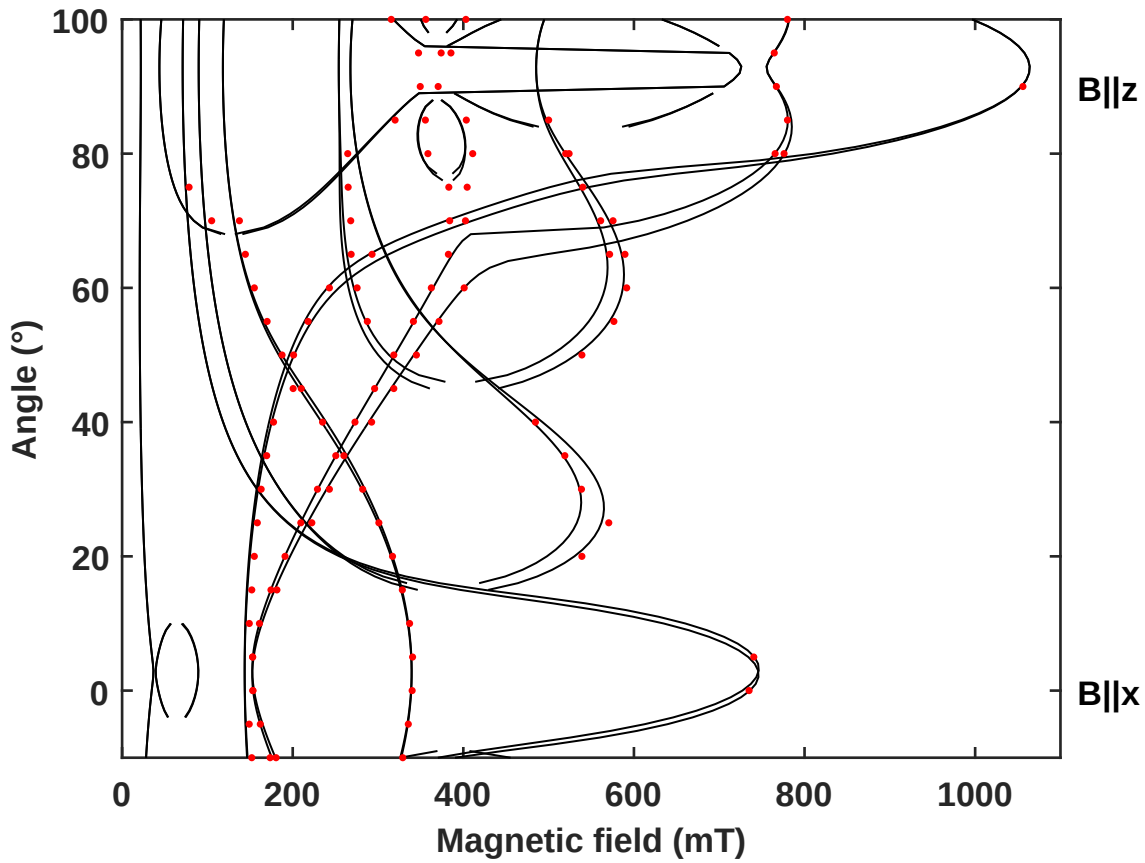

Figure 70: Measured (red dots) and simulated (black lines) angle dependence EPR spectra of iron single doped nearly stoichiometric lithium niobate (**21616**) for rotations of the crystal about the y axis with respect to the magnetic field. The simulated spectra were performed using the spin Hamiltonian parameters of Table 5. The magnetic field was approximately perpendicular and parallel to the principal axis z, when the sample was forming an angle of zero or ninety degrees respect to the magnetic field.

detected, respectively. As the reader can imagine, the angular scale is in principle arbitrary. Here, angle zero was defined when the magnetic field is approximately parallel to the y axis of the sample and the positive angle sense corresponds to rotations from y axis to z axis (i.e. clockwise looking at the sample from the top). That is exactly how the sample was rotated in the EPR spectrometer. Due to the manual manipulation of the sample, an offset angle is present in all measurements. As for example, in Figure 69 the offset angle is approximately 3°.

Lithium niobate includes a glide mirror symmetry in its C_{3v} symmetry (see Chapter 2 Materials). Therefore, two electrically equivalent iron centres (R and L) with the same absolute spin Hamiltonian parameters are present in iron doped lithium niobate. However, they are magnetically non-equivalent, as it can be seen in Figure 70 with the splitting of the EPR lines (see Figures 69 and 70 to note the double lines). Indeed, R centres can be transformed in L centres by the replacement of $x \rightarrow -x$. For Fe^{3+}, this symmetry operation does not change the axial g tensor but transforms B_4^3 (R) in $-B_4^3$ (L) (see Figure 21).

Clearly, the calculated spin Hamiltonian parameters (Table 5) fit successfully with the measured resonance peaks (Figures 69 and 70). Now that the spin Hamiltonian of iron single doped lithium niobate is known, the allowed and forbidden transitions can be associated to each EPR line owing to EasySpin (Figure 71).

With the aim of understanding the origin of each EPR line in iron doped lithium niobate, simulated EPR spectra are shown in Figure 71 using the spin Hamiltonian of Table 5. EasySpin calculates the resonance peaks of the system when the spin Hamiltonian is already known. Therefore, each transition can be associated to each calculated resonance peak. Energy levels are numerated from 1 to 6, i.e. from low to high energy levels (see Figure 73). EPR lines are coloured to distinguish each transition. Allowed EPR transition, as for example from 1 to 2, is marked in black and is observed along the three rotation panels. It should be noticed that this transition is angle dependent, since it is observed from B$\sim$150 mT (B$\|$y) until B$\sim$1050 mT (B$\|$z). In addition, transition 1 to 2 splits in two in the second panel (rotation about y axis) due to the mirror glide plane. Transition 2 to 3 is allowed and observed at two different magnetic fields in the rotation about the x and z axes. This fact is explained by the folding of the energy levels when the magnetic field increases. Under the application of a magnetic field, the Zeeman interaction causes a splitting of the iron energy levels (S=5/2) into six energy levels. Some of the energy levels increase in energy and others decrease, and even they seem to "cross" each other. However, it is observed that the energy levels do not cross, they fold themselves changing the direction (see Figure 73). Other allowed transitions (3 to 4, 4 to 5 and 5 to 6) occur analogously. In contrast, forbidden transitions (in red in Figure 71) are less probable than allowed transitions. Nonetheless, forbidden transitions can be observed due to a small perturbation in iron caused, for example, by the small electric field of a cation vacancy.

Allowed and forbidden transitions have been associated to the EPR lines of iron doped lithium niobate owing to the calculated spin Hamiltonian. The large fine structure splitting term (B_2^0) is responsible of the distorted EPR spectra leading to allowed and forbidden EPR transitions (see

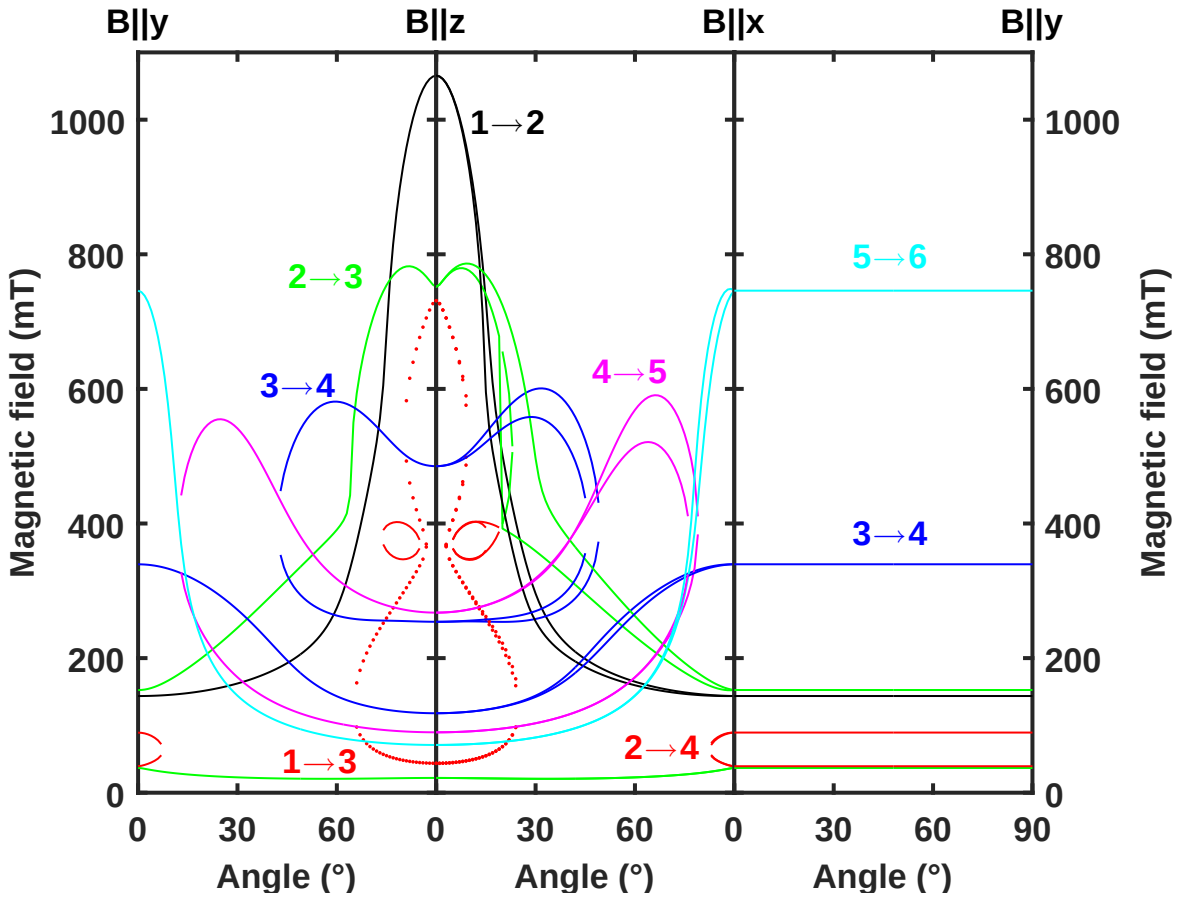

Figure 71: Simulated angular dependence of the EPR spectra of iron single doped lithium niobate for rotations about the x axis (left panel), y axis (central panel) and z axis (right panel) using the spin Hamiltonian of Table 5. The simulation was carried at 9.8 GHz at 5 K. In addition, the tilt and offset angles were considered zero, consequently coloured lines representing the transitions match between panels. The rotation about the x axis starts (angle of 0°) with the magnetic field parallel to the y axis of the sample and ends (angle of 90°) with the magnetic field parallel to the z axis. The rotation about the y axis, goes from the z axis (angle of 0°) to the x axis (angle of 90°). Finally, the rotation about the z axis begins with the magnetic field parallel to the x axis and ends when the magnetic field is parallel to the y axis. EPR lines are coloured to distinguish and visualize the transition lines. Transitions occur between six energy levels due to the Zeeman splitting of the single ground state of iron (^{6}S). They are numerated from 1 to 6 corresponding to the minimum and maximum energy levels, and are written next to the EPR lines. Therefore, allowed transition as for example the transition between the lowest energy levels 1 and 2 is denoted in black. Other allowed transitions are transition 2 to 3 in green, transition 3 to 4 in dark blue, transition 4 to 5 in pink and transition 5 to 6 in light blue. In contrast, forbidden transitions are represented with red dots (transition 1 to 3) and redlines (transition 2 to 4).

Figure 71). Furthermore, due to the mirror glide plane in the C_{3v} symmetry, the EPR lines split into two lines. This is reflected in the positive or negative sign of the absolute B_4^3 Stevens operator coefficient. This transforms one non-magnetically equivalent iron centre (R) into the other (L).

The spin Hamiltonian parameters are equal for both centres (R and L), the difference resides in the sign of the absolute B_4^3 value (see Figure 72).

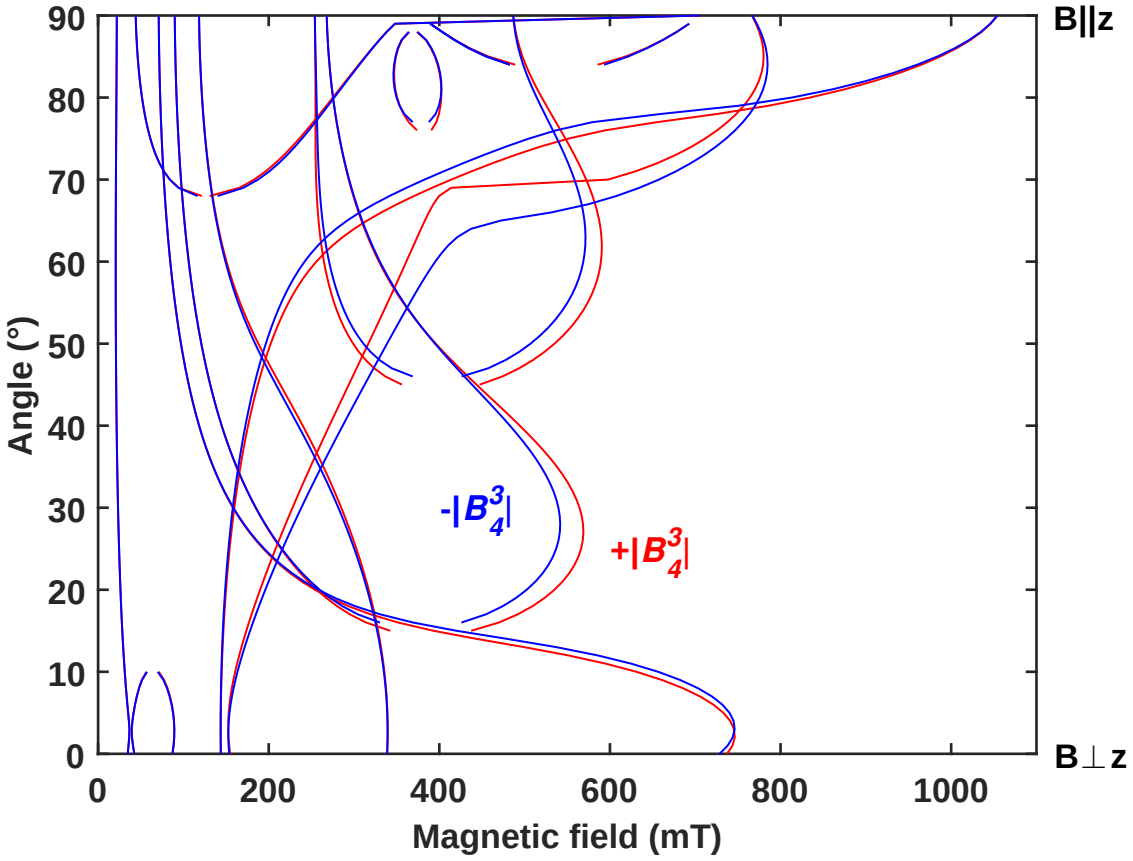

Figure 72: Simulated angle dependence of the EPR spectra of iron single doped lithium niobate (**21616**) rotated about the y axis. If just one centre (for example R) is considered in the simulation (values of Table 5): the $+B_4^3$ Stevens operator coefficient is denoted in red, whereas the $-B_4^3$ Stevens operator coefficient is represented in blue. However, if two centres are considered, red lines correspond to one centre (for instance R), whereas blue lines represent the other centre (L).

EPR lines split into two lines corresponding to two magnetically non-equivalent iron centres (for example red is the R centre and blue is the L centre, see Figure 72). Consequently, simulating the spin Hamiltonian parameters of Table 5 with $+B_4^3$, red lines (from the R centre for example) are observed and blue lines correspond to the other centre (L). However, if only one centre is considered (C_1 symmetry) the red lines are associated to the positive sign of the B_4^3 absolute value and the blue lines to the negative case. This is explained by the mirror glide plane of C_{3v} symmetry. The energy levels for both centres are shown in Figure 73.

Comparing the EPR splitting due to $+B_4^3$ and $-B_4^3$ in Figure 21 in Chapter 4 (Measurements), it is observed that the EPR resonance peaks for $+B_4^3$ are more intense that for $-B_4^3$. This fact could point out that there exist more iron centres with $+B_4^3$ than with $-B_4^3$. However, one would expect to obtain the same number of $+B_4^3$ than $-B_4^3$ iron ions centres. The difference in intensities is caused by transition probability, which is different for the $+B_4^3$ and the $-B_4^3$ case (as it can be seen in Figure 73). As a reminder, two magnetically non-equivalent iron centres are described by the same spin Hamiltonian parameters, except the sign of the coefficient B_4^3. These two centres seem to be far away from each other because no resonance peaks due to their interaction are observed. To visualize the EPR splitting, the energy levels schema for the rotation about the y axis when the magnetic field forms an angle of 30° with the z axis is represented in Figure 72. In the experimental ERP spectra, six resonance peaks are detected. However, in the energy levels simulation schema, more lines are expected (see Figure 73).

Comparing the transition probabilities (i.e. line colours) in Figure 73, transition 3 to 4 for a magnetic field near 600 mT is more probable (intense red) in the $+B_4^3$ case than the $-B_4^3$ case. Therefore, resonance peaks in EPR measurements are more intense. In addition, EPR transitions 4 to 5 and 5 to 6 at a magnetic field between 100 mT and 200 mT are not marked in Figure 73 because of their very small probability.

At the beginning of the section, an EPR spectrum with the magnetic field perpendicular to the principal axis was shown (Figure 19). There, only three peaks were obtained. Now, knowing the spin Hamiltonian equation, the reason can be understood. On the one hand, the energy levels schema (Figure 74) shows that transitions 1 to 2 and 2 to 3 overlap at the same magnetic field. Therefore, the resonance peak is more intense than for the transitions 3 to 4 and 5 to 6. On the other hand, the resonance peak of transition 3 to 4 is more intense than transition 5 to 6, because the linewidth of the last one is broader than the first one. Transition 4 to 5 is not obtained because the energy levels, (from the beginning) are separated enough to avoid a possible transition (see Figure 74 where no transition 4 to 5 is given). In addition, the transition at B$\sim$45 mT occurs from

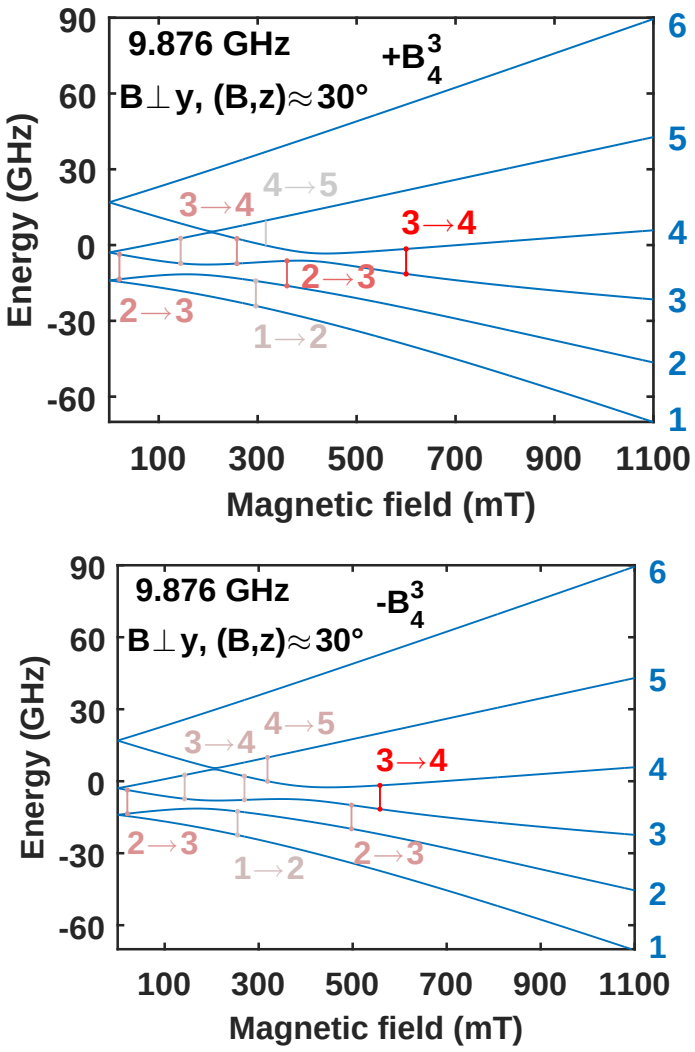

Figure 73: Simulated energy level splitting schema of iron single doped nearly stoichiometric lithium niobate for a rotation about the y axis and with the magnetic field and the z axis forming an angle of 30°. The simulation was carried at 9.877 GHz and using the spin Hamiltonian parameters of Table 5, as the considered sample (**21616**). The upper figure corresponds to the $+B_4^3$ coefficient (red lines in Figure 72) and the figure below was simulated with $-B_4^3$ (blue lines in Figure 72). The energy levels are denoted from 1 to 6 i.e. from lower to higher energy. The transitions are denoted with the energy levels at which they take place. The transition probability is depicted using a red-grey scale, where allowed transitions are denoted in red and forbidden transitions in grey. In addition, the EPR transitions between the energy levels are denoted in the same colour as the transition probability.

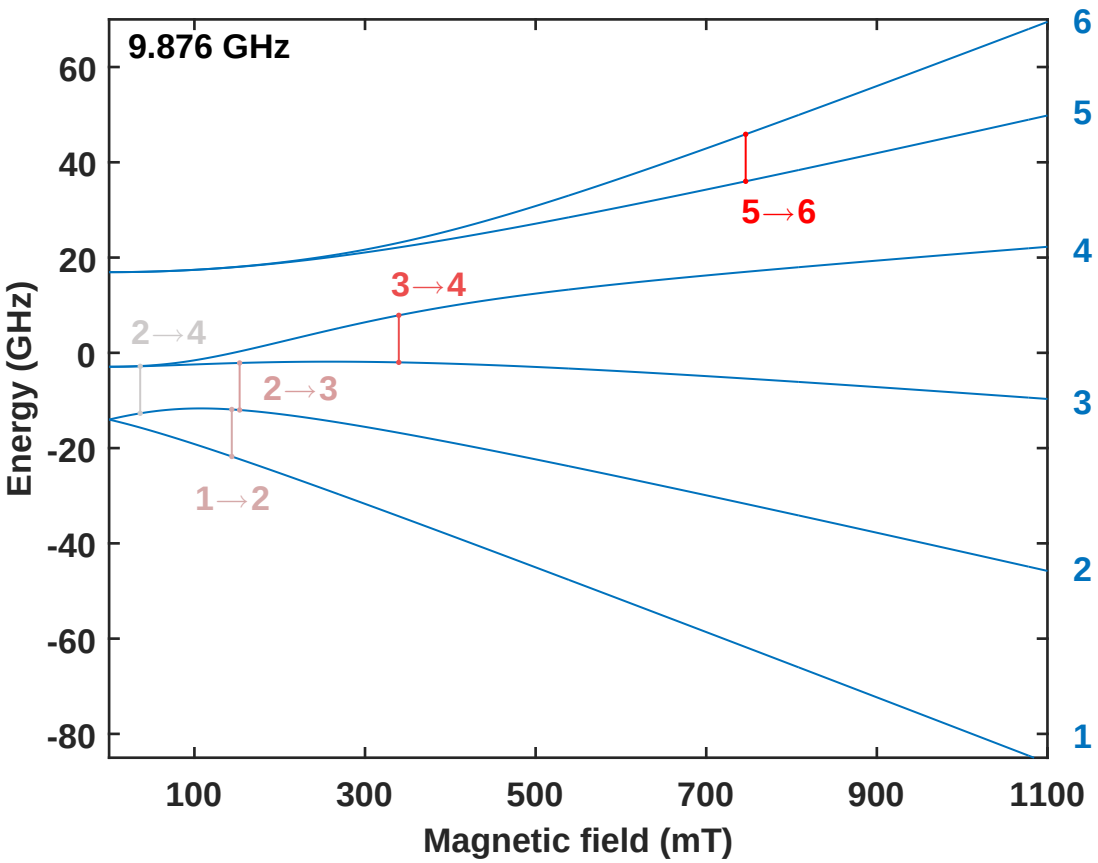

Figure 74: Simulated energy levels schema of iron single doped nearly stoichiometric lithium niobate for a magnetic field parallel to the y axis. The simulation was carried at 9.877 GHz and using the spin Hamiltonian parameters of Table 5, as the considered sample (**21616**). The energy levels are denoted from 1 to 6 i.e. from lower to higher energy. The transitions are denoted with the energy levels at which they take place. The transition probability is depicted using a red-grey scale, where allowed transitions are denoted in red and forbidden transitions in grey. In addition, the EPR transitions between the energy levels are denoted in the same colour as the transition probability.

2 to 3 and from 2 to 4, both with low transition probability. Although transition 2 to 3 is allowed, transition 2 to 4 is forbidden and consequently the transition probability is low. It should be noticed that transition levels 3 and 4 are degenerated for a small magnetic field (B$\sim$45 mT).

After a complete and detailed description of the process for obtaining spin Hamiltonian parameters, a compact roadmap of measured and simulated EPR spectra is given as a summary (see Figure

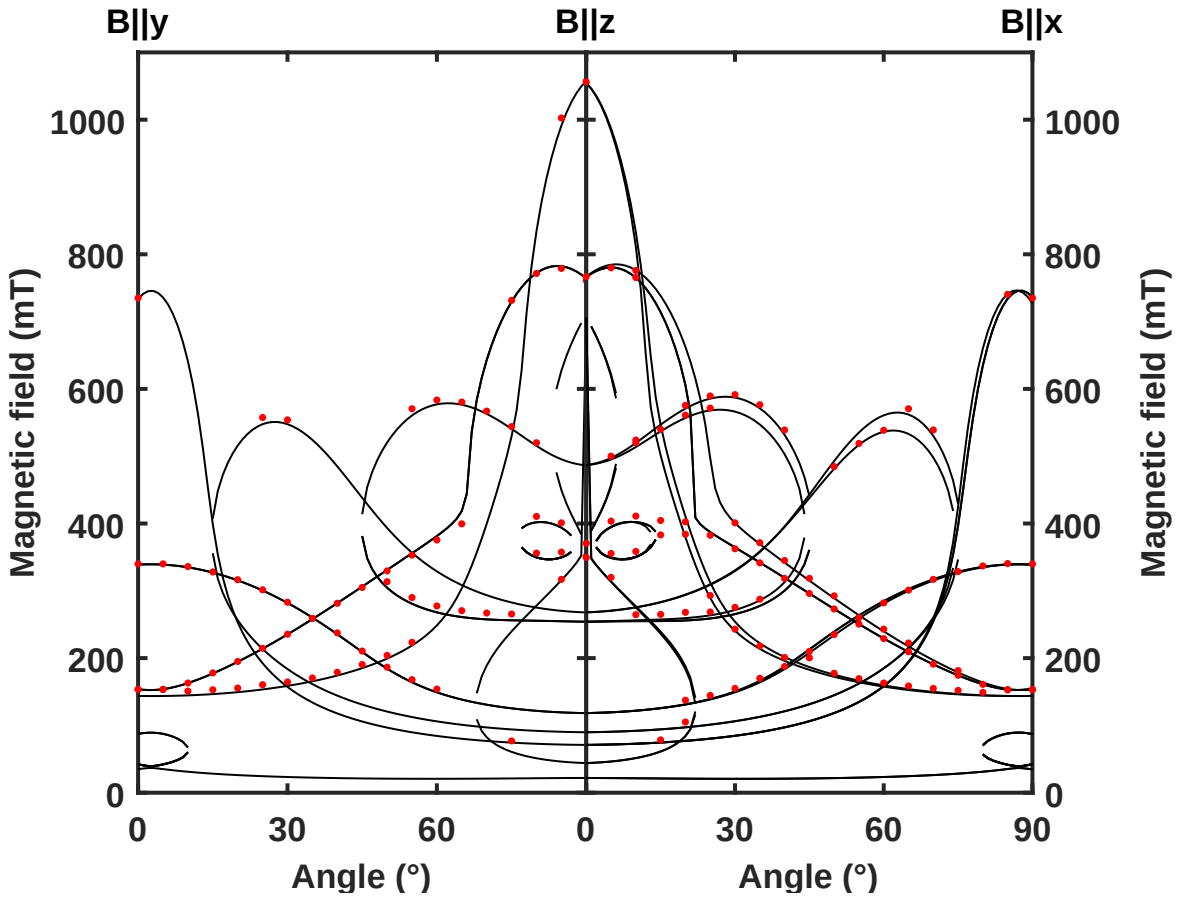

Figure 75: Measured (red dots) and simulated (black lines) angle dependent EPR spectra of iron single doped lithium niobate (**21616**) for rotations about the x axis (left panel) and y axis (right panel). The simulated spectra were performed using the spin Hamiltonian parameters of Table 5. In the rotation about x, an angle of 0° shows that the magnetic field is approximately parallel to y, whereas an angle of 90° denotes a magnetic field which is approximately parallel to z. In the rotation about y, an angle of 0° represents that the magnetic field is approximately parallel to z, whereas an angle of 90° denotes a magnetic field which is approximately parallel to y. Transition lines do not match exactly between panels, due to tilt and offset angles.

75). The rotation about the x axis (already shown in Figure 69) is given on the left panel and the rotation about y (shown in Figure 70) is represented on the right site. The road map (Figure 75) begins with the magnetic field parallel to the y axis (angle of 0°) and rotating the x axis ends

with the magnetic field parallel to z axis (angle of 90°). Similarly, the rotation about the y axis goes from the z axis (angle of 0°) to the x axis (angle of 90°). Unfortunately, the peak positions for a magnetic field parallel to the z axis in both panels do not match exactly, as it can be seen in Figure 75. This is due to the tilt and offset angles of the sample during the different rotation measurements. Nonetheless, a successful match is found between the experimental EPR data and the calculated spin Hamiltonian parameters.

In the following sections, the spin Hamiltonian parameters of the doped and co-doped lithium niobate samples and lithium yttrium borate are presented. To visualize the goodness of the obtained experimental results, a representation similar to Figure 75 is shown and the spin Hamiltonian parameters are summarized at the end of this chapter.

5.1.2 Iron single doped congruent lithium niobate

In the last section, the process of obtaining the spin Hamiltonian of iron single doped nearly stoichiometric lithium niobate was described in detail. In this section, iron single doped congruent lithium niobate (**155312**) is studied using the described procedure. It was already mentioned that the linewidth of the resonance peaks in congruent lithium niobate is larger than in nearly stoichiometric lithium niobate. Therefore, if two resonance peaks are at similar magnetic field positions, they could overlap making the magnetic field extraction of each resonance peak more difficult.

After applying the fitting program to the experimental data of iron single doped congruent lithium niobate, the spin Hamiltonian (Equation 9 Chapter 3 Methods) parameters were obtained (see Table 6).

g	B_0^2 (MHz)	B_3^4 (MHz)	B_0^4 (MHz)	B_{-3}^4 (MHz)
1.986 $\pm$ 0.09	1678 $\pm$ 16	104 $\pm$ 15	-3.5 $\pm$ 0.3	-63 ± 12

Table 6: Calculated spin Hamiltonian parameter of iron single doped congruent lithium niobate (**155312**). The g-factor is listed in the first column. The second order Stevens operator coefficient is given in the second column. The fourth order Stevens operator coefficients are indicated from the third to the fifth columns. The errors were calculated by a brute-force method.

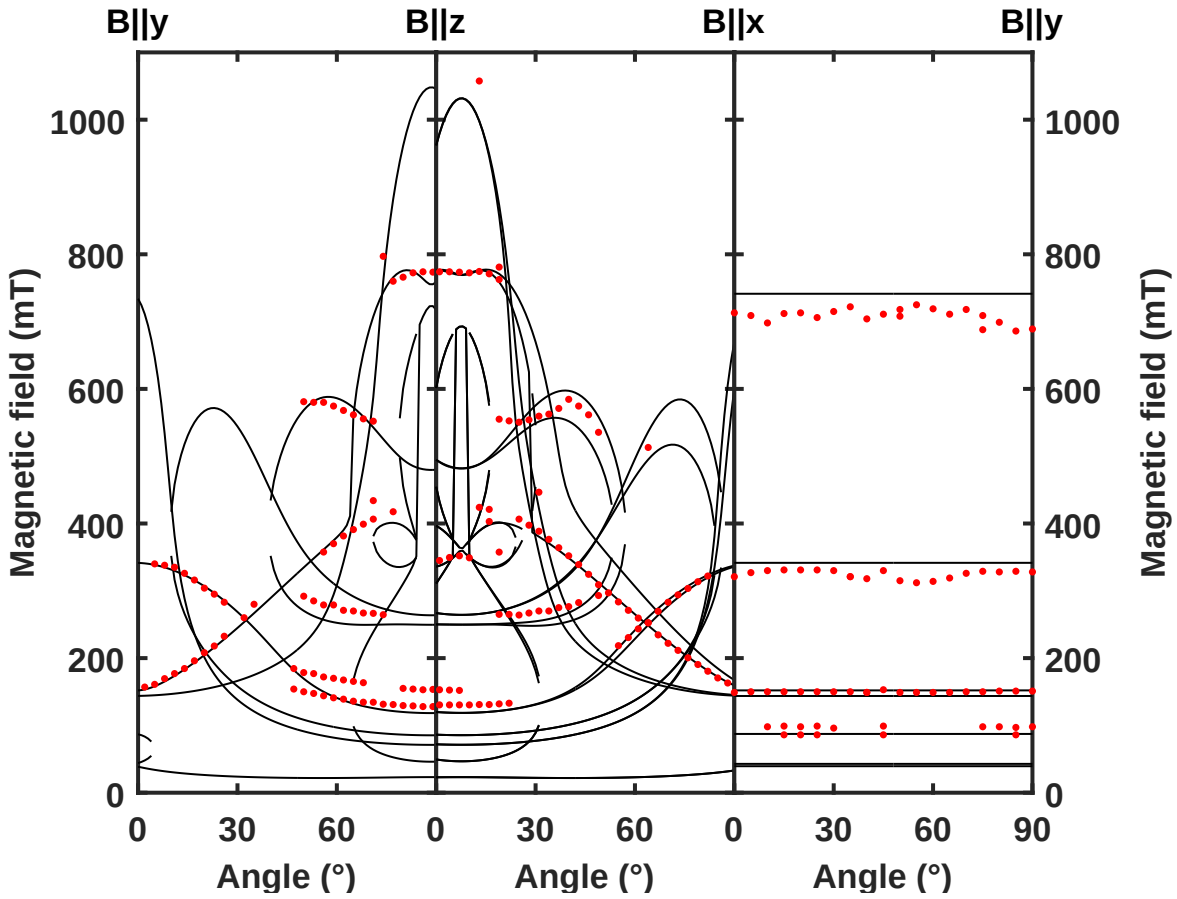

Figure 76: Measured (red dots) and simulated (black lines) angle dependence of the EPR spectra of iron single doped lithium niobate (155312) for rotations about the x axis (left panel), y axis (central panel) and z axis (right panel). The simulated spectra were modelled using the spin Hamiltonian parameters of Table 6. In the rotation about x, an angle of 0° shows that the magnetic field is approximately perpendicular to z, whereas an angle of 90° denotes a magnetic field which is approximately parallel to z. Transition lines do not match exactly between panels, due to tilt and offset angles.

Comparing the experimental and simulated data in the same figure allows for a rough estimate of the goodness of the obtained experimental results (Figure 13).

Almost all observed resonance peaks coincide with a transition line predicted in the simulation (see Figure 76). In addition, the spin Hamiltonian parameters in congruent lithium niobate differ

slightly from the parameters of the nearly stoichiometric crystal (Table 5). In spite of the slightly different crystal structure of the congruent and stoichiometric samples, the iron centre has the same behaviour in both cases. Comparing the road maps of iron doped in nearly stoichiometric (Figure 75) and congruent (Figure 76) lithium niobate, the experimental data in the first sample fit better with the simulated spin Hamiltonian. This fact can be explained owing to the broader linewidth in congruent samples. Due to the rotation about the y axis in the congruent sample, the EPR splitting is not appreciated (linewidth of the order of 4-5 mT in nearly stoichiometric samples compared to 12-15 mT in congruent lithium niobate). This fact directly influences the accuracy of the spin Hamiltonian parameters.

5.1.3 Titanium single doped nearly stoichiometric lithium niobate

Until now, iron single doping in nearly stoichiometric and congruent lithium niobate were presented. Before studying iron-titanium co-doped lithium niobate, titanium single doping in nearly stoichiometric lithium niobate (**170983**) is introduced. The paramagnetic titanium ion (Ti^{3+}) was obtained after a reduction at 900 °C in vacuum (residual pressure less than 1 mbar) during 30 min. The spin Hamiltonian for titanium in lithium niobate is given as (see Equation 10 in Chapter 3 Methods):

$$\widehat{H}_{Ti^{3+}} = \mu_B \mathbf{B_0}^T \cdot \tilde{g} \cdot \widehat{\mathbf{S}}$$

The experimental spin Hamiltonian parameters are listed in Table 7.

$g_\perp$	$g_\parallel$
1.850 $\pm$ 0.002	1.973 $\pm$ 0.002

Table 7: Calculated spin Hamiltonian parameters of titanium single doped nearly stoichiometric lithium niobate (**170983**). The g-tensor is, in this case, axial. The perpendicular g-tensor component is listed in the first column, whereas the parallel g-tensor component is written in the second column. The errors were calculated by a brute-force method.

The obtained g-tensor is axial and coincides with the crystal frame, i. e. the g-tensor is not tilted. Moreover, experimental and simulated data are compared in Figure 77 (roadmap), leading to

a good matching. Therefore, the error values from Table 7 are, in this case, small compared with other samples (as, for example, iron single doped lithium niobate Table 5 or 6). Initially, it could appear that titanium causes less disorder than iron ion in lithium niobate. However, this assumption depends on the lattice site and lattice symmetry. In Chapter 6 Discussion, the titanium ions interpretation is given.

Titanium single doped nearly stoichiometric lithium niobate has one resonance peak due to the transition 1 to 2. In addition, depending on the orientation of the sample with the magnetic field, the resonance peak position is different (for example $\sim$360 mT for an applied magnetic field parallel to z and $\sim$380 mT for a magnetic field perpendicular to z axis). The energy level schemas are shown in Figure 78.

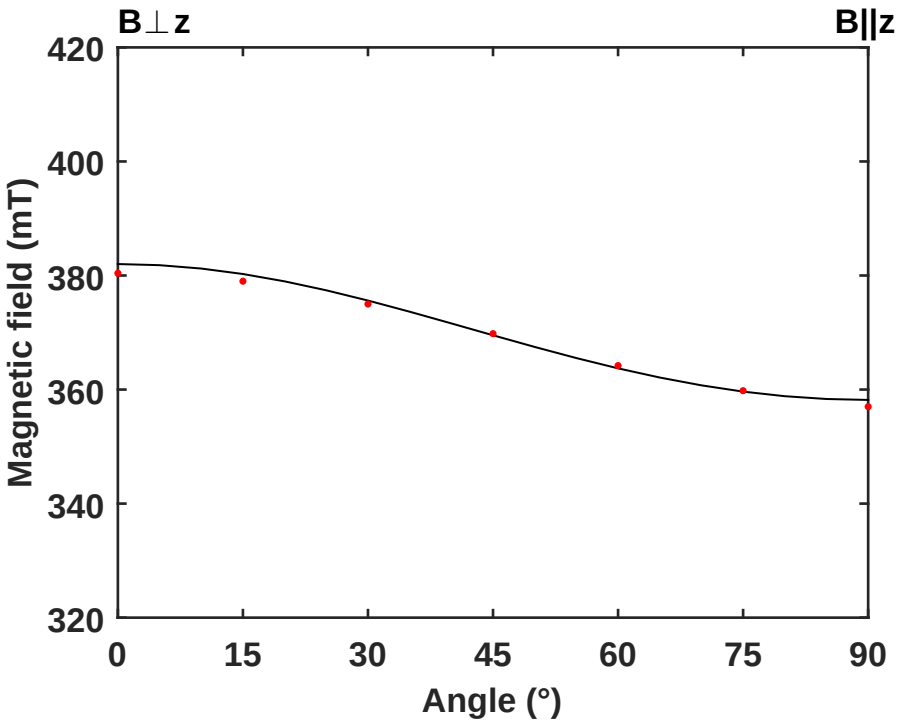

Figure 77: Measured (red dots) and simulated (black lines) angular dependence of the EPR spectra of titanium single doped nearly stoichiometric lithium niobate (**170983**) for rotations about the x axis. The simulated spectra were performed using the spin Hamiltonian parameters of Table 7. An angle of 0° indicates that the magnetic field is approximately parallel to z, whereas an angle of 90° denotes a magnetic field which is approximately perpendicular to z.

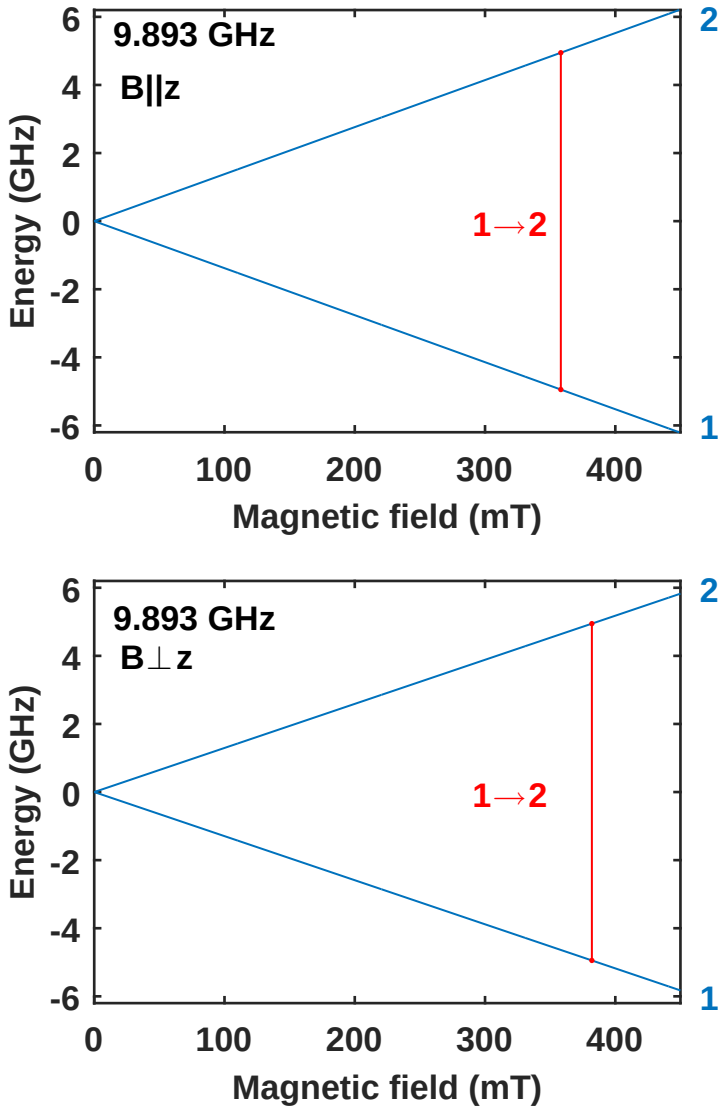

Figure 78: Simulated energy levels diagram of titanium single doped nearly stoichiometric lithium niobate for a magnetic field parallel to the z axis (top panel) and parallel to the y axis (bottom panel). The simulation was carried at 9.893 GHz, as the measured frequency of the considered sample (170983), and using the spin Hamiltonian parameters of the Table 7. The red lines represent allowed transitions.

5.1.4 Iron-titanium co-doped nearly stoichiometric lithium niobate

In the last sections, not only iron but also titanium single doped were considered. In this section, iron-titanium co-doped nearly stoichiometric lithium niobate is studied. Not only as grown but also reduced samples were investigated in order to determine the spin Hamiltonian parameters.

As grown iron-titanium co-doped nearly stoichiometric lithium niobate crystals (21615) were measured by EPR, as shown in Figures 27, 28 and 29 in Chapter 4 Measurements. Only Fe^{3+} was detected, therefore, the spin Hamiltonian is described by the iron ion:

$$\widehat{H}_{Fe^{3+}} = \mu_B \mathbf{B_0}^T \cdot \tilde{g} \cdot \widehat{\mathbf{S}} + B_2^0 O_2^0 + B_4^3 O_4^3 + B_4^0 O_4^0 + B_4^{-3} O_4^{-3}$$

However, comparing the spin Hamiltonian parameters of iron single doped and iron-titanium co-doped nearly stoichiometric lithium niobate, the difference resides in the g-tensor. In iron single doped samples, the g-tensor is isotropic (see Table 5 or 6), whereas in iron-titanium co-doped samples it is axial. The spin Hamiltonian parameters of iron-titanium co-doped samples (21615) are provided in Table 8.

$g_\perp$	$g_\parallel$	B_0^2 (MHz)	B_3^4 (MHz)	B_0^4 (MHz)	B_{-3}^4 (MHz)
1.98 $\pm$ 0.02	2.01 $\pm$ 0.02	1728 $\pm$ 34	38 $\pm$ 15	-2.6 $\pm$ 0.5	4 $\pm$ 16

Table 8: Calculated spin Hamiltonian parameters of as grown iron-titanium co-doped nearly stoichiometric lithium niobate (21615). The perpendicular g-tensor component is listed in the first column, whereas the parallel g-tensor component is written in the second column. The second order Stevens operator coefficient is given in the third column. The fourth order Stevens operator coefficients are indicated from the fourth to the sixth columns. The errors were calculated by a brute-force method.

As expected, iron has a g-tensor close to the value 2, however, the g-tensor is axial in iron-titanium co-doped nearly stoichiometric lithium niobate, because of the influence of titanium (see Chapter 6 Discussion). Comparing the measured with the simulated data (Figure 79), the obtained experimental results of Table 8 match very well with the EPR measurements (Figures 27 to 29, Chapter 4 Measurements).

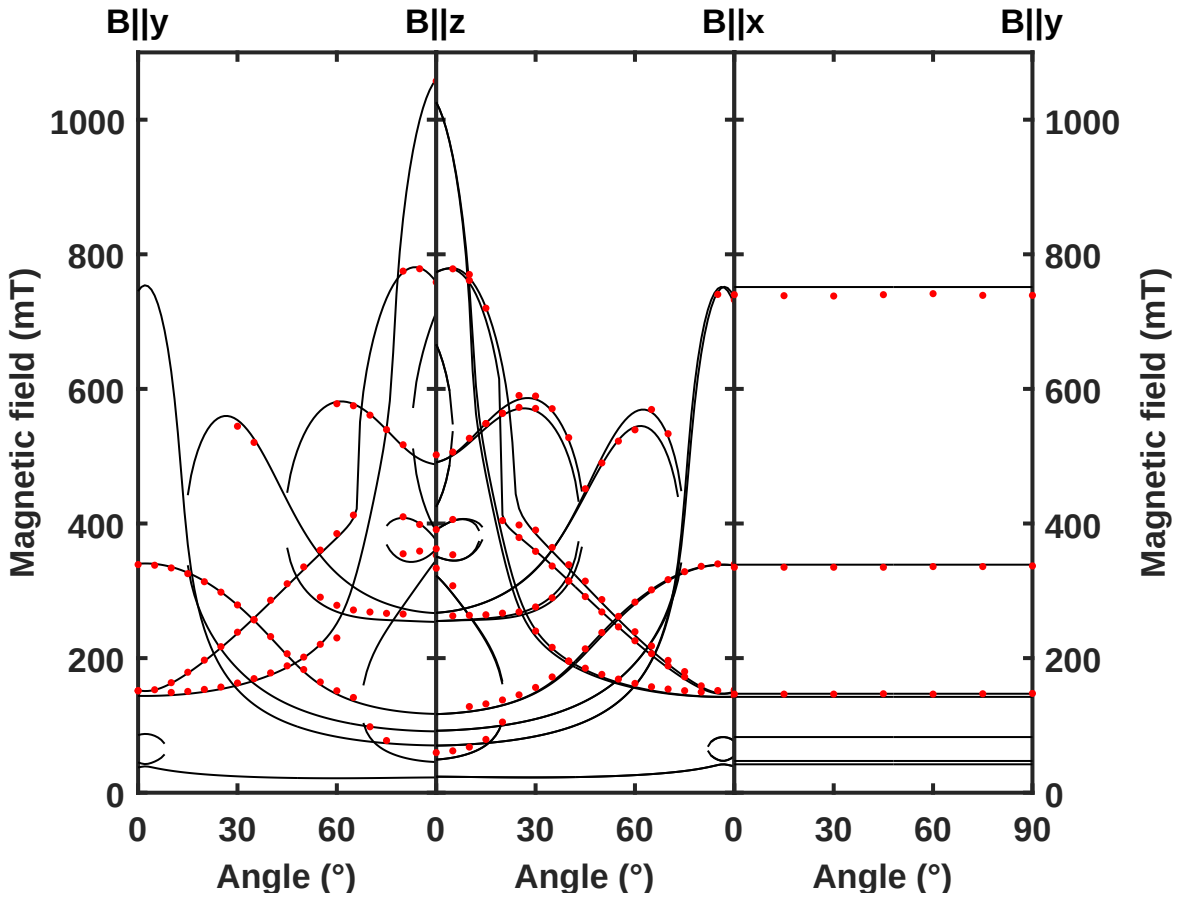

Figure 79: Measured (red dots) and simulated (black lines) angle dependent EPR spectra of as grown iron-titanium co-doped nearly stoichiometric lithium niobate (**21615**) for rotations about the x axis (left panel), y axis (centre panel) and z axis (right panel). The simulated spectra were calculated using the spin Hamiltonian parameters of Table 8. In the rotation about x, an angle of 0° indicates that the magnetic field is approximately parallel to y, whereas an angle of 90° denotes a magnetic field approximately parallel to z. In the rotation about y, an angle of 0° shows that the magnetic field is approximately parallel to z, whereas an angle of 90° denotes a magnetic field which is approximately parallel to y. In the rotation about z, an angle of 0° represents that the magnetic field is approximately parallel to x, whereas an angle of 90° denotes a magnetic field which is approximately parallel to y. Transition lines do not match exactly between panels, due to tilt and offset angles.

Iron-titanium nearly stoichiometric lithium niobate was annealed at 600 °C during 3 hours in vacuum (less than 1 mbar) (**21615+600**). In the ERP spectra not only single Fe^{3+} features but also single Ti^{3+} features were observed. Furthermore, no additional resonance peaks appear in the EPR spectra, indicating that iron and titanium do not form a classical bounded complex (see discussion in Chapter 6 Discussion). Therefore, the spin Hamiltonian equation of the co-doped crystal is the sum of both ions and no additional term must be considered. The spin Hamiltonian of iron-titanium co-doped nearly stoichiometric lithium niobate is:

$$\begin{aligned}\widehat{H}_{Fe,Ti} = &\widehat{H}_{Ti^{3+}} + \widehat{H}_{Fe^{3+}} = \left\{\mu_B \mathbf{B_0}^T \cdot \tilde{g} \cdot \widehat{\mathbf{S}}\right\}_{Ti^{3+}} + \\ &\left\{\mu_B \mathbf{B_0}^T \cdot \tilde{g} \cdot \widehat{\mathbf{S}} + B_2^0 O_2^0 + B_4^3 O_4^3 + B_4^0 O_4^0 + B_4^{-3} O_4^{-3}\right\}_{Fe^{3+}}\end{aligned} \tag{27}$$

Applying the fitting program to the experimental measurements, the spin Hamiltonian parameters are obtained. The results are listed in Table 9.

Ion	$g_\perp$	$g_\parallel$	B_0^2 (MHz)	B_3^4 (MHz)	B_0^4 (MHz)	B_{-3}^4 (MHz)
Fe^{3+}	1.99 ± 0.02	2.02 ± 0.02	1735 ± 37	26 ± 19	-2.5 ± 0.5	16 ± 48
Ti^{3+}	1.836 ± 0.004	1.958 ± 0.004	-	-	-	-

Table 9: Calculated spin Hamiltonian parameters of reduced iron-titanium co-doped nearly stoichiometric lithium niobate (**21615+600**). The annealing process was performed at 600 °C for 3 hours in vacuum (residual pressure less than 1 mbar). The considered ion is displayed in the first column. The perpendicular g-tensor component is listed in the second column, whereas the parallel g-tensor component is written in the third column. The second order Stevens operator coefficient is given in the fourth column. The fourth order Stevens operator coefficients are indicated from the fifth to the seventh columns. The errors were calculated by a brute-force method.

Comparing the measured and simulated data (see Figure 80), it can be seen that the extrapolated experimental results summarized in Table 9 have a good matching with the EPR measurements (Figures 32 and 33 in Chapter 4 Measurements).

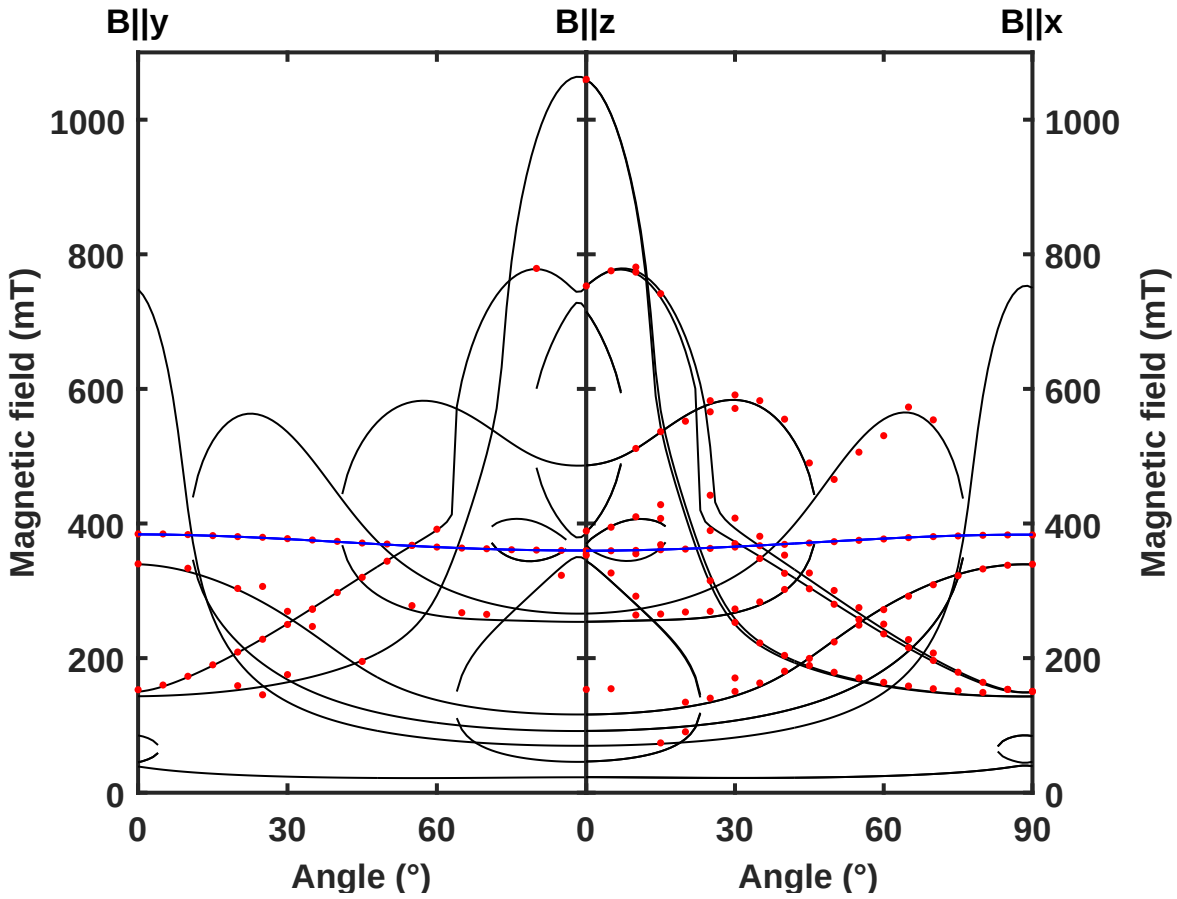

Figure 80: Measured (red dots) and simulated (black and blue lines) angular dependence of the EPR spectra of as grown iron-titanium co-doped nearly stoichiometric lithium niobate (**21615+600**) for rotations about the x axis (left hand panel) and y axis (right hand panel). Black lines are due to iron centres and blue line due to titanium. The annealing process was performed at 600 °C for 3 hours in vacuum (residual pressure less than 1 mbar). The simulated spectra were performed using the spin Hamiltonian parameters of Table 9. In the rotation about x, an angle of 0° represents that the magnetic field is approximately parallel to y, whereas an angle of 90° denotes a magnetic field which is approximately parallel to z. In the rotation about y, an angle of 0° represents that the magnetic field is approximately parallel to z, whereas an angle of 90° denotes a magnetic field which is approximately parallel to y. Transition lines do not match exactly between panels, due to tilt and offset angles.

On the one hand, the g-tensor of Fe^{3+} in annealed iron-titanium co-doped nearly stoichiometric lithium niobate is axial, as in as grown iron-titanium co-doped samples. Moreover, the parallel component of the g-tensor is larger than its perpendicular component, both in annealed and as grown samples, due to the interaction between iron and titanium. The B_2^0 Stevens operator coefficient has the same order of magnitude than in the as grown iron-titanium co-doped sample and is a little larger than in iron single doped samples. The Stevens operator coefficient B_4^0 has the same order of magnitude as in the as grown iron-titanium co-doped and iron single doped crystals. However, the Stevens operator coefficients B_4^3 and B_4^{-3} differ in both samples. B_4^3 and B_4^{-3} represent a small correction of the spin Hamiltonian, and therefore it is difficult to obtain an accurate value. Thus, it can be affirmed that the iron centre remains unchanged under reduction at 600 °C and the spin Hamiltonian parameters describe uniquely Fe^{3+} in the considered samples.

On the other hand, the g-tensor of Ti^{3+} in Table 9 is axial as in titanium single doped nearly stoichiometric lithium niobate (**170983**) (see Table 7). Due to the interaction between iron and titanium in the crystal, the spin Hamiltonian parameters are slightly different, however, they describe uniquely Ti^{3+} in lithium niobate.

Iron-titanium nearly stoichiometric lithium niobate was reduced at 900 °C for 30 min in vacuum (**21615+900**). In this case, only Ti^{3+} was detected, and the Fe^{3+} signatures disappeared (see discussion in Chapter 6 Discussion). Applying the fitting program to the experimental measurements, the spin Hamiltonian parameters are determined and the results are presented in Table 10.

$g_\perp$	$g_\parallel$
1.844 $\pm$ 0.002	1.967 $\pm$ 0.002

Table 10: Calculated spin Hamiltonian parameters of reduced iron-titanium co-doped nearly stoichiometric lithium niobate (**21615+900**). The annealing process was performed at 900 °C for 30 minutes in vacuum (less than 1 mbar). Only Ti^{3+} was detected and the g-tensor is axial. The perpendicular g-tensor component is listed in the first column, whereas the parallel g-tensor component is written in the second column. The errors were calculated by a brute-force method.

The extrapolated experimental values listed in Table 10 match with the EPR measurements. Figure 17 illustrates the comparison between measured and simulated data.

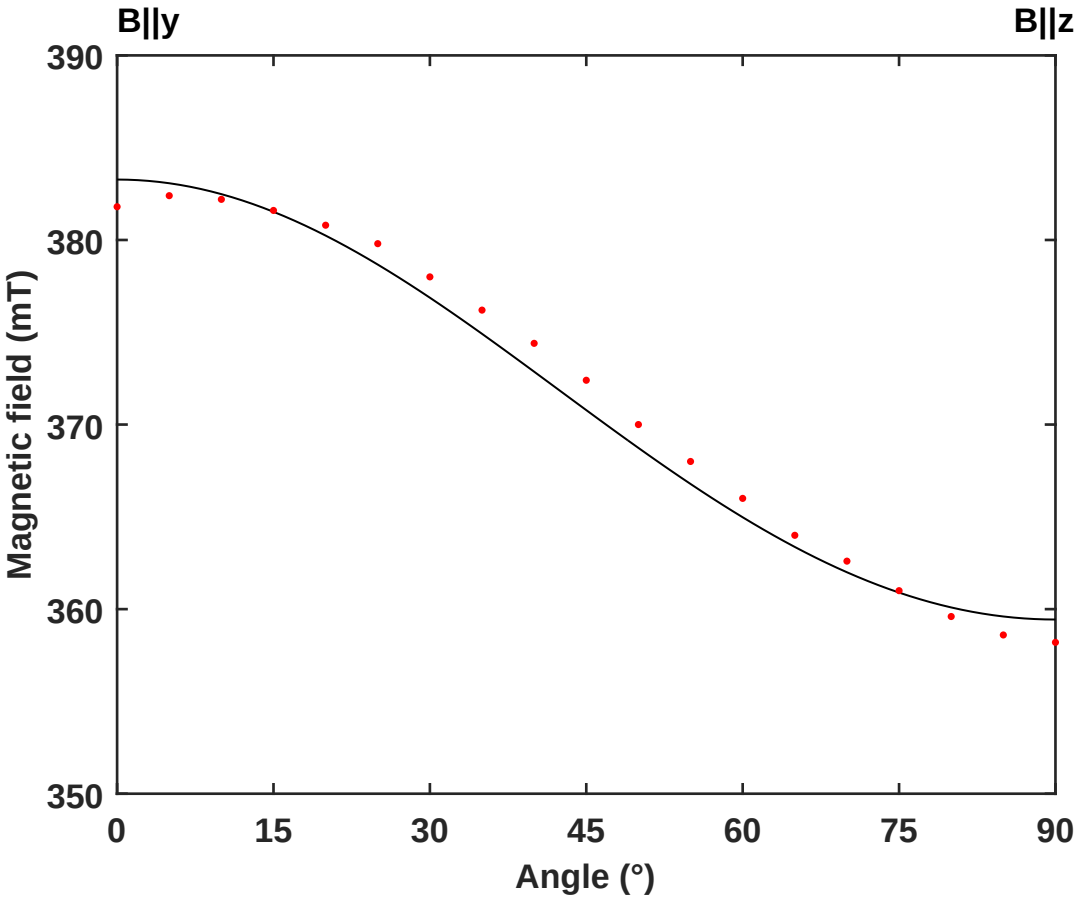

Figure 81: Measured (red dots) and simulated (black lines) angle dependent EPR spectra of iron-titanium co-doped nearly stoichiometric lithium niobate (**21615+900**) for rotations about the x axis. The simulated spectra were performed using the spin Hamiltonian parameters of Table 10. An angle of 0° indicates that the magnetic field is approximately parallel to y, whereas an angle of 90° denotes a magnetic field which is approximately parallel to z.

In annealed iron-titanium co-doped nearly stoichiometric lithium niobate (**21615+900**), the parallel component of the g-tensor is larger than the perpendicular one. This result was also obtained in titanium single doped lithium niobate (**170983**). The minor differences between the g-tensors in titanium single doped and co-doped samples are due to the interaction between iron and titanium in lithium niobate.

5.1.5 Iron-titanium co-doped lithium niobate

Until now, iron-titanium co-doped nearly stoichiometric lithium niobate crystals were discussed. In the following, iron-titanium congruent lithium niobate is considered. The doping process was performed during the crystal growth (bulk doping) for iron and by indiffusion for titanium (**155313vs**). In the as grown sample, only Fe^{3+} was detected and applying the fitting program, the spin Hamiltonian parameters were obtained (see Table 11).

$g_\perp$	$g_\parallel$	B_0^2 (MHz)	B_3^4 (MHz)	B_0^4 (MHz)	B_{-3}^4 (MHz)
1.98 $\pm$ 0.01	1.96 $\pm$ 0.01	1688 $\pm$ 30	0	-3.3 $\pm$ 0.6	37 $\pm$ 11

Table 11: Calculated spin Hamiltonian parameters of as grown iron-titanium co-doped congruent lithium niobate (**155313vs**). The doping process was performed during the crystal growth (bulk doping) for iron and by indiffusion for titanium. The perpendicular g-tensor component is listed in the first column, whereas the parallel g-tensor component is written in the second column. The second order Stevens operator coefficient is given in the third column. The fourth order Stevens operator coefficients are indicated from the fourth to the sixth column. The errors were calculated by a brute-force method.

Comparing the measured and the simulated data (Figure 82), it can be easily seen that the extrapolated experimental values of Table 11 match well with the EPR measurements.

Similarly to iron-titanium co-doped nearly stoichiometric lithium niobate, the Fe^{3+} g-tensor is axial instead of isotropic (as in iron single doped samples), due to the interaction between titanium and iron. It must be noticed in addition, that the number of points used to calculate the spin Hamiltonian was less than in other samples. For these reasons, the spin Hamiltonian parameters differ from the previous ones (as for example Tables 6, 8 or 9).

Iron-titanium co-doped congruent lithium niobate was annealed at 800 °C for three hours in argon, and no trace of titanium was found. Probably, titanium ions were not substantially reduced and only Ti^{4+} were available. In iron-titanium co-doped nearly stoichiometric lithium niobate it was shown that the iron centre does not vary substantially under annealing treatment. Therefore, the spin Hamiltonian of this sample was not recalculated.

Until now, the spin Hamiltonian parameters of the different single and co-doped lithium niobate samples were presented. To summarise, Fe^{3+} has isotropic g-tensor in iron single doped sample.

However, Fe^{3+} g-tensor becomes axial due to the interaction with titanium in co-doped lithium niobate. A summary of the calculated spin Hamiltonian parameters for the investigated samples is given in Table 12.

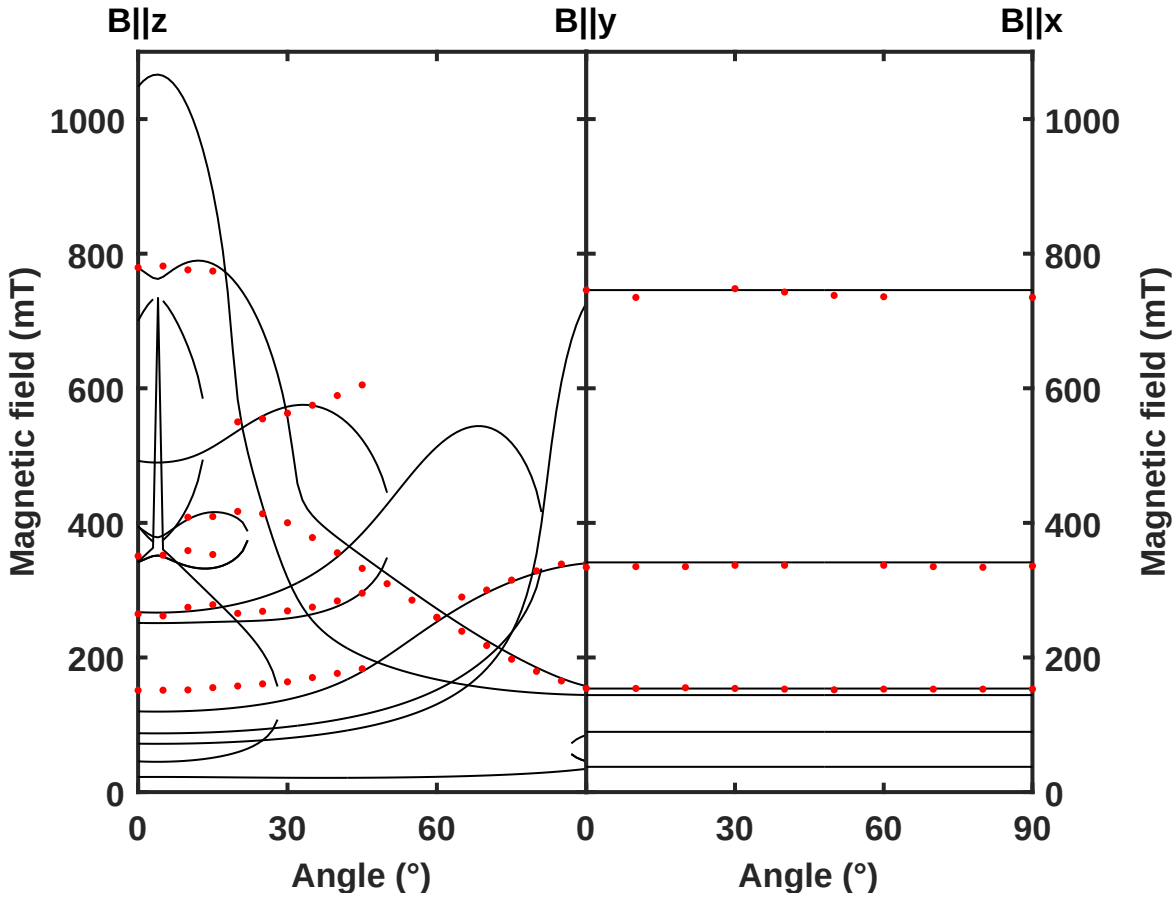

Figure 82: Measured (red dots) and simulated (black lines) angle dependent EPR spectra of as grown iron-titanium co-doped congruent lithium niobate (**155313vs**) for rotations about the x axis (left panel) and about the z axis (right panel). The simulated spectra were calculated using the spin Hamiltonian parameters of Table 11. In the rotation about x, an angle of 0° indicates that the magnetic field is approximately parallel to z, whereas an angle of 90° denotes a magnetic field approximately parallel to y. In the rotation about z, an angle of 0° shows that the magnetic field is approximately parallel to y, whereas an angle of 90° denotes a magnetic field which is approximately parallel to x. The transition lines do not match exactly between panels, due to tilt and offset angles.

Sample	Ion	$g_\perp$	$g_\parallel$	B_0^2 (MHz)	B_3^4 (MHz)	B_0^4 (MHz)	B_{-3}^4 (MHz)
21616	Fe^{3+}	1.99 $\pm$ 0.01	1.99 $\pm$ 0.01	1706 $\pm$ 17	106 $\pm$ 30	-2.7 $\pm$ 0.5	6 $\pm$ 3
155312	Fe^{3+}	1.986 $\pm$ 0.009	1.986 $\pm$ 0.009	1678 $\pm$ 16	104 $\pm$ 15	-3.5 $\pm$ 0.3	63 $\pm$ 12
170983	Ti^{3+}	1.850 $\pm$ 0.002	1.973 $\pm$ 0.002	-	-	-	-
21615	Fe^{3+}	1.98 $\pm$ 0.02	2.01 $\pm$ 0.02	1728 $\pm$ 34	38 $\pm$ 15	-2.6 $\pm$ 0.5	4 $\pm$ 16
21615 +600	Fe^{3+}	1.99 $\pm$ 0.02	2.02 $\pm$ 0.02	1735 $\pm$ 37	26 $\pm$ 19	-2.5 $\pm$ 0.5	16 $\pm$ 48
	Ti^{3+}	1.836 $\pm$ 0.004	1.958 $\pm$ 0.004	-	-	-	-
21615 +900	Ti^{3+}	1.844 $\pm$ 0.002	1.967 $\pm$ 0.002	-	-	-	-
155313vs	Fe^{3+}	1.98 $\pm$ 0.01	1.96 $\pm$ 0.01	1688 $\pm$ 30	0	-3.3 $\pm$ 0.6	37 $\pm$ 11

Table 12: Calculated spin Hamiltonian parameters of doped lithium niobate samples. As grown iron single doped nearly stoichiometric lithium niobate (**21616**) is shown in the first row and as grown iron single doped congruent lithium niobate (**155312**) is provided in the second row. Reduced titanium single doped lithium niobate is listed in the third row (**170983**). The annealing treatment was performed at 900 °C for 30 min in vacuum. As grown and reduced iron-titanium co-doped nearly stoichiometric lithium niobate are provided from the fourth to the sixth row. The thermal process was performed at 600 °C for 3 hours (fifth row, **21615+600**) and at 900 °C for 30 min (sixth row, **21615+900**) in vacuum. As grown iron-titanium co-doped congruent lithium niobate (**155313vs**) is shown in the seventh row. The doping process was performed during the crystal growth (bulk doping) for iron and by indiffusion for titanium. The sample number is written in the first column and the ion investigated in the sample is indicated in the second column. The perpendicular g-tensor component is listed in the third column, whereas the parallel g-tensor component is written in the fourth column. The second order Stevens operator coefficient is given in the fifth column. The fourth order Stevens operator coefficients are indicated from the sixth to the eighth column. The errors were calculated by a brute-force method.

In iron single doped lithium niobate samples, the g-tensor is isotropic due to the nature of iron, whose first excited energy levels are far from the ground state. Therefore, the g-tensor is close to that of the free electron. In contrast, the g-tensor is axial due to the presence of titanium in the co-doped samples. The second order Stevens operator coefficient ($B_2^0 \sim 1.7$ GHz) is neither small nor negligible compared with the excitation frequency (9.8 GHz). Consequently, the EPR spectra are distorted (as explained e.g. in Figure 19) notably increasing the difficulty of performing the required fit to obtain the spin Hamiltonian parameters. Finally, the fourth order Stevens operator coefficients slightly modify the spectra so as to fit as well as possible with the experimental data. Although they modify the EPR spectra slightly , the fourth order Stevens operators are necessary for the EPR interpretation. Of course, the tilt and offset angles were also considered for each sample, although they were not presented here. On the other hand, titanium centres present an axial g-tensor in single and co-doped samples due to the centre symmetry (for a detailed discussion see Chapter 6 Discussion).

At the beginning of the chapter, the observed transitions due to Fe^{3+} where assigned to the EPR spectral features. Furthermore, it could be found that iron and titanium are not bounded by a classical bound, because no additional resonance peak was detected in the co-doped samples. Owing to the developed fitting program, the spin Hamiltonian parameters of the investigated samples were successfully obtained. This fact was demonstrated in the visualization of measured and simulated data in the roadmaps, and summarized in Table 12.

5.2 Lithium yttrium borate samples

In the last section, the spin Hamiltonian parameters of single and co-doped lithium niobate samples have been extrapolated from our measurements. Using the same procedure, in this section the experimental results of erbium, ytterbium and iron doped lithium yttrium borate are presented. Therefore, the spin Hamiltonian parameters are calculated from the experimental data owing to the least square method. First erbium doped lithium yttrium borate is introduced, followed by ytterbium doped lithium yttrium borate and, finally, iron doped lithium yttrium borate.

5.2.1 Erbium doped lithium yttrium borate

Erbium doped lithium niobate was measured by EPR (Figures 46 to 50 in Chapter 4 Measurements) and resonance peaks with different intensity were found. In this case, one intense resonance peak is observed and next to it, eight weak peaks take place (Figure 83). This diversity in the peak intensity and the quantity of peaks is due to the erbium isotopes in the sample.

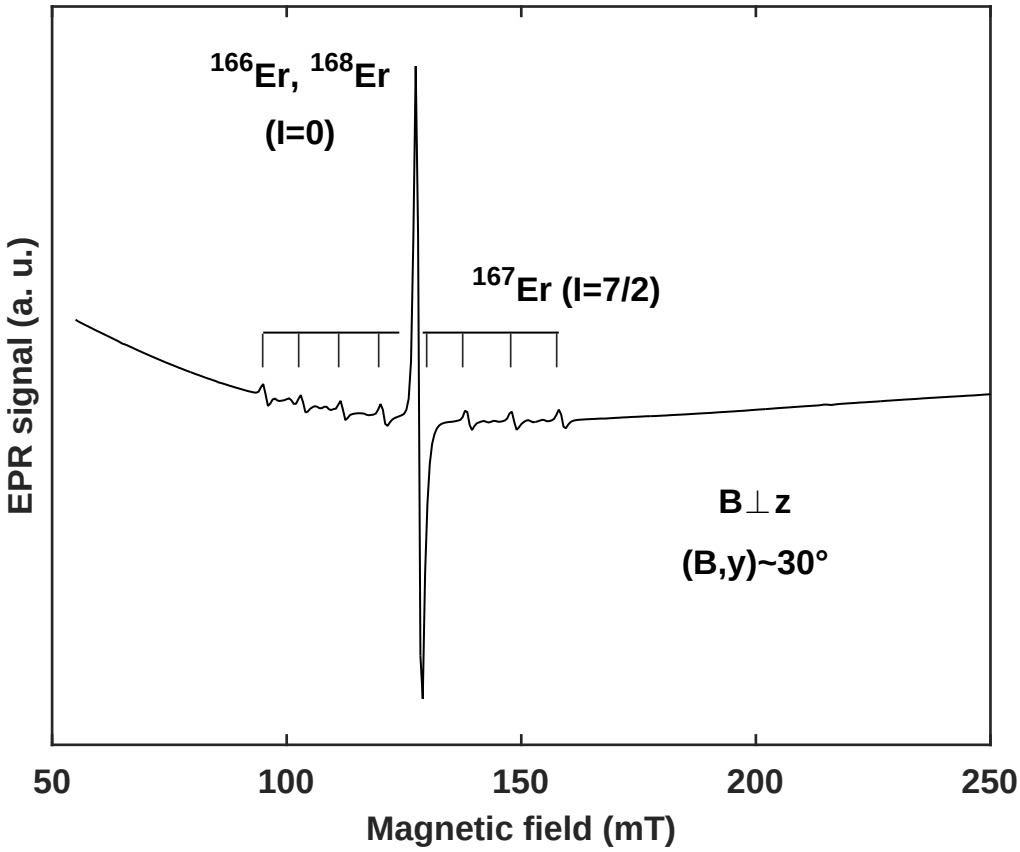

Figure 83: EPR spectrum of erbium doped nearly stoichiometric lithium yttrium borate (**91103**) when the magnetic field was approximately perpendicular to the principal axis z, and forming an angle of 30° with the y axis. The most intense resonance peak is due to erbium isotopes with nuclear spin zero (I=0) (as for example ^{166}Er and ^{168}Er). Eight resonance peaks with weak intensity are caused by the ^{167}Er isotope with nuclear spin I=7/2. They are marked with a comb to facilitate the visualization.

In nature, erbium (Er) has several isotopes with different natural abundance (indicated in the following in percent) and all of them can be observed by means of EPR spectroscopy: ^{162}Er (0.14%), ^{164}Er (1.61%), ^{166}Er (33.61%), ^{167}Er (22.93%), ^{168}Er (26.78%), ^{170}Er (14.93%). In addition, the nuclear spin of ^{167}Er is I=7/2, whereas the nuclear spin of the remaining erbium isotopes is zero. Now, knowing the natural abundance and the nuclear spin of the respective isotopes, the peak intensity and number of resonance peaks can be understood. Isotopes ^{162}Er, ^{164}Er, ^{166}Er, ^{168}Er and ^{170}Er have I=0, i.e. one intense resonance peak is observed (2I+1). On the other hand, ^{167}Er has I=7/2 and therefore, eight resonance peaks are observed (Figure 83). Moreover, the resonance peak intensity is related with the natural abundance, and therefore, the resonance peak of the isotopes with I=0 is almost five times more intense than the isotope ^{167}Er (with natural abundance 22.93%).

However, by rotating the sample with respect to the magnetic field, two intense resonances next to sixteen weak peaks are found. This is due to the C_{2h} symmetry of lithium yttrium borate. The horizontal symmetry plane causes a duplication of the intense resonance peak due to isotopes with I=0 next to the eight weak resonance peaks, therefore a total of eighteen resonance lines are detected in a spectrum (Figure 46 in Chapter 4 Measurements). This can be explained by the existence of two magnetically non-equivalent erbium centres with the same spin Hamiltonian parameters, whereby one centre is rotated by 180° with respect to the other one.

The spin Hamiltonian of erbium doped nearly stoichiometric lithium yttrium borate was written in Equation 11 Chapter 3 Methods. The effective spin is S=1/2 (see Appendix E). The spin Hamil-

Isotope	g_{xx}	g_{yy}	g_{zz}	α_g (°)	β_g (°)	γ_g (°)
^{166}Er	6.25 ± 2	0.67 ± 20	8.00 ± 2	-5.1 ± 3.0	46.0 ± 0.2	37.0 ± 0.2
	A_{xx} (MHz)	A_{yy} (MHz)	A_{zz} (MHz)	α_A (°)	β_A (°)	γ_A (°)
^{167}Er	657 ± 3	300 ± 200	847 ± 3	1.5 ± 3.0	44.4 ± 1.0	40.5 ± 1.0

Table 13: Calculated spin Hamiltonian parameters of as grown erbium doped nearly stoichiometric lithium yttrium borate (**91103**). The considered isotope is written in the first column. The x diagonal g-tensor component is listed in the second column, whereas the y diagonal g-tensor component is written in the third column and the z diagonal g-tensor component is provided in the fourth column. The Euler angles (α, β, γ) are shown from the fifth to the seventh column. The errors were calculated by a brute-force method.

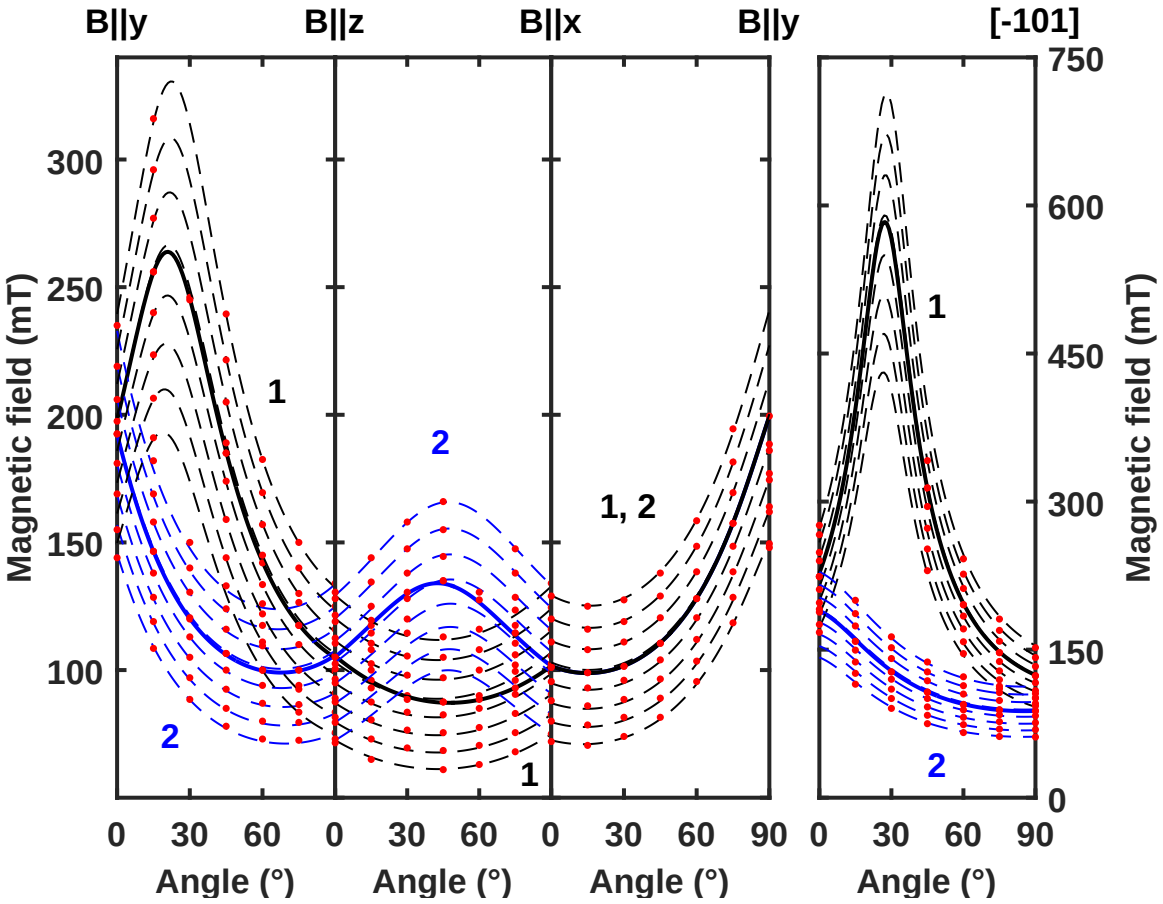

Figure 84: Measured (red dots) and simulated (black and blue lines) angle dependent EPR spectra of as grown erbium doped nearly stoichiometric lithium yttrium borate (**91103**) for rotations about (from left to right panel) the x axis, y axis, z axis and $<101>$. Two magnetically non-equivalent centres are observed (centre 1 in black and centre 2 in blue). Erbium isotopes with zero nuclear magnetic field are represented by a continuous line whereas ^{167}Er isotopes are denoted by a dashed line. The simulated spectra were performed using the spin Hamiltonian parameters of Table 13. In the rotation about x, an angle of 0° indicates that the magnetic field is approximately parallel to y, whereas an angle of 90° denotes a magnetic field approx. parallel to z. In the rotation about y, an angle of 0° shows that the magnetic field is approx. parallel to z, whereas an angle of 90° denotes a magnetic field which is approximately parallel to x. In the rotation about z, an angle of 0° represents a magnetic field approx. parallel to x, whereas an angle of 90° denotes a magnetic field which is approx. parallel to y. In the rotation about $<101>$ axis, an angle of 0° indicates that the magnetic field is approx. parallel to y, whereas an angle of 90° denotes a magnetic field which is approx. parallel to $<-101>$. Transition lines do not match exactly between panels, due to tilt and offset angles.

tonian is composed by two dominant terms: Zeeman and hyperfine splitting. The first contribution (Zeeman splitting) is due to the interaction of the electron with the magnetic field, and it is characterized by the isotopes with I=0. However, the second contribution (hyperfine splitting) is caused by the interaction of the electrons with the nuclear spin, and in this case, it is caused by ^{167}Er with I=7/2, i.e. eight resonance peaks.

The spin Hamiltonian parameters are calculated by the least square fit method of experimental data with the simulated (by EasySpin) data. In erbium doped lithium yttrium borate, the g-tensor and the A-tensor are orthorhombic and, in addition, they are tilted with respect to the crystal frame (see Appendix D). So, the tensor diagonal was calculated in the tensor frame and also the Euler angles (see Appendix B) from the tensor frame to the crystal frame. The spin Hamiltonian parameters are listed in Table 13.

The calculated spin Hamiltonian parameters were simulated and compared with the experimental measured data. The satisfying match of the obtained spin Hamiltonian with the measurement is shown in Figure 84.

Two magnetically non-equivalent centres are found in erbium doped lithium yttrium borate (see Figure 84). If the spin Hamiltonian parameters shown in Table 13 are simulated within the C_{2h} symmetry, centre 1 (black) and 2 (blue) are obtained. However, if one erbium centre is considered (C_1 symmetry) and rotating the sample from 0° to 90°, only one centre is observed (black lines). Nevertheless, rotating the sample from 180° to 270°, centre 2 is obtained (black lines in the first panel of Figure 84).

It is observed in Figure 84, for example in rotation about the y axis, that the hyperfine lines (dashed lines) are not equidistant between them and moreover they cross with the more intense resonance peak (continuous line). This is due to the hyperfine structure tensor (A-tensor). The Euler angles of the A-tensor slightly differ from the Euler angles of the g-tensor. This mismatch produces the crossing between the transition lines and, furthermore, asymmetric resonance peak disposition.

With the aim of checking the obtained g-tensor values of Table 13, the principal values are approximately found in the EPR measurements. In the tensor frame, the g-tensor is described by three principal parameters (g_{xx}, g_{yy} and g_{zz}). Owing to the Euler angles, the tensor frame can be transformed into the crystal frame (and vice versa). Therefore, using the rotation matrix from the tensor frame to the crystal frame, g_{xx}, g_{yy} and g_{zz} values can be written in the crystal frame components. Using this idea, the principal values of the g-tensor were roughly observed in the

measurement. To facilitate the visualization, Figure 85 shows the tensor frame directions in the crystal frame.

The largest g-tensor component (i.e. g_{zz}) is almost lying on the xz plane. Therefore, it is observed in the rotations about the y axis at an angle of about 45° (B∼87.5 mT). In addition, this point corresponds to the lowest point (in magnetic field) obtained in the Figure 84 (solid black line). As a reminder, the g-factor and the magnetic field are inversely proportional (hv=gμB). The smallest g-tensor component, g_{yy}, is observed at about 30° in the rotation about $<101>$ axis (B $\sim$ 600 mT). Therefore, the highest point in the magnetic field observed in the fourth panel of Figure 84 corresponds to the lowest g-tensor component. The last g-tensor component g_{xx} is observed at

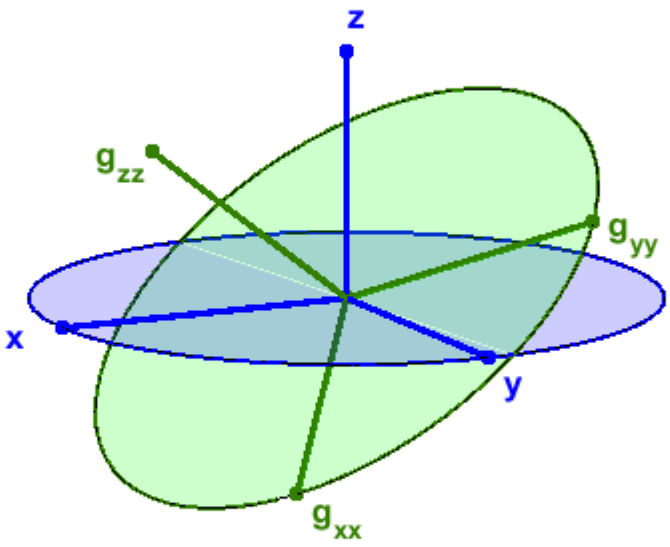

Figure 85: The tensor frame (dark green) and the crystal frame (blue) of erbium doped lithium yttrium borate. The Euler angles from Table 13 transform the crystal frame into the tensor frame. Here, x, y and z denote the unitary axes of the crystal frame, whereas g_{xx}, g_{yy} and g_{zz} represent the unitary axes of the tensor frame.

about 45° in the rotation about the <011> axis (B∼110 mT, see Figure 49 Chapter 4 Measurements).

Erbium doped lithium yttrium borate was also investigated at different temperatures. It has been shown that the resonance peaks broaden when increasing the temperature (see Figure 52 Chapter 4 Measurements). The two main peaks (at B ∼ 93.6 mT and B ∼ 106.6 mT) due to erbium

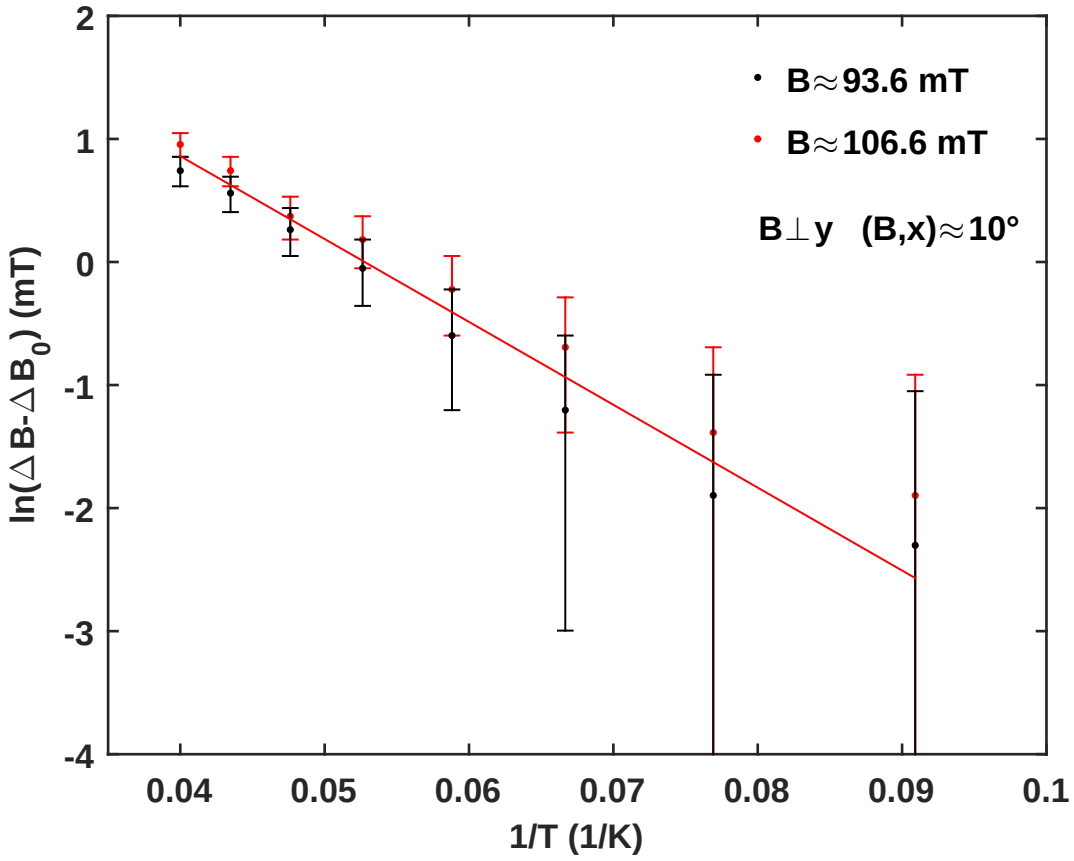

Figure 86: Temperature dependence of the resonance peaks linewidths of erbium doped lithium yttrium borate, when the magnetic field was approximately perpendicular to the y axis and forming an angle of 10° with the x axis. At this selected direction of the magnetic field, the two considered centre families were found approximately at 93.6 mT and 106.6 mT. The red line corresponds to the average slope.

with I=0 were analysed. Therefore, the linewidth of the resonance peaks and the measured temperature were considered and, applying the equation 29 of Appendix F, a linear behaviour was obtained (see Figure 86).

The EPR spectra show a fast temperature broadening and could not be observed above 25 K (see Figure 52 in Chapter 4 Measurements). In addition, the peak to peak linewidth showed an Arrhenius type temperature dependence (for more details, see Appendix F). This indicates an Orbach-type spin-lattice relaxation process by means of two phonons with the observed activation energy $\Delta E_a = (43 \pm 10)$ cm^{-1} and a coupling constant C=(26±8) mT. As a reminder, the activation energy is the energy needed to promote the ion from the ground state to the first excited state. The coupling constant is a pre-exponential factor independent from the activation energy. These parameters show only a weak orientation dependence within the error limits (see the slightly different linewidths shown for the two centre families in Figure 86), which can also be attributed to the slightly different magnetic fields. The activation energy determined from the EPR linewidth data is in good agreement with the energy of the first excited Stark sublevel derived from optical data [50], providing that spin-lattice relaxation takes place via thermal excitation to this level.

5.2.2 Ytterbium doped lithium yttrium borate

In the last section, erbium doped lithium yttrium borate was introduced. It has been shown that different erbium isotopes were observed in the EPR spectra. In this subsection, ytterbium doped lithium yttrium borate is presented and, similarly to erbium, several ytterbium isotopes are detected in the EPR spectra (see Figure 87). In addition, due to the C_{2h} symmetry, two different ytterbium centres are observed.

Ytterbium (Yb) has several isotopes in the nature with different natural abundance (in percent): ^{168}Yb (0.13%), ^{170}Yb (3.04%), ^{171}Yb (14.28%), ^{172}Yb (21.83%), ^{173}Yb (16.13%), ^{174}Yb (31.83%) and ^{176}Yb (12.76%). The isotopes with nuclear spin distinct of zero are ^{171}Yb and ^{173}Yb (I=1/2 and I=5/2 respectively). Therefore, the most intense peak is due to the isotopes with zero nuclear spin, the two resonance peaks with the same intensity correspond to ^{171}Yb and six resonance peaks with weaker intensity are consistent with ^{173}Yb. In addition, the peak intensity is related with the natural abundance of the isotopes. Accordingly to this fact, the resonance peak of zero nuclear spin is more intense that the isotopes ^{171}Yb and ^{173}Yb.

Applying the fitting program to the experimental results, the spin Hamiltonian parameters (Equation 12 Chapter 3 Methods) were calculated (see Table 14).

Comparing the calculated spin Hamiltonian parameters with the experimental measured data, a good matching can be observed, as shown in Figure 88. Similarly to erbium doped sample, two magnetically non-equivalent centres are found in erbium doped lithium yttrium borate (see Figure 88). Both centres have the same spin Hamiltonian parameters. However, they differ by a rotation

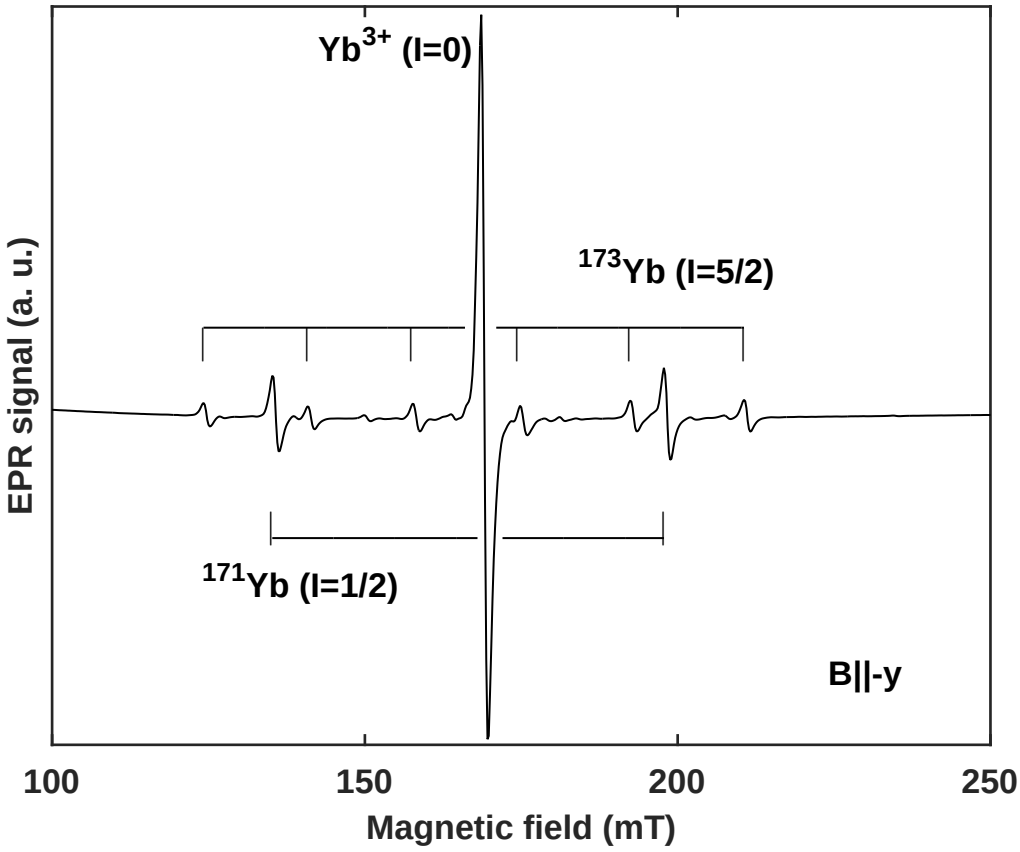

Figure 87: EPR spectrum of ytterbium doped nearly stoichiometric lithium yttrium borate (**91202**) when the magnetic field was approximately parallel to the y axis. The most intense resonance peak is due to ytterbium isotopes with nuclear spin zero (I=0) (see text). Two less intense resonance peaks are caused by ^{171}Yb isotope with nuclear spin I=1/2. Six weak resonance peaks are produced by ^{173}Yb isotope with nuclear spin I=5/2. ^{171}Yb and ^{173}Yb are marked with a comb to facilitate the visualization.

of 180°. ^{173}Yb resonance lines were not displayed in Figure 88 in order to make the representation as clear as possible, nonetheless the A-tensor was calculated as in the case of ^{171}Yb.

Isotope	g_{xx}	g_{yy}	g_{zz}	α_g (°)	β_g (°)	γ_g (°)
^{168}Yb	2.724 ± 0.05	2.442 ± 0.05	5.036 ± 0.1	62.10 ± 1.2	57.21 ± 1	41.37 ± 3
	A_{xx} (MHz)	A_{yy} (MHz)	A_{zz} (MHz)	α_A (°)	β_A (°)	γ_A (°)
^{171}Yb	2051.1 ± 400	1816.7 ± 300	3868.8 ± 200	62.28 ± 6	56.8 ± 6	32.26 ± 6
^{173}Yb	651.0 ± 130	620 ± 100	1098.9 ± 60	62.28 ± 6	56.8 ± 6	32.26 ± 6

Table 14: Calculated spin Hamiltonian parameters of as grown ytterbium doped nearly stoichiometric lithium yttrium borate (**91202**). The considered isotope is written in the first column. The x component of the diagonal g-tensor is listed in the second column, whereas the y component of the diagonal g-tensor is written in the third column and the z component of the diagonal g-tensor is provided in the fourth column. The Euler angles (α, β, γ) are shown from the fifth to the seventh column. The errors were calculated by a brute-force method.

Hyperfine lines (dashed lines in Figure 88) are not equidistant. This is due to the hyperfine structure tensor (A-tensor). The Euler angles of the A-tensor slightly differ from the Euler angles of the g-tensor since there is no a priori reason why the Euler angles should be the same. This mismatch produces the asymmetric resonance peak disposition. Negative axes in Figure 88 are due to the experimental procedure. The considered sample was unfortunately rotated, therefore negative axes appear.

As in the case of erbium doped LYB, the principal values of the obtained g-tensor values (see Table 14) are approximately observed in the EPR measurements. To facilitate the visualization, Figure 89 shows the tensors frame directions in the crystal frame.

The g_{yy} component is almost lying on the xz plane. Therefore, its projection is observed in the rotations about the y axis at an angle of about 50° (B$\sim$288 mT). In addition, this point corresponds to the highest point (in the magnetic field) obtained in the Figure 88 (solid black line in the second panel). The highest g-tensor component, g_{zz}, is observed at about 30° - 45° in the rotation about

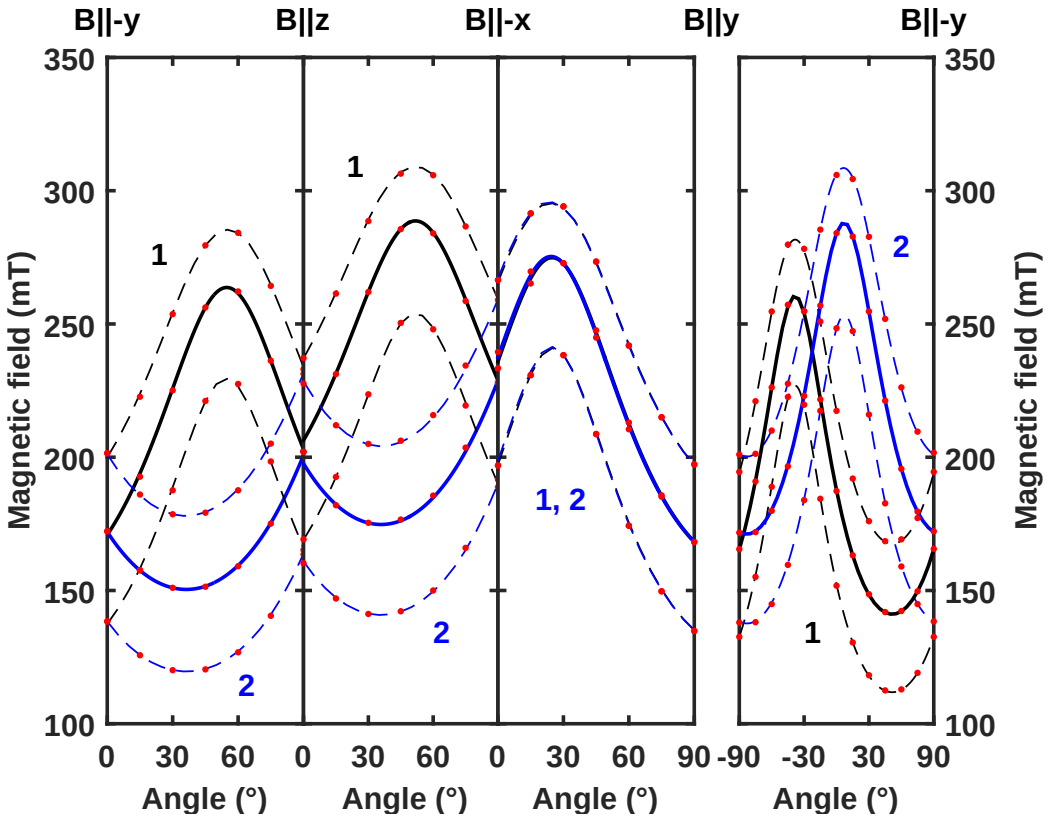

Figure 88: Measured (red dots) and simulated (black and blue lines) angular dependence of the EPR spectra of as grown ytterbium doped nearly stoichiometric lithium yttrium borate (**91202**) for rotations about (from left to right panel) the x axis, y axis, z axis and the $<10-1>$ crystallographic direction. Two magnetically non-equivalent centres are observed (centre 1 in black and centre 2 in blue). Ytterbium isotopes with zero nuclear magnetic field are represented by a continuous line, whereas ^{171}Yb is denoted by a dashed line. ^{173}Yb is not represented for the sake of simplicity. The simulated spectra were calculated using the spin Hamiltonian parameters of Table 14. In the rotation about x, an angle of 0° represents a magnetic field which is approximately parallel to $-y$, whereas an angle of 90° denotes a magnetic field which is approximately parallel to z. In the rotation about y, an angle of 0° shows that the magnetic field is approximately parallel to z, whereas an angle of 90° denotes a magnetic field which is approximately parallel to $-x$. In the rotation about z, an angle of 0° shows that the magnetic field is approximately parallel to $-x$, whereas an angle of 90° denotes a magnetic field which is approximately parallel to y. In the rotation about the $<101>$ axis, an angle of -90° represents that the magnetic field is approximately parallel to y, whereas an angle of 90° denotes a magnetic field which is approximately parallel to $-y$. Transition lines do not match exactly between panels due to tilt and offset angles.

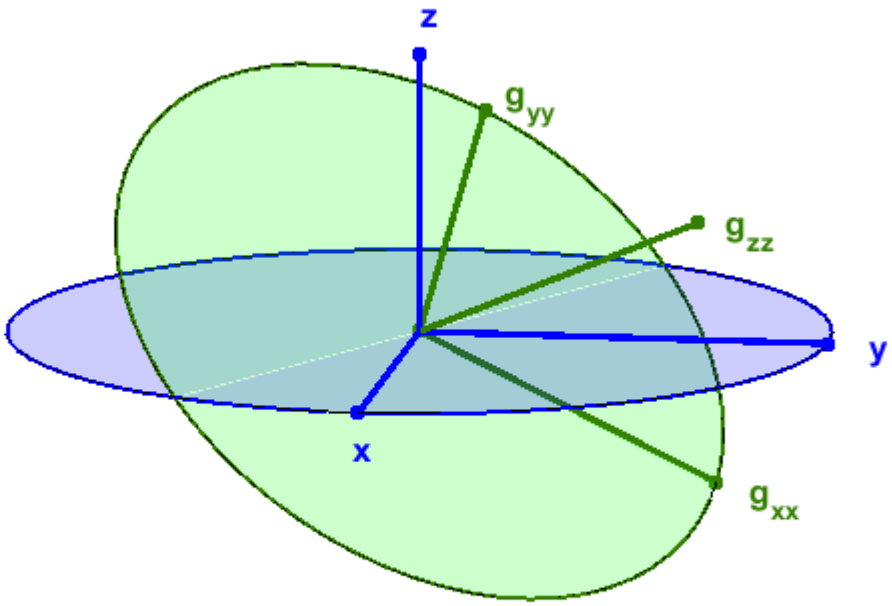

Figure 89: The tensor frame (dark green) and the crystal frame (blue) of ytterbium doped lithium yttrium borate. The Euler angles as indicated in Table 14 transform the crystal frame into the tensor Frame. Here, x, y and z denote the unitary axes of the crystal frame, whereas g_{xx}, g_{yy} and g_{zz} represent the unitary axes of the tensor frame.

the $<10-1>$ crystallographic axis (B$\sim$140 mT). Therefore, the lowest point in the magnetic field observed in the fourth panel of Figure 88 corresponds to the largest g-tensor component. The smallest g-tensor component g_{xx} is observed at about 95° - 100° in the rotation about the $<0-1-1>$ crystallographic axis (B$\sim$256 mT, see Figure 56, Chapter 4 Measurements).

Similarly to erbium, the resonance peaks of ytterbium doped lithium yttrium borate broaden with increasing temperature (see Figure 59, Chapter 4 Measurements). The two main peaks (at B$\sim$157.6 mT and B$\sim$181.6 mT) due to the two ytterbium centres with I=0 were analysed. Thereby, the linewidth of the resonance peaks and the measurement temperature were considered (see Figure 90).

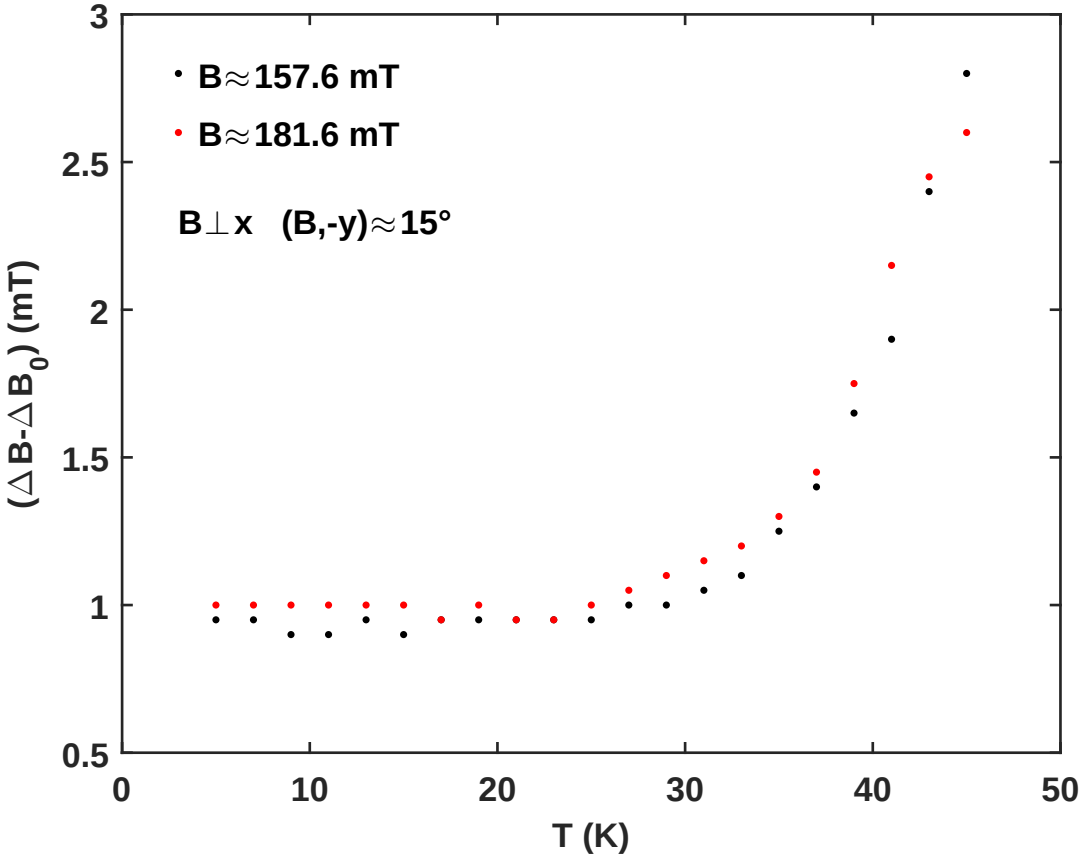

Figure 90: Temperature dependence of the resonance peaks linewidths of ytterbium doped lithium yttrium borate, when the magnetic field was approximately perpendicular to the x axis and forming an angle of 15° with the $-y$ axis. At this selected direction of the magnetic field, the two considered ytterbium centre families were found approximately at B∼157.6 mT and B∼181.6 mT.

A broadening of the EPR lines was observed with increasing temperature until 45 K, where the lines disappeared. Analysis showed that an Orbach-type exp(−ΔE/kT) exponential dependence with an activation energy in the range ΔE =(150 ± 80)cm$_{-1}$ could be used for fitting the data, however, the first excited Stark sublevel of the $^2F_{7/2}$ ground state was found at 369 cm$_{-1}$ [80]. Therefore, the dominant spin-lattice relaxation mechanism may be related to some more efficient processes, in which more than two phonons are considered.

5.2.3 Iron doped lithium yttrium borate

In the last sections, erbium and ytterbium doped lithium yttrium borate were examined. In this section, iron doped lithium yttrium borate is introduced. Iron is a transition metal ion, consequently the g-tensor is supposed to be isotropic, close to 2 and with a large fine structure splitting term.

In Chapter 4 Measurements, the EPR measurements were exposed (Figures 60 to 64) and four resonance peaks were observed. However, one would expect to observe at least six resonance peaks because of the high spin (S$=5/2$) of iron. The difficulty remains not only in the ordering of the resonance peaks with the EPR transition, but also in the guessing of good starting parameters. To obtain the spin Hamiltonian parameters, the fitting program was utilized. Nevertheless, a satisfactory fit of the experimental data could not be achieved at the time of writing. Further studies are required in this case. Iron doped lithium yttrium borate must be investigated deeply in order to obtain accurate spin Hamiltonian parameters.

6 Discussion

Lithium niobate single doped with iron and titanium and co-doped with both dopants has been investigated in this thesis. Parallel to this well-known ferroelectric, lithium yttrium borate doped with erbium, ytterbium and iron was also studied. In this chapter, the experimental results are summarized and discussed. As a reminder, the reader is kindly advised to review Chapter 4 Measurements and Chapter 5 Results, where the experimental measurements and results, respectively, are exposed. Following the structure of the last chapters, the discussion of the results is divided into two sections, each dedicated to one of the studied materials. In the first section, lithium niobate is discussed, whereas lithium yttrium borate is examined in the second section. Once more, the dopant ions are presented step by step. On the one hand, single doping of iron and titanium and co-doping of iron-titanium are discussed in this order. Furthermore, results from EPR and PL measurements are examined. On the other hand, the lithium yttrium borate section starts with erbium doping, followed by ytterbium doping and finally iron doping.

In this chapter, published results from the literature are collected and compared with the experimental results obtained in this thesis (see Chapter 5 Results). In addition, theoretical calculations aimed to help in the interpretation of the experimental data were developed at the Justus-Liebig-Universität in Giessen in the group of Professor S. Sanna.

6.1 Lithium niobate

In this section, the attention is focused on lithium niobate samples. First iron single doped lithium niobate is discussed, followed by titanium single doped lithium niobate and, finally, iron-titanium co-doped lithium niobate.

6.1.1 Iron doped lithium niobate

For more than half a century, lithium niobate has been investigated due to its very attractive combination of piezoelectric and optical properties [14]. Furthermore, many of its uses have been triggered by the presence of iron, as for example, holographic data storage due to promising high storage densities with short access times [27]. Several methods have been applied to give insight into the local site of incorporation, including magnetic resonance techniques, Mössbauer spectroscopy and extended x-ray absorption fine structure (EXAFS). Owing to electron nuclear double resonance (ENDOR) in combination with EPR experiments, good evidence of Fe^{3+} incorporated at the Li place has been provided [19]. Nonetheless, other EPR experiments have been interpreted as providing evidence for Fe incorporation at the Nb-site incorporation. In addition, the reported spin Hamiltonian parameters are not consistent.

$g_\perp$	$g_\parallel$	B_2^0 (MHz)	B_4^3 (MHz)	B_4^0 (MHz)	B_4^{-3} (MHz)	Site	Method	Ref.
1.995	1.995	1659	-	47	-	?	EPR (X)	[24]
1.99	1.99	1668	28	2.4	-	Li, Nb	EPR (X)	[25]
2.0024	2.0024	1658	-	-14	-	Li, Nb	EPR(X,Q)	[34]
1.983	2.019	1769	33	-2.5	-19	Li (Nb)*		[21]
1.984	1.992	1636	101	-2.7	4	Nb	SPM**	[23]
1.996	2.004	1644	59	-2.6	-14	Li, Nb	EPR	[27]
2.02	2.02	1680	50	-2.5	20	Li	EPR, ENDOR	[19]

Table 15: Spin Hamiltonian parameters of iron doped lithium niobate available from the literature. The perpendicular g-tensor component is listed in the first column, whereas the parallel g-tensor component is written in the second column. The second order Stevens operator coefficient is given in the third column. The fourth order Stevens operator coefficients are indicated from the fourth to the sixth columns. The supposed lattice site of iron ions in LN is written in the seventh column. The investigation method is provided in the eighth column. The last column indicates the reference in which the data were published (Ref.). * Lithium niobate was co-doped with iron and potassium. After reduction, iron ions were found in Li place and, moreover, iron-potassium complexes were built. **SPM: superposition model

Table 15 shows a selection of spin Hamiltonian parameters of iron doped lithium niobate previously reported in the literature.

It must be pointed out that not all publications about iron doped lithium niobate were listed in Table 15. Nevertheless, there is unfortunately a lack of unanimity, as it is shown in Table 15. Comparing the reported g-tensors of iron doped lithium niobate, not only isotropic [19, 24, 25, 34] but also axial g-tensor [21, 23, 27] are reported. Furthermore, a complete set of Stevens operator coefficients is not considered by a few authors [24, 25, 34]. In addition, some "scaling" factors f_k at the Stevens operator coefficients ($B_k^q = f_k b_k^q$) are missing [60]. Finally, the iron lattice site in lithium niobate is also a theme of discussion. Some studies show evidence of iron ions incorporated at the Li site, however, other investigations provide evidence of Nb substitution.

In November 2016 the structural analysis of iron centres in $LiNbO_3$ using EPR and ENDOR methods came to light [19]. Here, iron centres were described with an isotropic g-tensor and a complete set of Stevens operators was reported. It was found that iron substitutes lithium fairly well (seventh row in Table 15). Probably the reader has already remembered the spin Hamiltonian equation of iron doped lithium niobate used in this thesis (Equation 9 in Chapter 3 Methods). First, we also assume that iron ions have an isotropic g-tensor close to the free-spin value because in moderate crystal fields (as in the case of lithium niobate) the ground state is still essentially an orbital singlet. Second, due to the presence of five unpaired electrons a complete set of high order operators in the zero-field splitting term is required (i.e. Stevens operators). Finally, the crystal structure of the studied material determines the considered Stevens operators (B_2^0, B_4^3, B_4^0 and B_4^{-3}). Owing to these similarities with Grachev's et al. work, its spin Hamiltonian parameters (seventh row in Table 15) were used as starting parameters in the fitting program for the samples investigated in this thesis.

As the reader can see, comparing the experimental results of iron single doped nearly stoichiometric lithium niobate (**21616** Table 5 in Chapter 5 Results), the spin Hamiltonian parameters differ somewhat from the reference values [19]. Probably the growing conditions of the samples were different, however the studied system, i.e. Fe^{3+} centres in $LiNbO_3$, is nearly the same. We want to remark that the employed calculation program, EasySpin, stands out due to its computational accuracy. Simulations use various natural constants, which have non-zero uncertainty. Amongst all the fundamental constants involved, the Planck constant has the largest uncertainty, estimated in 10^{-7}. Because of this limiting uncertainty of the Planck constant, spectral line positions cannot be determined with more than 7 significant digits. Therefore, computed resonance peaks and simulated spectra are characterized by this degree of accurancy, if all computational algorithms

involved have numerical and modelling errors below 10^{-7} [57]. In addition, tilt and offset angles can be calculated and accounted for within our approach, whereas this option is not allowed in other fitting programs (as for example in the EPR-NMR program developed by Grachev). Therefore, the spin Hamiltonian provided in this thesis is in principle more accurate than the data provided in earlier publications, clarifying the microscopic and electronic structure of iron doped lithium niobate.

In Chapter 5 Results, the spin Hamiltonian parameters were calculated and used to explain the microscopic and electronic structures of iron single doped lithium niobate crystals. Similar roadmaps were found in nearly stoichiometric and congruent host samples. Therefore, iron centres behave similarly in both crystals. The g-tensor is close to the g-factor of a free electron, because the ground state behaves as a singlet. The second order fine structure splitting term (B_2^0) is not a small perturbation (of about 1.7 GHz) compared with the applied frequency (of about 9.8 GHz). Consequently, the EPR spectra interpretation is hindered by the presence of forbidden transitions. Furthermore, a complete set of high-order Stevens operators must be considered (B_4^3, B_4^0 and B_4^{-3}). Figure 69 and 70 in Chapter 5 Results show the good matching between the experimental measurements and the extrapolated spin Hamiltonian. In both calculations, the simulation error was comparable or lower than the experimental error. In addition, the errors of each involved parameter were calculated using the brute-force method. In such a way, a unique and accurate spin Hamiltonian is assured.

The environment of iron centres in lithium niobate is described by the spin Hamiltonian. Two electrically equivalent iron centres with C_3 symmetry (R and L) are present in lithium niobate. Both centres have the same absolute g-tensor and fine structure terms (B_k^q). However, due to the glide mirror plane in the $LiNbO_3$ lattice, the iron centres are magnetically non-equivalent: the centre R can be transformed into the centre L, replacing x to $-x$. That means: B_4^3 (R)$\rightarrow -B_4^3$ (L). The presence of these two non-equivalent centres leads to the observed splitting of Fe^{3+} transition lines rotating the sample about the y axis (Figure 69 and 70 in Chapter 5 Results, and for more details see Figure 72). Iron centres in lithium niobate are supposed to substitute lithium and/or niobium in lithium niobate (see Table 15). Experimental techniques as for example ENDOR (electron nuclear double resonance) spectroscopy provided evidences that iron substitutes lithium ions. In this configuration, the six oxygen atoms around the lithium atom form an octahedron which is slightly larger than the oxygen octahedron around the niobium atom. On the one hand, ionic lithium is smaller than ionic niobium and, on the other hand, the covalent bond between niobium and oxygen is stronger than the one between lithium and oxygen atoms.

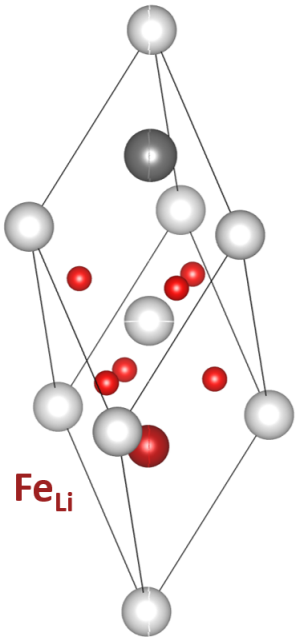

Figure 91: Unit cell of lithium niobate when an iron atom (in dark red) substitutes a lithium ion. The crystal structure is shown with oxygen atoms in red, lithium atoms in light grey and niobium in dark grey circles.

Furthermore, lithium niobate is known to be lithium deficient, i.e. lithium vacancies are present. The experimental spin Hamiltonian obtained in this thesis is very similar to the ones investigated with ENDOR spectroscopy [19, 20]. Therefore, it is assumed that iron substitutes lithium in LN (see Figure 91).

In 1960 Ludwig and Woodbury developed a model for the electronic structure of transition metal ions in silicon. This model gives an interpretation of the d-wavefunction of the electron spin of transition metals at different lattice sites in silicon, namely substitutional and interstitial sites. The model of Ludwig and Woodbury allows for a qualitative understanding of the electronic properties of single transition metal point defects in silicon from EPR data [81]. In addition, a microscopic justification was carried out by Gary et al. [82] and Beeler et al. [83], in which the calculated electronic structure of the neutral transition metal ions was calculated (see Figure 92).

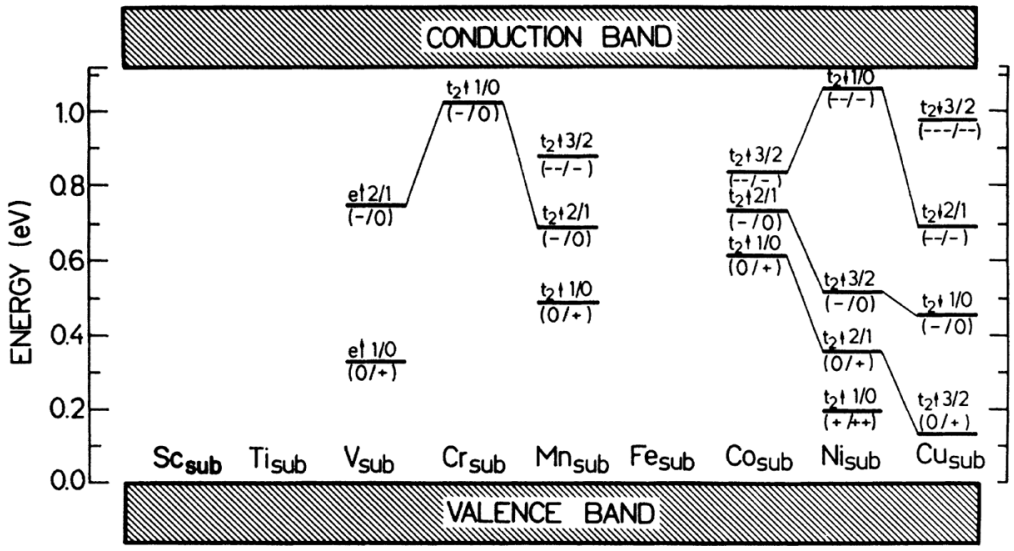

Figure 92: Donor and acceptor energy levels for substitutional 3d transition metal impurities in silicon resulting from spin-unrestricted calculation. For each level the related single-particle state and its occupation before and after the ionization is indicated.

The electronic structures of the substitutional and interstitial transition metal ions were calculated in silicon. Silicon has a tetrahedral symmetry and, moreover, silicon atoms are bounded covalently. Owing to this model, EPR spectra of transition metal ions can be interpreted in silicon. That is, the model is valid if the transition metal ion is covalently bound with the surrounding atoms or is placed in an interstitial site. In addition, this model assumes that the ground state has low spin configuration. This model represents one of the first DFT calculations that help in the interpretation of neutral transition metal ions in silicon. A similar approach was employed in this work for the investigation of iron doped lithium niobate. DFT calculations were carried out considering iron at the lithium place with the 3+ and 2+ valence states.

As a reminder, iron substitutes lithium in LN (see Figure 91). In addition, the d-orbitals of iron ion split in two degenerated and one non-degenerated energy states due to the octahedral symmetry with a trigonal distortion of the host material (see Figure 14 in Chapter 3 Methods). However, not only Fe^{3+} but also Fe^{2+} are incorporated in LN. Trivalent iron (Fe^{3+}) is described by an electronic configuration of [Ar] $3d^5$ $4s^0$, whereas divalent iron (Fe^{2+}) possesses one electron more ([Ar] $3d^6$ $4s^0$). Through DFT calculation carried out by S. Sanna, the energy levels of each configuration in LN can be calculated for a cell of eighty atoms (see Figure 93). For calculation details see Chapter 3 Methods.

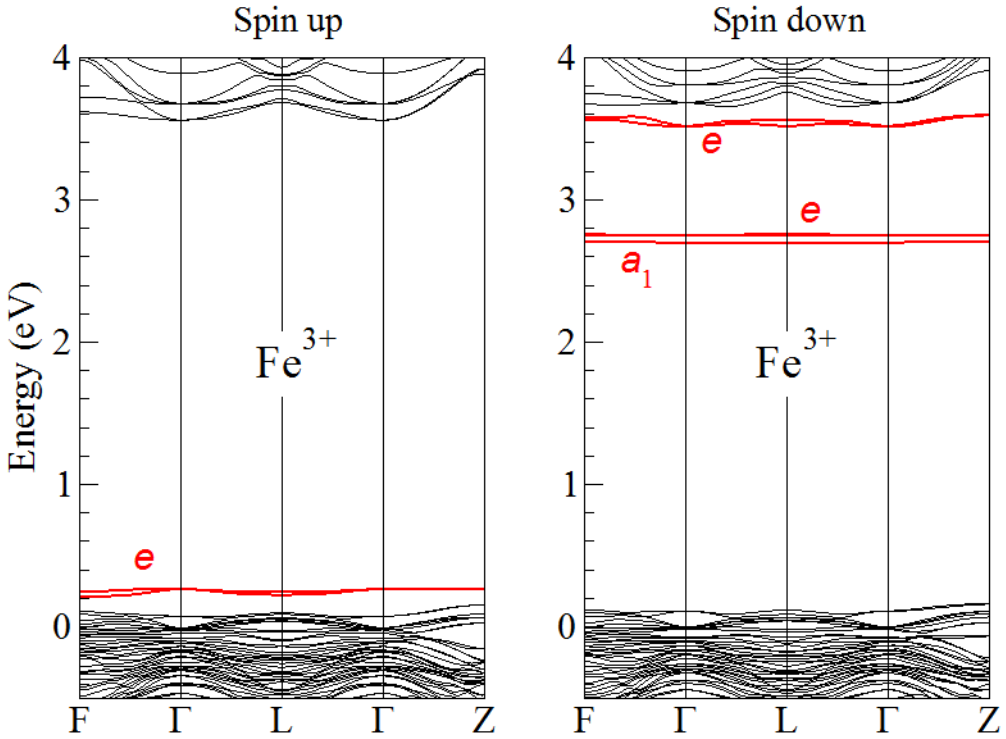

Figure 93: Calculated energy levels of trivalent iron (Fe^{3+}) substituting Li in lithium niobate. On the left side panel, the energy levels of the spin up channel are shown, whereas on the right side panel the energy levels of the spin down channel are presented. The calculations and figures were provided by S. Sanna.

Trivalent iron substitutes lithium in LN and the corresponding energy levels were calculated by means of DFT. Iron related electronic levels for the spin up channel are lower in energy than electronic levels for the spin down channel (see Figure 93). On the one hand, the highest energy level of the Fe electrons with spin up is just above the valence band, whereas the other energy levels (with e and a symmetry) are within the valence band. Considering the spin down channel, all the Fe related energy levels are localized within the band gap.

Similarly to the last energy levels diagram for trivalent Fe, divalent iron (Fe^{2+}) can be considered.

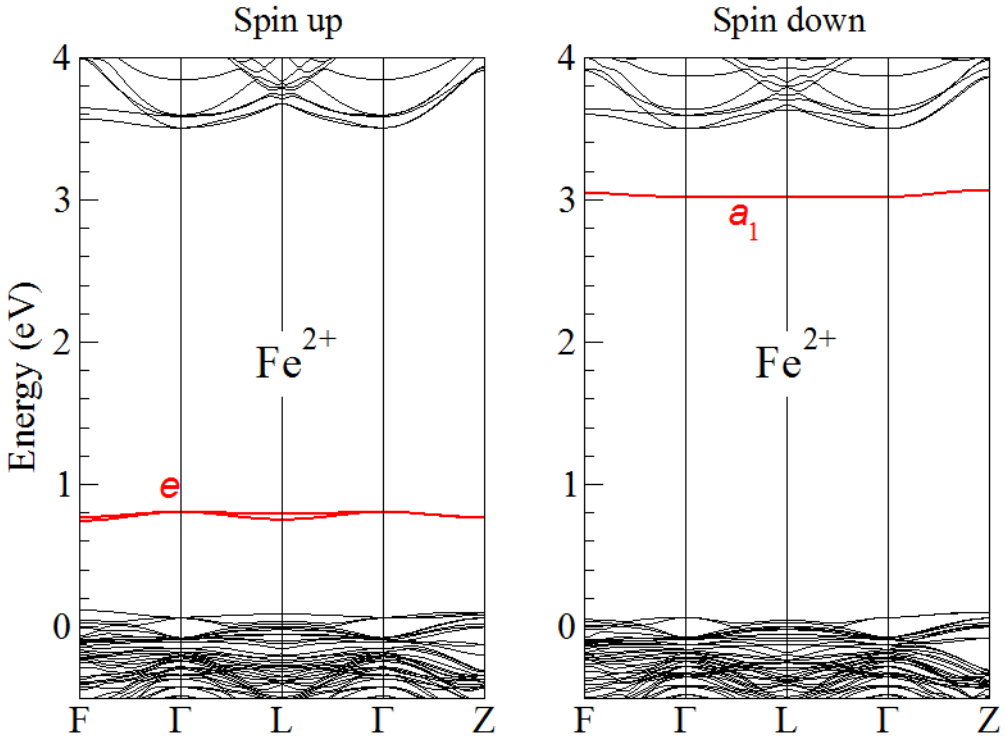

Figure 94: Calculated energy levels of divalent iron (Fe^{2+}) substituting Li in lithium niobate. On the left side panel, the energy levels for the spin up channel are shown, whereas on the right side panel the energy levels for the spin down channel are presented. The calculations and figures were provided by S. Sanna.

Divalent iron is also supposed to substitute lithium in LN and the energy levels are different than in the case of trivalent iron (Fe^{3+}). Analogously to the Fe^{3+}, electrons with spin up are characterized by a lower energy than electrons with spin down (see Figure 94). The highest energy level considering the spins up channel is just above the valence band, whereas the remaining energy levels (of e and a symmetry) are in the valence band. In the case of spin down channel, the lowest energy level is found in the band gap, however, the other two energy levels (of e and a symmetry) are in the conduction band.

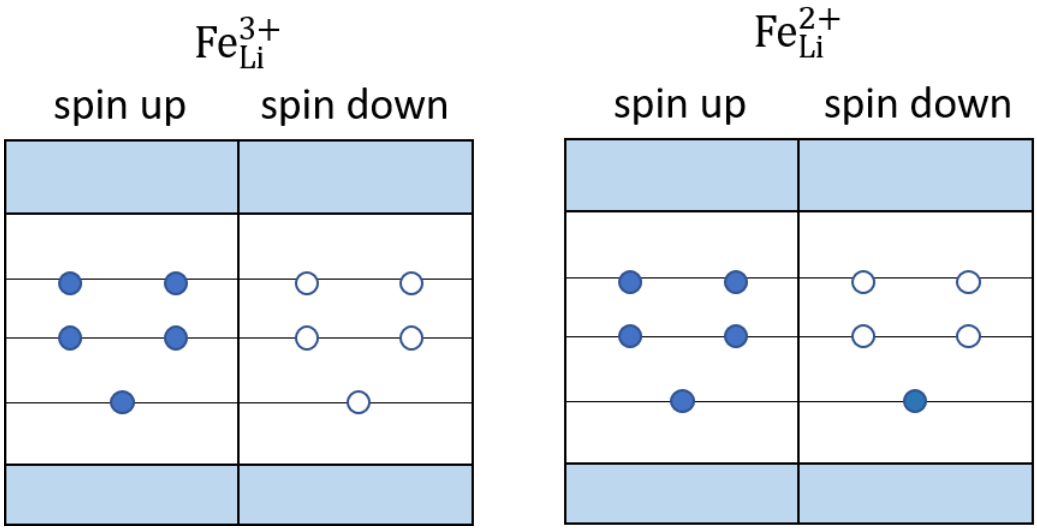

Figure 95: Schematic energy state diagram of isolated Fe^{3+} (left hand side) and Fe^{2+} (right hand side) substituting Li in lithium niobate. The blue rectangles represent the conduction (top blue rectangles) and the valence (bottom blue rectangles) bands. The band gap is shown in white. Schematically, the energy levels of Fe^{3+} and Fe^{2+} are represented as horizontal lines in the band gap. Energy levels are filled with electrons represented as blue circles. Empty energy levels are represented with a lack of electrons (with white circles). The figures were provided by S. Sanna.

Comparing Fe^{3+} with Fe^{2+}, the difference in energy for electrons with spins up is due to the Coulomb repulsion. Fe^{2+} has one electron more than Fe^{3+}, which leads to a repulsion between the electrons and therefore an increase in the energy of the electronic levels.

Once that the energy levels for electrons with spin up and down in the case of Fe^{3+} and Fe^{2+} in lithium place are known, the spin configuration of the Fe defects centres can be determined. Figure 95 shows the filling of the energy levels for Fe^{3+} and Fe^{2+} in LN, in a schematic form.

Electrons fill the energy levels from lower to higher energy (in analogy to Ludwig and Woodbury interpretation). On the one hand, energy levels of electrons with spin up for Fe^{3+} ions at the lithium place are energetically more favourable than energy levels of electrons with spin down. Consequently, five electrons with spin up are expected to fill the energy levels in Fe^{3+} in Li place. This kind of configuration is known as high spin (S=5/2) and it was observed in the EPR spectra. On the other hand, the additional electron of the Fe^{2+} centre cannot be hosted in the spin up half-shell and occupies therefore the lowest energy level of the with spin down channel. Therefore,

five electrons with spin up and one electron with spin down are expected to be found in Fe^{2+} substituting Li in LN. The net magnetization is thus $\Delta m=5$ for Fe^{3+} and $\Delta m=4$ for the Fe^{2+} centre.

As a reminder, also the high spin configuration for iron in lithium niobate was observed in the EPR measurements. In this case, iron substitutes Li^{+} site and, therefore, one electron of iron is required in the bounding with the surrounding atoms. The other four Fe valence electrons (or five in case of Fe^{2+}) are free electrons that can move in the host material. Charge compensation has to be obtained by lithium vacancies located rather far from the iron ion (see Chapter 2 Materials and [19].

The EPR spectra of iron doped lithium niobate were presented in Chapter 4 Measurements and only Fe^{3+} could be detected. As it can be seen in Figure 93, the filled energy levels of the spin up channel of Fe^{3+} at the lithium place are placed in the valence band and on the bottom of the band gap. Applying a magnetic field, the energy levels split into six energy levels ($S=5/2$) due to the Zeeman interaction. The splitting encompasses a range of about 200 GHz (see Figures 73 and 74 of the Chapter 5 Results), i.e. 0.0008 eV where the EPR absorption (9.9 GHz about 0.00004 eV) takes place from one energy state to the other. In the case of Fe^{3+}, where the energy levels are in the valence band and in the band gap, the EPR condition is fulfilled and spectra are recorded in Chapter 4 Measurements. However, in the case of Fe^{2+} where the fine structure term is huge, a very large frequency (of about 100-200 GHz) is needed to obtain an EPR absorption (see Figure 94). In addition, iron doped lithium niobate was reduced to partially transform Fe^{3+} in Fe^{2+}, nevertheless, no EPR resonance peaks due to Fe^{2+} were recorded. Furthermore, a thermal stimulation was also unsatisfactory. Increasing the temperature, the position of the Fermi level can be raised, facilitating the excitation of Fe^{2+} ions. However, no characteristics of Fe^{2+} were found.

For this reason, other spectroscopic techniques were employed. Indeed, not only EPR spectra but also photoluminescence spectra were measured and presented in Chapter 4 Measurements. A broad peak around 2.6 eV (see Figure 42 in Chapter 4 Measurements) was observed due to the electron transfer from Fe^{2+} to the conduction band. Upon illumination, the electron with spin up of Fe^{2+} ion is promoted to the conduction band. Owing to drift, diffusion and bulk photovoltaic effect, and it migrates until it is captured by Fe^{3+} centre. In addition, the electron transfer between Fe^{2+} and Fe^{3+} is responsible for the photorefractive effect. The observed broad peak at 2.6 eV in the visible range agrees with [66], [67] and [84]. Furthermore, after annealing treatment, the absorption coefficient increases at 3 eV and 1.9 eV. This is explained by the occurrence of polarons and bipolarons in the reduced sample [85]. The formation of polarons and bipolarons

was also observed in EPR measurements by means of resonance peak broadening.

As a summary, in contrast to the literature where a single unique sample was investigated (Table 15), in this thesis iron doped lithium niobate was investigated both in nearly stoichiometric and in congruent lithium niobate samples. In both cases, Fe^{3+} was supposed to sit at the lithium site with a g-tensor near to the free electron g-factor and a large fine structure term, which was calculated by means of a computational accurate program, EasySpin (see Table 5 in Chapter 5 Results). The g-tensor is isotropic because the ground state behaves as a singlet and the fine structure term needs to be described by a complete set of high order operators (see Steven's operators in Appendix C). Allowed and forbidden transitions were identified and classified (see Figure 71 in Chapter 5 Results). Finally, two electrically equivalent Fe^{3+} centres were found in lithium niobate; however, they are magnetically non-equivalent. The difference lies in the sign of the coefficient B_4^3, remaining the rest of the spin Hamiltonian parameters identical (see Figure 72 in Chapter 5 Results). After annealing, the microscopic and electronic structure of iron seems to remain unchanged, since the spin Hamiltonian parameters match with the as grown and annealed samples. On the other hand, the characteristic absorption D-band of iron doped lithium niobate was observed at 2.6 eV. This band represents the excitation of an electron from the Fe^{2+} energy level to the conduction band. After the annealing process, polarons and bipolarons are present and observed at 3 eV and 1.9 eV (see Figure 42 in Chapter Measurements). As a reminder, wider resonance peaks were observed in the EPR spectra after the annealing procedure due to the increase of the number of defects, such as polarons and bipolarons. Unfortunately, Fe^{2+} ions were not observed by EPR, although thermal stimulation was carried out.

In addition, iron seems to behave as a small bound polaron in lithium niobate [35]. The charge density probability is completely localized around the Fe ion, as expected for a small bound polaron (see Figure 96).

The electron which is captured to form the small bound polaron is represented in the Figure 96 as the electronic charge associated with the occupied spin down a^1 state in Fe_{Li}^{2+}. The electronic charge remains close to the Fe ion and resembles the atomic Fe dz^2 orbitals, suggesting a scarce hybridisation. This setting is consistent with the experimental results exposed in this thesis.

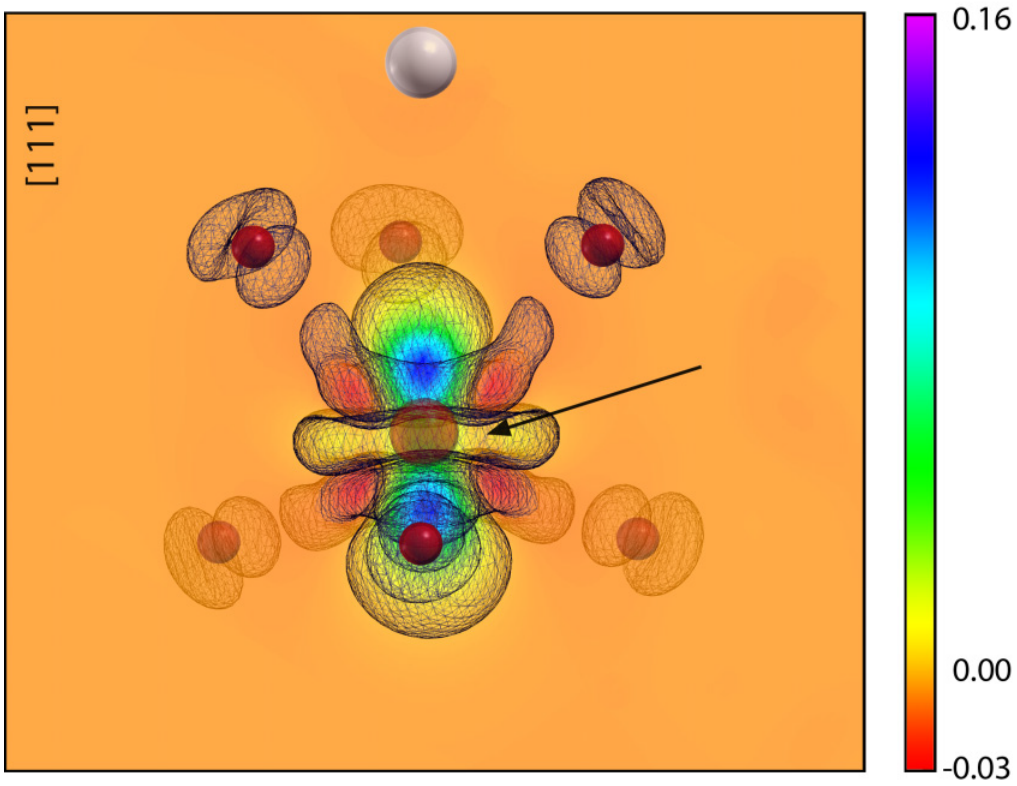

Figure 96: Electronic charge difference Fe^{2+}_{Li}-Fe^{3+}_{Li}. The electron is completely localized around the Fe ion in the transition Fe^{2+}/Fe^{3+} as it is expected from a small bound polaron. The electron charge distribution resembles the atomic dz^2 orbital of Fe.

6.1.2 Titanium doped lithium niobate

A standard dopant used for waveguide production in $LiNbO_3$ is titanium. It is incorporated as Ti^{4+}, a non-paramagnetic ion. However, after reduction it becomes paramagnetic (Ti^{3+}). In lithium niobate, Ti^{3+} was found not only at the lithium [44] but also at the niobium lattice site [46]. The EPR parameters available in the literature parameters are summarized in Table 16.

$g_\perp$	$g_\parallel$	Site	Ref.
1.84	1.96	Li	[44]
1.860	1.857	Nb*	[46]

Table 16: Spin Hamiltonian parameters of titanium doped lithium niobate as published in the literature. The perpendicular g-tensor component is listed in the first column, whereas the parallel g-tensor component is written in the second column. The proposed lattice site of titanium ions in LN is written in the third column. The last column indicates the reference where the data were published (Ref.). * $LiNbO_3$ was doped with 8 mol % Mg and 0.05 mol % Ti.

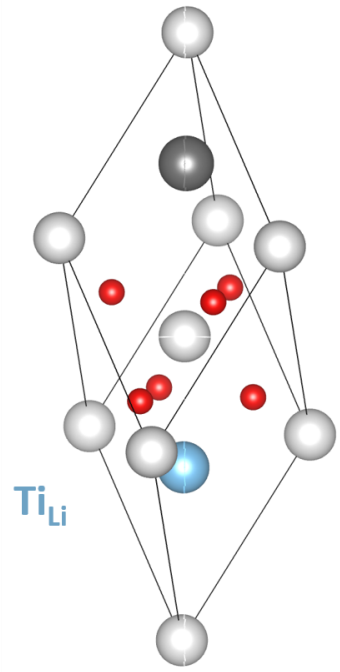

Figure 97: Unit cell of lithium niobate when titanium (in blue) substitutes lithium place. The crystal structure is shown with oxygen atoms in red, lithium atoms in light grey and niobium in dark grey circles.

Comparing the obtained experimental results (Table 7 in Chapter 5 Results) with the already published data (see Table 16), it seems that titanium substitutes lithium site in lithium niobate (see Figure 97). Furthermore, the obtained experimental results match rather well with Juppe's spin Hamiltonian parameters and even reach a more accurate value (down to the hundredths). According to our and previous data, it seems that titanium ions occupy the lithium place in otherwise undoped LN. In the case of lithium niobate co-doped with magnesium and titanium, magnesium ions are introduced at the lithium place and when all of them are occupied, magnesium and titanium ions are incorporated at niobium place. This can be explained by the fact that the ionic radius of magnesium is smaller than the one of titanium.

The interpretation of the axial g-tensor of Ti^{3+} in LN is not a straightforward task. Titanium is a transition metal with d-orbitals, and the crystal structure of the host material must also be considered. The axial g tensor is characterized by $g_{\parallel} > g_{\perp}$, with z along the trigonal axis of $LiNbO_3$. Therefore, the ground state symmetry should be $3z^2$-r^2 for lower spin-orbit admixtures as it was pointed out by Juppe et al. [44].

On the one hand, titanium enters as Ti^{4+} in lithium niobate with an electronic configuration [Ar] $3d^0$ $4s^0$. On the other hand, after annealing treatment trivalent titanium (Ti^{3+}) is described by the electronic configuration of [Ar] $3d^1$ $4s^0$ (for more details see Chapter 3 Methods). Owing to DFT calculation performed by S. Sanna, the energy levels of each configuration in LN can be calculated (see Figure 98).

The tetravalent titanium ion substitutes lithium in LN and the electronic energy levels were calculated by means of DFT. Schematically, both the spin up and the spin down channels have the very same energy levels (see Figure 98, next to the conduction band) as no unpaired electrons are present. After annealing treatment, Ti^{4+} captures an electron and the calculated energy levels of the trivalent titanium (Ti^{3+}) are shown in Figure 99.

In contrast to Ti^{4+}, where the energy levels of both spins up and down channels are similar, in Ti^{3+} they are different. The lowest energy level for electrons with spins up is occupied by one electron and shifts downwards in the band gap, while all other Ti related levels are empty and within the conduction band. However, in the case of the spin down channel all the Ti related energy levels are in the conduction band (therefore, none of them is visible in Figure 99).

With the knowledge of the occupation of the energy levels of Ti^{4+} and Ti^{3+}, the spin configuration of Ti defect centres can be determined. It is represented in Figure 100.

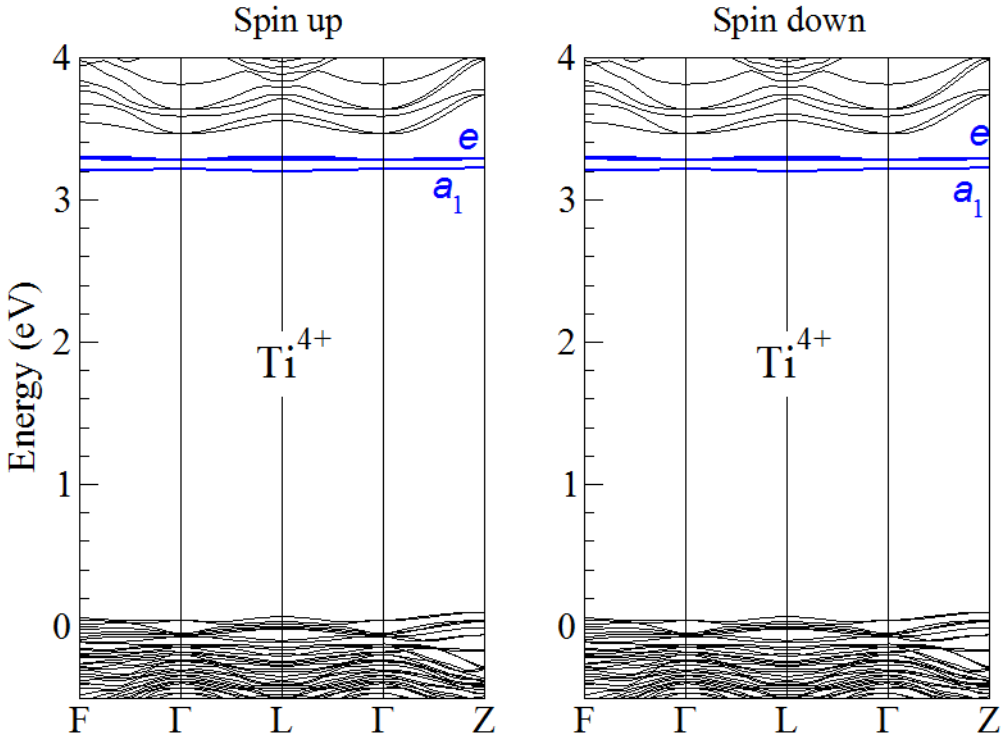

Figure 98: Schematic energy levels of tetravalent (Ti^{4+}) substituting Li in lithium niobate. On the left panel, the energy levels with spin up are shown, whereas on the right panel the energy levels with spin down are presented. The calculations and figures were carried out by S. Sanna.

Ti^{4+} ions have the same electronic configuration of argon ([Ar] $3d^0$ $4s^0$), i.e. they do not present any electron in the d-orbitals. Consequently, the energy levels in the left hand side of Figure 100 are empty (white circles). Nonetheless, after the capture of an electron (e.g. as induced by annealing treatment), Ti^{3+} possesses an electron in the d-orbitals.

At the beginning of the section, it was mentioned that Ti^{4+} is non-paramagnetic. Now, thanks to the theoretical calculation, this can be understood. Ti^{4+} lacks electrons that can be excited by applying a microwave field. Therefore, no resonance peaks are detected in EPR spectroscopy.

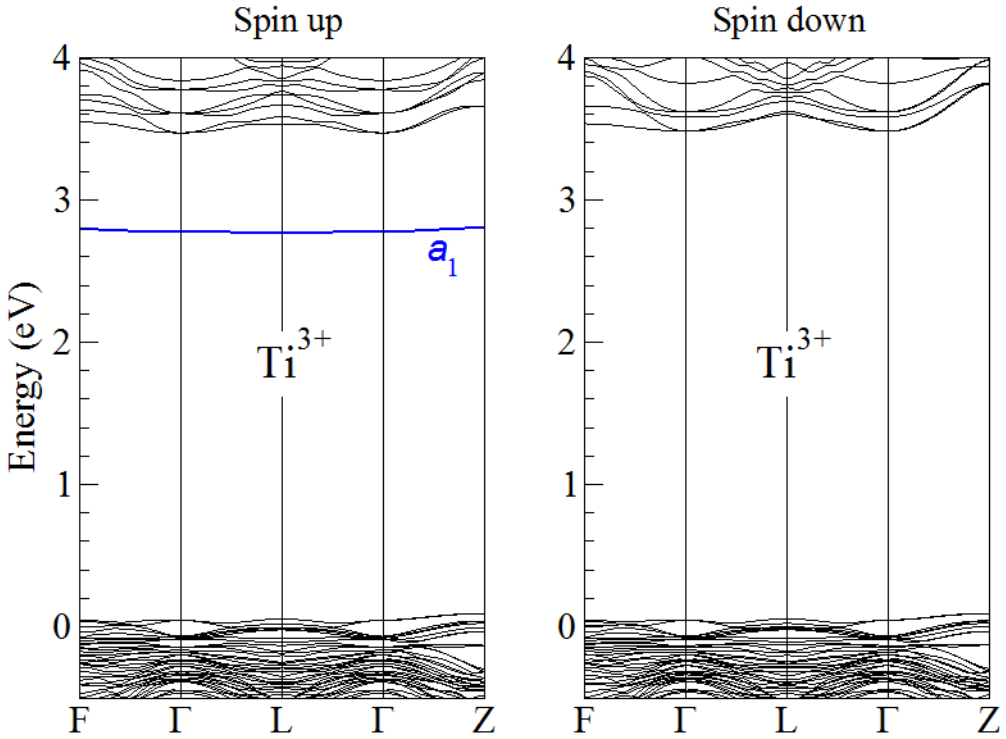

Figure 99: Calculated energy levels of trivalent titanium (Ti^{3+}) substituting Li in lithium niobate. On the left panel, the energy levels of electrons with spin up are shown, whereas on the right panel the energy levels of electrons with spin down are presented. The calculations and figures were provided by S. Sanna.

Nevertheless, after annealing, the occupied energy level of Ti^{3+} is placed in the band gap making EPR spectroscopy possible. Applying a magnetic field, the energy levels split into two energy levels due to the Zeeman interaction. The splitting is about 12 GHz (see Figure 78 in Chapter 5 Results), i.e. 0.00005 eV where the EPR absorption (9.9 GHz about 0.00004 eV) takes place from the lowest energy state to the highest. When the EPR condition is fulfilled, spectra are recorded (as it can be seen in Chapter 4 Measurements).

Titanium doped lithium niobate was investigated also with photoluminescence spectroscopy (see Chapter 4 Measurements). Absorption bands at 1.9 eV and 3.1 eV are observed in Figure 43 in

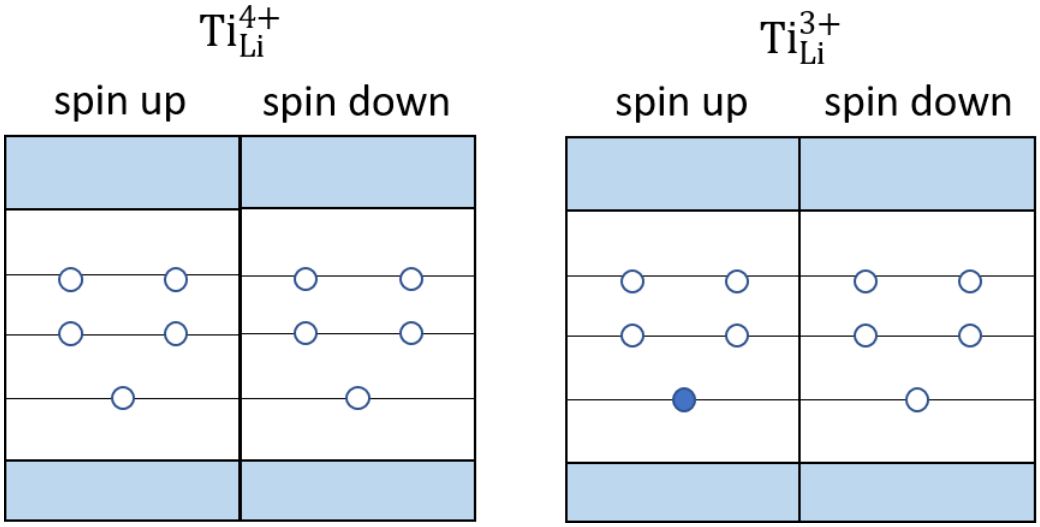

Figure 100: Schematic representation of the occupation of the Ti related energy levels of isolated Ti^{4+} (left hand side) and Ti^{3+} (right hand side) ions substituting Li in lithium niobate. The blue rectangles represent the conduction (top blue rectangles) and the valence (bottom blue rectangles) bands. The band gap is shown in white. Schematically, the energy levels of Ti^{4+} and Ti^{3+} are represented as horizontal lines in the band gap. Energy levels are filled with electrons represented as blue circles. Empty energy levels are represented (with white circles). The figures were provided by S. Sanna.

Chapter 4 Measurements. Looking at the literature, absorption bands at 1.8 eV and 3 eV are attributed to Ti_{Li}^{3+} [48], [45] and [86] and absorption bands at 1.6 eV and 2.6 eV are attributed to Ti_{Nb}^{3+} [48]. Therefore, photoluminescence spectra corroborate the substitution of lithium with titanium. After annealing treatment the observed absorption band at 1.9 eV increases, whereas the absorption band at 3.1 eV decreases. This feature was attributed to the thermally activated intervalence transfer $Ti^{3+} + Nb^{5+} \longleftrightarrow Ti^{4+} + Nb^{4+}$ [45].

In conclusion, titanium doped lithium niobate was studied in nearly stoichiometric lithium niobate crystals. After annealing treatment, Ti^{3+} is supposed to remain at the lithium place with an axial g-tensor due to the ground state symmetry ($3z^2$-r^2). In addition, the absorption bands observed at 1.9 eV and 3.1 eV are attributed to the thermally activated intervalence transfer $Ti^{3+} + Nb^{5+} \longleftrightarrow Ti^{4+} + Nb^{4+}$. Unfortunately, Ti^{4+} is a non-paramagnetic ion and could not be distinguished by means of EPR spectroscopy. However, our photoluminescence measurements suggest that it behaves in an analogous way as Ti^{3+}, substituting lithium in lithium niobate.

6.1.3 Iron-titanium co-doped lithium niobate

In the last previous sections, iron and titanium single doped lithium niobate crystals were discussed. In addition, it was mentioned that both iron and titanium are incorporated at the lithium site, and the spin Hamiltonian was calculated for different samples (see Chapter 5 Results). The corresponding photoluminescence measurements were characterized by different absorption bands (D-band at 2.6 eV for iron doping and two bands at 1.9 eV and 3.0 eV for titanium doping). In this section, iron and titanium co-doping is discussed by means of EPR and photoluminescence.

In the EPR spectra it was observed that iron and titanium ions interact weakly amongst themselves, not only for nearly stoichiometric but also for congruent lithium niobate samples (see Chapter 5 Results). Iron (Fe^{3+}) ions were observed in as grown samples and were described with a slightly axial g-tensor due to the weak interaction with titanium (Ti^{4+}) ions. After a reduction treatment at 600 °C, Ti^{3+} and Fe^{3+} were recorded by means of EPR, however no signs of a strong interaction were found. Consequently, iron and titanium centres do not form a strongly bound defect complex, nonetheless they have a weak interaction and this is reflected in the g-tensor of iron. In co-doped samples, the g-tensor of iron is slightly axial, whereas in single doped samples it is isotropic. This weak (but not negligible) interaction between iron and titanium ions is due rather to the lattice distortion introduced by the dopants than to the formation of hybrid orbitals. Indeed, Fe and Ti are located at neighbouring Li sites, next to each other but separated by 3.76 Å and are not bounded. Similarly to iron and titanium centres in single doping lithium niobate, iron and titanium in co-doped lithium niobate are supposed to occupy lithium site.

The EPR spectra of the different single and co-doped lithium niobate samples were measured and compared in Chapter 4 Measurements (see Figure 38 to 41). No resonance peaks were found in the iron-titanium indiffused lithium niobate samples (**155313ss**), probably because of the low iron concentration in the samples. In addition, it seems that iron indiffused in lithium niobate was not successfully incorporated in the samples compared to the bulk doping procedure (for example **155313vs**), although the iron concentration was nominally the same (see Table 2 in Chapter 3 Methods). On the other hand, iron doped nearly stoichiometric and congruent samples present similar EPR spectra confirming that iron substitutes lithium and behaves similarly in congruent and in nearly stoichiometric samples. Moreover, the resonance peaks in nearly stoichiometric samples are narrower than in congruent samples due to the lower number of intrinsic defects (as for example lithium vacances). In co-doped samples, iron and titanium interact only weakly, influencing the spin-lattice relaxation process. This causes an increase in the resonance peak

intensity of the co-doped samples observed in Figure 39 in Chapter 4 Measurements.

It should be noticed that the resonance peaks in Figure 39 in Chapter 4 Measurements are better defined (i.e. more intense and with less fluctuations) in comparison with Figure 38. As a reminder, the spectra were recorded with a magnetic field parallel to the principal axis (z) in Figure 38, whereas they were perpendicular to z in Figure 39. This fact can be explained by a different internal electromagnetic field (dependent on the crystallographic axis), since the crystal structure of lithium niobate is anisotropic. In the EPR spectra, it can be observed that the background is less pronounced when the magnetic field is perpendicular to the principal axis than when it is parallel to z (for example, comparing Figures 24 and 25 in Chapter 4 Measurements). Zeng et al. [29] suggest that iron at the lithium site induce a stronger ferromagnetism, however a different behaviour depending on the axis in lithium was not mentioned.

Furthermore, the absorption bands of both iron and titanium ions in co-doped lithium niobate samples are observed in the PL measurements. In the as grown nearly stoichiometric lithium niobate sample, the absorption band of iron at 2.6 eV and the absorption bands of titanium at 1.9 eV and 3.2 eV were detected. The absorption bands of the co-doped system strongly resemble the superposition of the PL bands of the singly doped samples, suggesting a weak interaction between iron and titanium. After the annealing treatment, the absorption coefficient increases at 3 eV and 1.9 eV. A similar feature has been obtained in iron single doped lithium niobate (see Figure 42 in Chapter 4 Measurements). This is explained by the occurrence of polarons and bipolarons in the reduced lithium niobate sample [85]. Surprisingly, iron-titanium indiffused in lithium niobate (**155313ss**) does not absorb light, probably due to the low ions concentration in the sample. On the other hand, the iron in bulk doped and titanium in surface co-doped lithium niobate sample (**155313vs+800**) annealed for 3 hours at 800 °C in argon lacks the characteristic absorption bands of iron and titanium. This seems to be caused by the annealing process in argon atmosphere. At annealing temperatures of 800 °C trivalent iron ions should have captured one electron, i.e. Fe^{2+} and the absorption band 2.6 eV should be visible. In addition, titanium bands seem to be also weaker than in other co-doped samples annealed in vacuum. Therefore, thermal treatment in argon atmosphere seems to be less effective than in vacuum. This could be also explained by the lack of titanium traces in EPR measurements.

As a reminder, iron and titanium were found to sit at the lithium site in iron and titanium single doped lithium niobate. In addition, similar spin Hamiltonian parameters were calculated for iron and titanium centres in co-doped samples. Therefore, iron and titanium centres seem to substitute lithium in iron-titanium co-doped samples. By means of EPR and PL, it was observed that iron

interacts weakly with titanium. With the aim of understanding how they interact in the host crystal, the energy levels of iron and titanium next neighbours pairs in LN have been calculated with DFT by S. Sanna (see Figure 101).

Considering iron (Fe_{Li}^{3+}) and titanium (Ti_{Li}^{4+}) as first neighbours, the calculated energy levels of iron (red lines in Figure 101) and titanium (blue lines in Figure 101) are similar to the superposition of the energy levels of isolated iron and titanium centres (see Figure 93 and 98 respectively). In addition, it seems that iron-titanium as basal pairs are slightly favoured over axial pairs or separated defects (see Table 17 for the DFT calculated total energies). This indicates a minor interaction amongst the two defects, which was also observed in the EPR spectra.

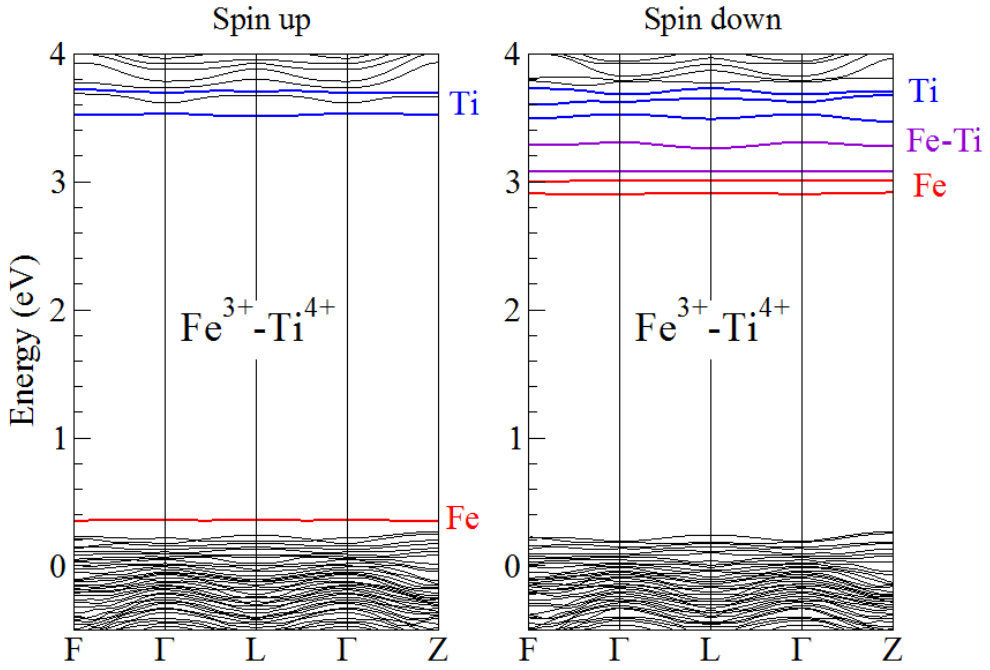

Figure 101: Electronic band structure of a supercell modelling iron and titanium co-doped lithium niobate. The tetravalent titanium(Ti^{4+}) and the trivalent iron (Fe^{3+}) are considered as first neighbours substituting Li. On the left panel, the energy levels for electrons with spins up are shown, whereas on the right panel the energy levels for electron with spins down are presented. Energy levels are in red for iron, blue for titanium and purple for hybridization of Fe and Ti states. The calculations and figures were provided by S. Sanna.

The calculated energy of the system Fe^{3+} and Ti^{4+}, demonstrates that the formation of a basal pair is preferable (see Table 17). The lowest calculated energy is for iron-titanium basal pair, followed by the axial pair. Iron centres separated more than 10 Å seem to be less favourable. Furthermore, the binding energy is small, indicating a weak interaction between iron and titanium. This fact was already observed by EPR. In the as grown iron-titanium co-doped nearly stoichiometric lithium niobate sample, iron and titanium ions interact weakly amongst themselves and therefore the g-tensor is slightly axial.

After the reduction treatment, spectroscopic signatures of both titanium and iron were recorded together, and like in the case of as grown LN, iron and titanium seem to interact weakly. In terms of DFT calculation, the Fe^{3+} and Ti^{4+} system was charged by introducing an additional electron. If charged defects are considered, i.e. iron and titanium ions placed in lithium site (Fe^{3+}-Ti^{4+}) with an additional electron, three different configurations are possible. On the one hand, iron captures the electron leading to the first configuration Fe^{2+}-Ti^{4+} (see Figure 102). On the other hand, titanium might catch the electron and two possible configurations are possible: Fe^{3+}-Ti^{3+} with high spin or Fe^{3+}-Ti^{3+} with low spin (see Figures 103 and 104 respectively).

With the aim of obtaining the most favourable situation in charged iron-titanium co-doped lithium niobate crystals, the energy levels of every possible configuration must be considered. The DFT calculations carried out by S. Sanna are listed in Table 18 (total energy).

Total energy calculations have demonstrated that the Fe^{2+}-Ti^{4+} charge configuration is not stable. Therefore, titanium captures the electron and, in addition, the basal pair situation is the most favourable. The high or low spin difference is minor, as the coupling of the two ions is weak. This fact seems not to confirm the statements of Gericke et al. [4]. That means that titanium does not stabilize iron Fe^{2+} against oxidation, since the Fe^{2+}-Ti^{4+} configuration seems not to be stable. In addition, this configuration was not observed by means of EPR. If the Fe^{2+}-Ti^{4+} configuration would occur, different spectroscopic signatures would have been observed. After annealing, iron captures the electron and the EPR spectra would have shown no traces of Fe^{2+} nor of Ti^{4+}. Since Fe^{2+} has a very large fine structure term, X-band EPR spectra does not record any resonance peaks. In addition, Ti^{4+} is non-paramagnetic and therefore it is not observed by EPR.

Considering two additional electrons in the iron (Fe^{3+}) and titanium (Ti^{4+}) system, also the basal pair is the lowest energy system. Consequently, iron and titanium are incorporated as basal pairs. Their binding energy, despite being low, is not negligible; as it was observed by means of EPR data. Moreover, the distance between the pair is 3.760 Å for Fe^{3+}-Ti^{4+}, 3.754 Å adding

one electron (Fe^{3+}-Ti^{4+}+$1e^-$) and 3.813 Å considering two electrons (Fe^{3+}-Ti^{4+}+$2e^-$). The energy levels of the charged iron-titanium basal pair were calculated and are shown in Figure 105.

Basal pair	Axial pair	Separated	Binding energy
-632.454 eV	-632.451 eV	-632.344 eV	0.110 eV

Table 17: DFT calculated total energy of the iron (Fe^{3+}) and titanium (Ti^{4+}) defect pairs in lithium niobate. The system was considered as a basal pair in the first column, as an axial pair (along the c axis) in the second column and as separated iron and titanium ions (by more than 10 - 15 Å) in the third column. The binding energy for Fe^{3+} and Ti^{4+} is given in the fourth column. The precision of the calculated energies is estimated in a few meV. The calculations were carried out by S. Sanna.

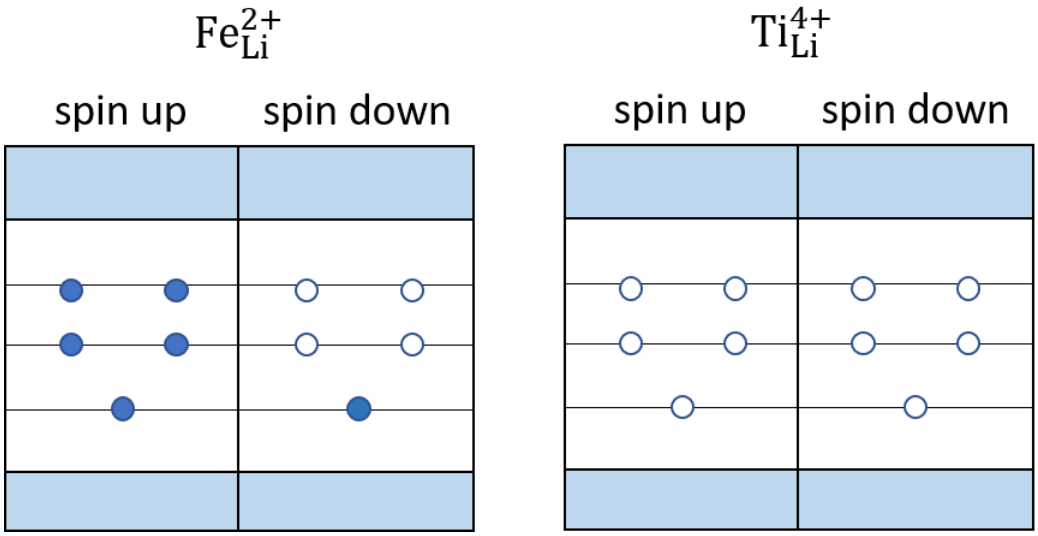

Figure 102: Schematic representation of the occupation of the Fe and Ti related energy levels of Fe^{2+} (left hand side) and Ti^{4+} (right hand side) both substituting Li in lithium niobate. The blue rectangles represent the conduction (top blue rectangles) and the valence (bottom blue rectangles) bands. The band gap is shown in white. Schematically the energy levels of Fe^{2+} and Ti^{4+} are represented as horizontal lines in the band gap. Energy levels are filled with electrons represented as blue circles. Empty energy levels are represented by white circles. The figures were provided by S. Sanna.

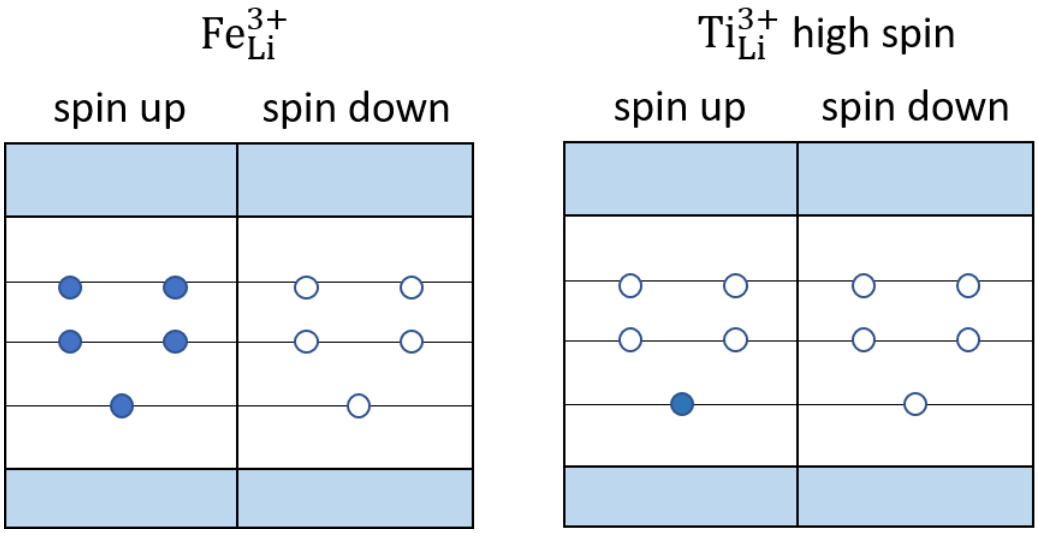

Figure 103: Schematic representation of the occupation of the Fe and Ti related energy levels of Fe^{3+} (left hand side) and Ti^{3+} high spin (right hand side) both substituting Li in lithium niobate. The high spin configuration is due to the electron with spin up in the titanium. The blue rectangles represent the conduction (top blue rectangles) and the valence (bottom blue rectangles) bands. The band gap is shown in white. Schematically, the energy levels of Fe^{3+} and Ti^{3+} are represented as horizontal lines in the band gap. Energy levels are filled with electrons represented as blue circles. Empty energy levels are represented by white circles. The figures were provided by S. Sanna.

Now it is easy to understand why Fe^{3+} and Ti^{3+} are recorded together by EPR spectroscopy after annealing treatment. Iron and titanium form a basal pair with Fe^{3+} and Ti^{4+} in iron-titanium co-doped lithium niobate. After annealing treatment, an electron is captured by titanium becoming paramagnetic, and therefore, both Fe^{3+} and Ti^{3+} are observed by means of EPR. As it can be seen in Figure 105, the occupied electronic level of Ti^{3+} in $LiNbO_3$ lies lower than the occupied level of Fe^{2+} in $LiNbO_3$. For this reason, titanium ($Ti^{4+} \rightarrow Ti^{3+}$) gets reduced before iron ($Fe^{3+} \rightarrow Fe^{2+}$). The charge distribution is shown in Figure 106. As a reminder, the annealing treatment produces polarons and bipolarons as it has been seen in the photoluminescence measurements in iron single doped lithium niobate. Therefore, optical absorption spectra in co-doped samples show features of titanium and iron in as grown lithium niobate, and after annealing a strong absorption shoulder due to the occurrence of polaron and bipolarons is observed (Figure 44 in Chapter 4 Measurements).

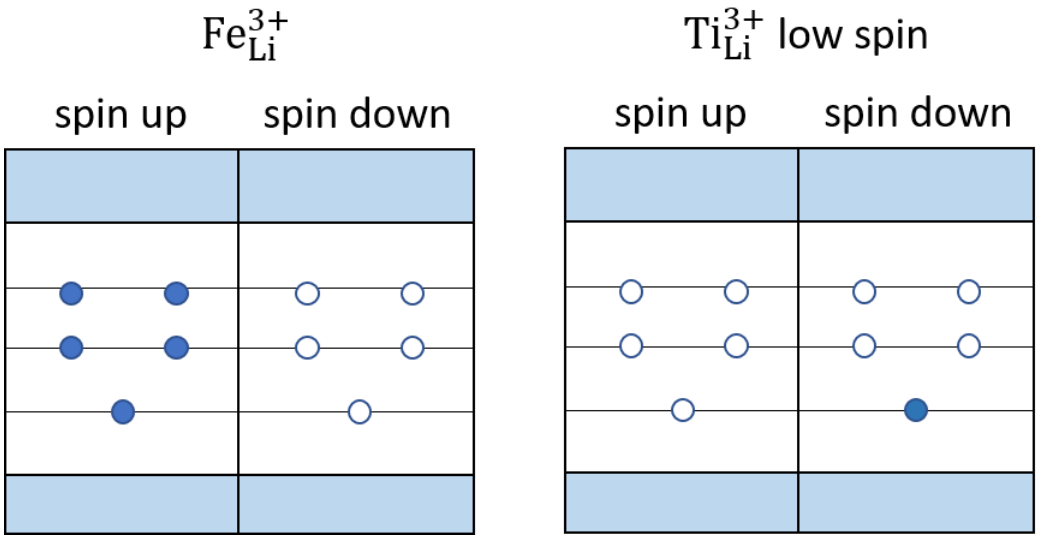

Figure 104: Schematic representation of the occupation of the Fe and Ti related energy levels of Fe^{3+} (left hand side) and Ti^{3+} low spin (right hand side) both substituting Li in lithium niobate. The down spin configuration is due to the electron with spin down in the titanium. The blue rectangles represent the conduction (top blue rectangles) and the valence (bottom blue rectangles) bands. The band gap is shown in white. Schematically, the energy levels of Fe^{3+} and Ti^{3+} are represented as horizontal lines in the band gap. Energy levels are filled with electrons represented as blue circles. Empty energy levels are represented by white circles. The figures were provided by S. Sanna.

Configuration	Basal pair	Axial pair	Separated	Binding energy
Fe^{2+}-Ti^{4+}	not stable	not stable	not stable	-
Fe^{3+}-Ti^{3+} high spin	-626.454 eV	-626.384 eV	-626.300 eV	0.154 eV
Fe^{3+}-Ti^{3+} low spin	-626.485 eV	-626.389 eV	-626.300 eV	0.184 eV

Table 18: Calculated energy of the iron (Fe^{3+}) and titanium (Ti^{3+}) defects in lithium niobate. The considered configuration is written in the first column. The system was considered as a basal pair in the second column, as an axial pair (along the c axis) in the third column and as separated iron and titanium ions (more than 10-15 Å) in the fourth column. The binding energy for Fe^{3+} and Ti^{3+} is given in the fifth column. The calculations were carried out by S. Sanna.

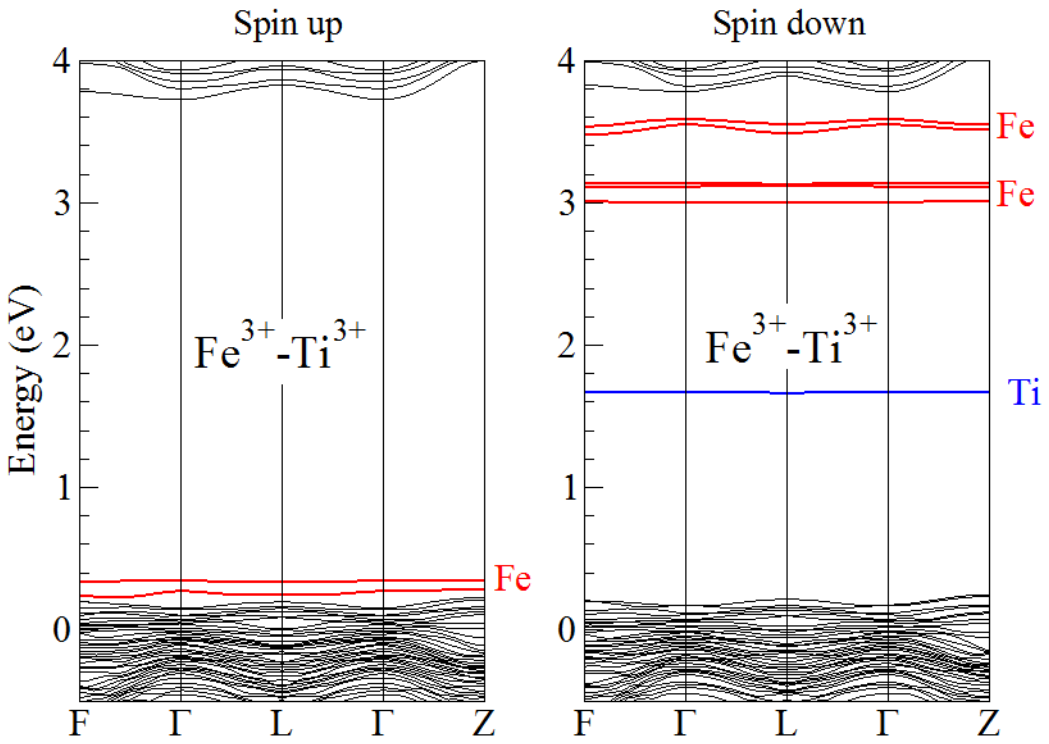

Figure 105: Calculated energy levels of charged (i.e. adding one electron) iron and titanium co-doped lithium niobate. Trivalent titanium(Ti^{3+}) and trivalent iron (Fe^{3+}) are considered as first neighbours substituting Li in lithium niobate and forming a basal pair. On the left panel, the energy levels for electrons with spin up are shown, whereas on the right panel the energy levels for electrons with spin down are presented. Energy levels are in red for iron and blue for titanium states. The calculations and figures were provided by S. Sanna.

The charge distribution of the charged basal pair (Fe^{3+}+Ti^{4+}+e^{-}) is represented in Figure 106. Before the thermal treatment, titanium and iron interact weakly as it was observed in the EPR measurements. After annealing, the electron tends to reduce titanium instead of iron ion and therefore, the titanium g-tensor is very similar as in single doped lithium niobate samples.

In conclusion, titanium and iron interact amongst themselves weakly as it was observed in the slightly axial g-tensor of iron. In addition, after reduction, Fe^{3+} and Ti^{3+} are recorded by means of

EPR and, the number of polarons and bipolarons increases leading to a strong shoulder in the PL spectra. At high reduction temperatures (900 °C), only Ti^{3+} is observable. Iron and titanium ions in co-doped lithium niobate crystals form a basal pair separated about 3.7 - 3.8 Å and with a small but not negligible binding energy. The EPR evidences of Fe^{3+} and Ti^{3+} are against the statement of Gericke et al. that titanium stabilizes iron against oxidation [4]. In addition, the DFT calculations made by S. Sanna show the instability of Fe^{2+} - Ti^{4+} complex against Fe^{3+} - Ti^{3+}. However, this fact matches with Sanz García et al. [3], since they suggest that Ti does not influence the reduction of behaviour of Fe. Therefore, the increase in the photorefractive sensitivity in the region with iron and titanium defects has to be explained by means of other impurities in lithium niobate.

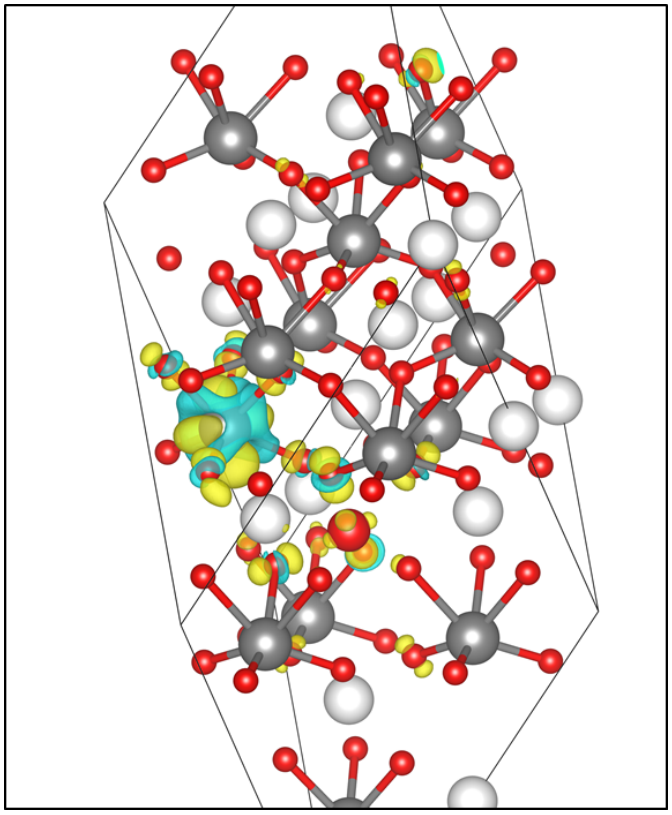

Figure 106: Charge distribution of the basal pair Fe^{3+} and Ti^{3+}. The crystal structure is shown with oxygen atoms in red, lithium atoms in white and niobium in dark grey circles. The charge distribution of the basal pair formed by titanium and iron (dark red circle) substituting lithium was calculated with (in blue) and without (yellow) and additional electron.

6.2 Lithium yttrium borate

In the last section, single doped and co-doped lithium niobate samples were discussed. In this section, lithium yttrium borate samples are considered. The discussion starts with erbium doped lithium yttrium borate, it follows the discussion of ytterbium doped lithium yttrium borate and, at the end, iron doped lithium yttrium borate is examined.

6.2.1 Erbium doped lithium yttrium borate

LYB single crystals are good candidates for laser materials due to their flexibility and the easy incorporation of the rare earth dopants e.g. erbium (Er^{3+}). Er^{3+} ions are especially interesting for their near infrared emission, suitable for optical telecommunication systems. With the aim of obtaining the microscopic and electronic structure of Er^{3+} in lithium niobate, EPR measurements were performed (see Chapter 4 Measurements). The spin Hamiltonian parameters that describe Er^{3+} in LYB were given in Chapter 5 Results. Two magnetically non-equivalent centre families are observed due to the C_{2h} point symmetry of the crystal. Each centre family has a C_1 point symmetry which is characteristic of the yttrium (Y) place. The yttrium replacement is reasonable due to the charge compensation and the ionic radii (see Chapter 2 Materials). In addition, the covalent bond between boron and oxygen is strong enough, preventing the boron substitution. Furthermore, different erbium isotopes were found in the EPR spectra. One isotope ^{167}Er with nuclear spin I=7/2 and with a natural abundance of 22.93 %, and other isotopes (e. g. ^{162}Er, ^{164}Er, ^{166}Er, ^{168}Er and ^{170}Er) with zero nuclear spin. Therefore, the resonance peak of erbium isotopes with zero nuclear spin is five times more intense than ^{167}Er isotope. No literature about erbium doped LYB has been found, which can be compared with the obtained spin Hamiltonian parameters. Nonetheless, erbium has been investigated in other host materials as for example $LiNbO_3$ [87], $YAl_3(BO_3)_4$ [51] or GaN [88]. In lithium niobate, two erbium centres with C_1 symmetry were found, with a strong anisotropic g-tensor. In addition, the hyperfine structure was also observed. In contrast, a single erbium centre with C_1 symmetry was detected in $YAl_3(BO_3)_4$ [51] and GaN [88].

The number of erbium centres in the host material depends on the lattice symmetry and the occupation site. As a reminder, erbium substitutes yttrium in LYB. Under EPR spectroscopy, a main resonance line due to the isotopes with I=0 and eight hyperfine resonance lines due to the ^{167}Er isotope are recorded. Rotating the sample in the spectrometer with respect to the direction of the applied magnetic field, all resonance lines vary their position within the magnetic field.

Indeed, the magnetic field range in which the resonance peaks are found is wide (almost 1 T) due to the strong anisotropy of g- and A-tensors. In addition, the Euler angles of A-tensor differ slightly from the ones of the g-tensor because there is no a priori reason why the Euler angles should be the same. In this fashion, it is how one erbium centre is described in LYB. However, due to the C_{2h} symmetry of the host material, not just one but two erbium centres are observed. Both erbium centres are described by the same spin Hamiltonian parameters and both substitute yttrium, however one centre is rotated by 180º and translated (due to the inversion point symmetry) with respect to the other erbium centre. Therefore, not just one but two erbium manifolds are recorded (called centre 1 and 2 in Figure 84 in Chapter 5 Result).

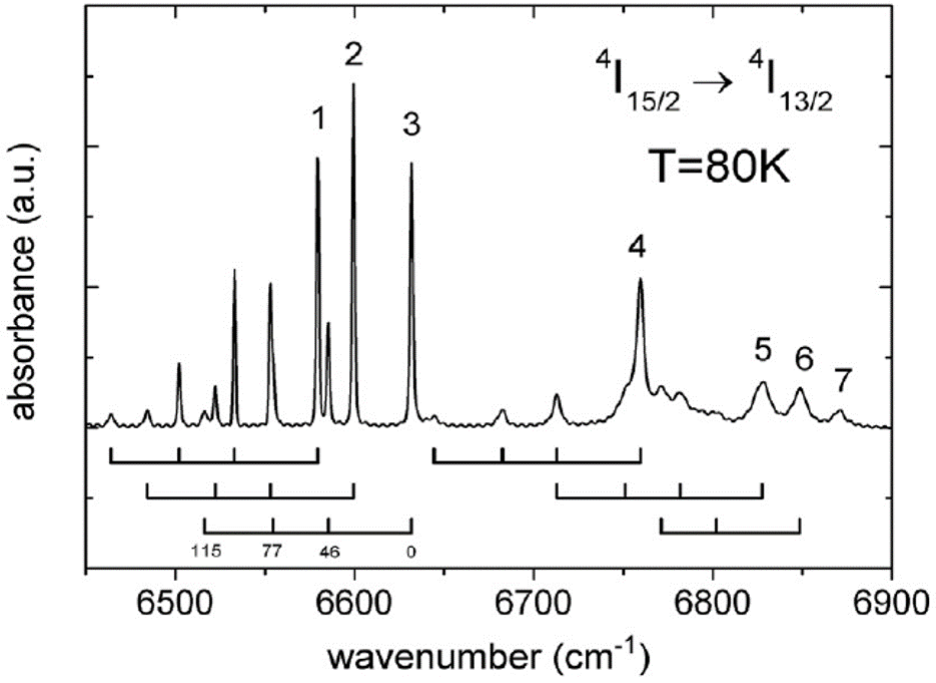

Figure 107: Absorption spectra for the $^4I_{15/2} \rightarrow {}^4I_{13/2}$ transition of Er:LYB at T=80 K. The transitions numerated 1-7 are also shown at 9 K and have satellites (indicated with the combs) corresponding to transitions from thermally populated higher Stark sublevels of the ground state to the same target level (46, 77 and 115 cm^{-1}). Figure was taken from [50]

In Kóvacs et al. [50], absorption spectra were measured using the same samples as in this thesis. There, additional lines were found in the absorption spectra and were attributed to the thermal population of higher Stark sublevels of the ground state. Most lines were found at 9 K, whereas at 80 K they acquire satellites corresponding to transitions from higher Stark levels of the ground state to the same target level. Up to three satellites with similar spacing of 46, 77 and 115 cm^{-1} can be observed (see the combs in the Figure 107)

The EPR spectra also showed fast temperature broadening and could not be observed above 25 K (see Figure 59 in Chapter 4: Measurements). An Orbach-type spin-lattice relaxation process with the activation energy $\Delta E_a = (43 \pm 10)$ cm^{-1} was obtained, which matches with the value obtained by optical data (see Figure 107) [50].

6.2.2 Ytterbium doped lithium yttrium borate

Ytterbium doped lithium yttrium borate is a promising laser material. The broad emission band characteristic of Yb^{3+} is very favourable for tuneable or ultra-fast lasers. Therefore, the spectroscopic properties of ytterbium doped lithium yttrium borate have been already investigated [9, 89]. Furthermore, EPR spectroscopy of ytterbium doped lithium yttrium borate powder crystal was investigated [90] and, crystal field calculations based on the superposition model were performed [91]. Nonetheless, the EPR experiments on ytterbium doped LYB single crystal were still missing.

In the frame of this thesis, ytterbium doped lithium yttrium borate single crystals were investigated. In Chapter 4 Measurements, the EPR spectra were shown and, in Chapter 5 Results, the spin Hamiltonian parameters for Yb^{3+} in LYB were obtained. Similarly to erbium doping, two magnetically non-equivalent centre families due to the C_{2h} point symmetry of the crystal are observed. Both centres are described by the same spin Hamiltonian parameters, although they differ in a rotation of 180°. Yb^{3+} centres substitute yttrium in analogy to erbium. In addition, different isotopes were found with zero nuclear spin (e.g. ^{168}Yb, ^{170}Yb, ^{172}Yb, ^{174}Yb and ^{176}Yb) and, ^{171}Yb with nuclear spin I=1/2 and ^{173}Yb with I=5/2. The natural abundance (14.28% for ^{171}Yb and 16.13% for ^{173}Yb) is related with the peak intensity. Therefore, the resonance peak of ytterbium isotopes with zero nuclear spin is more intense than ^{171}Yb and ^{173}Yb isotopes. Moreover, the resonance peaks of ^{171}Yb are more intense than the ones of ^{173}Yb, because the total area is distributed in two and six resonance peaks, respectively. Consequently, ^{173}Yb resonance peaks are less intense than the ^{171}Yb ones.

Comparing with the literature, the experimental results (Table 14 in Chapter 5 Results) match not only with the experimental [90] but also with the theoretical results [91]. Considering the ytterbium doped LYB powder sample, the match is confirmed by two facts. First, the average value of the g value (=3.43) given in [90] is close to the results presented in this thesis $(g_{xx}+g_{yy}+g_{zz})/3$=3.40 (Table 14 in Chapter 5 Results). Second, the most intense resonance peak of the powder spectrum (B=135 mT) corresponds to the largest g-tensor component (i.e. g_{zz} =5.0355±0.004 and B=140 mT). On the other hand, the calculated g- and A-tensors principal values match quite well with the experimental values presented in Table 14 in Chapter 5 Results. However, the tensor direction in the calculated version [91] does not coincide with the one presented in this thesis. In addition, Liu et al. [91] obtain the same directions of the g- and A-tensor, while in the experimental results the A-tensor is slightly tilted with respect to the g-tensor leading to a non equedistant EPR lines (see Figure 88 in Chapter 5 Results).

The EPR spectra also show a fast temperature broadening and could not be observed above 45 K (see Figure 59 in Chapter 4 Measurements). As it was shown in Chapter 5 Results, an Orbach-type exponential dependence could be used for fitting the data with an activation energy $\Delta E = (150\pm 80)\text{cm}^{-1}$. However, the first excited Stark sublevel of the $^2F_{7/2}$ ground state was found at 369 cm^{-1} [80]. Consequently, the dominant spin-lattice relaxation mechanism may be related to some more efficient process.

In conclusion, a detailed experimental EPR analysis of ytterbium doped lithium yttrium borate crystal was achieved for the first time. The knowledge of the microscopic and electronic structure of ytterbium defects in lithium yttrium borate is important in order to understand the crystal properties and to enhance their physical properties.

6.2.3 Iron doped lithium yttrium borate

Lithium yttrium borate was doped with iron with the aim of investigating EPR. In Chapter 4 Measurements the EPR spectra were shown, and the expected spin Hamiltonian is exposed in Chapter 5 Results. Iron doped lithium yttrium borate, similarly to iron doped lithium niobate, has an isotropic g-tensor and a large fine structure interaction that make the task of obtaining the spin Hamiltonian parameters more difficult.

On May 2017, manganese (Mn) doped lithium tetraborate ($Li_2B_4O_7$) came to light [92]. Mn^{2+} has the same electronic structure as Fe^{3+} (S=5/2), since the difference between Mn^{2+} and Fe^{3+}

lies in one proton. Therefore, the spin Hamiltonian should be similar. Mn was described by an isotropic g-tensor and a large fine structure term, as it was considered in this thesis. Unfortunately, the fitting program was not satisfactory and affected by a large error, even using the Romet et al. [92] spin Hamiltonian parameters as starting parameters. Nevertheless, for the first-time an iron doped lithium yttrium borate crystal was investigated. Although the microscopic and electronic structure could not be completely determined, an interpretation of iron in LYB was given with the aim of understanding the crystal properties. It is a first step and there are many studies on numerous defects to follow, which go beyond the scope of this work. This is only an initiation for many subsequent works on this interesting material.

7 Summary

By means of electron paramagnetic resonance spectroscopy, point defects in a host material have been characterized and analysed. Therefore, nearly stoichiometric and congruent crystals were measured by EPR and PL (see Chapter 4 Measurement), characterized using EasySpin (see Chapter 5 Results) and finally discussed (see Chapter 6 Discussion). On the one hand, titanium indiffused lithium niobate is commonly used as a waveguide, since titanium increases the refractive index in the host material without increasing the photorefractive effect. On the other hand, the presence of iron impurities in the waveguides produces optical damage and, therefore, causes degradation of the waveguide. Indeed, it was claimed that titanium stabilizes iron against oxidation, enhancing the photorefractive sensibility. Unfortunately, neither the complexes formed by titanium and iron nor the mechanism leading to the optical damage are known.

Our results suggest that titanium does not stabilize iron against oxidation. Indeed, our measurements do not provide any evidence for the coexistence of Fe^{2+} and Ti^{4+} defect centres. The previously observed stabilization of Fe^{2+} against Fe^{3+} in co-doped samples has thus to be traced back to the presence of other (unintentional) impurities and structural defects, or to thermal effects. To reach this assumption, not only nearly stoichiometric but also congruent lithium niobate crystals were investigated. In addition, iron and titanium single doped and iron-titanium co-doped lithium niobate samples were considered. EPR measurements in iron-titanium co-doped lithium niobate suggest a weak (but not negligible) interaction between iron (Fe^{3+}) and titanium (Ti^{4+} and after reduction Ti^{3+}). This weak interaction is observed in the axial g-tensor of iron in the co-doped samples, whereas the Fe^{3+} g-tensor is isotropic in iron single doped samples. On the other hand, titanium ions (Ti^{3+}) possess an axial g-tensor in single and co-doped samples after reduction.

Both iron and titanium ions were found to be incorporated at the lithium place, in agreement with ENDOR results [19, 20]. In iron single doped lithium niobate samples, two magnetically non-equivalent centres were observed. Both centres are described by the same absolute spin Hamiltonian parameters with a large fine structure term, however one centre is characterized by $+B_4^3$ and the other by $-B_4^3$, producing a splitting in the EPR spectra about y axis. The same feature was as well found in co-doped samples. Moreover, for the first time allowed and forbidden

resonance transitions were identified.

In addition, angle dependent EPR spectra in the lithium niobate samples suggest a different magnetization for a magnetic field parallel and perpendicular to the optical axis (z). Therefore, the resonance peaks at a magnetic field parallel to the optical axis were less intense compared with the ones perpendicular to the principal axis. This fact can be explained due to the anisotropic crystal structure of lithium niobate. Comparing the studied samples, congruent lithium niobate samples have a much higher concentration of intrinsic defects than nearly stoichiometric. This results in much broader EPR resonance peaks in congruent samples than in nearly stoichiometric samples. Furthermore, titanium seems to influence iron in co-doped lithium niobate in such a way that not only the g-tensor of iron is influenced but also the spin-lattice relaxation process. Therefore, their resonance peaks were a bit more intense than those of single doped samples.

Lithium niobate was doped using two different techniques: bulk and surface doping. EPR as well as PL measurements reveal the presence of titanium dopants in both indiffused lithium niobate samples and in samples doped during the crystal growth. While the iron doping is revealed by EPR and PL in volume doped samples, no signatures of iron were found in iron indiffused lithium niobate crystals.

The characteristic bands of iron and titanium were observed in the PL measurements; although this could not explain the colour diversity of the as grown and annealed samples. In addition, in co-doped samples, the influence of titanium over iron was observed and after annealing treatment, the occurrence of polarons was also observed.

The second part of this thesis was dedicated to lithium yttrium borate, a promising candidate for laser devices and also a good host material for rare earth ions. Erbium and ytterbium doped lithium yttrium borate has been already studied in the past, however a detailed EPR analysis was still missing. In addition, lithium yttrium borate was doped with iron, and the first EPR measurements were performed in the framework of this thesis.

Erbium and ytterbium substitute yttrium in lithium yttrium borate since they have similar ionic radii and valence configuration. In both ions, two magnetically non-equivalent centres were found. In addition, in erbium doped lithium yttrium borate, the ^{167}Er isotope with a nuclear spin of $7/2$ and ^{162}Er, ^{164}Er, ^{166}Er, ^{168}Er, ^{170}Er with I$=$0 were investigated and characterized. The g- and A-tensors were orthorhombic and the Euler angles were slightly different. In ytterbium doped lithium yttrium borate, different ytterbium isotopes were also investigated and examined (with I$=$0, $1/2$ and $5/2$), leading to orthorhombic g-tensor and A-tensors. Moreover, the g-tensor and

A-tensors are oriented closely, however the Euler angles are slightly different.

A fast temperature broadening was shown in the EPR spectra of erbium doped lithium niobate, leading to an Orbach-type spin-lattice relaxation process. In contrast, in ytterbium doped lithium niobate, the temperature broadening seems to be produced by another spin-lattice relaxation process.

Finally, iron doped lithium yttrium borate was measured using EPR spectroscopy. The microscopic and electronic structure of iron has been obtained for the first time, showing that there is still a lot of work to be done in order to completely clarify their structure in terms of spin Hamiltonian. Indeed, iron ions in LYB seem to behave similarly as iron ions in LN, i.e. with an isotropic g-tensor and a large fine structure term.

Appendix

A LN and LYB samples tables

Lithium niobate samples

In the frame of this thesis several doped lithium niobate samples were investigated. Not only iron and titanium single doped but also iron-titanium co-doped lithium niobate were considered in congruent and nearly stoichiometric crystals. In addition, two different doping techniques were contemplated: bulk and surface doping for congruent samples. Annealing treatment was performed in several samples that were grown in the same conditions (see Table 19 and Figure 108). To facilitate the identification of the samples, assorted colours were assigned to the number of the samples.

Sample	Stoichiom./ congruent	Dopant	Bulk/ surf. doping	Temperature treatment
21616	stoichiom.	Fe	bulk	as grown
21616+600	stoichiom.	Fe	bulk	600 °C in vacuum for 3 hours
178903	stoichiom.	Ti	bulk	as grown
178903+600	stoichiom.	Ti	bulk	600 °C in vacuum for 3 hours
178903+900	stoichiom.	Ti	bulk	900 °C in vacuum for 0.5 hours
21615	stoichiom.	Fe Ti	bulk bulk	as grown
21615+500	stoichiom.	Fe Ti	bulk bulk	500 °C in vacuum for 3 hours
21615+600	stoichiom.	Fe Ti	bulk bulk	600 °C in vacuum for 3 hours
21615+900	stoichiom.	Fe Ti	bulk bulk	900 °C in vacuum for 0.5 hours
155312	congruent	Fe	bulk	as grown
155313vs	congruent	Fe Ti	bulk surface	as grown
155313vs+800	congruent	Fe Ti	bulk surface	800 °C in argon for 3 hours
155313ss	congruent	Fe Ti	surface surface	as grown

Table 19: Investigated lithium niobate samples. The first column lists the name of the samples. Crystals grown from the same melt have identical sample number and therefore are identified with the same colour. The second column provides if the lithium niobate was grown in a congruent or stoichiometric (stoichiom.) melt. The third column indicates the dopant ions (Fe for iron and Ti for titanium). The fourth column shows the used doping technique: bulk or surface doping. Finally, the fifth column shows the annealing treatment condition if necessary.

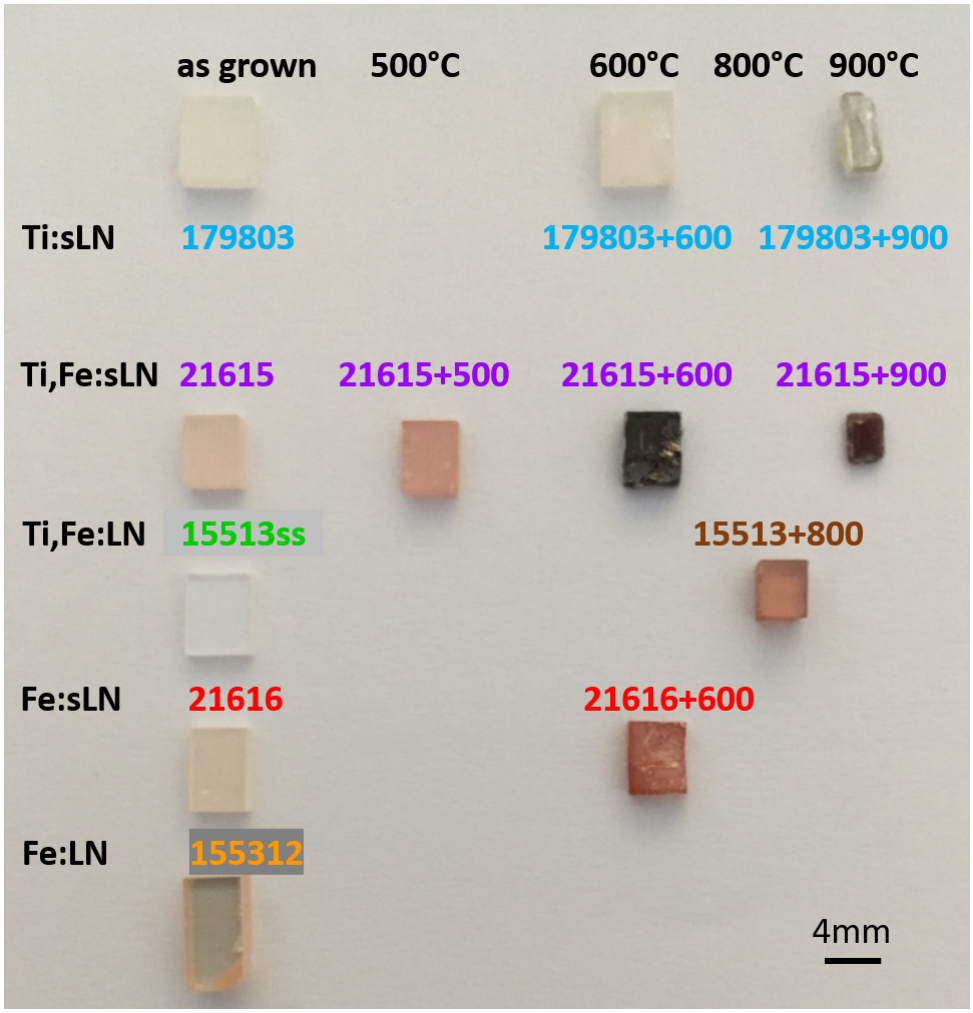

Figure 108: Picture of the studied lithium niobate samples. On the one hand, titanium single doped nearly stoichiometric samples are in the first row. Iron-titanium co-doped nearly stoichiometric lithium niobate are placed in the second row. Iron-titanium congruent lithium niobate samples are listed in the third row. Iron single doped nearly stoichiometric lithium niobate samples are exposed in the fourth row. Iron single doped congruent lithium niobate is in the last row. On the other hand, as grown samples are shown in the first column. Sample annealed at 500 °C for 3 hours in vacuum is placed in the second column. Samples annealed at 600 °C for 3 hours in vacuum are listed in the third column. Sample annealed at 800 °C for 3 hours in argon is located in the fourth column. Samples annealed at 900 °C for 0.5 hours in vacuum are presented in the sixth column. In addition, the number of the different samples is written directly below for the titanium single doped sample and above for iron single and iron-titanium co-doped lithium niobate.

LYB samples

Not only lithium niobate but also lithium yttrium borate was investigated. Relevant dopants as erbium, ytterbium and iron were studied. All of them were bulk doped using the Czochralski method. None of the samples were annealed. However, for completeness, the Table 20 is organizes as Table 19 for lithium niobate.

Sample	Stoichiom./ congruent	Dopant	Bulk/ surf. doping	Temperature treatment
91103	stoichiom.	Er	bulk	as grown
91105	stoichiom.	Er	bulk	as grown
91202	stoichiom.	Yb	bulk	as grown
91501	stoichiom.	Fe	bulk	as grown

Table 20: Studied lithium yttrium borate samples. The name of samples is given in the first column. The second column provides if the lithium niobate was grown in a congruent or stoichiometric (stoichiom.) melt. The third column indicates the dopant ions (Er for erbium, Yb for ytterbium and Fe for iron). The fourth column shows the used doping technique: bulk or surface doping. Finally, the fifth column shows the annealing treatment condition if necessary.

B Euler angles

The well known Euler angles are three angles that parameterise a real orthogonal 3×3 matrix R. It gives the relative orientation between two orthogonal right handed reference systems in Cartesian coordinates. Suppose a starting reference system called xyz. The Euler angles (α, β, γ) deliver the appropriate steps to arrive to the final reference system called ABC. Figure 2 shows a schema of the application of Euler angles to the starting reference system xyz. First, the starting reference system is rotated counterclockwise an angle α about its z axis and the "new" reference system $x'y'z'$ is obtained. Second, the "new" reference system is rotated counterclockwise in its y' axis an angle β and $x''y''z''$ is the "new new" reference system. Finally, $x''y''z''$ is rotated counterclockwise an angle γ about its z'' axis to obtain the final reference system ABC.

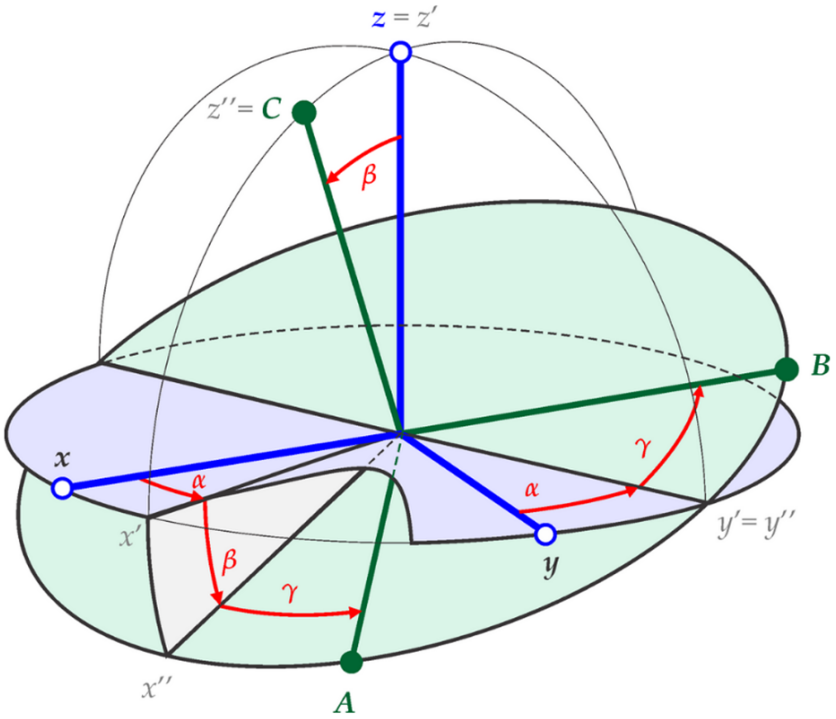

Figure 109: Schematic representation of the application of the Euler angles (α, β, γ) that gives the relative orientation between two orthogonal right handed 3D Cartesian coordinate systems. Picture was taken from [57].

C Stevens operators

In systems with S>1/2, the fine structure interaction has to be taken into account. Usually, this interaction is described by the second order D and E parameters and, if necessary, the fourth order a and F parameters. However, for special cases a complete set of high-order operators is needed: the extended Stevens operators O_k^q.

$$\widehat{H}_{FI} = \sum_{k,q} B_k^q O_k^q(S_x, S_y, S_z)$$

k	q	O_k^q
2	0	$3S_z^2 - sI$
	±1	$c_\pm \left[S_z, S_+ \pm S_-\right]_+$
	±2	$c_\pm \left(S_+^2 \pm S_-^2\right)$
4	0	$35S_z^4 - (30s-25)S_z^2 + (3s^2-6s)I$
	±1	$c_\pm \left[7S_z^3 - (3s+1)S_z, S_+ \pm S_-\right]_+$
	±2	$c_\pm \left[7S_z^2 - (s+5)I, S_+^2 \pm S_-^2\right]_+$
	±3	$c_\pm \left[S_z, S_+^3 \pm S_-^3\right]_+$
	±4	$c_\pm \left(S_+^4 \pm S_-^4\right)$
6	0	$231S_z^6 - (315s-735)S_z^4 + (105s^2-525s+294)S_z^2 - (5s^3-40s^2+60s)I$
	±1	$c_\pm \left[33S_z^5 - (30s-15)S_z^3 + (5s^2-10s+12)S_z, S_+ \pm S_-\right]_+$
	±2	$c_\pm \left[33S_z^4 - (18s+123)S_z^2 + (s^2+10s+102)I, S_+^2 \pm S_-^2\right]_+$
	±3	$c_\pm \left[11S_z^3 - (3s+59)S_z, S_+^3 \pm S_-^3\right]_+$
	±4	$c_\pm \left(11S_z^2 - (s+38)I, S_+^4 \pm S_-^4\right)_+$
	±5	$c_\pm \left[S_z, S_+^5 \pm S_-^5\right]_+$
	±6	$c_\pm \left(S_+^6 \pm S_-^6\right)$

Table 21: Extended Stevens operators O_k^q. The expression $[A,B]_+$ indicates the symmetrized products $(AB+BA)/2$ and $s = S(S+1)$, $c_+ = 1/2$ and $c_- = 1/2i$. The table was taken from [57].

These operators O_k^q are hermitian and their coefficient B_k^q is always real. The Stevens operators are a lineal combination of the spin Hamiltonian operators S_x, S_y and S_z. There are two types of Stevens operators: (i) the usual or conventional Steven operators, originally defined with $q \geq 0$ [93] and (ii) the extended Stevens operators introduced by Rudowicz in 1987 [94] with negative q [60]. In Table 21 the most common Stevens operators are listed.

In this thesis, iron with S=5/2 was investigated in lithium niobate as well as in lithium yttrium borate. In both cases, the high spin of iron possesses a fine structure splitting described by the extended Stevens operators. Depending on the host material symmetry, some extended Stevens operators are relevant [61]. In iron doped lithium niobate the spin Hamiltonian is written as:

$$\widehat{H}_{Fe^{3+}} = \mu_B \mathbf{B_0}^T \cdot \tilde{g} \cdot \widehat{\mathbf{S}} + B_2^0 O_2^0 + B_4^3 O_4^3 + B_4^0 O_4^0 + B_4^{-3} O_4^{-3}$$

In the last equation, B_k^q were fitted with EasySpin and the extended Stevens operators can be obtained from table 21:

$$\begin{aligned}
O_2^0 &= 3S_z^2 - S(S+1)\mathbb{1} \\
O_4^3 &= \frac{1}{2}\left\{\frac{S_z(S_+^3 + S_-^3) + (S_+^3 + S_-^3)S_z}{2}\right\} \\
O_4^0 &= 35S_z^4 - [30S(S+1) - 25]S_z^2 + \left[3S^2(S+1)^2 - 6S(S+1)\right]\mathbb{1} \\
O_4^{-3} &= \frac{1}{2i}\left\{\frac{S_z(S_+^3 - S_-^3) + (S_+^3 - S_-^3)S_z}{2}\right\}
\end{aligned}$$

Owing to the raising operators S_+ and S_-:

$$\begin{aligned}
S_+ &= S_x + iS_y \\
S_- &= S_x - iS_y
\end{aligned}$$

Then, O_4^3 and O_4^{-3} can be written:

$$O_4^3 = \frac{1}{2}\left[S_z S_x^3 - S_z S_y S_x S_y - S_z S_y^2 S_x - S_z S_x S_y^2 + S_x^3 S_z - S_y S_x S_y S_z - S_y^2 S_x S_z - S_x S_y^2 S_z\right]$$
$$O_4^{-3} = \frac{1}{2}\left[S_z S_x^2 S_y + S_z S_x S_y S_x + S_z S_y S_x^2 - S_z S_y^3 + S_x^2 S_y S z + S_x S_y S_x S_z + S_y S_x^2 S_z - S_y^3 S_z\right]$$

When the magnetic field is zero, only B_2^0 and B_4^0 contribute to the energy levels splitting. The reason is that O_2^0 and O_4^0 possess terms depending only on S, the total electronic spin of the system. In addition, B_2^0 has a larger influence on the energy levels splitting than B_4^0, because B_2^0 is a second order approximation and B_4^0 a fourth order approximation.

Applying a magnetic field, every term influences somehow in the energy levels for different considered orientations. For a static magnetic field parallel to the principal axis (z), the four extended Stevens operators depend on S_z, and therefore changes in B_k^q influence the energy levels splitting. Similarly, when the magnetic field is parallel to the x and y axis, only O_4^{-3} and O_4^3 depend on S_x and S_y. However, changes in B_2^0 and B_4^0 also affect the energy level splitting for a magnetic field parallel to x or y axis, because in B_2^0 and B_4^0 modify the energy levels at a zero magnetic field. Moreover, due to the glide mirror symmetry of iron in lithium niobate, changing the $+B_4^3$ sign to $-B_4^3$, the two centres (R and L) are obtained.

In iron doped lithium yttrium borate, the fine structure term is also described by the extended Stevens operators:

$$\widehat{H}_{Fe^{3+}} = \mu_B \mathbf{B_0}^T \cdot \tilde{g} \cdot \widehat{\mathbf{S}} + B_2^2 O_2^2 + B_2^0 O_2^0 + B_2^{-2} O_2^{-2} + B_4^4 O_4^4 + B_4^2 O_4^2 + B_4^0 O_4^0 + B_4^{-2} O_4^{-2} + B_4^{-4} O_4^{-4}$$

B_k^q were fitted using EasySpin and O_k^q operators are described in Table 21:

$$O_2^2 = \frac{1}{2}(S_+^2 + S_-^2)$$
$$O_2^0 = 3S_z^2 - S(S+1)\mathbb{1}$$
$$O_2^{-2} = \frac{1}{2i}(S_+^2 - S_-^2)$$
$$O_4^4 = \frac{1}{2}(S_+^4 + S_-^4)$$

$$O_4^2 = \frac{1}{2}\left[\frac{(7S_z^2-(S(S+1)+5)\mathbb{1})(S_+^2+S_-^2)+(S_+^2+S_-^2)(7S_z^2-(S(S+1)+5)\mathbb{1})}{2}\right]$$

$$O_4^0 = 35S_z^4-[30S(S+1)-25]\,S_z^2+\left[3S^2(S+1)^2-6S(S+1)\right]\mathbb{1}$$

$$O_4^{-2} = \frac{1}{2i}\left[\frac{(7S_z^2-(S(S+1)+5)\mathbb{1})(S_+^2-S_-^2)+(S_+^2-S_-^2)(7S_z^2-(S(S+1)+5)\mathbb{1})}{2}\right]$$

$$O_4^{-4} = \frac{1}{2i}(S_+^4-S_-^4)$$

Owing to the raising operators S_+ and S_-:

$$\begin{aligned} O_2^2 &= S_x^2-S_y^2 \\ O_2^{-2} &= i(S_xS_y-S_yS_x) \end{aligned} \tag{28}$$

D Coordinate frames

In order to describe the spin Hamiltonian properly, the relative orientation between the tensors frame and the laboratory frame should be clearly defined. The laboratory frame is referred to the fixed laboratory with the x_L, y_L and z_L axes. The z_L axis is, by universal convention, along the static magnetic field. The x_L axis is along the magnetic component of the frequency and y_L is perpendicular to x_L and z_L.

The crystal frame, which is fixed to the crystal, follows the x-ray convention. For a C_{2h} point group, y_C is along the unique axis and, for C_{3v} point group, z_C is along the three-fold axis and x_C is along one of the two-fold axis [57].

The tensor frame is the eigenframe of each tensor (g, A, D, etc.). Indeed, the g-, A-, D-tensor, etc. are diagonal in its eigenframe i.e. the tensor axes are aligned to the principal axes. Knowing the Euler angles that relate the tensor and crystal frames, the tensor (g, A, D, etc.) can be written in the cartesian coordinates of the crystal frame using a rotation matrix.

E Effective spin

In chapter 3 Methods, the EPR resonance condition ($h\nu = g_J \beta B$, Equation 1 in Chapter 3 Methods) and the spin-orbit coupling (J=L+S) were described. For a free atom, the Zeeman splitting leads to a group of (2J+1) levels degenerated when the magnetic field is zero (B=0 mT) and well separated from other levels ($g_J \beta B << \Delta$), where Δ is the energy difference from the next level or group levels [55].

Nevertheless, in solid state a paramagnetic ion is surrounded by diamagnetic ions (the nearest at distance of 0.2 to 0.3 nm). These charged "ligand" ions interact strongly with the paramagnetic ion, producing a strong electrostatic field (the "ligand" field), through which the paramagnetic electrons must move. The energy associated between the paramagnetic ion and the ligand field is about 100 - 10000 cm^{-1}. This produces a "Stark splitting" of the orbital levels of the paramagnetic ion. Electrons in the lowest energy level avoid the negatively charged ligand ions, thus reducing the energy due to their electrostatic repulsion. A more sophisticated approach is considering electrons no longer regarded as localized in the central ion, but shared with the ligand ions and spread out over the complex. Thus, electrons occupy molecular orbitals instead of atomic orbitals and may take part in both σ- and π-bonding. In any adopted approach, the result is a splitting of levels, leaving group with small degeneracy [55].

In electron paramagnetic resonance, the ground state of a paramagnetic ion frequently consists of a set of electronic levels with transitions of the order of few cm^{-1}, while the other electronic levels lie considerably higher. This is due to the ligand field interaction of the paramagnetic ions with the neighbouring diamagnetic ions or atoms in the crystals. The behaviour of the ground state group can be represented by an effective spin S′ with a (2S′+1) total number of levels. The effective spin S′ is a fictitious angular momentum that under a magnetic field splits into (2S′+1) energy levels. It is useful to set an "effective spin Hamiltonian" that describes correctly the behaviour of the group of levels in terms of a free atom or ion [16].

An example is erbium in LYB. The energy levels $^4I_{15/2}$ and $^4I_{13/2}$ are separated by an energy of more than 6000 cm^{-1}, while the separation between the electronic levels in the ground state ($^4I_{15/2}$) is from 30 cm^{-1} to 300 cm^{-1} [50]. In this case, erbium in LYB is described by an effective spin of $S' = 1/2$ and an anisotropic g-tensor ($g_{xx} \neq g_{yy} \neq g_{zz}$). Therefore, the degenerated energy levels at B=0 can be explained with an effective spin Hamiltonian like in Equation 11 in Chapter 3 Methods.

F Orbach-type spin-lattice relaxation process

In Chapter 4 Measurements, it was observed that EPR resonant peaks are broader at high temperature than at low temperature. This is due to the interaction between spin and lattice amongst each other by means of phonons. Suppose that the paramagnetic ion has a ground doublet at energies 0 and $h\nu$. Applying an oscillatory magnetic field of a determined frequency, transitions between levels are induced. The up transitions correspond to absorption of a quantum of energy from the radiation field, whereas the down transitions radiate energy to the radiation field by means of induced emission (see Figure 110) by the molecular motion of the solid, i.e. lattice vibrations [55].

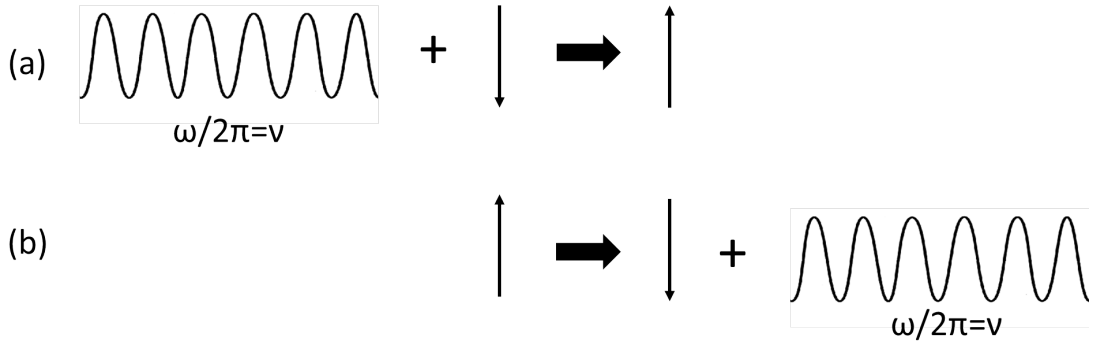

Figure 110: Schematic illustration of the direct process. (**a**) A phonon of magnetic resonance frequency ($\omega/2\pi = \nu$) is absorbed by a spin which makes a transition to the upper level. (**b**) A spin makes the transition to the lower level emitting a phonon at the resonant frequency. Redrawn from reference [55].

In order to attain thermal equilibrium, there must be some interaction between the spin system and the thermal fluctuations. Since the population between the levels can only be altered by transition between them, such transitions must be induced by the thermal fluctuations, i.e. molecular motion in the solid (lattice vibrations).

The Orbach process involves absorption of a phonon in a direct process to excite the spin system to a much higher level, at energy Δ, followed by the emission of another phonon of slightly different energy (see Figure 111). In this way, the magnetic ion is indirectly transferred from one level to the other within the ground level. This process has a strong temperature dependence, being determined by the number of phonons of energy Δ available to excite the ion to the upper state at Δ. Experimentally it is shown in the EPR resonance peak linewidth. The peak to peak linewidth

(ΔB) shows an Arrhenius type temperature dependence:

$$\Delta B = \Delta B_0 + Ce^{\left(\frac{-\Delta E_a}{kT}\right)} \tag{29}$$

Where ΔB_0 is the peak to peak linewidth at the lowest temperature, C is the coupling constant, ΔE_a the activation energy, k the Boltzman constant and T the measurement temperature [50].

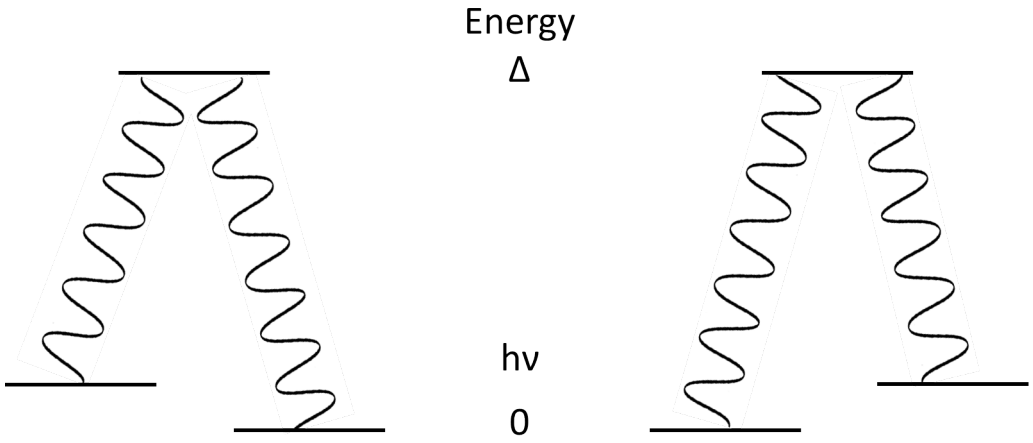

Figure 111: Schematic illustration of the Orbach process. The paramagnetic ion has a ground doublet with energies 0 and $h\nu$ and an excited state with energy Δ. Phonons at frequencies Δ and $(\Delta - h\nu)$ are absorbed and emitted by direct process, causing transitions between the ground doublet state and the excited state. Redrawn from reference [55].

G Hafnium doped lithium niobate

As it was already mentioned, lithium niobate has a wide range of applications in electro-optic and integrated optical devices. However, the optical damage worsens the applications of periodically poled lithium niobate crystals in optical communication devices. Therefore, optical resistant dopants are required to decrease the optical damage effects. In particular, doping congruent LN with MgO at molar concentrations between 5 mol % and 6 mol % was found to be very effective for reducing photorefraction. However, it is difficult to grown LN crystals with good optical properties with high doping concentrations (as in the case of MgO). On the other hand, it has been found that doping with HfO_2 is very effective in reducing the photorefraction and, in addition, hafnium doped LN crystals can be periodically poled during growth [95–97].

With the aim of investigating hafnium doped lithium niobate crystals by means of electron paramagnetic resonance, a sample was specifically grown for it (see Figure 112).

Figure 112: As grown hafnium doped nearly stoichiometric lithium niobate crystal. The sample is defined by the number **21304**. Pristine lithium niobate samples are rather transparent, although this sample was doped with hafnium, it is still transparent.

The sample was grown using the high temperature top seeded solution growth (HTTSSG) technique [52] at the Wigner Research Centre for Physics in Budapest (Hungary). It was doped with 0.2 mol % of Hf (see Figure 112). EPR measurements were performed at 5 K in a magnetic field range of almost 1 T, however, no resonance peaks were recorded, probably due to the small concentration.

Bibliography

[1] H. Söthe (1989) ENDOR-Untersuchungen zur Strukturbestimmung von Defekten in gestörter, ionischer Gitterumgebung (Doctoral dissertation).

[2] J.P. Nisius and E. Krätzig, Solid State Commun. 53 9 (1985) 743-746.

[3] J.A. Sanz-García, E. Dieguez, F.J. López and F. Argulló-López, Sol. State Commun. 72 12 (1989).

[4] V. Gericke, P. Hertel, E. Krätzig, J. P. Nisius and R. Sommerfeldt, Appl. Phys. B 44 (1987) 155-162.

[5] Z.D. Luo, H. Zhang, Y.D. Huang, M.W. Qiu, Y.C. Huang, C.Y. Tu, A.D. Jiang, Cryst. Res. Technol. 26 (1991) K5-K8.

[6] J. Sablayrolles, V. Jubera, J.-P. Chaminade, I. Manek-Hönninger, S. Murugan, T. Cardinal, R. Olazcuaga, A. García, F. Salin, Opt. Mater. 27 (2005) 1681-1685.

[7] Y. Zhao, X. Gong, Y. Lin, Z. Luo and Y. Huang, Mater. Lett. 60 (2006) 418-421.

[8] Y.W. Zhao, X.H. Gong, Y.J. Chen, L.X. Huang, Y.F. Lin, G. Zhang, Q.G. Tan, Z.D. Luo and Y.D. Huang, Appl. Phys. B 88, (2007) 51–55.

[9] M. Delaigue, V. Jubera, J. Sablayrolles, J.-P- Chaminade, A. Garcia and I. Manek-Hönninger, Mode-locked and Q-switched laser operation of the Yb-doped $Li_6Y(BO_3)_3$ crystal, Appl. Phys. B 87 (2007) 693–696.

[10] A. Brenier, A. Yoshikawa, K. Lebbou, A. Jouini, O. Aloui-Lebbou, G. Boulon and T. Fukuda, Growth and spectroscopic properties of Yb^{3+}-doped $Li_6Y(BO_3)_3$ single crystal.

[11] T. Volk and M. Whölecke. Lithium niobate. Defects, photorefraction and ferroelectric switching. Springer series in Material Science. Springer, (2008).

[12] R.S. Weis and T.K. Gaylord, Lithium niobate: summary of physical properties and crystal structure, Appl. Phys. A 37 (1985) 191-203.

[13] http://www.uvm.edu/ dahammon/Demonstrations/otherlattices.html

[14] A. Räuber, Chemistry and physics of lithium niobate, in: Current Topics in materials Science I, 481-601, (North Holland, Amsterdam, 1978).

[15] O.F. Schirmer, O. Thiemann and M. Wöhlecke, Defects in $LiNbO_3$-I. Experimental aspects, J. Phys. Chem. Solids 52, 1, 185-200 (1991).

[16] S.C. Abrahams and P. Marsh, Defect structure dependence on composition in lithium niobate, Acta Cryst. B42, 61-68 (1986).

[17] O.F. Schirmer and D. von der Linde, Appl. Phys. Lett. 33, 35(1978).

[18] O.F. Shirmer, M. Imlau, C. Merschjanm and B. Schoke, Electron small polarons and bipolarons in $LiNbO_3$, J. Phys.: Condens. Matter 21 (2009).

[19] V.G. Grachev, R.T.Petersen, E.P. Kokanyan, O.F. Shirmer and G.I. Malovichko, J. Appli. Phys. 120, 193901 (2016).

[20] H. Söthe and J.M. Spaeth, J. Phys.: Condensed Matter 4, 9901 (1992).

[21] G.I. Malovichko, V.G. Grachev, O.F. Schirmer, and B. Faust, J. Phys.: Condens. Matter 5, 3971 (1993).

[22] G.I. Malovichko, G. Grachev and S.N. Lukin, Soviet Phys. - Solid State 28, 553 (1986).

[23] T.H. Yeom, S.H. Choh, Y.M. Chang and C. Rudowicz, phys. stat. sol. (b) 186, No. 1 (1994).

[24] F. Mehran and B.A. Scott, Solid State Commun. 11, 15 (1972).

[25] H.H. Towner, Y.M. Kim, and H.S. Story, J. chem. Phys. 56, 3675 (1972).

[26] A. Böker, H. Donnerberg, O.F. Schirmer and Feng Xiqi, J. Phys.: Condens. Matter 2 (1990).

[27] D.J. Keeble, M. Loyo-Menoyo, Y. Furukawa, and K. Kitamura, Phys. Rev., B 71, 224111 (2005).

[28] R.C. Santana, M.C. Terrile, A.C. Hernandes, M.R.B. Andreeta, and G.E. Barberis, Solid State Commun. 103, 61–64 (1997).

[29] F. Zeng, P. Sheng, G.S. Tang, F.Pan, W.S. Zan, F.C. Hu, Y. Zou, Y.Y. Huang, Z. Jiang, D.Guo, Materials Chemistry and Physics 136 783 (2012).

[30] G.I. Malovichko and V.G. Grachev, Soviet Phys. - Solid State 27, 1678 (1985).

[31] W. Keune, S.K. Date, U. Gonser and H. Bunzel, Ferroelectreics, 13 (1976).

[32] A. Putzka and H.D. Pfannes, Ferroelectrics, 56 (1984).

[33] W. Hui, X. Kuang, D. Dong, Y. Xiong, K. Zhou, Physica B 367 53 (2005).

[34] J.B. Herrington, B. Dischler, and J. Schneider, Solid State Commun. 10, 509 (1972).

[35] A. Sanson, A. Zaltron, N. Argiolas, C. Sada, M. Bazzan, W. G. Schmidt, and S. Sanna, Phys. Rev. B 91, 094109 (2015).

[36] S.A. Basun, T.J. Evans, D.R. Bunning, S. Guha, J.O. Barnes, G. Cook, and R.S. Meltzer, J. Appl. Phys. 92, 7051 (2002).

[37] T. Vitova, J. Hormes, M. Falk, and K. Buse, J. Appl. Phys. 105,013524 (2009).

[38] L. Arizmendi and F. Agulló-López, MRS Bulletin 19 32 (1994)

[39] M. Kösters 2010, Optical cleaning of lithium niobate crystals (Doctoral dissertation). Retrieved from https://d-nb.info/100246174X/34

[40] M. Simon, St. Wevering, K. Buse and E. Krätzig, J. Phys. D: Appl. Phys. 30 144 (1997)

[41] M. V. Ciampolillo (2009), Diffusion of iron in lithium niobate for applications in integrated optical devices (Doctoral dissertation). Retrieved from paduare-search.cab.unipd.it/2922/1/MAIN.pdf

[42] M. Luennemann, K. Peithmann, U. Hartwig and K. Buse, Ukr. J. Phys. 49 5 (2004).

[43] J. Villarroel, J. Carnicero, F. Luedtke, M. Carrascosa, A. García-Cabanes, J.M. Cabrera, A. Alcazar and B. Ramiro, Opt. Express, 18 20 (2010).

[44] S. Juppe and O.F. Schirmer, Phys. Lett. A 117, 150 (1986).

[45] O. Thiemann, H. Donnerberg, M. Wöhlecke, and O.F. Schirmer, Phys. Rev. B 49, 5845 (1994).

[46] G. Corradi, I.M. Zaritskii, A. Hofstaetter, K. Polgár and L.G. Rakitina, Phys. Rev. B 58 13 (1998).

[47] A. Thomas (2010), Photon pair sources in periodically poled Ti:$LiNbO_3$ waveguides (Doctoral dissertation). Retrieved from https://d-nb.info/1036551563/34

[48] G. Corradi, M. Meyer, L. Kovács, and K. Polgár, Appl. Phys. B 78, 607 (2004).

[49] Á. Péter, K. Polgár, M. Tóth, J. Cryst. Growth 346 (2012) 69-74.

[50] L. Kovács, S. Arceiz Casas, G. Corradi, É. tichy-Rács, L. Kocsor, K. Lengyel, W. Ryba-Romanowski, A. Strzep, A. Sholle, S. Greulich-Weber, Opt. Mater. 72 (2017) 270-275.

[51] A. Watterich, P. Aleshkevych, M.T. Borowiec, T. Zayarnyuk, H. Szymczak, E. Beregi and L. Kovács, Optical and magnetic spectroscopy of rare-earth-doped yttrium aluminium borate ($YAl_3(BO_3)_4$) single crystals, J. Phys.: Condens. Matter 15 (2003) 3323–3331.

[52] K. Polgár, Á. Péter, L. Kovács, G. Corradi and Zs. Szaller, J. Crys. Growth 177 (1997) 211-216.

[53] S. Dagdale, V. PAhurkar and G. Muley, Macromol. Symp., 362 (2016) 139–141.

[54] J.-M. Spaeth, J.R. Niklas and R.H. Bartram, Structural analysis of point defects in solids, an introduction to multiple magnetic resonance spectroscopy, Springer Series of Solid State Sciences Vol. 43, Springer-Verlag, Heidelberg (1992)

[55] A. Abragam and B. Bleaney, Electron Paramagnetic Resonance of Transition Ions, Clarendon Press, Oxford (1970)

[56] M. Pohl (1998), Konstruktion un Bau eines EPR/ENDOR-Kryostaten (Doctoral dissertation).

[57] S. Stoll and A. Schwiger, J. Magn. Reson. 178 (2006) 42-55. Retrieved from http://easyspin.org/

[58] T. Nolte (1997), Lumineszenzeffekte in Silizium (Doctoral dissertation).

[59] M.G. Misra and R. Kripal, Molecular Physics, 110 24 (2012) 3001-3013.

[60] C. Rudowicz, J. Phys.: Condens. Matter 12 (2000) 417-423.

[61] H.A. Buckmaster and R. Chatterhee, Phys. Stat. Sol. B 209 (1998) 433-441.

[62] D.G. McGavin, J. Magn. Reson. 74 (1987) 19-55.

[63] S.K. Misra, J. Mag. Reson. 23 (1976) 403.

[64] S.K. Misra and S. Subramanian, J. Phys. C, 15 (1982) 7199-7207.

[65] S.K. Misra, Physica 121B (1983) 193-201.

[66] M.G. Clark, F.J. DiSalvo, A.M. Glass, and G.E. Peterson, Electronic structure and optical index damage of iron-doped lithium niobate, J. Chem. Phys., 59 12 (1973) 6209-6219.

[67] H. Kurz, E. Krätzig, W. Keune, H. Engelmann, U. Gonser, B. Dischler, and A. Räuber, Photorefractive centers in $LiNbO_3$ studied by optical, Mössbauer and EPR methods, Appl. Phys„ 12 (1977) 355-368.

[68] M. H. Yükselici, Ç. Allahverdi, and A. V. Tunç, Temperature shift of the Fe^{2+} absorption band in $LiNbO_3$:Fe crystal, Phys. Stat. Sol. (b) 241, 13 (2004) 3041–3046.

[69] L. Kovács, G. Ruschhaupt, K. Polgár, G. Corradi and M. Wöhlecke, Appl. Phys. Lett. 70 21 (1997) 2801-2803.

[70] M.C. Payne, M.P.Teter, D. C.Allan, T.A. Arias and J.D.Joannopoulos, Iterative minimization techniques for ab initio total-energy calculations: molecular dynamics and conjugate gradients, Reviews of Modern Physics, 64, 4 (1992) 1045-1097.

[71] S. Sanna (2007), (Doctoral dissertation).

[72] G. Kresse and J. Furthmüller, Phys. Rev. B 54, 11169 (1996).

[73] J. P. Perdew and W. Yue, Phys. Rev. B 33, 8800(R) (1986).

[74] S. Sanna, C. Dues and W.G. Schmidt, Modeling atomic force microscopy at $LiNbO_3$ surfaces from first-principles, Computational Materials Science 103 (2015) 145–150.

[75] G. Rollmann, A. Rohrbach, P. Entel, and J. Hafner, Phys. Rev. B 69, 165107 (2004).

[76] 8. H. H. Nahm and C. H. Park, Phys. Rev. B 78, 184108 (2008).

[77] 9. V. I. Anisimov, F. Aryasetiawan, and A. I. Lichtenstein, J. Phys.: Condens. Matter 9, 767 (1999).

[78] 10. S. L. Dudarev, G. A. Botton, S. Y. Savrasov, C. J. Humphreys, and A. P. Sutton, Phys. Rev. B 57, 1505 (1998).

[79] A. Zaltron (2010), Local doping of lithium niobate by iron diffusion: a study of photorefractive properties (Doctoral dissertation). Retrieved from http://paduaresearch.cab.unipd.it/3767/1/TESI_29-01-2010.pdf

[80] G. Mandula, Z. Kis, É. Tichy-Rács, K. Komlai, L. Kovács, K. Lengyel and G. Corradi, EURODIM 2014 conference.

[81] L.G. Ludwig and H.H Woodbury, Physical Review Letters, 5 3 (1960) 98-100.

[82] G.G DeLeo, GD. Watkins and W. Beall Fowler, Physical Review B, 23 4 (1981) 1851-1858.

[83] F. Beeler and O.K. Andersen, Phys. Rev. B 41, 3 (1989) 1603-1624.

[84] B. Dischler, J.R. Herrington, A. Räuber and H. Kurz, Solid State Communications, 14 (1974) 1233-1236.

[85] M. Esseling, A. Zaltron, N. Argiolas, G. Nava, J. Imbrog, I. Cristiani and C. Denz, Appl. Phys. B (2013) 191-197.

[86] H.J. Reyher, R. Schulz and O. Thiemann, Phys. Rev. B 50, 6 (1994) 3609-3619.

[87] G. Malovichko, V. Grachev, J. Jorgensen, M. Meyer, M. Munro, B. Todj, Ian Vrable, D. Kokanyan, V. Bratus and S. Okulov, Magnetic Resonance Study of Non-Equivalent Centers Created by 4f-Ions in Congruent and Stoichiometric Lithium Niobate, MRS Proceedings, 1111 D01-03 (2011).

[88] A. Konopka, S. Greulich-Weber, V. Dierolf, H.X. Jiang , U. Gerstmann, E. Rauls, S. Sanna and W.G. Schmidt, Microscopic structure and energy transfer of vacancy-related defect pairs with Erbium in wide-gap semiconductors, Optical Materials 33 (2011) 1041–1044.

[89] J. Sablayrolles, V. Jubera, F. Guillen, R. Decourt, M. Couzi, J.-P. Chaminade and A. Garcia, Opt. Commun. 280 (2007) 103-109.

[90] V. Jubera, M. Chavoutier, A. Artemenko, P. Veber, M. Velazquez and A. Garcia, ChemPhysChem 12 (2011) 1288-1293.

[91] H.G. Liu and W.C. Zheng, Theoretical investigations of the optical spectra and EPR parameters for the isolated and pairs of trivalent ytterbium ions in $Li_6Y(BO_3)_3$ crystal, Optical Materials 49 (2015) 337–342.

[92] I. Romet, M. Buryi, G. Corradi, E. Feldbach, V. Laguta, É. Tichy-Rács and V. Nagirnyi, Recombination luminescence and EPR of Mn doped $Li_2B_4O_7$ single crystals, Optical Materials 70 (2017) 184-193.

[93] K. W. H. Stevens, Matrix elements and operator equivalents connected with the magnetic properties of rare earth ions, Proc. Phys. Soc. 65, (1952) 209.

[94] C. Rudowicz, J. Phys. C: Solid State Phys., 20 (1987) 6033-6037.

[95] E.P. Kokanyan, L. Razzari, I. Cristiani, V. Degiorgio, J.B. Gruber, Appl. Phys. Lett. 84(11), 1880 (2004).

[96] L. Razzari, P. Minzioni, I. Cristiani, V. Degiorgio, E.P. Kokanyan, Appl. Phys. Lett. 86(13), 131914 (2005).

[97] P. Minzioni, I. Cristiani, J. Yu, J. Parravicini, E.P. Kokanyan, V. Degiorgio, Optics Express 15, 14171 (2007).

List of publications

Related to the present thesis:

- Arceiz Casas, S. (July 2016). EPR and DFT investigation of Fe and Fe-Ti doping in LiNbO3. ICDIM (International conference on defects in insulating materials) 2016, Lyon (France).
- Arceiz Casas, S. (July 2016). EPR spectroscopy of Er3+ in lithium yttrium borate (LYB) single crystals. ICDIM (International conference on defects in insulating materials) 2016, Lyon (France).
- Arceiz Casas, S. (March 2017). EPR and DFT investigation of Fe and Fe-Ti doping in LiNbO3. DPG-Frühjahrstagung 2017, Dresden (Germany).
- Arceiz Casas, S. (March 2017). EPR spectroscopy of Yb3+ in lithium yttrium borate (LYB). DPG-Frühjahrstagung 2017, Dresden (Germany).
- L. Kovács, S. Arceiz Casas, G. Corradi, É. Tichy-Rács, L. Kocsor, K. Lengyel, W. Ryba-Romanowski, A. Strzep, A. Sholle, S. Greulich-Weber, Opt. Mater. 72 (2017) 270-275.

Previous to the dissertation work:

- S. Greulich-Weber, S. Arceiz and N. Weber, Low temperature nanocrystalline zinc oxide for photovoltaic applications, IOP Conf. Series: Materials Science and Engineering 80 (2015).